

STUDY ON CHEMICAL REDUCTION OF GRAPHENE OXIDE INTO GRAPHENE – THEIR PHYSICOCHEMICAL BEHAVIOR

Ph. D. THESIS

by

MAHIMA KHANDELWAL



**DEPARTMENT OF CHEMISTRY
INDIAN INSTITUTE OF TECHNOLOGY ROORKEE
ROORKEE- 247 667 (INDIA)
DECEMBER, 2015**

**STUDY ON CHEMICAL REDUCTION OF GRAPHENE
OXIDE INTO GRAPHENE – THEIR PHYSICOCHEMICAL
BEHAVIOR**

A THESIS

*Submitted in partial fulfilment of the
requirements for the award of the degree
of*

DOCTOR OF PHILOSOPHY

in

CHEMISTRY

by

MAHIMA KHANDELWAL



**DEPARTMENT OF CHEMISTRY
INDIAN INSTITUTE OF TECHNOLOGY ROORKEE
ROORKEE- 247 667 (INDIA)
DECEMBER, 2015**

**©INDIAN INSTITUTE OF TECHNOLOGY ROORKEE, ROORKEE–2015
ALL RIGHTS RESERVED**



INDIAN INSTITUTE OF TECHNOLOGY ROORKEE ROORKEE

CANDIDATE'S DECLARATION

I hereby certify that the work which is being presented in this thesis entitled “**STUDY ON CHEMICAL REDUCTION OF GRAPHENE OXIDE INTO GRAPHENE – THEIR PHYSICOCHEMICAL BEHAVIOR**” in partial fulfilment of the requirements for the award of the Degree of Doctor of Philosophy and submitted in the Department of Chemistry of the Indian Institute of Technology Roorkee is an authentic record of my own work carried out during a period from July, 2010 – December, 2015 under the supervision of Dr. Anil Kumar, Professor, Department of Chemistry and Dr. R. Nath, Professor, Department of Physics, Indian Institute of Technology Roorkee, Roorkee.

The matter presented in this thesis has not been submitted by me for the award of any other degree of this or any other Institute.

(**MAHIMA KHANDELWAL**)

This is to certify that the above statement made by the candidate is correct to the best of our knowledge.

(Anil Kumar)
Supervisor

(R. Nath)
Supervisor

The Ph.D. Viva-Voce Examination of **Mahima Khandelwal**, Research Scholar, has been held on

Chairman, SRC

Signature of External Examiner

This is to certify that the student has made all the corrections in the thesis.

Signature of Supervisor(s)

Head of the Department

Dated: _____

ABSTRACT

Over the last two decades nanoscience and nanotechnology have grown up in both fundamental research and emerging technologies. An enormous development in these areas has made intense societal impact. The physicochemical properties of nanomaterials viz. ceramics, semiconductors and metals, can be modulated due to quantum confinement and surface effects. When the size of the material is reduced either less than or equal to the magnitude of de Broglie wavelength, the quantum confinement effect starts controlling their physicochemical properties. The physicochemical properties of the nanomaterials could also be manipulated/enhanced extensively by modification/passivation of their surface. These effects have been extensively explored for their applications in wide ranging multidisciplinary areas viz. electronics, energy, environment and health. All these factors allowed fabricating nanomaterials at the atomic or molecular level to develop new nanostructures with tunable properties.

These advancements have been further strengthened by the discoveries of variety of carbon nanomaterials such as fullerenes, carbon nanotubes, and graphene. In this area, a spectacular growth has taken place, contributed by various factors such as varied bonding configurations, dimensionalities, aspect ratios, chirality, tunable band gaps, and presence of surface defects/edge chemistry. After the ground breaking experiment in 2004 by K. S. Novoselov and A. K. Geim on the discovery of graphene, which fetched them to the noble prize of physics in 2010, the research on graphene has attracted global attention. This material due to its remarkable properties and tremendous potential for wide ranging applications has generated a wave of excitement among the researchers in the 21st century. It has made carbon based research as one of the most enthralling topics in the materials research.

Graphene due to its unique optical, electrical, electronic, mechanical, thermal and electrochemical properties finds its diversified applications in sensing, field effect transistors, catalysis, light emitting diodes, NEMS, transparent conductive electrode, Li-ion batteries and supercapacitors. A number of protocols are being pursued for enhancing its physicochemical properties such as changing their morphology, doping and making its nanocomposites with metals, semiconductors and chalcogenides.

A number of physical and chemical methods have been adopted for the synthesis of graphene. Chemical methods have been widely employed due to the ease of synthesis, a better control on their size and shape by carrying out desired functionalization. Among different chemical methods, chemical reduction of graphene oxide (GO) for the production of graphene has been considered to be one of the most effective approaches because of its being economical, easy manipulation and bulk production. The literature survey on these systems revealed that a large number of reducing agents have been employed to perform the reduction of GO to yield graphene. But several of these are of corrosive nature. Thus it required to develop protocols which make use of mild/environmental friendly reducing agents. It also needs to carry out a systematic exploration of the effect of different parameters for controlling their physicochemical behavior.

In view of the above gaps, the present thesis work explores relatively mild/environmental friendly reducing agent(s) for the reduction of GO to produce graphene. The effect of various parameters such as concentrations of precursor(s), pH of the media considering its effect on the nucleophilicity of reducing agent(s) and heating time have been investigated systematically by performing the reduction of GO at relatively lower temperature. Based on the analysis of the physicochemical behavior, their possible applications have been suggested.

The entire work presented in this thesis has been divided into six chapters. A brief account of the contents of these chapters has been furnished below:

The *first chapter* presents a brief introduction on variety of nanomaterials investigated over last two decades. These nanomaterials have been categorized into ceramics, semiconductors, metallic and carbonaceous nanomaterials. A brief description of ceramics, metallic and semiconductor nanostructures about their present status has been discussed. A specific emphasis has been made on carbon nanostructures and these have been classified on the basis of their dimensionalities with a brief description of each of the categories. In the later sub section of carbon nanomaterials, graphene and its various factors that leads to the change in their physicochemical properties have been discussed more elaborately. This chapter also enumerates the objectives of the present work along with their brief outcome.

The *second chapter* furnish experimental details of the used materials/reagents, equipment and techniques. The as-synthesized graphene nanostructures have been characterized in terms of their optical, structure, morphology, electrical and electrochemical properties by making use of advanced analytical techniques such as Ultraviolet-Visible (UV-Vis), Raman, X-ray diffraction (XRD), atomic force microscopy (AFM), field emission scanning electron microscopy (FESEM), transmission electron microscopy (TEM), Fourier transform infrared (FTIR), ^{13}C solid-state magic angle spinning (MAS) nuclear magnetic resonance (NMR), X-ray photoelectron spectroscopy (XPS), current-voltage (I-V) and cyclic voltammetry (CV). A brief account of the methodologies used for performing their characterization, different equations and formulae used for the data analyses have been provided. It also includes the experimental procedure used for the synthesis of GO and general procedure used for the modification of working electrode.

The *third chapter* presents the synthesis of ultrathin graphene sheets (GRH-MA) employing malonic acid as a reducing agent under mild experimental conditions. Optical, infrared and Raman spectroscopy, increased C/O ratio in FESEM and TEM analyses indicate the effective reduction of GO. This observation is also supported by the XPS and ^{13}C solid-state NMR spectra which exhibited an increase in the graphitic character. AFM analysis gives their thickness to be 0.41 ± 0.03 nm. For GRH-MA, I-V measurements showed about four orders of magnitude higher conductivity (4.4 S/cm) as compared to that of GO (3.05×10^{-4} S/cm). Under similar experimental conditions, the reduction of GO by oxalic acid (GRH-Ox) was observed to take relatively much longer heating time (9 h) and it was also indicated to be less efficient by optical, Raman spectroscopy, and I-V measurements. The efficient reduction of GO by malonic acid is thus understood by the presence of active methylene group, which makes it as an effective nucleophile. XRD of GRH-MA sheets exhibited the 'd' spacing of 0.36 nm and annealing of this sample at a mild temperature of $300\text{ }^{\circ}\text{C}$ (GRH-MA300) reduced the interlayer spacing to 0.35 nm suggesting the increased ordering of graphene sheet upon annealing. This observation is also supported by HRTEM analysis of GRH-MA300 which showed a similar 'd' spacing of 0.35 ± 0.01 nm with hexagonal structure. IR analysis of this sample exhibited a significant reduction in the oxygen functionalities and I-V measurement showed more than 4-fold increase in conductivity (18.1 S/cm) as compared to that of GRH-MA (4.4 S/cm). Galvanostatic charge-discharge measurements of GRH-MA shows the high specific capacitance (C_s) value of 220 F/g at 1 A/g which is much higher to that of GO (2.5 F/g at 1 A/g). Moreover, it also shows fairly good cyclic stability for 1000 cycles of charge-discharge at 10 A/g. It also exhibited the energy density of 15.35 Wh/kg at a power density of 3947 W/kg having fairly high coulombic efficiency of 100-101%. These features clearly demonstrate its potential for energy storage applications.

The *fourth chapter* presents a novel one-step wet chemical approach to synthesize graphene nanoribbons (GNRs) by the reduction of GO using malonic acid as a reducing agent. The optical, XRD, HRTEM, Raman, IR, XPS and ^{13}C NMR demonstrated the effective reduction of GO. FESEM analysis indicated the formation of curled and entangled graphene nanoribbons which is found to be 150-300 nm wide by TEM measurements. The average thickness of GNRs has been estimated by AFM at 3.3 ± 0.2 nm, which is reduced significantly to 1.1 ± 0.5 nm upon its annealing at 300°C (GNRs-300). In the process of nucleation and growth, the intermediate(s) formed between the malonic acid and GO undergo twisting/folding involving supramolecular interactions. In the process of self assembly it yields ~ 0.15 to 1 mm long curled GNRs. ^{13}C NMR demonstrates a significant increase in sp^2 character of nanoribbons following the order: $\text{GO} < \text{GNRs} < \text{GNRs-300}$ as was also evidenced by the conductivity measurements which also followed the same order. GNRs exhibited high C_s value of 301 F/g at 1 A/g with good cyclic stability for 4000 charge-discharge cycles at 15 A/g, and high energy density/power density (16.84 Wh/kg/5944 W/kg) having coulombic efficiency of 100% in aqueous electrolyte demonstrating their tremendous potential as electrode material for energy storage applications.

The *fifth chapter* has been divided into two sections. Section A reports the one-pot synthesis of N-doped graphene-Ag nanocomposites (GRH-GlyAg) involving *in-situ* generation of Ag nanoparticles (NPs). The simultaneous reduction of GO and Ag^+ to produce GRH-GlyAg has been achieved under mild reaction conditions using environmental benign reducing agent, glycine, in aqueous medium without adding any external stabilizer. XRD and selected area diffraction (SAED) analyses revealed the presence of Ag in face-centered cubic (fcc) structure. HRTEM analysis shows the 'd' spacing of 0.236 nm corresponding to the highest intense (111) plane of Ag matching to the fcc structure. The N-

doping of graphene and its uniform decoration by Ag NPs (with an av. dia. of 17.5) in GRH-GlyAg with relatively low surface atomic % of Ag (0.309) is evidenced by TEM and XPS analyses, respectively. Raman spectroscopy also revealed the decoration of GRH-Gly with Ag NPs resulted in the enhancement of the D and G bands by about 365%. The presence of Ag in GRH-GlyAg prevents the folding of graphene and is assigned due to the supramolecular interactions of Ag with different moieties of N. It was further evidenced by IR, ^{13}C NMR and XPS analyses of GRH-GlyAg, which resulted in the enhancement of its surface area and electrical conductivity as compared to that of GRH-Gly. The presence of Ag NPs on GRH-Gly increased the current response in cyclic voltammetry by more than seven-fold as compared to that of GRH-Gly. These nanocomposites exhibited fairly high SERS activity for 4-aminothiophenol, employed as the probe molecule and allowed its detection at 50 nM concentration even for the fairly small sized Ag NPs used in the present work.

Section B of this chapter describes the 2-aminoisobutyric acid (AIB), a derivative of glycine, mediated functionalization and reduction of GO using an environmental benign protocol for producing N-doped graphene. The reduction of GO by AIB occurs efficiently in both acidic and mild basic pH conditions. Relatively faster reduction by AIB at pH 10.5 (3 h) compared to that at pH 4.5 (7 h) has been attributed to the increased nucleophilicity of amino and carboxyl groups. The reduction of GO by AIB was also found to be more efficient than to that of glycine at both high and low pH(s). The reduction of GO to graphene by using AIB as a reducing agent at pH 10.5 is indicated by the optical and IR studies, which is further evidenced by ^{13}C solid-state MAS NMR and XPS spectroscopy. AFM, FESEM and TEM studies exhibit the formation of graphene sheets. SAED and HRTEM analyses suggest crystalline nature of these sheets and its 'd' spacing was estimated to be 0.38 nm, respectively. The as-synthesized N-doped graphene exhibits high

conductivity (6.3 S/cm) as compared to that of GO (2.7×10^{-4} S/cm) suggesting the restoration of graphitic character. IR, Raman, ^{13}C NMR and XPS suggested the functionalization of graphene with N. An increase in $I_{\text{D}}/I_{\text{G}}$ ratio for GRH-AIB (1.02) compared to GO (0.89) suggests an increase in the number of smaller sp^2 domains. GRH-AIB exhibited high C_s value of 228 F/g at 1 A/g with fairly good cyclic stability for 1000 cycles at 10 A/g. It also exhibited high energy density value of 20.26 Wh/kg at a power density of 400 W/kg. These features suggest its potential for energy storage applications. A mechanism for the functionalization and reduction of GO by amino acids is discussed.

The *sixth chapter* presents the conclusions arrived from third, fourth and fifth chapters. A comparison of the effect of precursors and reaction conditions on the morphology and physicochemical properties of the as-synthesized graphene nanostructures will be presented. Based on these properties their applications for energy storage devices and sensing have been suggested.

The future directions for this type of work have also been proposed.

ACKNOWLEDGEMENTS

I would like to thank **GOD** for His blessings and constant grace without which this work would never have been accomplished.

Foremost, I would like to express my deepest gratitude to my supervisor **Dr. Anil Kumar**, Professor & Head, Department of Chemistry, Indian Institute of Technology Roorkee, Roorkee. I am really indebted to my supervisor for his cool temperament, continuous support, patience, motivation, enthusiasm, and immense knowledge. His simplicity and positive attitude always inspired and encouraged me throughout my research work. His invaluable guidance, backed up by deep knowledge and experience has widened my horizon as a researcher. The critical analysis, comments and suggestions rendered by him during the discussions are highly appreciated.

I would also like to thank my other supervisor **Dr. R. Nath**, Professor, Department of Physics Indian Institute of Technology Roorkee, Roorkee for his continuous support.

I am thankful to the members of my Student Research committee, Prof. Mala Nath (Chairman), Prof. V.K. Gupta (Former Chairman), Prof. Anjan Sil (External member), Prof. Vijaya Aggarwala (Former External Member) and Prof. S.M. Sondhi (Internal member) for their invaluable suggestions, support, time and encouragement throughout my research work. I sincerely express my gratitude towards the present and the former Heads of the Department of Chemistry, I.I.T. Roorkee, for providing me the vast and advanced research facilities to accomplish this research work.

I would also like to express my heartfelt gratitude to Prof. M.R. Maurya, (Chairman, Departmental Research Committee), Prof. U.P Singh (Former Departmental Research Committee Chairman) for their warm personal approach, encouragement, insightful comments throughout this research work.

I will always be thankful to **Prof. T. Pradeep**, Department of Chemistry, Indian Institute of Technology, Madras, Chennai, India. His encouragement and constant guidance helped me to venture into the amazing world of nanoscience, in a short span while working under him in a project. It was an enlightening experience. I would also like to thank Mrs. Anita Maheshwari, my supervisor's wife for her affection, care and providing homely feeling.

I also thank to the present and previous Heads of Institute Instrumentation Centre, I.I.T. Roorkee, Roorkee for providing the instrumental facilities such as FESEM, AFM, XRD, TEM and TGA. Here, I would also like to mention the names of S. D. Sharma sir, Virendra Dutt sir, Shiv Kumar sir, Anil Kumar Saini sir and Mr. Mukesh who helped me during the operation of these instruments.

I would like to acknowledge the help of Dr. Balasubramanian Viswanathan, Emeritus Professor, Indian Institute of Technology Madras, Chennai for recording the XPS data for a few samples. I also acknowledge the help of Mr. Rahul Bhardwaj, University of Delhi, New Delhi for recording TEM and HRTEM images for a few samples. I would also like to thank Mr. Harsh, University of Delhi, New Delhi for recording Raman data for two samples.

I am thankful to Mr. Abdul Haq, Mr. Meena and Mr. Pankaj for their technical assistance and timely help in the Department of Chemistry. Thanks are also due to the staff in the Department, especially to S. P. Singh sir and K. C. Tiwari sir for all the official help. I would like to sincerely thank to Madanpal ji, Ramesh ji, Tilakram ji, Amar Singh ji, Manoj ji, Deepak, Ankur, Ashu, and Rohit for their timely help.

I sincerely express my thanks to my seniors Dr. Vinit Kumar, Dr. Reshma Rani, Dr. Sudhir Kumar Gupta, Dr. Bhupendra Singh and Mr. Umesh Gaur for their suggestions and co-operation during this work. I would like to extend my thanks to my batchmate and dear

juniors Mandeep Kaloti, Komal Gupta, Priyanka and Sahil Thareja for their co-operation and joyful company. Here, I would also like to acknowledge my ex-juniors Anuj, Linu, Queeny, Kanchan, Neetu, Harsh, Sneha, Avdhesh and Kriti.

I would like to extend my appreciation and heartfelt thanks to **Dr. Jolly Puri** for being a true friend and making me smile in tough times. Her selfless affection, help and care are the only reasons behind my joyful stay at Roorkee. Her valuable suggestions and continuous support helped me a lot for the smooth completion of this work. She always spared time for me and my work from her research work. I enjoyed the sweet relationship with her and I will always remember the fun we had together. This work was doubtfully possible without her support. I will always be thankful to my dear friends Sweety Rathi, Richa Pahuja, Mridula and Rashmi Rani, for their cheerful company and moral support throughout this period. I would also like to express my heartfelt thanks to Mrs. Anuradha Mehta and Mr. Rajesh Mehta for their affection and providing homely feeling at Roorkee.

This acknowledgement will be incomplete without thanking my parents, **Mr. Atul Kumar Khandelwal** and **Mrs. Uma Khandelwal** for their patience, love, support and faith in me. I would also like to thank my elder sister **Sonam Khandelwal** and jiju **Prateek Khandelwal** and younger brother **Sandeep Khandelwal**. I dedicate this thesis to my parents who always gave me freedom to do whatever I wanted to and always backed up with my decision. I would like to especially thank my elder sister who has always been there to dispense all my responsibilities at home and encouraged me at each and every stage of this journey to achieve my goals.

The financial assistance from Ministry of Human Resource and Development, (MHRD), New Delhi, India is also gratefully acknowledged.

Dated: December, 2015

(MAHIMA KHANDELWAL)

LIST OF RESEARCH PUBLICATIONS

Research Papers Published/Communicated to Journals:

1. A. Kumar and **M. Khandelwal**, “Amino acid mediated functionalization and reduction of graphene oxide- synthesis and formation mechanism of N-doped graphene”. *New Journal of Chemistry*, 38, 3457-3467, 2014.
2. A. Kumar and **M. Khandelwal**, “A novel synthesis of ultra thin graphene sheets for energy storage applications using malonic acid as a reducing agent”. *Journal of Materials Chemistry A*, 2, 20345-20357, 2014.
3. **M. Khandelwal** and A. Kumar “One-step wet chemical synthesis of graphene nanoribbons from graphene oxide for their high performance supercapacitor applications” *Journal of Materials Chemistry A*, 3, 22975-22988, 2015.
4. **M. Khandelwal** and A. Kumar “One-step environmental friendly amino acid mediated synthesis of N-doped graphene-silver nanocomposites with enhanced multifunctional behavior” (**Communicated**).
5. **M. Khandelwal** and A. Kumar “High performance supercapacitor applications of N-doped graphene” (**Under preparation**)

Conferences participated/attended:

1. **Malonic acid mediated synthesis of one-atom thick graphene sheets and its supercapacitor applications**” presented in the 5th International Conference on “**Recent Trends in Applied Physical, Chemical Sciences, Mathematical/Statistical and Environmental Dynamics**” Organized by “Krishi Sanskriti” at Jawaharlal Nehru University, New Delhi, 2-3rd May, 2015.
2. “**Recent trends in Instrumental Methods of Analysis**” at Department of Chemistry, I.I.T. Roorkee, India, February 18 – 20, 2011.

LIST OF ABBREVIATIONS

nm	nanometer
cm	centimeter
μm	micrometer
mm	millimeter
mL	millilitre
nM	nanomolar
min	minute
s	second
h	hour
a.u	arbitrary unit
V	voltage
kV	kilovolt
eV	electron volts
mV/s	millivolts per second
g	gram
mg	milligram
mg/mL	milligram per milliliter
mg/cm^2	milligram per square centimeter
N/m^2	Newton per square meter
kg	kilogram
Hz	hertz
kHz	kilohertz
MHz	megahertz
A	current
TPa	terapascal
GPa	gigapascal
W/kg	watt per kilogram
Wh/kg	watt-hour per kilogram
L	litre
E	energy density
P	power density

S/cm	Seimens per centimeter
Ω .m	ohm.meter
Ω .cm	ohm.centimeter
F/g	Faraday per gram
σ	conductivity
ρ	resistivity
λ	wavelength
η	Coulombic efficiency
T_d	discharging time
T_c	charging time
K	kelvin
W/m.K	watts per meter kelvin
V.s	Volt.second
av.	average
dia.	diameter
no.	number
conc.	concentrated
fcc	face-centered cubic
rpm	revolutions per minute
HET	heterogeneous electron transfer
CVD	chemical vapor deposition
NPs	nanoparticles
LEDs	light emitting diodes
CV	cyclic voltammetry
C_s	specific capacitance
SPR	surface plasmon resonance
SERS	surface-enhanced Raman scattering
EM	electromagnetic
CM	chemical
CNTs	carbon nanotubes
GQDs	graphene quantum dots
GNRs	graphene nanoribbons
SWNTs	single-walled carbon nanotubes

DWNTs	double-walled carbon nanotubes
MWNTs	multi-walled carbon nanotubes
QHE	quantum hall effect
EDLC	electric double layer capacitance
GO	graphene oxide
UV-Vis	Ultraviolet-Visible
XRD	X-ray diffraction
XPS	X-ray photoelectron spectroscopy
SAED	selected area electron diffraction
MAS	magic angle spinning
NMR	nuclear magnetic resonance
AFM	atomic force microscopy
TEM	transmission electron microscopy
HRTEM	high resolution transmission electron microscopy
FTIR	Fourier transform infrared
FESEM	field emission scanning electron microscopy
rGO	reduced graphene oxide
CCD	charge-coupled detector
EDAX	energy dispersive X-ray analysis
GCD	galvanostatic charge-discharge
DIW	deionized water
4-ATP	4-aminothiophenol
AIB	2-aminoisobutyric acid
GCE	glassy carbon electrode
TGA	thermogravimetric analysis
I-V	current-voltage
DLS	dynamic light scattering
ITO	Indium titanium oxide
FWHM	full width half maximum

Sample(s)	Composition
GO	graphene oxide (0.5 mg/mL)
GRH-MA	graphene synthesized by using malonic acid at pH 10.5
GRH-MA300	GRH-MA annealed at 300 °C
GRH-Ox	graphene synthesized by using oxalic acid at pH 10.5
GRH-OH ⁻	graphene synthesized by using NaOH at pH 10.5
GNRs	graphene nanoribbons synthesized by using malonic acid at pH 6.0
GNRs-300	GNRs annealed at 300 °C
GRL-Ox	graphene synthesized by using oxalic acid at pH 6.0
GRL	graphene synthesized by using NaOH at pH 6.0
GRH-Gly	graphene synthesized by using glycine at pH 10.5
GRH-GlyAg	graphene-Ag nanocomposites synthesized by using glycine and Ag ⁺ at pH 10.5
GO-Ag	graphene oxide-Ag nanocomposites synthesized by using Ag ⁺ at pH 10.5
Gly-Ag	Ag NPs synthesized by using glycine at pH 10.5
GRH-AIB	graphene synthesized by using 2-aminoisobutyric acid at pH 10.5
GRL-AIB	graphene synthesized by using 2-aminoisobutyric at pH 4.5
GRL-Gly	graphene synthesized by using glycine at pH 4.5

TABLE OF CONTENTS

ABSTRACT	i
ACKNOWLEDGEMENTS	ix
LIST OF RESEARCH PUBLICATIONS	xiii
LIST OF ABBREVIATIONS	xv
TABLE OF CONTENTS	xix
CHAPTER 1	
INTRODUCTION	1
1.1 Ceramic Nanomaterials.....	3
1.1.1 Nanoceramic Oxides.....	3
1.1.2 Non-oxide Nanoceramics.....	5
1.1.3 Ceramic Nanocomposites.....	6
1.2 Semiconductor Nanomaterials.....	7
1.3 Metal Nanoparticles.....	10
1.3.1 Silver Nanostructures.....	12
1.4 Carbonaceous Nanomaterials.....	13
1.4.1 Fullerenes.....	15
1.4.2 Carbon Nanotubes (CNTs).....	17
1.4.3 Graphene.....	19
1.4.3.1 Introduction.....	19
1.4.3.2 Physicochemical Properties.....	21
1.4.3.3 Graphene for Energy Storage Applications-Supercapacitor..	24
1.4.3.4 Synthesis of Graphene.....	27
1.4.3.5 Graphene Nanoribbons.....	34
1.4.3.6 Doping of Graphene.....	37
1.4.3.7 Graphene Nanocomposites.....	42
CHAPTER 2	
EXPERIMENTAL SECTION	47
2.1 Materials and Reagents.....	47
2.2 Equipment.....	47

2.2.1 UV-Visible Spectrophotometer.....	47
2.2.2 X-ray Diffractometer (XRD).....	47
2.2.3 Raman Spectrometer.....	48
2.2.4 Zetasizer.....	49
2.2.5 Atomic Force Microscopy (AFM).....	50
2.2.6 Field Emission Scanning Electron Microscopy (FESEM).....	51
2.2.7 Transmission Electron Microscope (TEM).....	52
2.2.8 Fourier Transform Infrared (FTIR) Spectrophotometer	52
2.2.9 Nuclear Magnetic Resonance (NMR).....	53
2.2.10 X-ray Photoelectron Spectroscopy (XPS).....	54
2.2.11 Surface Area Analyzer.....	54
2.2.12 Thermogravimetric Analysis (TGA).....	54
2.2.13 Current-Voltage (I-V) Measurements	55
2.2.14 Electrochemical Measurements.....	55
2.2.15 pH Meter.....	56
2.2.16 Refrigerated Circulating Water Bath.....	56
2.2.17 Centrifuge.....	57
2.2.18 Vacuum Oven.....	57
2.2.19 Furnace.....	57
2.2.20 Hot Plate.....	57
2.2.21 Sonicator.....	58
2.2.22 Ultrasensitive Balance.....	58
2.3 Methodology.....	58
2.3.1 UV-Vis Spectrophotometer.....	58
2.3.2 XRD.....	58
2.3.3 Raman Spectrometer.....	59
2.3.4 AFM.....	60
2.3.5 FESEM.....	60
2.3.6 TEM.....	61
2.3.7 BET Measurements.....	61
2.3.8 NMR and XPS Measurements.....	61
2.3.9 I-V Measurements.....	61
2.3.10 Electrochemical Measurements.....	62

2.3.11 Synthesis of Graphene Oxide (GO).....	63
2.3.12 Modification of Working Electrodes.....	65

CHAPTER 3

SYNTHESIS OF ULTRA THIN GRAPHENE SHEETS USING MALONIC ACID AS A REDUCING AGENT FOR ENERGY STORAGE APPLICATIONS 67

3.1 Optimization of Various Parameters for the Effective Reduction of GO to Synthesize Graphene Sheets.....	68
3.1.1 Optimization of the Amount of Malonic Acid.....	68
3.1.2 Optimization of the Heating Time	69
3.1.3 Optimization of the pH	70
3.1.4 Synthesis of Graphene under Optimized Reaction Conditions.....	70
3.2 Characterization of Graphene Sheets (GRH-MA).....	71
3.2.1 Optical Studies.....	71
3.2.2 Raman Spectroscopy.....	73
3.2.3 XRD Studies.....	75
3.2.4 AFM Analysis.....	76
3.2.5 FESEM Analysis.....	77
3.2.6 TEM and SAED Analysis.....	80
3.2.7 FTIR Spectroscopy.....	82
3.2.8 XPS Studies.....	83
3.2.9 Solid-State ¹³ C NMR Spectroscopy.....	84
3.2.10 TGA Measurements.....	85
3.2.11 I-V Measurements.....	86
3.2.12 Electrochemical Studies.....	87
3.3 Discussion.....	90

CHAPTER 4

ONE-STEP CHEMICALLY CONTROLLED WET SYNTHESIS OF GRAPHENE NANORIBBONS FROM GRAPHENE OXIDE FOR HIGH PERFORMANCE SUPERCAPACITOR APPLICATIONS 99

4.1 Optimization of Various Parameters for the Reduction of GO to Produce Graphene Nanoribbons.....	100
---	-----

4.1.1 Amount of Malonic Acid.....	100
4.1.2 Optimization of the Heating Time	100
4.1.3 Optimization of the pH	101
4.1.4 Synthesis of Graphene Nanoribbons under Optimized Reaction Conditions.....	102
4.2 Characterization of Graphene Nanoribbons (GNRs).....	102
4.2.1 Optical Spectra.....	102
4.2.2 XRD Studies.....	104
4.2.3 AFM Analysis.....	105
4.2.4 FESEM Analysis.....	106
4.2.5 TEM and SAED Analysis.....	109
4.2.6 FTIR Spectroscopy.....	111
4.2.7 Raman Spectroscopy.....	112
4.2.8 XPS Analysis.....	114
4.2.9 Solid-State ¹³ C NMR Spectroscopy.....	116
4.2.10 I-V Measurements.....	117
4.2.11 Electrochemical Measurements.....	118
4.3 Discussion.....	122

CHAPTER 5 (SECTION A)

GLYCINE MEDIATED SYNTHESIS OF N-DOPED GRAPHENE AND ITS SILVER NANOCOMPOSITES WITH ENHANCED MULTIFUNCTIONAL BEHAVIOR..... 129

5A.1 Optimization of Various Parameters for the Effective Reduction of GO to Produce N-doped Graphene (GRH-Gly).....	131
5A.1.1 Optimization of the Amount of Glycine.....	131
5A.1.2 Optimization of the Heating Time and pH.....	132
5A.1.3 Synthesis of N-doped Graphene (GRH-Gly) under Optimized Reaction Conditions.....	133
5A.2 Optimization of Various Parameters for the Simultaneous Reduction of GO and Ag ⁺ to Synthesize N-doped Graphene-Ag Nanocomposites.....	133
5A.2.1 Optimization of the Amount of Silver Nitrate.....	133
5A.2.2 Optimization of the Heating Time.....	134

5A.2.3 Synthesis of N-doped Graphene-Ag Nanocomposites under Optimized Reaction Conditions.....	136
5A.2.4 Electrochemical Measurements.....	136
5A.2.5 SERS Measurements.....	137
5A.3 Characterization of N-doped Graphene (GRH-Gly) and N-doped Graphene-Ag (GRH-GlyAg) Nanocomposites.....	137
5A.3.1 Optical Studies.....	137
5A.3.2 XRD Studies.....	139
5A.3.3 Raman Spectroscopy.....	140
5A.3.4 AFM Analysis.....	142
5A.3.5 FESEM Analysis.....	144
5A.3.6 TEM and SAED Analysis.....	146
5A.3.7 FTIR Spectroscopy.....	148
5A.3.8 Solid-State ¹³ C NMR Spectroscopy.....	150
5A.3.9 XPS Measurements.....	151
5A.3.10 TGA Measurements.....	153
5A.3.11 I-V Studies.....	154
5A.3.12 Electrochemical Measurements.....	155
5A.3.13 SERS Measurements.....	157
5A.4 Discussion.....	158

CHAPTER 5 (SECTION B)

2-AMINOISOBUTYRIC ACID MEDIATED REDUCTION OF GRAPHENE OXIDE TO PRODUCE N-DOPED GRAPHENE – ITS FORMATION MECHANISM AND ENERGY STORAGE APPLICATIONS.....	167
5B.1 Optimization of Various Parameters for the Reduction of GO to Synthesize N-doped Graphene.....	168
5B.1.1 Optimization of the Amount of AIB.....	168
5B.1.2 Optimization of the Heating Time and pH.....	168
5B.1.3 Synthesis of N-doped Graphene (GRH-AIB) under Optimized Reaction Conditions.....	170
5B.2 Characterization of N-doped Graphene	170
5B.2.1 Optical Studies.....	170

5B.2.2 Raman Spectroscopy.....	171
5B.2.3 XRD Analysis.....	173
5B.2.4 AFM Measurements.....	174
5B.2.5 FESEM Analysis.....	175
5B.2.6 TEM and SAED Analysis.....	176
5B.2.7 FTIR Studies.....	177
5B.2.8 ¹³ C Solid-State NMR Spectroscopy.....	179
5B.2.9 XPS Analysis.....	179
5B.2.10 TGA Analysis.....	181
5B.2.11 I-V Measurements.....	182
5B.2.12 Electrochemical Measurements.....	183
5B.3 Discussion.....	188

CHAPTER 6

CONCLUSIONS.....	197
-------------------------	------------

BIBLIOGRAPHY.....	203
--------------------------	------------



Chapter 1

INTRODUCTION

1. INTRODUCTION

Nanotechnology is the multifaceted area of science, engineering, electronics, information technology and medicine, which has gained significant importance in the last two decades. The concept of nanotechnology was first discussed by famous physicist, Nobel laureate Richard P. Feynman in his lecture on “There is Plenty of Room at the Bottom” in 1959 [1]. The advent of new tools and techniques with high resolution and precision has revolutionized the research in the area of nanotechnology, which allowed a better understanding, control and manipulation of synthetic protocols at the nanoscale level. These methodologies have allowed fabricating new materials viz. ceramics, semiconductors, metals and carbonaceous of varied size, shape and morphology with enhanced physicochemical features finding multidisciplinary applications to meet the vital societal needs.

Nanomaterials in general have at least one dimension lying in the range of 1-100 nm different to those of atom(s) (~ 0.1 nm) and bulk materials. The properties of nanomaterials can be modulated due to quantum confinement and surface effects. When the size of the material is reduced either less than or equal to the magnitude of de Broglie wavelength, then the quantum confinement effect starts controlling their physicochemical properties [2]. The properties of the nanomaterials could also be manipulated/enhanced extensively by modification/passivation of their surface. These effects have been extensively explored for their applications in wide ranging multidisciplinary areas viz. electronics, energy, environment and health [2,3]. Among different nanomaterials carbon allotropes exhibit unique physicochemical features due to the presence of varied bonding configurations, dimensionalities, aspect ratios, chirality, tunable band gaps, presence of surface defects, and edge chemistry [3].

Introduction

Depending on the dimensionalities, nanomaterials can be broadly categorized as: zero-dimensional (quantum dots/fullerenes) in which charge carriers are confined in all three dimensions; one-dimensional (nanotubes/nanorods) where two dimensions are confined; two-dimensional (nanosheets/nanoribbons/nanoprisms/nanoplates) with confinement in one dimension, and three-dimensional (dendritic structures/ nanoflowers) in which none of the dimension is confined.

The methodologies for the fabrication of nanomaterials is mainly divided into two approaches, i.e. top-down, in which bulk materials are cut down into nanoscale level and the other, bottom-up approach, in which the molecules are self assembled to form bigger materials of nanoscale range. Both approaches have been widely used for the synthesis of nanomaterials and are extensively explored for their wide applications in the field of electronics, catalysis, sensing, energy storage and nanobiotechnology [4-7]. A number of physical methods have been used for the synthesis of nanomaterials such as lithography, sputtering, ball milling, laser ablation, chemical vapor deposition (CVD), plasma-enhanced CVD sputtering and electric arc discharge [6,8-10] but chemical methods have been widely adopted due to their cost effectiveness, ease of synthesis, easy functionalization, better control on their size and shape, which are responsible for altering their physicochemical properties, and thus making it convenient for bulk production [11,12]. These include – chemical reduction, electrochemical, sonochemical, solvothermal, sol-gel, template, hydrothermal, microwave, hydrolysis and radiolysis [13-17].

Using these approaches, extensive research has been carried out for the synthesis of wide range of nanomaterials, which may be categorized as: ceramic nanomaterials, semiconductor nanomaterials, metallic nanoparticles (NPs), and carbonaceous nanomaterials.

1.1 Ceramic Nanomaterials

Ceramics are inorganic crystalline materials consisting of metal and a non-metal, which are prepared by heating to a high temperature followed by its cooling. The word ceramic is derived from a Greek word “Keramikos” meaning “of pottery” or “for pottery”. It reminds us the conventional products such as tiles, pots, bricks and dinnerware etc. These materials exhibit a wide range of characteristic features such as ability to withstand very high temperature, high hardness, wear resistant, brittle, refractory, thermal insulators, electrical insulators, oxidation resistant, and chemically stable. Although, the ceramics are accompanying mankind since ancient times but nanoceramic materials have drawn wide attention over the past years due to their enhanced optical, electrical, electronic, magnetic, mechanical, thermal, dielectric, and catalytic properties [18]. Due to these unique properties, nanoceramics have surpassed the bulk ceramics and makes it viable material for their wide ranging applications as sensors, catalysts, field effect transistors, electronics, magnetic devices, space vehicles, thermal insulators (thermal barrier coating), capacitors, and biomedical implants [19-22].

Nanoceramics can be broadly categorized as oxides, non-oxides and their composites and a brief discussion of each category is presented below:

1.1.1 Nanoceramic Oxides

Nanoceramic oxides display several interesting physicochemical properties such as optical, catalytic, magnetic, ferroelectric, electrical, and electrochemical, and have been modulated by bringing a change in their size and shape [23-27]. These materials display several characteristic features like high melting point, high hardness and are corrosion and wear resistant. Some of the widely studied nanosized ceramic oxides are CuO [25,27-29], TiO₂ [30-32], ZnO [23,33,34], MgO [35-37], and Al₂O₃ [38-40]. A number of chemical and physical methods have been used to synthesize various nanostructures of ceramic oxides

Introduction

such as sol-gel, solvothermal, hydrothermal, microwave, CVD, electrochemical [28,32,38,41], and ball milling [42].

CuO is a narrow band gap (1.2 eV) semiconductor having monoclinic crystalline structure exhibits intriguing electrical, optical, magnetic and ferroelectric properties. In recent past, an assortment of CuO nanostructures have been synthesized by controlling their shape and morphology [28,29]. These nanostructures have been suggested to find its potential applications in the wide ranging areas such as sensing, catalysis, solar cells, supercapacitors, field effect transistors, and as electrode material for Li-ion batteries [28,29].

TiO₂ is a wide band gap (3.05 eV) semiconductor and is another very promising ceramic oxide due to its nontoxicity, chemical inertness, high surface area, low cost, photostability besides unique optical, electronic and thermal properties. These unique properties makes it interesting and widely explored material for the applications in solar cells, sensors, photovoltaics, electrochromic devices, photocatalysis, and biomedical [30,32,43]. Apart to this, it has also been extensively used as pigment in: paints, foods, cosmetics, pharmaceuticals, and toothpastes [44].

ZnO is a wide band gap (3.3 eV) semiconductor and has been extensively investigated for its optical, photocatalytic, antiseptic and antibacterial properties, which have been utilized for its applications in sensing, catalysis/photocatalysis, solar energy conversion and field emission devices [34,45]. Its non-toxicity makes it harmless, biosafe and biocompatible and these features have been explored for its applications as drug carriers and manufacturing of beauty care products, ointments and food packaging materials [46,47].

MgO is a wide band gap (7.8 eV) insulator and has been of incredible interest due to its fascinating physicochemical properties such as optical, electronic, catalytic, adsorption, magnetic and antibacterial. Because of these remarkable properties and its several other distinctive features such as low cost, high chemical stability and environmentally benign, it has been exhaustively explored in the field of catalysis, sensing, toxic metal removal from

water and food packaging [35,48-50]. Wang *et al.* [37] have lately synthesized different morphologies of MgO (nanosheets, nanodisks and nanofibres) using hydrothermal approach and investigated their catalytic activity. The higher catalytic activity was found for nanosheets and nanodisks than the nanofibers, which has been attributed to the large number of basic sites present on their surface.

Al_2O_3 (8.4 eV) is one of the most widely explored nanoceramic oxide due to its chemical inertness, hardness, high wear resistance, high surface area, high corrosion resistance, elastic modulus, high strain rate, bending strength, fracture toughness and porosity. These properties have been utilized for sensing, catalysis, adsorption, for the synthesis of dielectric and heat resistant materials, and construction of orthopedic joints [38,51,52].

1.1.2 Non-oxide Nanoceramics

Non-oxide nanoceramics have several characteristic physicochemical properties ranging from optical, thermal, electronics to mechanical displaying various interesting features such as high: melting point, corrosion and thermal shock resistance, chemical corrosion resistance, oxidation resistance, wear resistance, temperature resistance, thermal conductivity, mechanical strength, and fracture toughness. These outstanding features have aroused their usage in vast variety of applications such as coatings, high power electronics, catalysts, light emitting diodes (LEDs), lasers, engines, nuclear reactors, and biotechnology [53-58]. The advanced synthetic protocols and characterization of these materials with diverse size, morphology and dimensionality have allowed their applications in cutting edge innovations [59,60]. Among the different non - oxide nanoceramics, silicon carbide (SiC) [61-63], gallium nitride (GaN) [59,64,65] and aluminium nitride (AlN) [60,66,67] have drawn considerable attention.

SiC is a wide direct band gap (3.2 eV) semiconductor with superior electronic, thermal and mechanical properties, which makes it suitable candidate for the applications in

Introduction

the field of power electronics at high temperature [54], catalysis [55], fuel cells [62], LEDs [68], and electrode material for Li-ion batteries [69]. In the recent past, a change in the morphology of SiC has been explored to alter its photoluminescence properties [61]. Its biocompatible nature has attracted its usage for biomedical applications [58].

GaN, being direct band gap (3.4 eV) semiconductor, is accepted to be one of the most viable material for optoelectronic devices such as lasers [56], field emitters, solar cells, logic gates [59], UV-blue LEDs [64,65] and for high-temperature and high-power electronic devices [70]. One-dimensional nanostructures of GaN have significantly attracted the attention of researchers due to its potential applications for the fabrication of these devices. The non-toxicity, biocompatibility and aqueous stability of GaN has enhanced its usage in biological applications [71,72].

AlN due to its wide direct band gap (6.2 eV), low electron affinity, outstanding chemical and thermal stability and mechanical strength has made it a promising material for high-frequency/high-power electronics, optoelectronics and piezoelectric devices [66,67]. Wu *et al.* [66] have synthesized Mg and Si doped AlN nanocone using CVD method, which improved its conductivity and charge mobility resulting in the enhanced field emission properties. In this regard, Si-doped AlN is found to be better as compared to those of Mg doped and undoped AlN.

1.1.3 Ceramic Nanocomposites

Ceramic nanocomposites are being investigated exhaustively due to their improved properties by the synergistic effect of individual components, and ability to control and manipulate the morphology of hybrid [73,74]. Their distinctive components such as polymers, metal NPs, metal oxide NPs and carbonaceous nanomaterials are adding to their increasing applications due to the enhancement in their mechanical, optical, magnetic, thermal, electrical, catalytic, electrochemical and biomedical properties [75-81].

Walker *et al.* [75] have incorporated the silicon nitride particles with homogeneously dispersed graphene platelets of thickness less than 2 nm ($\sim 1.5\%$ by volume fraction) using spark plasma sintering and they found the increment in the fracture toughness of ceramic nanocomposites by about $\sim 235\%$ (from ~ 2.8 to ~ 6.6 MPa. m^{1/2}).

Dong *et al.* [80] have synthesized the nanocomposites of ZnO nanorods on three-dimensional graphene and investigated their electrochemical behavior in 2.0 M KOH. The cyclic voltammetry (CV) curves of the hybrid showed a pair of redox couple indicating the pseudo-capacitive behavior originating from ZnO. The examination of the capacitive behavior of hybrid using galvanostatic charge-discharge (GCD) measurements showed the high value of specific capacitance (C_s) (316 F/g) at a current density of 6.70 A/g which is very high as compared to that of bare graphene (56 F/g at 6.0 A/g). Moreover, it also exhibited the long cycle life demonstrating its potential for high performance supercapacitor applications due to the synergistic effect.

Huang *et al.* [81] have reported the multifunctional synthesis of magnetic ceramics nanocomposites in which superparamagnetic Fe₃O₄ were integrated as nanocores and biocompatible hydroxyapatite as nanoshells. The potential application of these nanocomposites was also investigated for antitumor drugs and bone tissue engineering.

1.2 Semiconductor Nanomaterials

The research on semiconductor nanomaterials has garnered the huge attention because of their unique size and shape dependent physicochemical properties arising due to quantum confinement [82]. In recent years, the effect of size, shape, morphology, dimensionality and surface has been explored extensively for their tremendous influence on optical, electronic, magnetic, electrochemical, photonic and catalytic properties of semiconductors [83-87]. These properties have been widely exploited for the high-tech applications in the field of sensing, optoelectronics, nanoelectronics, energy storage and conversion, photovoltaics, photocatalysis, removal of environmental pollutants, and

Introduction

biomedicine [82,88]. Such a wide usage of these nanomaterials has prompted the scientific community to develop the versatile synthetic protocols [89-91]. A number of physical methods have been adopted for the synthesis of semiconductor nanomaterials such as CVD, metal-organic chemical vapor deposition (MOCVD), laser ablation, sputtering, plasma sintering, molecular beam epitaxy and thermal evaporation [92,93]. However, the use of physical methods for their synthesis are restricted due to their poor solubility in aqueous/non-aqueous media in the absence of functionalization, attachment to the matrix, and it requires sophisticated equipment, thereby, limiting their practical applications.

In order to have precise control over size, shape, morphology, dimensionality and removing the above shortcomings for synthesizing semiconducting nanomaterials, a number of chemical methods such as solvothermal, hydrothermal, coprecipitation, photochemical, sol-gel, microwave, sonochemical, capping agent mediated soft synthesis and radiolysis [94-97] have been devised over the years.

Semiconductors have been categorized in different classes such as: II-VI (Zn and Cd chalcogenides – sulphides, selenides and tellurides) [89,92,95], IV-VI (Ge, Sn and Pb chalcogenides – sulphides, selenides and tellurides) [88], III-V (In and Ga – arsenides and sulphides) [98,99] and nano oxides (GeO_2 , SnO_2 , PbO_2 , Fe_2O_3 , ZnO and TiO_2) [88,100,101]. Some of the most widely studied semiconductor nanomaterials are: ZnS , ZnSe , ZnTe , CdS , CdSe and CdTe [89,92,95], GeS , GeSe , GeTe , SnS , SnSe and SnTe [88,102], PbS , PbSe and PbTe [88,103]; TiO_2 [30,32], ZnO [33] and Fe_2O_3 [104].

Semiconductor nanocomposites provide a novel way to further improve its physicochemical properties by enhancing their optical, electrical, electronic, photonic, catalytic, electrochemical, magnetic, and biomedical properties due to the synergistic effect of each component. The semiconductor nanomaterials have been well exploited for their integration with metals [105], polymers [106], their binary/ternary hybrids [107] and carbonaceous materials [108], and have been utilized for the extensive array of applications

in: solar cells, photovoltaic cells, luminescent displays, memory devices, photocatalysis, removal of pollutants, and biological imaging [105-107].

A variety of semiconductor nanocomposites have also been synthesized using chemical methods over the years. Some of the most widely studied are: β -Fe₂O₃/Ag [109], ZnO/Ag [110], Ag/TiO₂ [111], Ag/CdS [112], PbSe/Au [113], Au/ZnTe [114], Fe₂O₃/Au [115], Au/ZnO [116], TiO₂/Au [117], CdS/Au [118], β -Fe₂O₃/CdS [119], β -Fe₂O₃/Ag/CdS [119], CdS/ZnS [107], ZnS/PbS [120], ZnS/PbS/ZnS [121], graphene-ZnO, graphene-TiO₂, graphene-CdS, and graphene-ZnS [121,122]. Several reviews have recently appeared on such nanocomposites and these will not be discussed in details [90,105,106,108]. However, a few of the semiconductor nanocomposites synthesized from our laboratory are briefly mentioned below.

Kumar and Chaudhary [112] have reported the biotemplated synthesis of Ag/CdS nanocomposites and investigated its optical, electronic, fluorescence and time resolved fluorescence features suggesting their potential applications for sensing and photonic device(s).

The guanosine monophosphate mediated binary (β -Fe₂O₃/CdS) and ternary (β -Fe₂O₃/Ag/CdS) nanocomposites have been synthesized for investigating the dynamics of charge carriers in the irradiated nanosystems by using CdS as the fluorescence probe. In these nanohybrids the effect of aging was explored for the observed transformation in their morphologies from nanoparticles *via* nanorods to nanowires and these changes were correlated with their optical, photophysical and magnetic properties [119].

Kumar and Kumar [107] have reported the RNA-mediated CdS/ZnS tubular nanostructures in aqueous medium at a low temperature of 15 °C assisted by the supramolecular interactions. The changed morphological transformation of the nanohybrids with enhanced optical, fluorescence, and rotational correlation times indicated its immense potential in the areas of sensing, fluorescence imaging and nanoelectronics.

1.3 Metal Nanoparticles

Metal nanoparticles (NPs) have entranced the researchers for the past decade due to their enormous potential for applications in the field of nanotechnology. Metal NPs are being used since ages as decorative pigments in the glass of famous Lycurgus cup, the colorants to the glasses, potteries and medicinal agent [123]. In 1857, it was first perceived by Michael Faraday that the coloration in ruby glass is due to the colloidal metallic gold [124] and this sensation was further explained by Mie [123] theoretically by solving Maxwell's equation. The most attractive feature of the metal NPs is the surface plasmon resonance (SPR) phenomenon, and has been attributed to demonstrate the color in some of the colloidal solutions of metals. The phenomenon of SPR has been assigned to the absorption of electromagnetic radiation causing a collective oscillation of conductance electrons at a resonant frequency characteristic for the metal lattice [2].

Apart to the unique optical properties, nanosized metallic NPs also exhibits distinctive electronic, photonic, electrochemical, catalytic and antibacterial properties [123,125,126]. These properties have been explored extensively by manipulating their size, shape, morphology, aggregation nature, environment and band width for their wide applications in the field of biomedical, sensing, electronics, photonics, photovoltaics, electrochemical, electrocatalysis and catalysis [126,127-129]. Among the different morphologies, nanorods and ellipsoids show two separate plasmonic absorption bands corresponding to the transverse and longitudinal electron oscillations in the metals unlike to that of one band for spherical NPs. For a typical case of the Au nanorods, the transverse mode exhibits the plasmonic band peaking at around 520 nm and the longitudinal mode shows a red shifted plasmonic resonance peak at about 800 nm, as compared to that of spherical Au NPs peaking at ~ 520 nm, and showed their dependence upon the aspect ratio [130,131].

Another important aspect for the transition metal NPs, especially Au, Ag and Cu is that the adsorbed molecule(s) on their surface results into surface-enhanced Raman scattering (SERS) effect, which has been explained to occur through either electromagnetic (EM) [132,133] or chemical (CM) [132,134] enhancement mechanisms. The EM enhancement takes place due to the excitation of localized surface plasmons on the metal leading to the formation of strong localized EM field which results in the enormous enhancement of the Raman signal ($\sim 10^6$ - 10^{11}), whereas the CM has been considered to arise through the formation of charge-transfer complexes between excited metal and the SERS substrate resulting in relatively lower enhancement ($\sim 10^1$ - 10^2). The overall enhancement in SERS is virtually the contribution from both the mechanisms (EM and CM). Due to this, SERS has become a very advanced and highly sophisticated tool in the various field of science and has been widely utilized in the application areas of sensing, spectroelectrochemistry and for the detection of various molecule(s) [134,135].

A number of physical and chemical methods have been used for the synthesis of metal NPs belonging to the transition metal series namely, Fe, Co, Ni, Cu, Ag [136-138], Au [123], Pt and Pd [129]. Among these, the chemical methods have been found to be more precise for controlling of their size, shape, morphology and aggregation [127,136-140].

Recently the progress has also been made for the synthesis of their bimetallic alloys such as Au-Ag, Au-Pt, Au-Pd, Ag-Pd, Ag-Pt, Pd-Pt, Pd-Cu, Fe-Co, Pt-Fe, Pt-Co, Pt-Ni, and Cu-Ni [141-143] due to their ability to exhibit unique and superior properties as compared to their monometallic analogue because of the synergistic effects between the two metals [142]. The synergistic effect arise due to the different binding configuration of the two metals modulating the charge-transfer between them, surface element distribution, surrounding coordination, and lattice strain [143].

Among the noble metal NPs, Au and Ag are the most widely explored and reviewed metal NPs due to their chemical stability, interesting optical, electronic and biological

Introduction

properties [123,136,144]. The usage of these NPs has been well exploited for their applications in catalysis [123], electrocatalysis, electrochemical sensing [128], bioimaging, SERS, photonics, optoelectronics and microelectronics [144-146]. Some of the recent papers on the synthesis and optical properties of Ag nanostructures are discussed below briefly:

1.3.1 Silver Nanostructures

Different morphologies of Ag nanostructures (spherical, polygonal, rod-, flower-, wire- and nono-ant) have been synthesized by Premkumar *et al.* [147] using cyclodextrin as a green, biocompatible reducing and capping agent under aqueous alkaline medium at room temperature. The change in the concentration of NaOH and temperature of the reaction mixture were found to be responsible for varied morphologies. They have also examined the SERS behavior of these nanostructures by using 4-aminothiophenol (4-ATP) as a probe molecule and found the enhancement effect is higher for aggregated Ag nanostructures as compared to that of smaller Ag NPs.

Alam *et al.* [148] have developed a facile method for the synthesis of dendritic Ag nanostructures in aqueous medium without using any surfactant/template. These nanostructures have been characterized by using various spectroscopic and microscopic techniques. The size of Ag dendritic nanostructure was estimated to be 800 nm in which the size of silver NPs component lies in the range of 5-10 nm as was evidenced by its TEM analysis. They have also demonstrated the potential application of these nanostructures as a SERS substrate for detecting *p*-aminobenzenethiol at a very low concentration of 1×10^{-8} M.

Saha *et al.* [149] have synthesized spherical, crystalline Ag NPs of size < 10 nm by employing calcium alginate gel beads as a reducing as well as stabilizing agent using green photochemical approach. These NPs were used as a catalyst for performing the reduction of 4-nitrophenol to 4-aminophenol in the presence of excess sodium borohydride (NaBH_4). The catalytic efficiency of Ag NPs was compared with Au NPs and was found to be more for Ag NPs by following the zero-order kinetics.

Li *et al.* [150] have developed a green method for the synthesis of Ag nanostructures (nanodendrites) claiming ultra high purity and crystallinity. The as-synthesized Ag nanodendrites exhibited excellent SERS sensitivity towards rhodamine 6G up to the concentration of 5×10^{-16} M having a very high enhancement factor of 10^{13} surpassing the theoretical limit. The antimicrobial activity of these nanostructures for *Escherichia coli*, *Candida albicans* and *Staphylococcus aureus* have been found to be 10 times better than Ag NPs.

1.4 Carbonaceous Nanomaterials

Carbon is the sixth element in the periodic table and is one of the most abundant and versatile elements. It has the unique ability to form covalent bond with itself and transform into different materials involving varied degree of hybridization (sp , sp^2 and sp^3) [3,151]. It also has the ability to form stable bonds with other nonmetallic elements and exist in the form of wide range of structures accompanied by quite contrast and interesting physical and chemical properties. The presence of elemental carbon in the form of natural carbon allotropes such as graphite and diamond was perceived over the centuries ago. Both allotropes exhibit distinctive properties due to the difference in their hybridization. The term graphite was derived from Greek word '*graphein*' meaning 'to write'. The structural identification of graphite was done by John D. Bernal in the beginning of 20th century and since then it has become one of the most studied carbon materials [152]. In graphite, carbon atom is bonded to three other carbon atoms and one atom remains free which makes it electrically conducting. The layered structure of graphite consists of several graphene monolayers in which sp^2 carbon atoms are tightly packed in a 2D hexagonal lattice. The layers in graphite are held by weak van der Waals forces which make the layers to get separated easily. The distance between the two graphene layers is 0.3354 nm and the C-C bond length in graphene layer is 0.142 nm (Fig. 1.1a) [153]. On the other hand, in diamond each carbon atom is tetrahedrally bonded (sp^3 hybridized) to four other carbon atoms with

Introduction

the C-C bond length of 0.154 nm (Fig. 1.1b). It is the hardest known natural material and has highest thermal conductivity ($\sim 2,200$ W/m.K) as well [154].

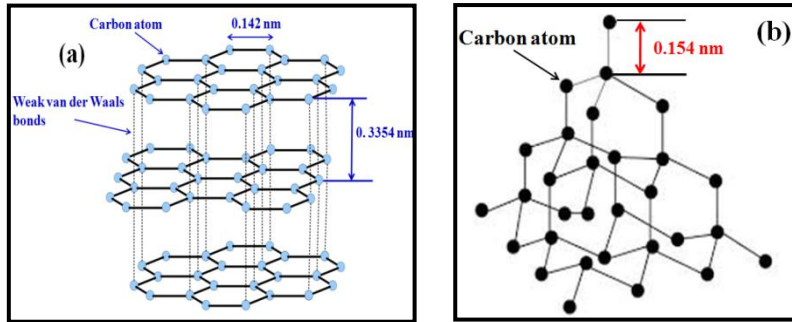
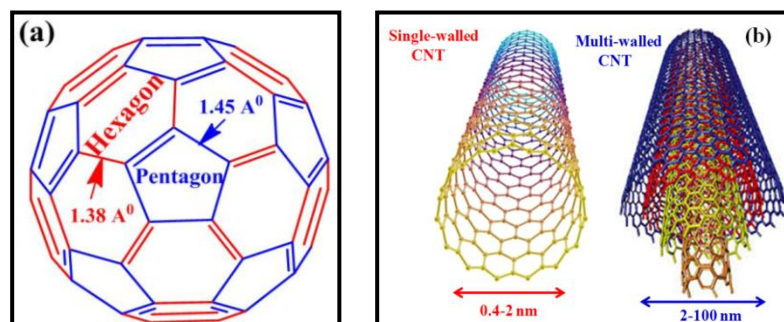


Fig. 1.1: Structures of graphite (a) and diamond (b).

This family was enriched by the discovery of fullerene (Fig. 1.2a) in 1985, third carbon allotrope of the carbon family for which Harold W. Kroto, Robert F. Curl and Richard E. Smalley in 1996 have been awarded the noble prize of chemistry [155,156]. Soon afterwards, the new member added to this family in 1991 discovered by Sumio Iijima [157], known as carbon nanotubes (CNTs) (Fig. 1.2b) which made the stormy beginning in the field of carbonaceous nanomaterials. The recent and youngest member of this family is graphene (Fig. 1.2c), which is the building block of graphite. Although its existence was anticipated over the decades ago and identified by Boehm *et al.* in 1962 [3,158,159], but for the very first time it was isolated and characterized by Konstantin S. Novoselov and Andre Geim in 2004 [160] and this novel discovery fetched them to the noble prize of physics in 2010. This material due to its remarkable properties and tremendous potential for wide ranging applications generated a wave of excitement among the researchers in the 21st century and made carbon based research as one of the most enthralling topics in the materials science [161].



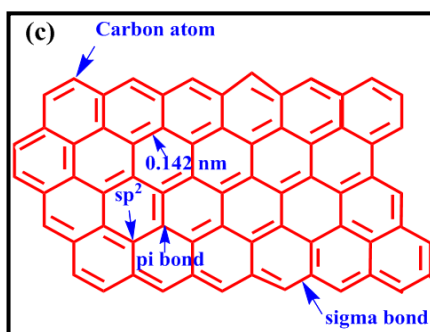


Fig. 1.2: Structures of fullerene (a), CNTs (b) and graphene (c).

On the basis of different dimensionalities, carbonaceous nanomaterials can be classified into different nanostructures such as fullerenes/carbon dots/graphene quantum dots (GQDs) (zero dimension), CNTs, (one dimension) and graphene/graphene nanoribbons (GNRs) (two dimension) (Fig. 1.3) [3]. These categories have been discussed below in detail:

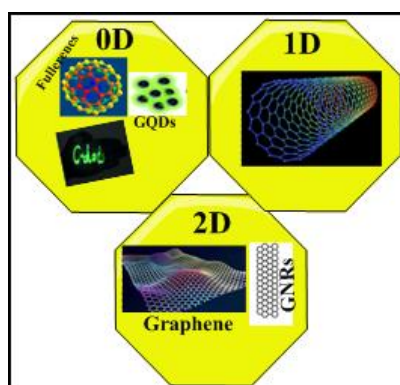


Fig. 1.3: Classification of the carbonaceous nanomaterials depending upon their dimensionalities.

1.4.1 Fullerenes

The research on carbon nanomaterials blossomed with the serendipitous discovery of fullerene, in which carbon atoms are arranged in closed shell [155]. Kroto *et al.* [155] produced clusters of carbon atoms (C_{60} and C_{70}) and found the higher abundance and stability of C_{60} . This new allotrope of carbon was named as buckminsterfullerene, having an analogous structure matching to that of the geodesic dome (designed in 1967 for Montreal world exhibition), after the name of its American architect, R. Buckminster Fuller. Fullerene has icosahedral symmetrical closed cage structure consisting of 20 hexagonal and 12 pentagonal rings. It consists of two different types of C-C bond lengths, hexagon-hexagon

Introduction

($\sim 1.38 \text{ \AA}$) and hexagon-pentagon ($\sim 1.45 \text{ \AA}$) as were determined by the X-ray crystal structure [162]. Each carbon atom in C_{60} is trigonally bonded to three other carbon atoms resulting in sp^2 hybridization. It is a spherical molecule having an external diameter of 0.71 nm [155]. C_{60} molecule is not superaromatic and, thereby results in poor electron delocalization behaving like an electron deficient alkenes having the tendency to react rapidly with electron rich species. Apart to this, several other lower and higher carbon clusters such as C_{20} , C_{26} , C_{32} , C_{38} , C_{42} , C_{46} , C_{52} , C_{70} , C_{76} , C_{78} , C_{82} , and C_{84} have also been identified [163,164]. These carbon clusters result in the formation of closed cage structure.

A number of methods have been developed to synthesize fullerenes and its derivatives such as vaporization of graphite using laser irradiation, plasma/arc discharges [165,166], pyrolysis and combustion of simple hydrocarbons [165]. Chemical methods have also been applied for their synthesis *via* bottom-up approach [167].

C_{60} is soluble in many organic solvents such as toluene, carbon disulphide and hexane [168]. It has been observed that C_{60} form aggregates in benzonitrile at the concentration $> 100 \mu\text{M}$ and remains in equilibrium with its monomer [169]. The unusual solvatochromisms for C_{70} has been analyzed by its optical absorption and fluorescence studies. The aggregation behavior of this fullerene was found to be controlled by their solubility in the solvent/solvent mixture [170].

C_{60} and related molecules have attracted worldwide attention due to its unique physicochemical and photophysical features such as strong electron-acceptor character, significant electronic absorption bands in the entire UV-Vis region, singlet oxygen sensitizing ability, interesting non-linear optical properties and superconductivity upon doping with alkali metals [171,172]. Due to these features they have been widely explored in various fields such as photovoltaics, light harvesting devices, sensing, electronics, medicine, as antimicrobial agent for water purification, antioxidants in biological systems [171,173-175] and voltage stabilizers for insulation of power cable [176].

Carbon dots (CDs) are another class of carbon nanomaterials with zero dimensionality having size less than 10 nm. CDs are generally amorphous and contain sp^3 hybridized carbon. These nanomaterials display interesting photoluminescing properties exhibiting dependence upon their size, functionalization and excitation wavelength. CDs contained D and G bands in their Raman spectra usually exhibit relatively higher I_D/I_G ratio indicating the high sp^3 carbon component. In recent years a number of physicochemical methods have been developed for the synthesis of CDs such as laser ablation, electrochemical, solvothermal, hydrothermal, ultrasonic carbonization and microwave. CDs are being extensively explored for their biomedical, LEDs, solar cells and sensing applications [3 and references therein].

1.4.2 Carbon Nanotubes (CNTs)

CNTs are defined as the tubular nanostructures having high aspect ratio (length to diameter ratio) formed by the rolling of graphene sheets in which sp^2 carbon atoms are arranged in the hexagonal lattice [3,177]. CNTs can be classified, depending upon the diameter and the mode of rolling of graphene sheets, into single-walled carbon nanotubes (SWNTs), double-walled (DWNTs) and multi-walled carbon nanotubes (MWNTs). SWNTs is formed by the rolling of single layer of graphene sheet and having diameter in the range of about 0.4-2 nm and length of these nanotubes could vary from nm to several μm . On the other hand, DWNTs and MWNTs formation depends on the rolling of number of graphene layers into the tubular or cylindrical structure, respectively [3]. MWNTs possess diameter in the range of \sim 2-100 nm and the nanotubes are 0.34 nm apart to each other [178]. The interesting features of the nanotubes are their high aspect ratio and chirality and the latter is defined as the angle between the hexagonal rings and the nanotubes axis. The angle at which the rolling of graphene sheets takes place with respect to nanotube is defined by the integers (n,m) where 'n' and 'm' are the number of real space unit vectors of the graphene sheet (Fig. 1.4). When the vector indices $n - m$ is the multiple of 3, it causes the crossing of bands at

Introduction

Fermi level, demonstrating it to be metallic otherwise it is semiconducting [2,178]. Thus it is referred that when $n = m$, the CNTs are achiral and present in armchair configuration and expected to be metallic. When, $n \neq m$, it is said to be chiral and semiconducting and when $m = 0$, it is said to be semiconducting and present in achiral zigzag configuration [2]. Thus, the electronic properties of the nanotubes depend on their diameter and chirality [179,180].

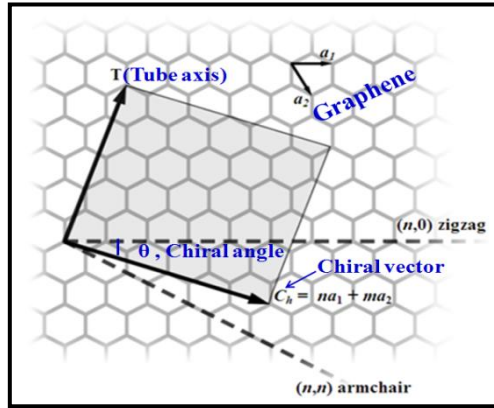


Fig. 1.4: Schematic diagram depicting the formation of CNTs from graphene sheet along the chiral vector (C_h).

The most common techniques used for the production of CNTs include arc discharge, laser ablation, and CVD [181,182]. The CVD technique works at comparatively lower temperature (< 800 °C) and inexpensive, and has been employed for its large production [182]. The other methods employed are: flame synthesis, pyrolysis of plastics and hydrocarbons, solar energy route, and electrolysis [182-184].

CNTs display excellent electronic, electrical, optical, optoelectronic, thermal, mechanical, chemical and electrochemical properties [181,185,186]. Both theoretical and experimental work have shown that the SWNTs has higher conductivity (400,000 S/cm) and mobility ($100,000$ cm^2/Vs) [185] and exhibits superior electronic properties to that of MWNTs. Due to these unique physicochemical properties of CNTs it has been widely used for the applications such as for field effect transistors, transparent electrodes, LEDs, sensors, photoconversion, catalysis, energy storage and Li-ion batteries [173,185-187]. The solubilization of CNTs *via* their functionalization [188] has advanced their usage in the field

of nanobiotechnology such as for biosensing, bioimaging, biomedical and drug delivery [189,190].

1.4.3 Graphene

1.4.3.1 Introduction

Over the years, it was argued that the 2D crystals are thermodynamically unstable [191]. But these arguments did not stop researchers to explore the 2D materials and several scattered efforts had been made by many scientists in earlier times. In 1859, Brodie [192] treated graphite with strong acids, the product of this reaction as of now is known as graphene oxide [193]. Ruess *et al.* [194] in 1948 used TEM analysis to determine the structure and thickness of graphene oxide. In 1962, Boehm and his co-workers [158,159] analyzed the reduced graphene oxide using TEM and the thinnest fragments were identified as monolayers [193,195]. His group in 1986 coined the term graphene for reduced graphene oxide for the first time in which the term “graph” was derived from “graphite” and the suffix “ene” from polycyclic aromatic hydrocarbon [196].

After the ground breaking experiment of K.S. Novoselov and A.K. Geim in 2004 [160], about the successful peeling of single-layer of graphene using mechanical exfoliation of graphite *via* top-down approach, the two-dimensional materials have become the most widely studied carbon allotropes as is also reflected by the storm of publications in this area [197]. Graphene, the mother of all graphitic materials, is defined as the single-atomic thick sheet of sp^2 hybridized carbon atom in which the carbon atoms are arranged in a 2D hexagonal lattice.

In its structure, the 2s orbital of carbon overlaps with the $2p_x$ and $2p_y$ orbitals of nearest carbon atoms and gives rise to stable sigma bond (sp^2 hybridization) and the remaining free $2p_z$ orbital of carbon atom overlap with the another $2p_z$ orbital of nearest carbon atom resulting in the formation of delocalized covalent π -bonds having C-C bond

Introduction

distance and interplanar spacing between the two layers to be 0.142 and 0.335 nm, respectively [198].

The graphene unit cell consists of two non-equivalent carbon atoms (A and B) spanning around a triangular sub-lattice (Fig. 1.5). The real space basis vectors of this unit cell are a_1 and a_2 . An armchair and zigzag edge in the hexagonal lattice of graphene have been shown in Fig. 1.5. Graphene lattice also shows the array of points corresponding to the particular set of lattice planes of the crystal with the 'd' spacing values of 0.213 and 0.123 nm corresponding to $\{10\bar{1}0\}$ and $\{11\bar{2}0\}$ lattice planes, respectively [198].

Graphene can be categorized depending upon the number of layers: monolayer, bilayer, a few layers (< 10 layers) and the structure with > 10 layers (graphite films) [198,199]. Monolayer graphene usually found with no stacking of sheet, bilayer graphene can be found in AA/AB arrangement (not shown) and a few-layer graphene can be found in different stacking arrangements such as: AAA (simple hexagonal), ABAB (hexagonal Bernal stacking) and ABCABC (rhombohedral) (Fig. 1.6) [198-200]. The few-layer graphene with no particular stacking arrangement is known as 'turbostatic' graphene. The value of interlayer spacing differs for turbostatic and pristine graphene and was found to be > 0.342 nm and 0.334 nm, respectively [199]. The interlayer spacing in Bernal stacking and rhombohedral has been found to be 0.335 and 0.337 nm, respectively [198].

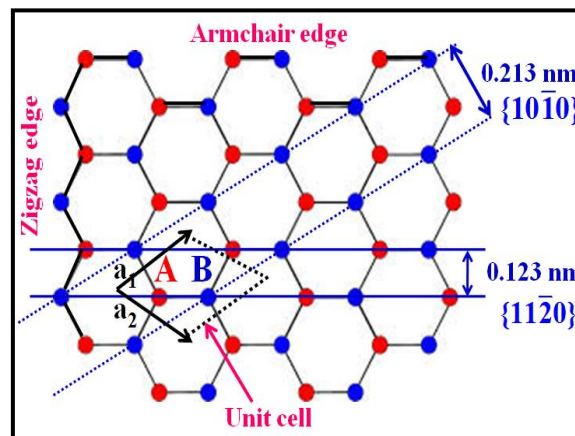


Fig. 1.5: Hexagonal lattice structure of graphene (2D) in real space.

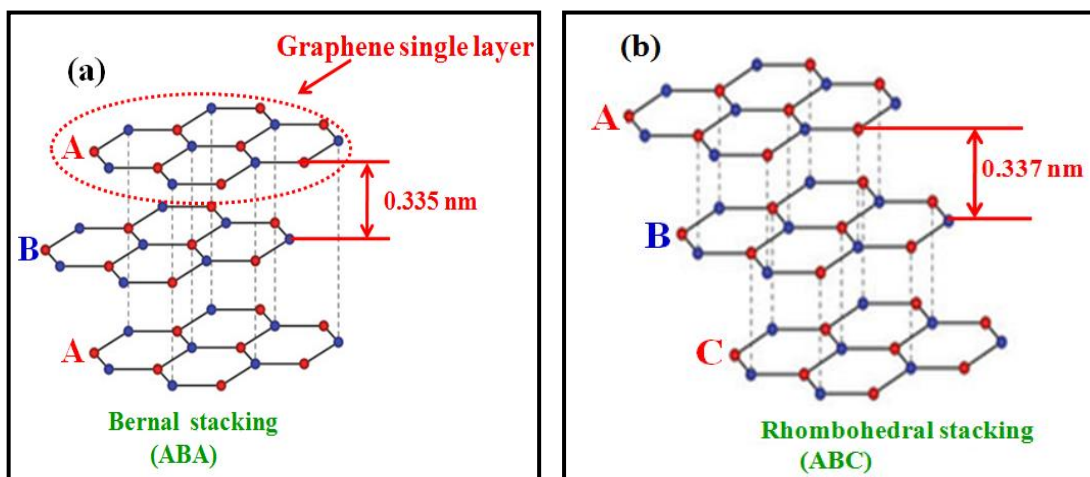


Fig. 1.6: Stacking arrangement in a few-layer graphene: Bernal stacking (ABA) (a) and rhombohedral stacking (ABC) (b).

1.4.3.2 Physicochemical Properties

Graphene exhibits several interesting physicochemical properties *viz.* electronic, surface, optical, thermal, thermoelectric, mechanical, magnetic and electrochemical which have tremendous potential for the fabrication of advanced materials (*vide infra*). These properties have shown dependence on the number of layers [200] and some of these are discussed below:

Electronic Properties – One of the most unique and exciting property of graphene which has attracted the worldwide attention of researchers is its electronic properties. The uniqueness in the electronic property of graphene is due to its band structure in which the conduction and valence bands meet each other, which is called Dirac point (Fig. 1.7a). It is considered as a zero bandgap semiconductor showing semi-metallic behavior because at the Fermi level its density of state is zero [198]. The band gap of graphene can be tuned in the range varying from 0 – 2.5 eV by applying the gate voltage across the structure (Fig. 1.7b) [3]. It can also be opened experimentally in several other ways such as by doping, changing its morphology, and forming its hybrids/nanocomposites without affecting its other properties [201]. The usage of zero bandgap graphene is limited for field effect transistors because it gives low on/off switching ratio. So, it can be made viable material for electronic devices by opening its band gap [201]. The electronic property of graphene also depends

Introduction

strongly on the number of layers [200]. Only monolayer and bilayer pristine graphene is zero bandgap semiconductor having single type of electron and hole [202]. For a few-layer graphene, there is overlapping between conduction and valence bands and several charge carriers appears [3,200]. The charge carriers in monolayer graphene behave as massless Dirac fermions and move with a Fermi velocity of 10^6 m/s [203]. It also exhibits ambipolar electric field effect with the charge carrier concentration up to 10^{13} cm^{-2} and mobilities of $\sim 10,000$ cm^2/Vs at room temperature when the gate voltage is applied [160]. In addition to this, it also exhibits significantly high mobility value of $\sim 200,000$ cm^2/Vs at low temperature for carrier density of $< 5 \times 10^9$ cm^{-2} , which has made it as an excellent conductor of electricity [204]. Apart to these, an unusual half-integer quantum Hall effect (QHE) in graphene has been observed for charge carriers by tuning the chemical potential [205]. Such QHE can also be observed at room temperature [206].

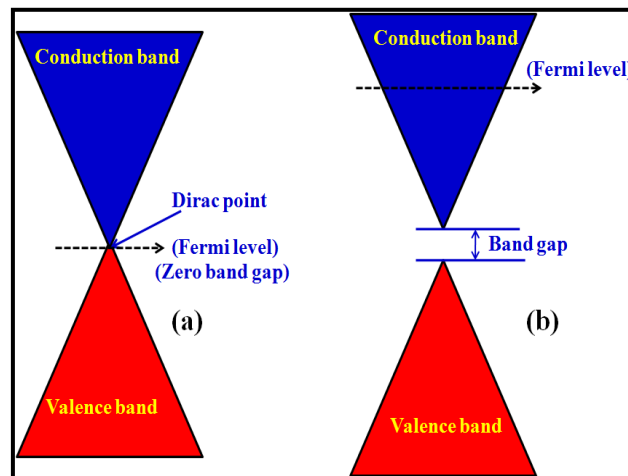


Fig. 1.7: Band structure of graphene: without band gap (a) and with band gap (b).

Surface Properties – Single-layer of graphene exhibits high specific surface area of ~ 2630 m^2/g which is significantly higher to that of graphite (~ 10 m^2/g) and this value is about two-fold higher than that of SWNTs (~ 1315 m^2/g) [207]. It has been observed that the surface area of graphene depends on the number of layers and decreases from monolayer (~ 2630 m^2/g) to a few-layers graphene (~ 100 - 1550 m^2/g) [208].

Optical Properties - Suspended single-layer graphene exhibits extraordinary optical properties with the opacity of $2.3 \pm 0.1\%$ independent of wavelength and negligible reflectance ($< 0.1\%$) [209]. It has been found that the opacity increases linearly with the increase in the number of layers and each layer adds another 2.3% [209]. These observations were also in line with the theoretical evidence [202]. The optical absorption in graphene ranging from far-infrared *via* mid-infrared to ultraviolet can be attributed to low photon energies (intraband transitions) and high photon energies (interband transitions) [210]. Apart to this, it has also been found that the optical transitions of single and bilayer graphene can be tuned through electrical gating which finds its application for infrared optics and optoelectronics [211]. Another remarkable feature of graphene is its ability to show photoluminescence by tuning its band gap [212].

Thermal Properties - Monolayer graphene sheet exhibits remarkably higher thermal conductivity value of ~ 5000 W/mK at room temperature as compared to those of graphite (140-500 W/mK along **a** and **b** axes and 3-10 W/mK along **c** axis) and diamond (~ 2200 W/mK) [213-215]. This value of conductivity is about 1.4 and 1.5 times higher to those of SWNTs (3500 W/mK) and MWCNTs (~ 3000 W/mK), respectively [213]. However, the thermal conductivity of single-layer graphene supported on amorphous silica decreased drastically to about 600 W/mK at room temperature. But this value is still about 1.5 and 4 times higher to those of copper (~ 400 W/mK) and silicon (~ 148 W/mK), respectively, widely used metals in electronics [214].

Mechanical Properties - Monolayer graphene is known to be the strongest material investigated ever due to its remarkable breaking strength (42 N/m) and elastic properties, measured by using atomic force microscopy (AFM) based nanoindentation [216]. Assuming the thickness of graphene sheet to be 0.335 nm, its young modulus, intrinsic strength and elastic stiffness (Young modulus x thickness) were found to be ~ 1.0 TPa, 130 GPa and 335 N/m^2 [198], respectively.

Introduction

Electrochemical Properties - Graphene sheet consists of two types of surface for the electrons to participate in heterogeneous electron transfer (HET) namely, basal and edge planes (Fig. 1.8). It has been found that the edge plane of graphene shows higher HET rate constant (~ 0.01 cm/s) as compared to that of basal plane (10^{-9} cm/s) and has been attributed to the presence of defects on edge plane [217] which facilitates the electrochemical behavior of graphene [217].

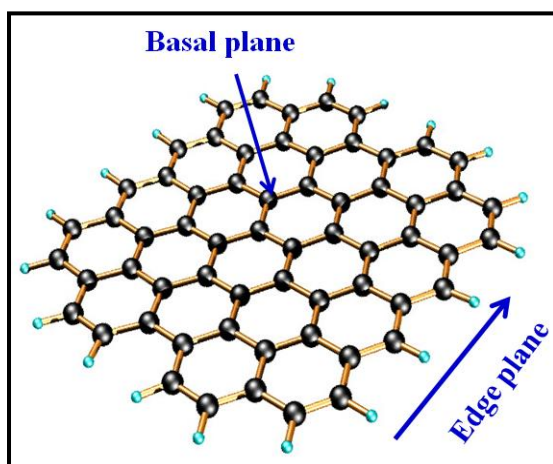


Fig. 1.8: Structure of graphene showing its basal plane and edge plane-like sites.

Graphene due to its unique physicochemical properties such as high surface area, electrical conductivity, mechanical and chemical stability has captured the attention of electrochemists. These characteristic features have been considered to be the most suitable for electrode material as regards to sensing, biosensing and energy storage applications [207,217-219].

1.4.3.3 Graphene for Energy Storage Applications – Supercapacitor

The increased global demand for renewable energy resources has necessitated developing the efficient, high performance, cheap and environmental friendly energy storage devices [220]. It makes important to improve the technologies for the production and storage of electrical energy. It has led to the development of batteries and fuel cells, but these options are restricted due to their low power capabilities and involve relatively high cost [221,222]. Hence, in the recent past graphene based supercapacitors have drawn worldwide attention due to their low cost, high charge-discharge rate, long cycle life and

high power density. These features have enhanced their application in portable electronics, hybrid electric vehicles and power backup [221,222]. The supercapacitors consists of two electrodes dipped in an electrolyte separated by a porous separator and are also known as ultracapacitors or electrochemical capacitors. There are three types of supercapacitors, which have been classified based on their energy storage mechanism, *i.e.* electric double layer (EDL) capacitor, pseudo-capacitor and hybrid capacitor (Fig. 1.9a) [222,223]. In EDL capacitor, charge storage takes place non-faradaically through the fast adsorption of ion at the electrode/electrolyte interface (Fig. 1.9b). On the other hand, in pseudo-capacitors charge storage takes place faradaically by the transfer of electron between electrolyte and electro-active species on electrode (Fig. 1.9b) [222-224]. The most commonly used electro-active species are: metal oxides (ruthenium oxides, manganese oxides and vanadium nitride) [225], conducting polymers (polypyrrole and polyaniline) [226] and oxygen and nitrogen functionalities that are present on the surface of carbon nanostructures [224]. Hybrid capacitors works with both the mechanism for energy storage, *i.e.* electric double layer capacitance (EDLC) and pseudo-capacitance. Graphene supercapacitors based on EDLC are stable exhibiting long cycle life [227] and high power density but low energy density. On the other hand, pseudo-capacitors exhibits high: specific capacitance and energy density as compared to that of EDL capacitors but are restricted for practical applications due to their low power density arising from the poor electrical conductivity, thereby limits the fast transport of electron and are also unstable for long cycle life [223]. Therefore, lately hybrid capacitors are being used in order to achieve high energy as well power density without losing its cycling stability.

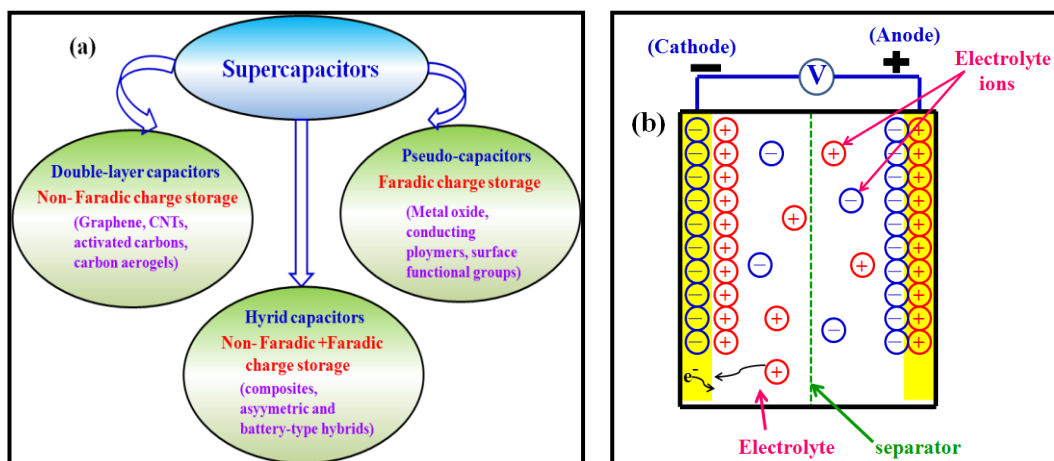


Fig. 1.9: Classification of supercapacitors (a) and schematic diagram of EDLC and pseudo-capacitance (b).

A number of aqueous, organic and ionic electrolytes have been used for graphene supercapacitors [222,228]. The working potential window of aqueous electrolytes (KOH, H_2SO_4 , KNO_3 and Na_2SO_4) is though limited to 1 V as compared to those of organic (acetonitrile and propylene carbonate) and ionic $(\text{C}_2\text{H}_5)_4\text{NBF}_4$ and EMIMBF₄ electrolytes having higher potential window of 2.5 to 3.5 V and up to 4 V, respectively. But the aqueous electrolytes have certain advantages over organic electrolytes due to their high ionic conductivity and low cost [228].

Other characteristic features of graphene such as surface area, pore size and size distribution and electrical conductivity also contribute to the high performance of supercapacitor with EDLC behavior [229]. EDLC is directly related to the surface area at the electrode/electrolyte interface, which is often limited due to the aggregation causing poor wetting between graphene electrode and electrolyte. It eventually results in the decreased capacitive performance and low energy density [230,231]. Therefore, the presence of electro-active species on the graphene electrode is often necessary for enhancing the specific capacitance and, thereby leading to high energy density [224]. The interaction between graphene and electro-active species at the electrode/electrolyte interface is expected to improve the wettability of the electrode and permeability of electrolyte solution due to the

hydrophilic nature of these species and, thereby preventing the aggregation of the sheets [229-232]. Thus, the enhanced specific capacitance is due to the contribution of EDLC and pseudo-capacitance which can be utilized for the high performance of supercapacitors [230-232]. However, the controlling of the density of functional groups is also important so as to maintain the conjugation and electrical conductivity of the graphene nanostructure [231].

The performance of supercapacitors has also been enhanced by doping of graphene sheet with heteroatoms, which may enhance the electrical conductivity, improved wettability and provide pseudo-capacitance, thereby, increasing the overall capacitance due to the co-contribution of EDLC and pseudo-capacitance [233,234].

The vast ranging unique physicochemical properties of graphene (*vide supra*) have been extensively exploited for its interdisciplinary applications such as for field effect transistors [235], stretchable transparent electrodes [236], solar cells [237], photonics and optoelectronics [238], thermal interface materials [239], nanoelectromechanical resonators [240], catalysis, bioimaging, biomedicine [212], biological/chemical sensing, supercapacitors, Li-ion batteries, fuel cells, electrochemical sensing, water splitting and hydrogen storage [218, 221].

1.4.3.4 Synthesis of Graphene

A number of methods have been used for the synthesis of graphene involving bottom-up (atom by atom) and top-down (exfoliation from bulk) approaches. Bottom-up approach includes CVD, plasma enhanced CVD, epitaxial growth, solvothermal reaction, organic synthesis, laser ablation, and arc discharge [197,202,218]. These methods produce graphene with nearly perfect structure due to low amount of defects and excellent properties but the large scale production of graphene employing these approaches remains a challenge [241].

Top-down approach involves exfoliation of: graphite mechanically, electrochemically; graphite intercalated compounds employing solvent and thermal assisted

Introduction

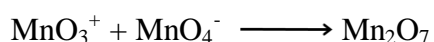
approaches [199,202,242] and exfoliation of graphite oxide followed by its chemical reduction [11,12]. Single-layer of graphite oxide, obtained by its exfoliation is known as graphene oxide. Although, there is no difference between graphite oxide and graphene oxide in terms of their structure and properties, but the former contains stacked layers in contrast to graphene oxide which contains single layer.

Graphene Oxide - Graphene oxide (GO) is a two-dimensional sheet of carbon having oxygen functionalities namely hydroxyl and epoxy groups on its basal plane and carboxyl, ketone, ester and lactol groups on its edge planes, but the distribution of these groups still remains uncertain [243]. The presence of oxygenated functionalities on its surface makes it hydrophilic in nature. Hence, it can be dispersed easily in aqueous as well as in organic solvents [244].

The synthesis of GO has been accomplished for a long by the oxidation of natural graphite powder or flakes. In 1840s, a few studies were reported about the exfoliation and intercalation of graphite with sulphuric acid (H_2SO_4) and nitric acid (HNO_3) [245]. In 1859, graphite oxide was prepared by Brodie for the first time by treating graphite with an oxidation mixture of potassium chlorate (KClO_3) and fuming HNO_3 [192]. The resultant product was found to be dispersible in pure or alkaline water but not in acidic medium, and for this reason it is named as “graphic acid” with the molecular formula, $\text{C}_{2.19}\text{H}_{0.80}\text{O}_{1.00}$. This process evolved the release of toxic gases (NO_2 and N_2O_4) and generation of reactive species such as dioxygen and could not be characterized appropriately [245]. Later on Brodie’s method was modified by Staudenmaier in 1898 [246] by adding multiple aliquots of KClO_3 in the reaction mixture during the course of reaction rather than in one step and fuming HNO_3 was replaced by conc. H_2SO_4 , which is used to increase the acidity of the reaction mixture. The final product ended up with the same composition as with Brodie’s product having the carbon/oxygen (C/O) ratio of 2.89. But this method was unsafe and

tedious as it evolved the formation of harmful gas (chlorine dioxide) and still had room for its improvement.

In 1958, Hummers and Offemann developed a new non-hazardous strategy for the oxidation of graphite to graphite oxide [12,247]. In their experiment, graphite was oxidized by using potassium permanganate (KMnO₄) as oxidant in the water-free mixture containing conc. H₂SO₄ and sodium nitrate (NaNO₃). This method results in the production of *in situ* HNO₃ and thus avoids the usage of corrosive fuming HNO₃ [12]. In this case, C/O ratio was found out to be 2.25. The chemical reactions occurring in Hummers method are given below:



The above reactions generate a more reactive species, dimanganese heptaoxide (Mn₂O₇), serving as an effective oxidizing agent for the oxidation of graphite to graphite oxide [248]. The residual permanganate and manganese dioxide were reacted with hydrogen peroxide (H₂O₂) in order to reduce it to manganese sulphate [247].

Later on, several modifications to the Hummers method have been performed in order to improve its effectiveness and safety by keeping the main strategy to be the same [249-251]. Therefore, these methods are named as “*modified Hummers method.*” One such modification is done by Kovtyukhova *et al.* [249] in which a pre-oxidation step was performed so as to achieve complete oxidation following the original Hummers method. This is one of the most widely adopted methods till date for the synthesis of GO and has been followed in the present work. In this method, the graphite was pretreated with a mixture of H₂SO₄, potassium persulphate (K₂S₂O₈) and phosphorous pentoxide (P₂O₅) at 80 °C. The GO thus produced had a thickness of about 1 nm and dimension of several microns with the chemical composition of C:O:H to be 4:2.95:2.5 [249] and has the advantages in terms of degree of oxidation and yield of the final product.

Introduction

Over the years, a number of graphite oxide structural models have been proposed by Hofmann, Ruess, Scholz-Boehm, Nakajima-Matsuo, Lerf-Klinowski, and D  kany [12,243,245 and references therein]. The most widely adopted structure is proposed by Lerf-Klinowski (nonstoichiometric model), which contain hydroxyl and epoxide groups at the basal plane, where as carboxyl groups at the edges (Fig. 1.10) [12,241,243,245]. Other researchers have made slight modification to the structure including the presence of 5 and 6 membered lactol rings on the edges along with the esters of the tertiary alcohols on the surface [241,245,252,253].

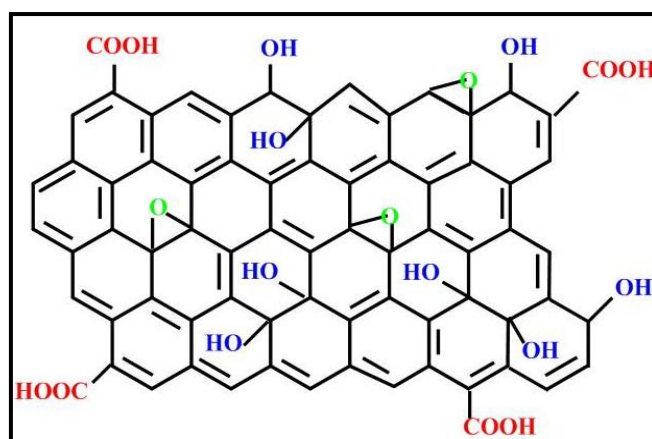


Fig. 1.10: Proposed structure of GO based on Lerf-Klinowski model.

The harsh oxidation conditions used for the synthesis of GO leads to the generation of oxygen functionalities on its surface which creates defects/vacancies, thereby, causing the disruption of sp^2 conjugation and acts as an insulator. In order to recover the sp^2 conjugation and to make it electrical conducting, it is required to reduce the oxygen functionalities from its surface. Several methods have been adopted for the reduction of GO to graphene: chemical (reducing agents [12], solvothermal [254] and hydrothermal [255]) [241], thermal annealing, microwave [241,256], electrochemical [241,257], pulsed laser irradiation [258] and photoirradiation [259,260]. These methods results in the varying physicochemical properties. A number of investigations have also been focused on the functionalization of graphene using covalent and non-covalent approaches [261].

In the present report, we would focus on the chemical reduction of GO only, as it has several advantages as regards to easy synthesis, functionalization and tunable morphologies making it suitable for its bulk preparation [11,12,262]. The large scale solution-based method besides being versatile and providing easy functionalization is also cost effective [11]. It may, however, be mentioned that the graphene synthesized from this method generally introduces defects [263].

A number of reducing agents have been used till date for the reduction of GO to synthesize graphene/reduced graphene oxide and some of the most commonly used are: NaBH_4 [253,264], lithium aluminium hydride (LiAlH_4) [265], hydrohalic acids [266,267] and strong alkaline solution (NaOH/KOH) [268]. Most of these reducing agents are corrosive and toxic for the human health and environment [263]. Some of such reducing agents have been discussed below briefly:

Shin *et al.* [264] have used NaBH_4 as the reducing agent for the reduction of GO and investigated its reduction mechanism. The extent of reduction of GO was monitored by varying the concentration of reducing agent from 15-150 mM. For its typical concentration (150 mM), the C/O ratio of graphene film was found out to be 8.6 having the sheet resistance at minimum ($2.6 \times 10^3 \Omega \text{ sq}^{-1}$) with the resistivity and conductivity to be $2.2 \times 10^{-4} \Omega \text{ m}$ and 45 S/m, respectively. In the subsequent work, Gao *et al.* [253] demonstrated the reduction of GO in two-step method using NaBH_4 as a reducing agent for removing the oxygen functionalities from GO followed by its treatment with H_2SO_4 . The resulting product exhibited the formation of single-layer graphene sheet as was indicated by its selected area electron diffraction (SAED) pattern. It exhibited the conductivity of about $1.66 \times 10^3 \text{ S/m}$ and its ^{13}C NMR spectrum showed upfield shift in the sp^2 graphitic carbon peak (119 ppm) along with its enhancement. Its subsequent annealing in Ar/H_2 for 15 min at 1100°C resulted in an increase in the conductivity to $2.02 \times 10^4 \text{ S/m}$ with a further upfield shift in graphitic sp^2 carbon peak (105 ppm).

Introduction

Ambrosi *et al.* [265] have used LiAlH_4 as a reducing agent for the reduction of GO. In a comparison of its reducing efficiency with NaBH_4 , it acted as a powerful reducing agent, exhibiting the C/O ratio of 12.0 as compared to that of NaBH_4 (9.5). The extent of GO reduction was examined by monitoring the remaining carboxylic groups on graphene which was found to be 2 and 6% in the case of LiAlH_4 and NaBH_4 , respectively. However, the lower electrical conductivity and HET rate was found for graphene synthesized by employing LiAlH_4 to that of NaBH_4 and has been attributed to the presence of lesser defect sites and C-H moieties.

Fan and his co-workers [268] used strong aqueous NaOH solution (8 M) for the reduction of GO (0.5-1 mg/mL) at moderate temperature of 80°C for few minutes. It resulted in the production of single-layer graphene sheet with a thickness of 0.8 nm. Its ^{13}C NMR spectrum showed the reduction in the hydroxyl and epoxide functionalities along with the enhanced sp^2 carbon peak at 90-150 ppm.

In the recent past, a number of mild and natural/environmental friendly reducing agents have been chosen for the reduction of GO. Some of the mild reducing agents with relatively low toxicity are: malic acid, tartaric acid and oxalic acid [269,270]. The natural/environmental friendly reducing agents are such as: sugars (glucose, fructose, sucrose and dextran) [271,272], vitamins (pyridoxine, pyridoxamine and riboflavin) [273], acids (caffeic acid and gallic acid) [274,275], metal powders (Al, Zn and Sn) [276-278], phenols (green tea) [279], plant extracts (tobacco leaves, *Pulicaria Glutinosa*, *Colocasia esculenta* and *Citrus sinensis*) [280-282], food stuff (mung beans and starch based materials) [283,284], microbes (baker's yeast, *Escherichia coli*, *Shewanella* and wild carrot roots) [285-288], protein (bovine serum albumin) [289], ascorbic acid [290-292], sodium citrate [293], and rose water [294].

Song *et al.* [270] have reported the reduction of GO (0.3 mg/mL) using oxalic acid (78 mg/mL) as a reducing agent at 75°C upon heating for 18 h. In order to remove the

remaining oxalic acid, this reaction mixture was further heated at 150 °C for an hour. The resultant product contained multilayer graphene structure as was confirmed by its SAED pattern. Its electrical conductivity was estimated to be 1000 S/m, which is six orders of magnitude higher than that of GO. It also exhibited excellent electrocatalytic activity towards methanol oxidation.

Teng and co-workers [269] have reported the synthesis of graphene using acids such as oxalic, tartaric, and malic. In this study, the reaction mixture contained relatively lesser amount of acid (10:1 weight ratio of acid:GO) and was heated at 95 °C, for a longer period of about 24 h. The reduction was found to be efficient in the order: tartaric acid < malic acid < oxalic acid which has been attributed to the decrease in steric hindrance. GCD measurements exhibited the C_s (F/g) values of 147, 100.8 and 112.4 for oxalic, tartaric and malic acids, respectively at a current density of 0.1 A/g in 1 M H₂SO₄. The difference in the values of C_s was attributed to the steric hindrance and ionization constant of these acids.

A green approach has been adopted for the reduction of GO (0.1 mg/mL) using reducing sugars namely glucose, fructose and sucrose (1.6 mg/mL) under mild alkaline conditions at 95 °C [271]. The reduction of GO to graphene was demonstrated by several spectroscopic and microscopic techniques viz. Ultraviolet-Visible (UV-Vis), X-ray diffraction (XRD), Raman, X-ray photoelectron spectroscopy (XPS), atomic force microscopy (AFM) and transmission electron microscopy (TEM). The synthesized graphene nanosheets exhibited good electrocatalytic activity towards catecholamines (dopamine, epinephrine and norepinephrin).

Liu *et al.* [277] have developed the green, novel and ultrafast method to reduce GO using Zn powder under mild alkaline conditions with the aid of ultrasonication at room temperature. For the ultrasonication time(s) of 10 and 60 min, the C/O ratio of reduced GO was determined to be 8.09 and 8.58, respectively. The high resolution transmission electron microscopy (HRTEM) examination of reduced GO obtained upon 10 min of ultrasonication

Introduction

revealed the presence of a mixture of single- and a few-layered graphene. The GCD measurements of this sample exhibited the C_s value of 116 F/g at 0.05 A/g in 6 M KOH and it also showed fairly cyclic stability for 5000 cycles at 5 A/g with an increase in the initial capacitance value by about 112 %. This behavior has been attributed to the presence of residual functional groups.

Kim *et al.* [278] have carried out the reduction of GO using Sn/HCl at room temperature and 50 °C. The reduction was found to be efficient at 50 °C as compared to that at room temperature which was revealed by its electrical conductivity and electrochemical measurements. XRD and XPS analyses confirmed the presence of SnO₂ particles on graphene synthesized at 50 °C which resulted in the high C_s value arising due to pseudo-capacitance. The C_s value was calculated to be 152 F/g at 1.5 A/g and it showed fairly good cyclic ability for 1500 charge-discharge cycles having retention of 92 % of the initial capacitance value.

Zhang *et al.* [290] have used L-ascorbic acid as a reducing agent for the reduction of GO (0.1 mg/mL) at room temperature (~ 23 °C) for 48 h. The reduction of GO was confirmed by UV-Vis, XRD, Raman, Fourier transform infrared (FTIR) and XPS analyses. The conductivity of the reduced GO was found to be 800 S/m. Its HRTEM image showed the discontinued fringes which has been attributed to the presence of defects.

The physicochemical properties of graphene have been further tuned by varying its morphology (GQDs, GNRs and graphene onions) [295,296,200] as well as by doping with heteroatoms [297,298]. The effect of changes in morphology and doping on the properties of graphene are discussed below briefly:

1.4.3.5 Graphene Nanoribbons (GNRs)

GNRs are elongated strip of monolayer graphene whose dimensions are limited to a few to hundreds of nm in the x-y plane (basal plane) [3,299] and have been categorized as zigzag and armchair depending upon its edge structure, behaving as a conductors and semi-

conductors, respectively [300]. Similar to graphene, GNRs can also be bilayer, a few-layer and multilayer thick [3]. In recent years, GNRs have been widely explored material and attracted considerable attention due to their high aspect ratio with increased edges, width and edge dependent electronic properties and easy functionalization [200,299,301]. These features are being explored for their applications in the field of spintronics [200], sensing [299], electronics [302], optoelectronics [303], solar cells [304], nanoelectromechanical systems [305], electrocatalysis [306], Li-ion batteries and energy storage [306-308].

A number of methods have been developed for the synthesis of GNRs such as CVD, chemical, lithographic, sonochemical, electrochemical [3,200,310] and longitudinal unzipping of CNTs. The longitudinal unzipping has been carried out by employing plasma etching, catalytic cutting by metal NPs, intercalation-exfoliation, [3,200,309] and solution-based oxidative protocol [311]. Tour and co-workers [311] have reported the solution-based oxidative unzipping of MWNTs using the combination of conc. H_2SO_4 and KMnO_4 resulting into the production of GO nanoribbons. A number of reducing agents have been employed for their reduction to produce water soluble GNRs in bulk amount [200,309,311,312]. But this approach resulted in the distortion of structure and properties of GNRs due to the excessive oxidation involved in the process and resulted in the lowering of conductivity [313]. This problem has been suggested to overcome by using the non-covalent approach, which is expected to preserve the electrical properties without disrupting their electronic structure [314].

Choucair *et al.* [315] have reported the chemical synthesis of GNRs by using pyrolysis of solvothermal product of sodium and propanol (1:1 molar equivalent) in air. SEM and TEM images revealed the formation of bundled GNRs consisting of curls, twists, crimpling and ripples. It resulted in the mixture of single- and few-layered GNRs having number of layers up to 15 with the interlayer spacing of 0.35 nm as was evidenced by TEM.

Introduction

The length of these GNRs was estimated to be about 10 μm by using SEM and TEM analyses.

Zhang *et al.* [316] have reported the synthesis of millimeter long multilayer GNRs by varying the mass ratio(s) of NaOH:GO from 10 to 33. It consists of five steps of synthesis involving its treatment at various temperatures ranging from 100-800 $^{\circ}\text{C}$. At different mass ratio(s) (indicated in the bracket), it exhibited different morphologies varying from crimped (10) *via* ribbon (26) to isolated ribbon (33) for which the $I_{\text{D}}/I_{\text{G}}$ ratio in Raman Spectroscopy was observed to vary from 1.05, 1.64 to 1.72, respectively. From FESEM images, the dimension of GNRs (mass ratio = 33) was estimated to be > 1 mm long with a width of about 10 μm .

Damein *et al.* [310] have reported the unique approach for the synthesis of GNRs with a width of about 50-100 nm by using aqueous lithium-bis-trifluoromethylsulphonylimide assisted electrochemical exfoliation of graphite electrodes. It exhibited curved morphology, which helped in preventing the stacking and, thereby increased its surface area. The C_s values (F/g) of this sample at a current density of 1 A/g were determined to be 140 and 90 in aqueous (6 M KOH) and organic (1.5 M tetraethylammoniumtetrafluoroborate in acetonitrile) electrolytes, respectively. The electrochemical performance of these curved GNRs was also compared with the chemically reduced GO (RGO). However, the C_s value of the later was decreased to 120 and 66 F/g in the used aqueous and organic electrolytes, respectively. The observed C_s of GNRs in organic electrolyte showed the high value of energy density (78 Wh/kg) as compared to that of RGO (58 Wh/kg).

Sahu *et al.* [308] have reported the chemical synthesis of lacey reduced graphene oxide nanoribbons (LRGONR) by the chemical unzipping of MWCNTs involving strong oxidizing agents ($\text{H}_2\text{SO}_4:\text{HNO}_3$ and KMnO_4). The opened MWCNTs were further treated with the varied composition of the same oxidizing agents for 8 h to create the additional

defects in nanoribbons, thereby, increasing the edge sites. The LRGONR exhibited the high C/O ratio of 15.6 with a stacking of 2-4 layers, the later was evidenced by TEM and Raman analyses. The LRGONR exhibited ultrahigh performance of supercapacitor in aqueous (2 M H₂SO₄), organic (1 M TEABF₄/acetonitrile) and ionic (1 M BMIM BF₄/acetonitrile) electrolytes with high energy densities (W h/kg) of: 15.06, 90, and 181.5 at power densities (W/kg) (current density in A/g) of: 807 (1.7), 2046.8 (1.8), and 2316.8 (1.6), respectively. Its high energy and power densities in all the three electrolytes have been attributed to the utilization of maximum surface of graphene for ion adsorption. The high C_s (F/g) values at 5 mV/s for LRGONR in aqueous (621), organic (~ 1272) and ionic (~ 1324) electrolytes have been attributed to the combination of EDLC from basal plane and pseudo-capacitance from the oxygenated groups at the edge plane.

1.4.3.6 Doping of Graphene

The doping of graphene with heteroatoms is another very important approach for altering its optical, electrical, electronic, magnetic and electrochemical properties by bringing a change in the structural and electronic behavior possibly due to the polarization. In the recent past, several heteroatoms (boron, phosphorous, sulphur and nitrogen) have been explored for the doping of graphene lattice, which resulted in the enhancement of these features [234,297,317]. Among these, the doping of N has attracted significant attention due to its electron rich nature, comparable size to that of C and larger electronegativity (3.04 on pauling scale) in comparison to that of C (2.55 on the pauling scale), and thus might provide an appropriate location to fit into the graphene lattice [318]. Moreover, the doping of N yields different bonding configurations with carbon namely, pyridinic-N, pyrrolic-N, quaternary-N (graphitic-N), pyridinc-N oxides and interstitial/adatoms in the graphene lattice. The most commonly observed N-moieties are pyridinic-N, pyrrolic-N and quaternary-N (Fig. 1.11) in which pyridinic-N and pyrrolic-N contributes one and two p electron(s) to the π -conjugation of graphene, respectively. Whereas, quaternary-N substitute

Introduction

the N atom in place of carbon atom present in the hexagonal ring of graphene [318]. Among the different types of N, pyridinic-N and quaternary-N are sp^2 hybridized and pyrrolic-N is sp^3 hybridized. N-doped graphene exhibits n-type behavior and is expected to influence the charge carrier mobility and electrical properties of pristine graphene significantly by tuning its band gap by introducing basal and edge defects [234,318]. Due to these features, N-doped graphene has been widely explored for manipulating the electrochemical behavior by improving the electrical conductivity and wettability at the electrode/electrolyte interface [318,319] and has been well exploited for its myriad of applications in the field of catalysis, sensing, light emitting diodes, field effect transistors, fuel cells, hydrogen storage, Li-ion batteries and supercapacitors [234,318].

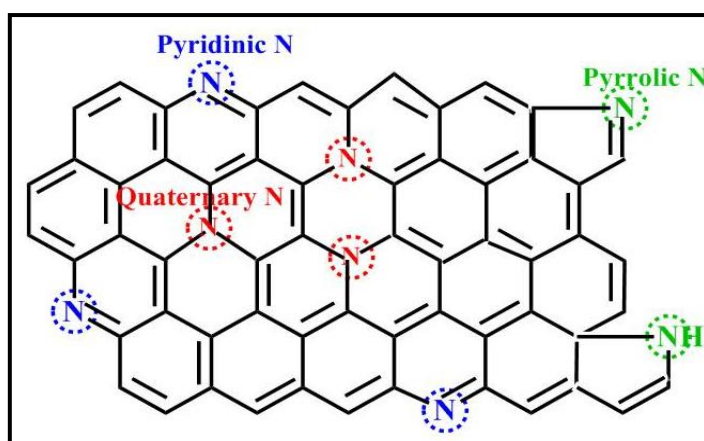


Fig. 1.11: Structure of N-doped graphene showing different moieties of N.

A number of approaches have been used till date to achieve the synthesis of N-doped graphene such as CVD, arc discharge, segregation, nitrogen plasma, thermal annealing (with N_2H_4 and NH_3), but these approaches require sophisticated equipment, involves high cost, low yield and low N-doping besides using toxic reagents for their preparation. Moreover, the resultant solid product exhibits poor dispersibility in liquid medium [234,318,320]. An alternative way to synthesize N-doped graphene is by employing solvothermal and hydrothermal approaches which involve the reduction of GO by using various organic solvents with high boiling point (*N,N*-dimethylformamide or *N,N*-dimethylacetamide), and using water with certain temperature and pressure, respectively [263,321-323]. A number of

chemical reducing agents used for the synthesis of N-doped graphene are: hydrazine [324-327], dimethylhydrazine [328], p-phenylenediamine [329], organic amines (ethylenediamine, diethylenetriamine, tetraethylenepentamine, n-propylamine and n-butylamine) [330], hydroxylamine [331], hydroquinone [332], urea [321,333], ammonia [334,335], pyrrole [336], hexamethyltetraamine [337] and dicyandiamide [338]. Unfortunately most of these reagents are corrosive, hazardous and takes relatively longer time for the reduction of GO [263,324,331]. Some of these reducing agents have been discussed below briefly:

Stankovich *et al.* [324] for the first time made use of hydrazine hydrate (1 mL of 32.1 mmol) as a reducing agent for the reduction of GO (1 mg/mL) at 100 °C for 24 h. It exhibited high C/O ratio of 10.3 as compared to that of GO (2.7) along with the C/N ratio of 16.1. It also displayed high conductivity (~ 200 S/m) to that of GO (~ 0.002 S/m). The reduction of GO and doping of N was also evidenced by the XPS analyses which showed the peak at 285.9 eV and has been attributed to the formation of C-N bond.

Lately, Zhang *et al.* [326] have also used the hydrazine hydrate (15.5 μ l) as a reducing agent for the reduction of GO (0.5 mg/mL) and the reaction mixture was heated for various time durations ranging from 10 to 90 min at 95 °C. The degree of reduction, surface state and functionalities on the surface was controlled by varying the reduction timings. The reduction product obtained after 60 min exhibited the highest C_s value (51.85 F/g at 15 mV/s) and has been assigned to the combined effect from EDLC and pseudo-capacitance. An increase in the reduction time from 60 to 90 min results in the removal of oxygen functionalities causing the loss of pseudo-capacitance. It leads to the reduction in the C_s value to 23.26 F/g and an increase in the conductivity, contributing mainly to the EDLC.

Chen *et al.* [330] have reported the controlled hydrothermal synthesis of N-doped graphene hydrogel by using GO (2 mg/mL) and organic amines (ethylenediamine, diethylenetriamine, tetraethylenepentamine, n-propylamine, n-butylamine) at 180 °C for 12

Introduction

h. These hydrogels were tested for their electrochemical performance in 5 M KOH and exhibited excellent performance for ultrafast supercapacitors. The N-doped graphene hydrogel synthesized by using ethylenediamine showed the C_s value of 109.4 F/g at a very high current density of 250 A/g with a power density of 173 kW/kg and exhibited superior electrochemical performance as compared to other organic amines and has been attributed to the presence of pyridine and pyrrolic-N at the basal plane and porous structure. The porous network results in the fast adsorption and diffusion of K^+ ion on the surface of electrode, which is responsible for the ultrafast charge-discharge rate and high power density.

Sun *et al.* [333] have synthesized N-doped graphene nanosheets (NGS) *via* one-step hydrothermal reaction between GO and urea with a high N content (10.13%). Doping level of N has been tuned by varying the mass ratio(s) of urea:GO and reaction temperature. NGS with mass ratio of 300:1 (urea:GO) exhibited high surface area (593 m^2/g) with the C_s value of 326 F/g at 0.2 A/g. It displayed the superior cyclic stability and coulombic efficiency (99.58 %) for 2000 cycles with high energy density of 25.02 Wh/kg at a power density of 7980 W/kg by using two-electrode cell.

In order to minimize the hazardous effects of some of the above mentioned reducing agents, enormous efforts have been put to employ environmental friendly reducing agent(s)/protocols for the synthesis of N-doped graphene on large scale. Some of such reducing agents are: amino acids (glycine, arginine, histidine, tryptophan, aspartic acid and valine) [273, 339-342], microorganism [343] and human urine [344].

Bose *et al.* [339] have explored the dual role of glycine (1.25 mg/mL or 10 mM) as a functionalizer and reductant for the reduction of GO (0.25 mg/mL). The reaction mixture was stirred for 12 h at room temperature followed by its refluxing for 24 h at 95 °C. The resultant N-doped graphene exhibited C/O ratio of 11.24 with the crystalline nature of the sheets consisting of a mixture of monolayer and a few layers. FTIR analysis showed the removal of oxygenated groups along with development of new peaks in the region 1286-

1335 cm^{-1} and 1543 cm^{-1} which have been attributed to the C-N stretching and N-H bending vibrations, respectively. The reduction of GO as well as the doping of N was further evidenced by XPS analysis in which the C 1s spectrum showed the enhanced intensity of C=C peak (284.4 eV) as compared to that of GO along with the appearance of a new peak at 285.6 eV arising due to the C-N bond formation and N 1s spectrum exhibiting the peaks at 398.9 and 401.4 eV.

In the subsequent work, Wang *et al.* [340] have developed one-step hydrothermal approach for the synthesis of N-doped hydrogels using different amino acids (DL-aspartic acid – acidic (NGasp), L-glycine – neutral (NGgly) and L-arginine – basic (NGarg)). The hydrogels synthesized by using NGasp, NGgly and NGarg resulted in the formation of porous 3D network, folded and wrinkled, and crumpled (stacked) graphene sheets, respectively. The surface area (m^2/g) of these hydrogels followed the order: NGasp (367.1) > NGgly (207.3) > NGarg (10.5). Raman spectroscopy showed the I_D/I_G ratio(s) for NGasp, NGgly and NGarg to be 0.98, 0.99 and 1.00, respectively which are higher as compared to that of RGO (0.97) and has been attributed to the formation of defects due to the N-doping. The doping level of N in at.% (pyrrolic-N content) in NGasp, NGgly and NGarg was revealed by XPS analyses and is found to be: 1.0 (0.59), 3.0 (2.06) and 8.9 (6.55) respectively. For these samples, the C_s (F/g) values at 3 A/g in 6.0 M KOH was found to be 246, 161 and 105, respectively. The low C_s values of NGgly and NGarg despite of having high doping level of N has been attributed to the stacking/agglomeration and low surface area.

Fan *et al.* [343] have developed a simple, efficient and environmental friendly method to synthesize N-doped graphene by the reduction of GO using mixed microorganisms from the anode chamber of microbial fuel cells. It was found that the N is homogeneously distributed on the surface of graphene with the N/C ratio of 8.14 % and found to be haemocompatible, benign and aqueous dispersible.

Introduction

1.4.3.7 Graphene Nanocomposites

The morphological and physicochemical features of undoped and N-doped graphene could further be improved/modified by forming their nanocomposites/hybrids with polymers, metal NPs, metal oxides, semiconductors, and conducting polymers [202,345-348]. These nanocomposites find its potential applications in the field of fuel cells, photovoltaic cells, photocatalysis, sensors, batteries, supercapacitors [202,345-348]. The nanocomposites of undoped and N-doped graphene with metal NPs (Pd, Pt, Au and Ag) have lately drawn considerable attention due to their enhanced physicochemical properties such as electrical, chemical and thermal stability, catalytic, and electrochemical [345,349,350]. Among different metal NPs (Pd, Pt, Au and Ag), Ag being economical and electrically conducting is largely used in microelectronics and LED devices for making electrical contacts [351]. Silver electrodes are relatively expensive and it would be desirable to replace them by fabricating Ag coated graphene electrodes. Specifically, the presence of Ag NPs on N-doped graphene sheet would allow their interaction with N as well as their immobilization may also prevent the aggregation of graphene sheet by involving supramolecular interaction(s) with its delocalized π bonds. It is thus expected to result in an increase in its surface area besides enhancing the electrical conductivity, chemical and thermal stability, catalytic activity and electrochemical behavior. Undoped and N-doped graphene-Ag nanocomposites have been demonstrated to act as a SERS substrate for various probe molecule(s), which are expected to show high SERS activity [352-355] due to adsorption, π - π and electrostatic interactions [352,355]. These nanocomposites have also been demonstrated its significant potential for applications in catalysis, electrochemical sensing and supercapacitor(s) [273,353,356]. In literature several surfactants and hazardous reagents [355-360] have been employed for the synthesis of undoped and N-doped graphene-Ag nanocomposites which involve multiple steps and require complex manipulation [361,362]. Lately, attention has been paid to the synthesis of undoped and N-

doped graphene-Ag nanocomposites employing environmentally benign reducing agents which includes: tannic acid [353], sodium citrate [363], ascorbic acid/ water vapour [364], plant extract (*Potamogeton pectinatus*) [365], mussel-inspired dopamine [366], glucose and lactulose [367,368], gelatin [369], gum arabic [370], histidine and tryptophan [273], L-arginine [354] and glycine [371], respectively.

Dutta *et al.* [355] have synthesized Ag NPs decorated reduced graphene oxide (rGO) nanosheets by a simple wet chemical approach employing co-reduction of GO (0.5 mg/mL) and AgNO₃ (0.5 mmol) by using dimethylformamide as a reducing agent at 85 °C for 20 h. Polyvinylpyrrolidone was used additionally as a growth controlling agent for Ag NPs. TEM images exhibited the uniform distribution of Ag NPs (20-40 nm) on graphene sheet. The Ag NPs were closely related to each other at various places and are designated as “hot spots”. The aggregated Ag NPs serving as hot spots have been exploited for the SERS activity using uranyl ion as the probe molecule with a detection limit of 10 nM.

Zhang *et al.* [353] have demonstrated a benign, cost-effective and one-pot environmental friendly method for the synthesis of Ag nanoparticles-graphene nanocomposites using tannic acid as a reducing agent. These nanocomposites acted as an excellent SERS substrate with the detection limit of 1×10^{-8} M for 4-ATP as a probe molecule. The utility of these nanocomposites was also demonstrated for the electrochemical detection of glucose in human blood serum and also exhibited the remarkable catalytic performance for H₂O₂ reduction.

Hsu and Chen [354] have adopted the microwave-assisted green approach for the reduction of GO and AgNO₃ (0.1 M) by using L-arginine (38.3 mM) as a reducing and stabilizing agent. The cycle number of microwave irradiation (2.45 GHz, 900 W) was varied as: 1, 4 and 8 which resulted in an increase in Ag NPs size to 10.3 ± 4.6 , 21.4 ± 10.5 and 41 ± 12.6 nm, respectively. The SERS activity of the Ag/rGO nanocomposites was determined

Introduction

by using 4-ATP as a probe molecule and was found to increase with increasing the particle size with the minimum detection limit of 10^{-10} M.

Mayavan *et al.* [371] have synthesized N-doped graphene-Ag nanocomposites (NG-Ag) by the thermal treatment of GO with glycine and AgNO_3 at 500°C under Ar atmosphere for 2 h. The thermal treatment of the mixture of GO, glycine and AgNO_3 (mass ratio = 1:2:2) was carried out at different temperatures ranging from 100 - 500°C resulting in the formation of Ag NPs at 100°C and the reduction of GO at 200°C . At 300 and 500°C it leads to the generation of pyrrolic-N and pyridinic-N moieties in graphene, respectively along with the enhancement of C=C peak in C 1s spectra as was evidenced by their XPS analyses. At these temperature(s), the Raman spectra showed an increased in the I_D/I_G ratio(s) as compared to that of GO which has been attributed to the reduction of GO and presence of structural/edge defects due to the N-doping. TEM images of NG-Ag showed the formation of a few-layered graphene sheet decorated with the Ag NPs (15-20 nm).

The above literature survey reveals that a number of reducing agents have been employed for the reduction of GO to produce graphene [12,219,241,263] and this number is still growing rapidly. But most of these reducing agents are toxic, corrosive and restricts their usage for bulk production and, therefore, requires making use of environmentally benign reductant(s). Some of these reports have investigated the effect of different parameters like: heating time [326], temperature [371], pH of the media [372] and concentration of the reducing agent for manipulating the characteristic features of graphene. But to the best of our knowledge, we did not come across the systematic investigations, which explored the effect of each of these parameters for performing the reduction of GO.

In view of the above gaps, in the present work we have employed relatively mild/environmental friendly reducing agent(s) for the preparation of graphene and optimized their physicochemical features by changing various parameters such as concentrations of precursor(s), pH of the media considering its effect on the nucleophilicity

of reducing agent(s) and heating time for performing the reduction of GO at relatively lower temperature. The effect of changing these parameters on the morphology and functionalization has also been explored. These systems have also been examined for their supercapacitor applications.

In particular the present thesis work explores the reduction of GO by using malonic acid as a mild reducing agent, which under specific conditions of: pH (10.5), amount of malonic acid (1.6 mg/mL) and at 95 °C allowed the production of ultra thin graphene sheets with fairly high conductivity and fairly good electrochemical features. At mild pH of 6.0 it could become possible to transform its morphology from graphene sheets to graphene nanoribbons (GNRs) involving supramolecular interactions which further modulated its electrochemical behavior. We have also made use of the environment friendly reducing agent(s) such as glycine and its derivative for performing the reduction of GO into graphene. It allowed the simultaneous reduction of GO into graphene and its functionalization with N exhibiting enhanced electrochemical features with those reported in previous investigations. The physicochemical properties of N-doped graphene have been further modified by decorating its surface by Ag NPs to produce graphene-Ag nanocomposites. These nanocomposites have also been explored for SERS applications.



Chapter 2

***EXPERIMENTAL
SECTION***

2. EXPERIMENTAL SECTION

2.1 Materials and Reagents

Natural graphite flakes (+75 mesh), 2-aminoisobutyric acid (Aldrich); hydrochloric acid, hydrogen peroxide (30%), potassium permanganate, phosphorous pentoxide, malonic acid (SD Fine-chemical Ltd.); nitrogen gas (Grade 1, purity > 99.99%) (Sigma, India); dimethylformamide, silver nitrate, perchloric acid, potassium persulphate, potassium nitrate (Merck); sulphuric acid (Thomas Baker); oxalic acid (Rankem); glycine, sodium hydroxide pellets (Himedia); 4-aminothiophenol (Sigma-Aldrich) and ethanol (Changshu Yangyuan Chemical Co., Ltd.). All the chemicals were of analytical grades and used as received without any further purification. Dialysis tubing (seamless cellulose tubing) and dialysis tubing closures were purchased from Sigma. All glassware used in the present work were of Borosil make. All solutions were prepared freshly in Millipore water (Bedford, MA, USA) with the resistivity of 18.2 M Ω at 25 °C due to the sensitivity of the studied systems towards impurities.

2.2 Equipment

2.2.1 UV-Visible Spectrophotometer

The optical absorption spectra were recorded on a Shimadzu 2100S spectrophotometer in the UV–Vis range (200-800 nm). UV-Vis spectrophotometer consisted of two lamps as the light sources: deuterium arc lamp (185-350 nm) and tungsten filament-halogen lamp (350-900 nm) and R928 photomultiplier tube (190-860 nm) as a detector.

2.2.2 X-ray Diffractometer (XRD)

X-ray diffraction (XRD) patterns were recorded on a Bruker D8 Advance X-ray diffractometer using Cu K α line (0.15418 nm) as the X-ray source (Fig. 2.1). The diffractometer is equipped with two types of detector: scintillation detector for high resolution data and LynxEye detector for ultrafast measurement. In the present work, XRD

Experimental Section

measurements were recorded by using LynxEye detector as it is fast and the data measurement time is reduced significantly.

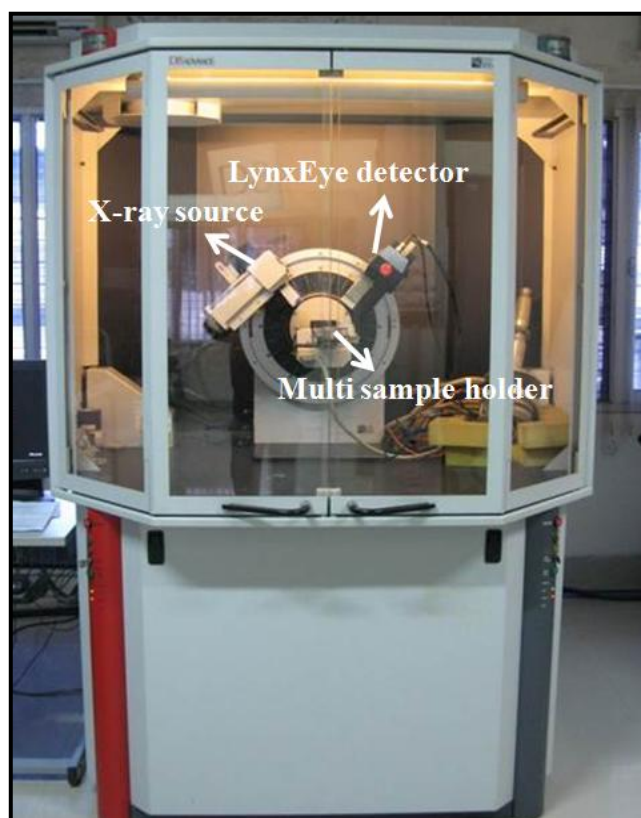


Fig. 2.1: Bruker D8 Advance powder X-ray diffractometer.

2.2.3 Raman Spectrometer

Raman spectra were recorded on a Renishaw inVia Raman spectrometer (serial no. 021R88) using Argon ion as the excitation source (514 nm, 1200 l/mm grating), equipped with Leica microscope and computer controlled XYZ motorized stage; different objective lenses (5x, 10x, 50x and 100x) and thermoelectric cooled charge-coupled device (CCD) detector (576 pixels) composed of silicon (Fig. 2.2). Raman spectrum of one sample was also recorded on Renishaw inVia Raman spectrometer (serial no. H33197) using Ar^+ as the excitation source (514 nm). The data were processed by using Wire 3.4 software.

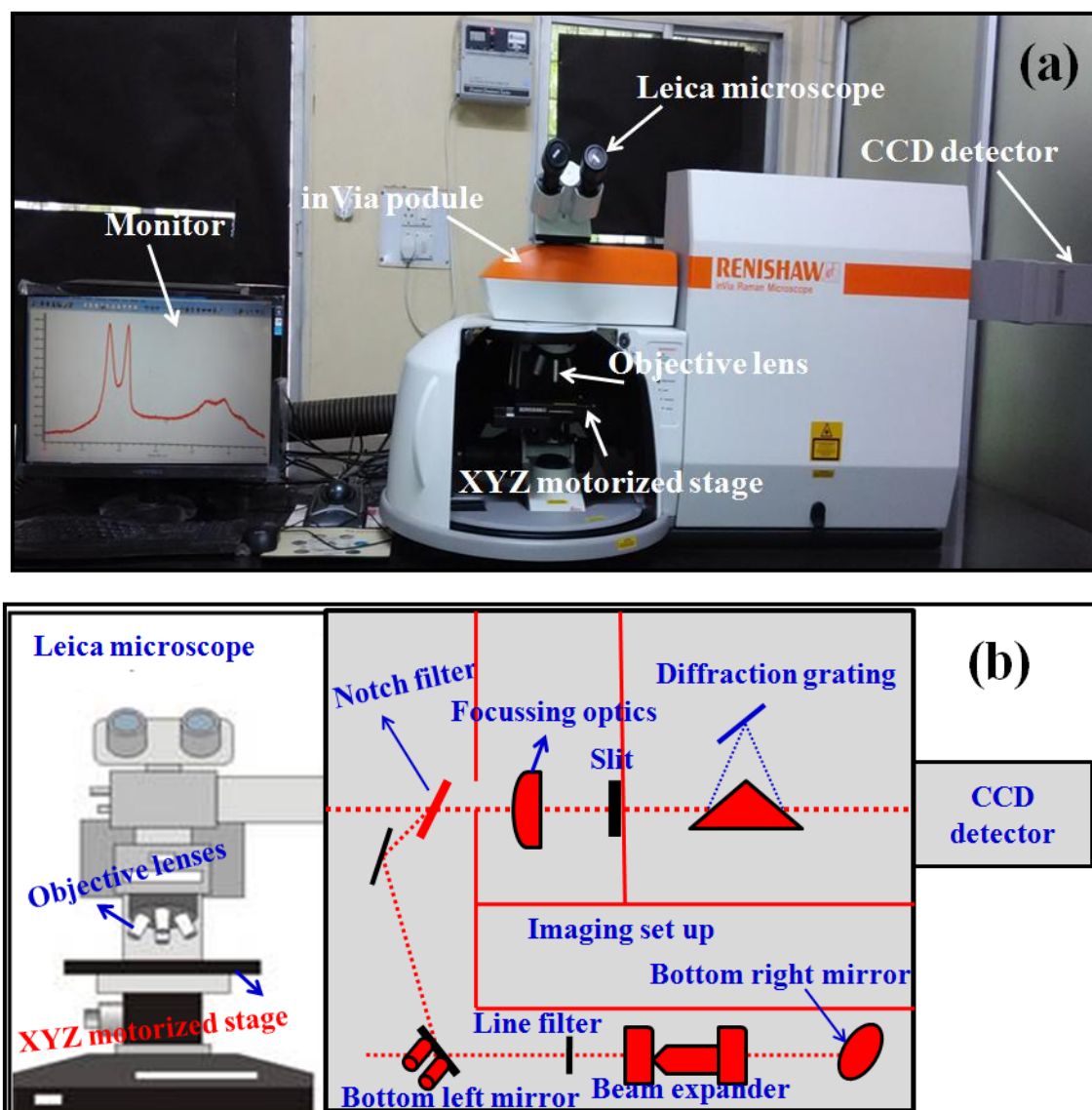


Fig. 2.2: Renishaw inVia Raman spectrometer (a) and its schematic diagram (b).

2.2.4 Zetasizer

The stability of the as-synthesized samples was performed on a Malvern Zetasizer Nano ZS90 equipped with a He-Ne laser (632 nm) as the light source (Fig. 2.3). For the zeta (ζ)-potential measurements folded capillary clear disposable cuvette was used. The obtained data were processed by using Zetasizer software version 7.02.



Fig. 2.3: Zetasizer Nano ZS90.

2.2.5 Atomic Force Microscopy (AFM)

The surface topography of as-synthesized carbon nanostructures was analyzed by recording 2D images on NTEGRA atomic force microscope (AFM) (Fig. 2.4). It has a resolution of 0.2 nm along x and y axes and 0.04 nm along z axis. Due to the high resolution along z axis, it has been mainly used to determine the surface height of carbon nanostructures. The surface height of the samples at various locations was measured by using NOVA software, procured from M/s Molecular Tools and Devices for Nanotechnology (NT-MDT).

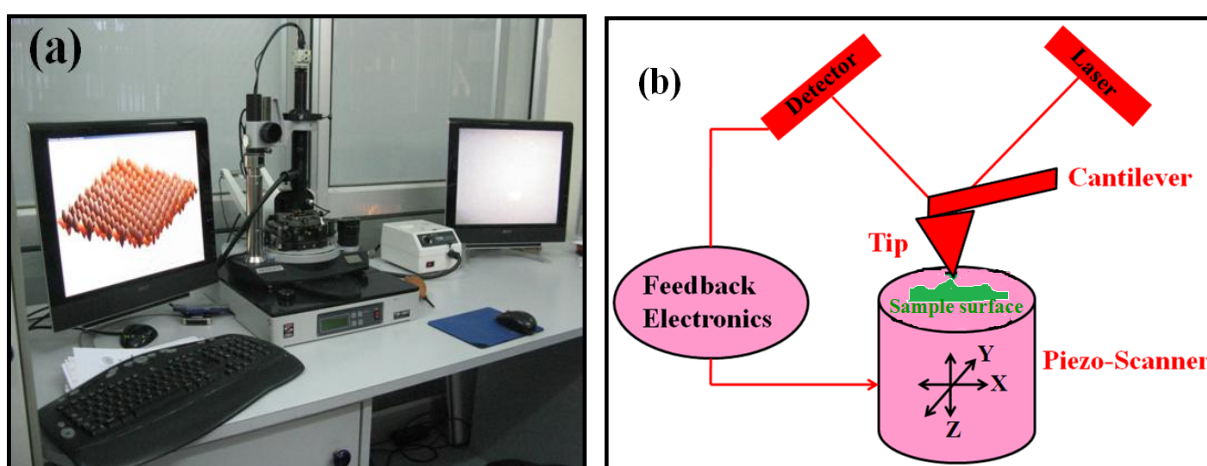


Fig. 2.4: NTEGRA AFM (a) and its working principle (b).

2.2.6 Field Emission Scanning Electron Microscopy (FESEM)

Surface morphologies and elemental analyses of the as-synthesized carbon nanostructures were performed by using QUANTA 200-FEG field emission scanning electron microscope (FESEM) from FEI, Netherlands equipped with CCD camera (Fig. 2.5). Elemental analyses of the FESEM images at different locations and their mapping were performed by using energy dispersive X-ray analysis (EDAX) facilities from Oxford instruments and AMETEK materials analysis division, AMETEK inc., having AZtec energy analysis and Genesis softwares, respectively. FESEM has a resolution of < 2 nm at an accelerating voltage of 30 kV and the acceleration voltage range could be varied from 20-200 kV. It has a varied magnification range from 12 to $> 100,000\times$. It has two operating modes: high vacuum mode for conducting sample and low vacuum mode for insulating materials. It is equipped with back scattered electron and secondary electron detectors to capture the images.

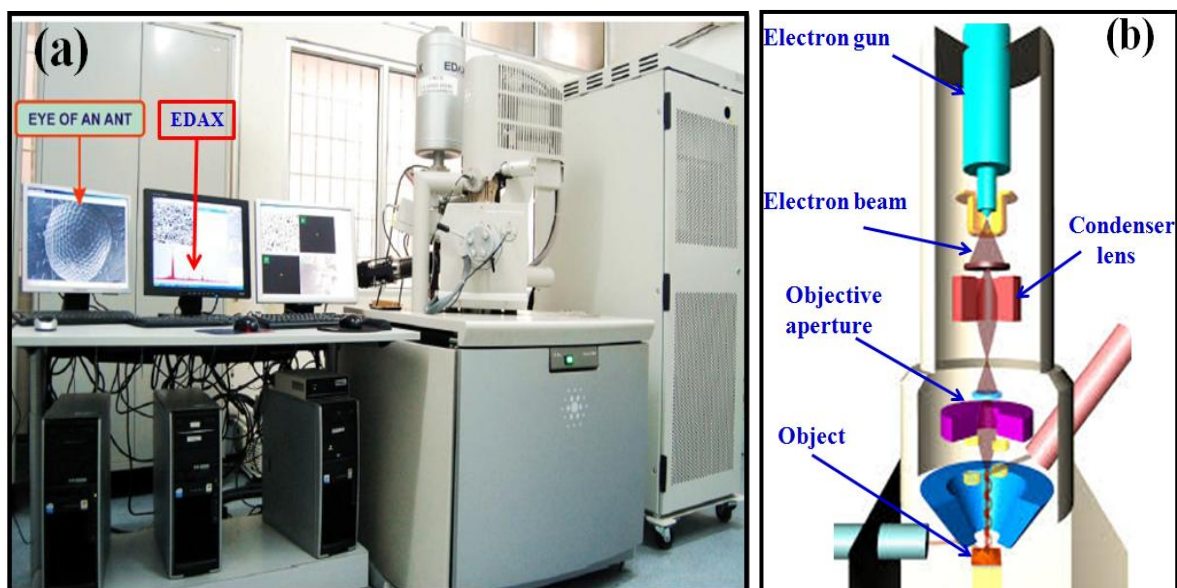


Fig. 2.5: QUANTA 200-FEG FESEM (a) and its working scheme (b).

Experimental Section

2.2.7 Transmission Electron Microscopy (TEM)

Transmission electron micrographs (TEM), high resolution transmission electron micrographs (HRTEM) and selected area electron diffraction (SAED) measurements were obtained on a FEI-Tecnai G2 20 S-TWIN operating at an accelerating voltage of 200 kV using LaB₆ as a source of electron and equipped with CCD camera (Fig. 2.6) having magnifications of $\geq 110,000\times$. It has point and line resolutions of 0.24 and 0.14 nm, respectively. Some TEM and HRTEM micrographs were also recorded on FEI-Tecnai G2 30 S-TWIN operating at an accelerating voltage of 300 kV for different magnifications.

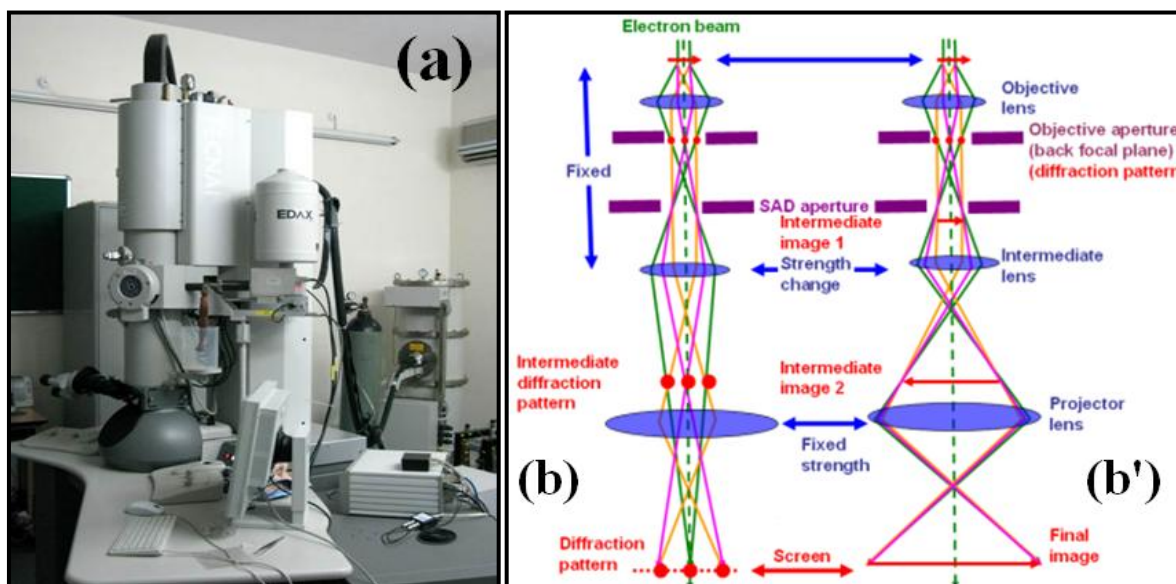


Fig. 2.6: FEI-Tecnai G2 20 S-TWIN TEM (a) and scheme depicting the operation of TEM during projection: SAED pattern on screen (b); TEM image on screen (b'). (The scheme has been taken from <http://www.globalsino.com/EM/page3891.html>).

2.2.8 Fourier Transform Infrared (FTIR) Spectrophotometer

Fourier transform infrared (FTIR) spectra of the solid samples were recorded on a Thermo Nicolet Nexus FTIR spectrophotometer in the mid-IR range of 4000-500 cm⁻¹ in KBr medium and the data were processed by using OMNIC v6.1 software (Fig. 2.7).

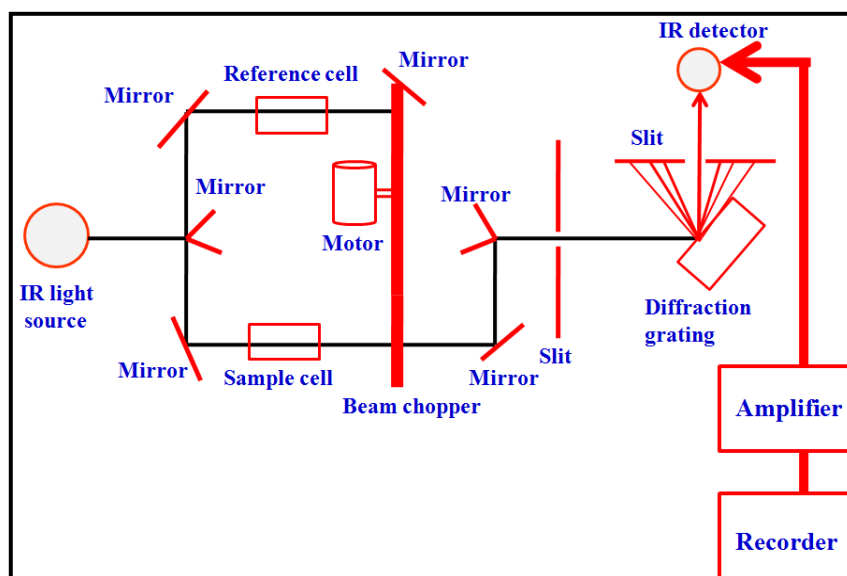


Fig. 2.7: Schematic diagram showing the working principle of IR spectrophotometer.

2.2.9 Nuclear Magnetic Resonance (NMR)

The solid-state ^{13}C single-pulse magic angle spinning (MAS) nuclear magnetic resonance (NMR) spectra were recorded on a JEOL 400 MHz NMR spectrometer (Model ECX 400 II) (Fig. 2.8). The samples were packed into 4 mm rotor and spun at 12 kHz. The spectra were averaged for more than 3000 scans using 10 s relaxation delays and $2.4 \mu\text{s}$ 90° pulse exciting over a bandwidth of 100 MHz without decoupling. Solid adamantane (29.4 ppm) was used as the external reference for ^{13}C spectrum based on tetramethylsilane scale.



Fig. 2.8: JEOL 400 MHz NMR spectrometer (Model ECX 400 II).

Experimental Section

2.2.10 X-ray Photoelectron Spectroscopy (XPS)

X-ray photoelectron (XPS) spectra were recorded on an Omicron NanoTechnology instrument using an Mg K α energy source. The base pressure of the analysis chamber was kept at 2×10^{-10} mbar during the scan [373]. The spectra were recorded at an interval of 0.05 eV. Data were processed by using the CasaXPS program (Casa Software Ltd., UK). XPS measurement of one sample was carried out at 1×10^{-10} mbar pressure on a custom built laboratory version ambient pressure photoelectron spectrometer (Lab-APPES) (Prevac, Poland) equipped with VG Scienta's R3000HP analyzer and Al K α monochromator (MX650) [374].

2.2.11 Surface Area Analyzer

Brunauer-Emmett-Teller (BET) surface area measurements for some of the samples were carried out on Autosorb-iQ (Quantachrome Instruments, USA) at 77 K.

2.2.12 Thermogravimetric Analysis (TGA)

Thermogravimetric analyses (TGA) of the solid samples were performed on a SII TG/DTA 6300 EXSTAR (Fig. 2.9) at a heating rate of 10 °C/min under N₂ atmosphere in the temperature range of 25-800 °C.



Fig. 2.9: SII TG/DTA 6300 EXSTAR.

2.2.13 Current-Voltage (I-V) Measurements

Current-voltage (I-V) measurements were performed on the unit supplied from Photo Emission Tech. Inc., USA equipped with Keithley 2400 source meter at room temperature. Some I-V measurements were also made on a Keithley 4200-SCS set up. For these measurements, the aluminum electrodes were deposited on the film(s) of the samples by using HINDHIVAC 12" vacuum coating unit (model no. 12A4D). The thickness of the film was measured by using high accuracy Digimatic Micrometer (Mitutoyo Products).

2.2.14 Electrochemical Measurements

Cyclic voltammetry (CV) and galvanostatic charge-discharge (GCD) measurements were performed on a computer controlled CHI760E electrochemical workstation (CH Instruments, USA) using a three electrode configuration at room temperature. Glassy carbon electrode (GCE) of 3 mm diameter (0.07065 cm^2 area) was employed as a working electrode, Pt wire as a counter electrode and Ag/AgCl (3 M NaCl) as a reference electrode (Fig. 2.10). Most of the electrochemical measurements were performed in 1 M H_2SO_4 as an aqueous supporting electrolyte. Other used electrolyte has been mentioned in particular chapter.

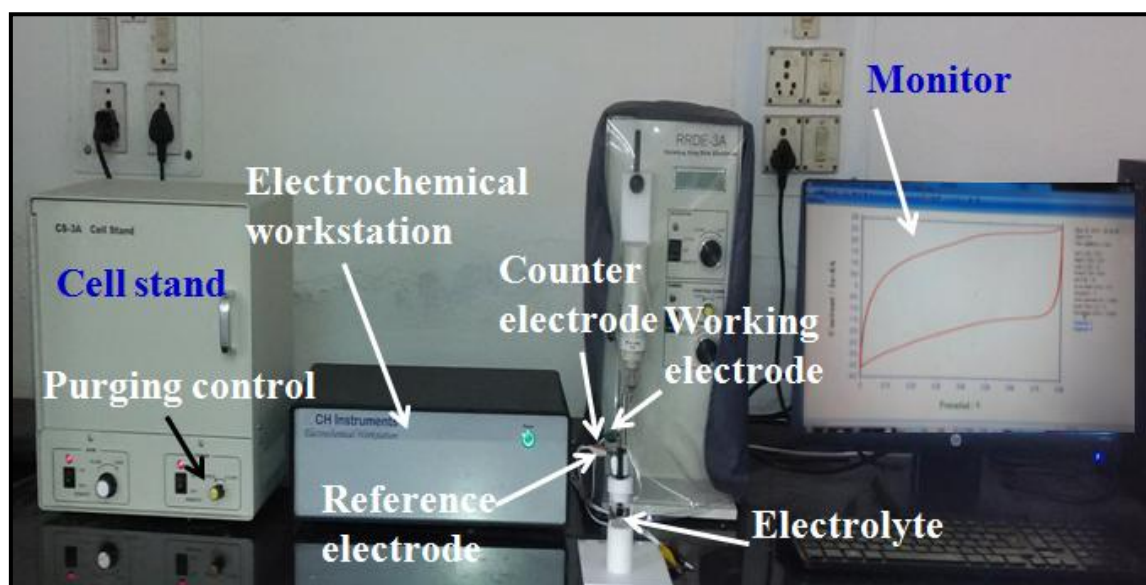


Fig. 2.10: CHI760E electrochemical workstation

Experimental Section

2.2.15 pH Meter

The pH of the reaction mixtures was maintained by using Toshniwal digital pH meter (model CL 54 +) having the sensitivity limit of ± 0.01 pH. The calibration of the pH meter was performed by using buffers of pH 4.0 (potassium hydrogen phthalate) and pH 7.0 (potassium dihydrogen phosphate/disodium hydrogen phosphate). For maintaining the acidic and basic pHs of the reaction mixture, dilute aqueous solutions of perchloric acid and sodium hydroxide, respectively were used.

2.2.16 Refrigerated Circulating Water Bath

For performing the reactions at constant temperature, refrigerated circulating water bath(s) from Lab companion (models RW-0525G and 1025G) equipped with an accessory for varying the temperature in the range from -25 to 150 °C with an accuracy of ± 0.5 °C were used (Fig. 2.11). In most of the experiments, the temperature of the reaction mixture was maintained at 95 °C.



Fig. 2.11: Lab Companion refrigerated circulating water bath.

2.2.17 Centrifuge

The samples were centrifuged by using REMI microprocessor research compufuge (model PR-24) at a centrifugation speed of 13 000/14 000 rpm by using rotor no. 4 (Fig. 2.12).



Fig. 2.12: REMI microprocessor research compufuge.

2.2.18 Vacuum Oven

The as-synthesized samples were dried at 50-60 °C in order to avoid any further oxidation in a vacuum oven, procured from Labtech, Daihan Labtech Co. Ltd, New Delhi.

2.2.19 Furnace

The annealing of the as-synthesized samples was performed on a Metrex programmable high temperature furnace equipped with microprocessor temperature controller with a temperature ranging from ambient to 1500 °C having the temperature accuracy of ± 1 °C.

2.2.20 Hot Plate

IKA C-MAG HS 7 hot plate having the facility to vary the temperature from ~ 50-450 °C equipped with IKA ETS-D5 temperature sensor was used for heating the reaction mixture directly.

Experimental Section

2.2.21 Sonicator

The samples were sonicated by using SAKOVA ultrasonic cleaner at a frequency of 50 Hz and voltage of 230 V.

2.2.22 Ultrasensitive Balance

METTLER-TOLEDO XS205 ultrasensitive analytical balance with an accuracy of 0.01 mg/0.1 mg (81 g/220 g) was used for verifying the mass loading of active materials deposited on the electrodes used for electrochemical measurements.

2.3 Methodology

2.3.1 UV-Vis Spectrophotometer

The electronic spectra of the liquid samples were recorded in the wavelength range of 200-800 nm at room temperature using double beam spectrophotometer. The optical absorbance of the samples was recorded in 1 mm path length quartz cuvette in order to bring the absorption within the absorbance range of the equipment. The three dimensional optical absorption spectra figures were made by using MATLAB software version R2011b.

2.3.2 XRD

X-ray diffraction patterns of the solid samples were recorded in the 2θ range of 5-85° at a scan rate of 0.2°/0.3°/step using Cu K α (0.15418 nm) as a X-ray source. For these measurements, a voltage of 40 kV and a current of 30 mA were applied. The obtained X-ray diffraction patterns were compared with the Joint committee for powder diffraction standards (JCPDS) database for the phase identification and confirmation of structure of the material by using PANalytical X'pert high score software from PANalytical B. V., Almelo, Netherlands.

In crystal structures, atoms are arranged in a regular and repeating order. When X-rays are incident on the crystal, they will undergo diffraction either through constructive/destructive interference, depending on the path difference. When the path

difference is equal to an integer multiple of λ (Fig. 2.13), the scattered radiation will undergo constructively interference following the Bragg's law:

$$n\lambda = 2d \sin \theta \quad (2.1)$$

Where, n is an integer, λ is the wavelength of used X-rays, 'd' is the path difference and θ is the scattering angle.

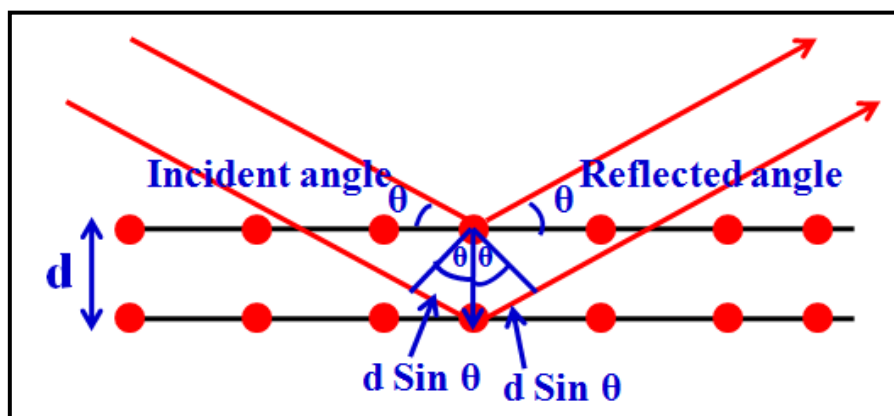


Fig. 2.13: Diagrammatic representation of Bragg's law.

The crystallite size (L) of the samples was determined by using the Scherrer equation [375] assuming a Gaussian function fit for the peak:

$$L = \frac{K \lambda}{\beta \cos \theta} \quad (2.2)$$

Where, K is a dimensionless shape factor and in the present thesis its value is taken as 0.9 [375], λ is the wavelength of the Cu $K\alpha$ radiation (0.15418 nm), β is full width half maxima (FWHM) and θ is the Bragg's angle.

2.3.3 Raman Spectrometer

For Raman measurements the solid/liquid samples applied on the glass plate were placed on the clean glass substrates. The used Raman spectrometer equipped with different objective lens(es) along with the Leica microscope allows to achieve the higher spatial resolution. The spectral data were recorded in the wavenumber range of 500-3500 cm^{-1} with a spectral resolution of 0.5-1 cm^{-1} in Raman shift. All spectra were measured by using 50x objective lens at low laser power of 0.5-1 mW for an exposure time of 30-60 s in order to

Experimental Section

avoid any damage to the samples. Prior to the measurements, the Raman spectrometer was calibrated by using internal silicon as a reference, which exhibited Raman band at 520 cm^{-1} . The 3D images of the Raman spectra were made by using MATLAB software, version R2011b. The in-plane crystallite size (L_a in nm) for the carbon nanostructures was determined by using Tuinstra-Koenig relation [318]:

$$L_a = \frac{(2.4 \times 10^{-10}) \lambda^4}{I_D/I_G} \quad (2.3)$$

Where, λ is the Raman excitation wavelength (514 nm).

2.3.4 AFM

The sampling for the AFM analyses of different carbon nanostructures was carried out by applying a drop of diluted sample on the clean glass plate followed by its drying under ambient conditions. For solid sample(s), their small amount was dispersed upon sonication in the deionized water. The 2D images of different samples were recorded under semi-contact mode by varying the scanning frequency in the range of 1.56 to 3.13 Hz at room temperature.

2.3.5 FESEM

For FESEM analyses, samples were prepared by applying a small amount of solid sample on the double sided tape which was then fixed on the aluminum stub. For liquid samples, a drop of the dilute sample was applied on the clean glass plate followed by its drying under ambient conditions and the glass plate was stucked on to the aluminum stub using double sided tape. The contact between double sided tape/glass plates with aluminum stub was made by using silver paste. In order to make the surface of these samples conducting, gold was sputtered on their surface under inert environment of helium maintaining the high vacuum at $30\text{ }\mu\text{A}$ for 50-70 s. In the present work, the FESEM images, their EDAX spectra and elemental mapping were performed at a working distance of 10-11 mm by applying an acceleration voltage of 20 kV at different magnifications.

2.3.6 TEM

The TEM analyses of different carbon nanostructures were carried out by applying a drop of dilute sample onto a carbon coated copper grid G-200 (size 3.05 mm). For the solid sample(s), its small amount was dispersed in deionized water and sonicated for about 15-20 min. The grids were subsequently dried overnight in dark at room temperature in order to evaporate the remaining moisture prior to their examination. The electron micrographs, EDAX spectra and SAED pattern of the samples were recorded by applying an acceleration voltage of 200 or 300 kV at different magnifications. Indexing of the diffraction patterns and size distribution of NPs were performed by using imageJ 1.42q software from NIH, USA. The Gaussian fitting of the size distribution of NPs was done by using OriginPro 8 software from OriginLab Corporation, USA.

2.3.7 BET Measurements

For BET measurements, the samples were degassed at 120 °C for about 12 h under vacuum prior to its analysis. The samples were prepared in the form of pellets (~ 1-2 mm thick) using hydraulic press by applying a pressure of ~11 tons. NovaWin software was used to fit the data in Brunauer-Emmett-Teller (BET) model within the pressure range (P/P_0) of 0.05-0.3 in order to determine the specific surface area.

2.3.8 NMR and XPS Measurements

The solid samples were used for NMR and XPS measurements. The NMR data were processed by using Delta NMR processing and control software. The XPS data were deconvoluted into multiple peaks by using Gaussian peak function in OriginPro 8 software from OriginLab Corporation, USA.

2.3.9 I-V Measurements

The uniform film of the samples for I-V measurements were prepared by applying the drop(s) of liquid sample onto a transparent conducting indium titanium oxide (ITO) substrate. Aluminum electrodes were deposited on the as-prepared films by using thermal

Experimental Section

deposition technique under vacuum followed by its drying overnight at 50 °C. In some cases the contacts were also made by using silver paste.

In the present work four-probe method was used to determine the conductivity of carbon nanostructures as it allows stable, accurate and precise measurements. It avoids the unwanted voltage drop arising due to the contact resistance between probes and the sample. Electrical conductivity was calculated by the reciprocal of resistivity.

The resistivity was calculated by employing the below given equation (2.4) [376]:

$$\rho = \left(\frac{\pi t}{\ln 2} \right) \left(\frac{V}{I} \right) \quad (2.4)$$

Where, ρ (Ω cm) is the resistivity, t (cm) is the thickness of the samples, V (V) is the applied potential and I (A) is the current flowing through the material.

The conductivity (σ) has been calculated by using $\sigma = 1/\rho$ (S/cm).

2.3.10 Electrochemical Measurements

In the present work, the specific capacitance (C_s) (F/g) from CV curves was calculated by using the below given equation 2.5 [267]:

$$\frac{1}{2m \cdot \Delta V \cdot s} \left(\int_{0.8}^0 idV + \int_0^{0.8} idV \right) \quad (2.5)$$

Where, m (g) denotes the mass of the active material applied on the electrode, ΔV (V) denotes the change in potential window, s (mV/s) is the scan rate and

$\int_{0.8}^0 idV + \int_0^{0.8} idV$ (A) denotes the total current obtained by the integration of positive and negative sweep in cyclic voltammetry.

C_s from GCD curves was calculated by using the below given equation 2.6 [278]:

$$C_s = \frac{I \cdot \Delta t}{\Delta V \cdot m} \quad (2.6)$$

Where, I (A) is the discharging current, Δt (s) is the discharging time, ΔV (V) is the potential change during discharging step and m (g) denotes the loading mass of the active material. The CV and GCD measurements were performed in the same potential window of 0.0-0.8 V. The Coulombic efficiency (η) of different carbon nanostructures modified electrodes was calculated from their charge-discharge curves using the below given equation 2.7 [377]:

$$\eta = \frac{T_d}{T_c} \times 100\% \quad (2.7)$$

Where, η represents the Coulombic efficiency, T_d and T_c are the discharging and charging time, respectively.

Energy density and power density of carbon nanostructures modified electrodes was calculated by using the below given equations 2.8 and 2.9, respectively [378]:

$$E = \frac{C_s \Delta V^2}{2 \times 3.6} \quad (2.8)$$

$$P = \frac{E \times 3600}{t} \quad (2.9)$$

Where, C_s (F/g) stands for the specific capacitance at different current densities, ΔV (V) is the change in potential window, E (Wh/kg) is the energy density, P (W/kg) is the power density and t (h) represents the discharging time.

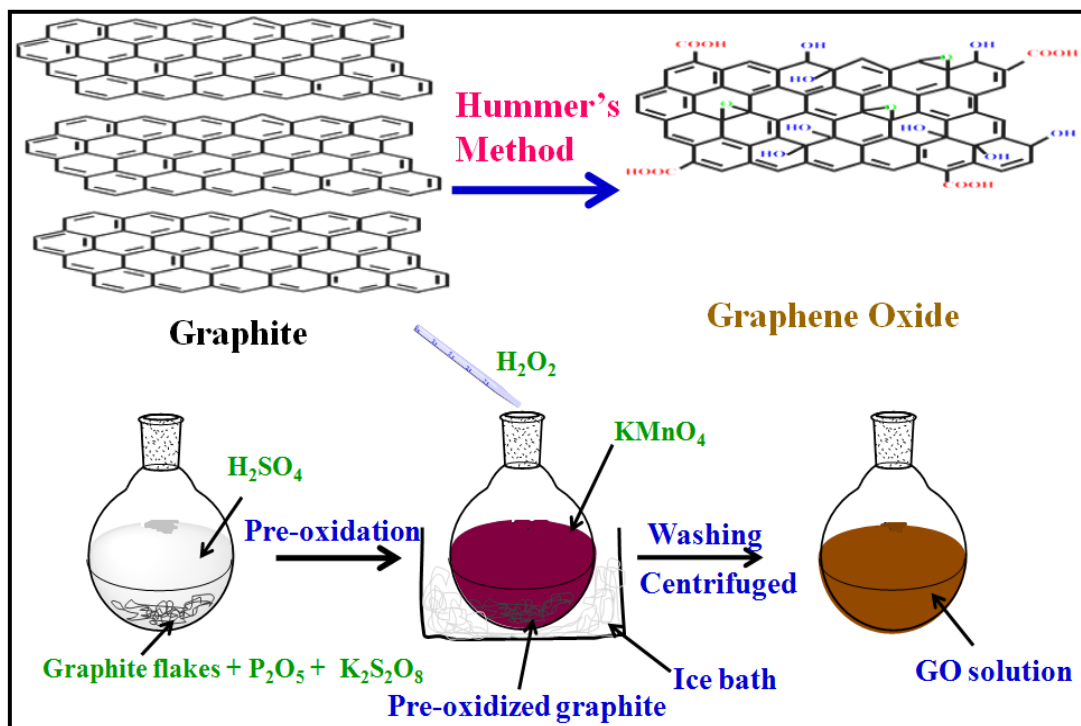
2.3.11 Synthesis of Graphene Oxide

Graphene oxide (GO) was prepared from natural graphite flakes adopting the modified Hummers method (Scheme 2.1) [247,249]. Graphite flakes (1.5 g) were added into the solution containing the preheated mixture of conc. H_2SO_4 (6 mL), $K_2S_2O_8$ (1.25 g) and P_2O_5 (1.25 g) at 80 °C. The resulting mixture was stirred on an oil bath maintained at 80 °C for about 4.5 h followed by its cooling to room temperature. Thereafter, it was diluted with

Experimental Section

deionized water (DIW) and left overnight. Subsequently, the resulting mixture was filtered and washed repeatedly with DIW using a 2-20 micron filter to remove the residual acid. The product thus obtained was dried overnight under ambient conditions in vacuum desiccator. The pre-treated graphite flakes were then put into ice cold concentrated H_2SO_4 (60 mL) maintained at 0°C . To this solution, KMnO_4 (7.5 g) was added gradually under stirring by maintaining the temperature $< 20^\circ\text{C}$. The resulting mixture was stirred for about 2 h on an oil bath at 35°C followed by the addition of 125 mL DIW in an ice bath to keep the temperature $< 50^\circ\text{C}$. The mixture was further stirred for 2 h at 35°C , and then additional 350 mL of DIW and 10 mL of 30% H_2O_2 was added into it sequentially. It resulted in a change in color of mixture from greenish black to brilliant yellow. This mixture was left undisturbed for 24 h. Thereafter, it was centrifuged and washed with 10% aqueous HCl (~1 L) followed by about 1 L of DIW to remove any remaining acid. The brown product thus obtained was dried at 50°C for 24 h. The resulting solid GO was diluted to make its dispersion (5 mg/mL) in DIW. This GO dispersion was then dialyzed for one week to remove the remaining metal species if any.

Out of this, 0.5 mg/mL of GO dispersion was exfoliated into DIW by sonication under ambient conditions for 30 min. The resulting homogeneous yellow-brown dispersion was stable for several months and was employed as precursor for performing reactions.



Scheme 2.1: Pictorial representation for the synthesis of GO following modified Hummers method.

2.3.12 Modification of Working Electrodes

The GCE electrodes were polished sequentially by making slurry of alumina powder having size 1 μm followed by 0.5 and 0.03 μm using microcloth pad. The electrodes were rinsed thoroughly in an ultrasonic bath sequentially by using DIW and ethanol for about 10-15 min, respectively. GCE electrodes were then dried under the flow of N_2 . Carbon nanostructures dispersion was prepared by suspending them in dimethylformamide (DMF) (0.5 mg/mL) by ultrasonication for about 20-30 min. In the present work, the loading of carbon nanostructures on the working electrode was carried out without employing any binder [379-381], as it might influence the electrochemical behavior of the electrode material [382]. This homogeneously prepared solution was drop-casted repeatedly after drying each time onto the surface of GCE electrode. The electrode surface was then allowed to dry overnight at room temperature. The loading mass on the working electrode was kept at 0.015 mg (0.21 mg/cm^2), which was also verified by weighing the electrode before and after loading of the sample using ultrasensitive METTLER-TOLEDO balance. A Similar

Experimental Section

procedure was adopted for the preparation of GO modified working electrode with the mass loading of 0.015 mg (0.21 mg/cm²) and 0.004 mg (0.057 mg/cm²) for CV and GCD measurements, respectively. The electrolyte (1 M H₂SO₄) was purged strongly with N₂ for about 5 min in order to remove any dissolved oxygen prior to performing electrochemical measurements.



Chapter 3

***SYNTHESIS OF ULTRA THIN
GRAPHENE SHEETS USING
MALONIC ACID AS A REDUCING
AGENT FOR ENERGY STORAGE
APPLICATIONS.***

3. SYNTHESIS OF ULTRA THIN GRAPHENE SHEETS USING MALONIC ACID AS A REDUCING AGENT FOR ENERGY STORAGE APPLICATIONS

In the literature a number of mild reducing agents containing carboxylic groups with relatively less toxicity such as: oxalic acid, tartaric and malic acid have been employed for the reduction of GO to produce graphene [269,270]. However, these reducing agents take relatively a longer time (~18-24 h) for accomplishing the reduction of GO and makes use of their fairly high concentration (≥ 5 mg/mL) [269,270]. Apart from the nature of reducing agent, the effective reduction of GO to produce graphene requires to optimize the effect of various parameters like concentration of reducing agent, pH, temperature and the heating time of reduction under mild conditions.

In the present chapter malonic acid (Fig. 3.1), a dicarboxylic acid having an active methylene group, has been employed as a reducing agent for the reduction of GO. The malonic acid being dibasic acid like oxalic acid, but having additionally an active methylene group, is expected to act as an efficient reducing agent under mild basic pH conditions because of the different possible resonating structures (Fig. 3.2). The complete reduction of GO (0.5 mg/mL) required relatively much lower concentration of malonic acid (1.6 mg/mL or 15.38 mM) and only 6 h of heating at 95 °C. The as-synthesized ultrathin graphene sheets exhibits fairly high conductivity, specific capacitance and long-term cyclic stability suggesting its potential for high performance supercapacitor applications.

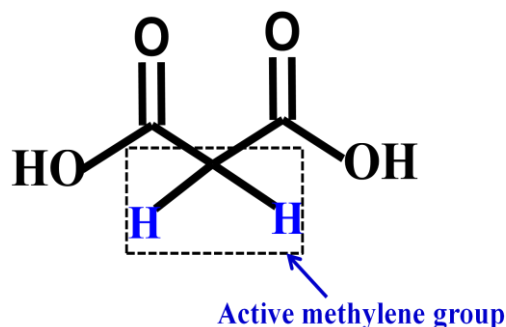


Fig. 3.1: Structure of malonic acid.

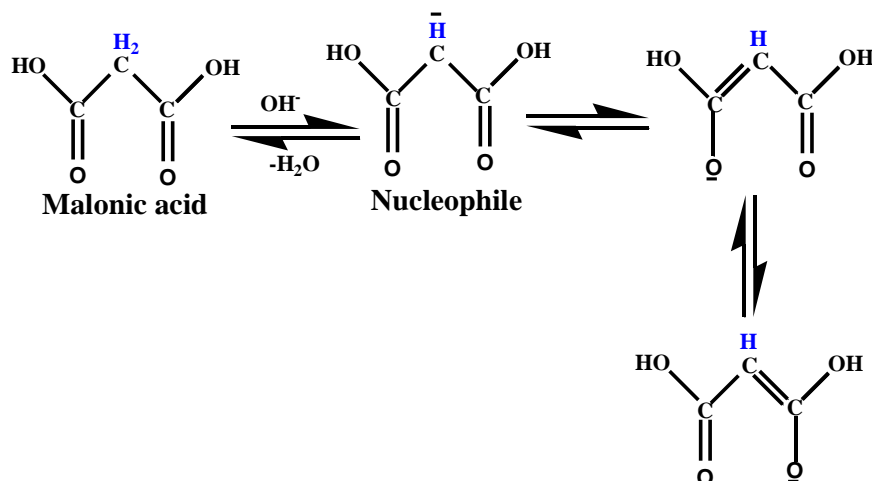


Fig. 3.2: Resonating structures of malonic acid in mild basic condition.

3.1 Optimization of Various Parameters for the Effective Reduction of GO to Synthesize Graphene Sheets

3.1.1 Optimization of the Amount of Malonic Acid

The ratio of the amount of malonic acid to GO was optimized by monitoring its optical absorption spectra (Fig. 3.3). The mass ratio(s) of malonic acid:GO were varied from 1.2-5.2:1 by keeping the time of heating and pH of the reaction mixture constant at 6 h and 10.5, respectively (Fig. 3.3). At lower mass ratio of malonic acid:GO (1.2:1) it exhibited the absorption maximum at 260 nm, indicating the incomplete reduction of GO (Fig. 3.3a). The maximum absorbance in the entire UV-Vis region was obtained for the malonic acid:GO mass ratio of 3.2:1 showing the absorption maximum at 263 nm (Fig. 3.3b). Thereafter, the increase in the mass ratio of malonic acid:GO to 5.2:1 did not bring any change in the absorption maximum (Fig 3.3c) but the absorbance decreased slightly in the entire UV-Vis region. Therefore, the mass ratio of malonic acid:GO was kept to be 3.2:1.

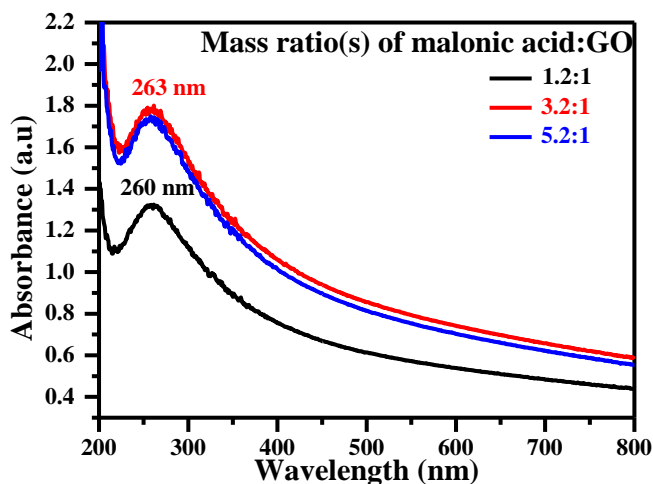


Fig. 3.3: Optical absorption spectra for the reduction of GO as a function of mass ratio(s) of malonic acid:GO varying from 1.2-5.2:1.

3.1.2 Optimization of the Heating Time

The heating time of the reaction mixture containing malonic acid and GO was varied up to 8 h by keeping the mass ratio of malonic acid:GO and pH constant at 3.2:1 and 10.5, respectively. The changes in the absorption peak of the reaction mixture as a function of heating time up to 6 h is shown in Fig. 3.4A. It clearly shows that the absorption maximum is gradually red shifted from 230 to 263 nm associated with a regular change in the color from yellowish-brown to black. After 6 h, the reaction mixture did not show any shift in the absorption maximum and increase in absorbance (Fig. 3.4B). Therefore, the heating time of the reaction mixture was kept to be 6 h.

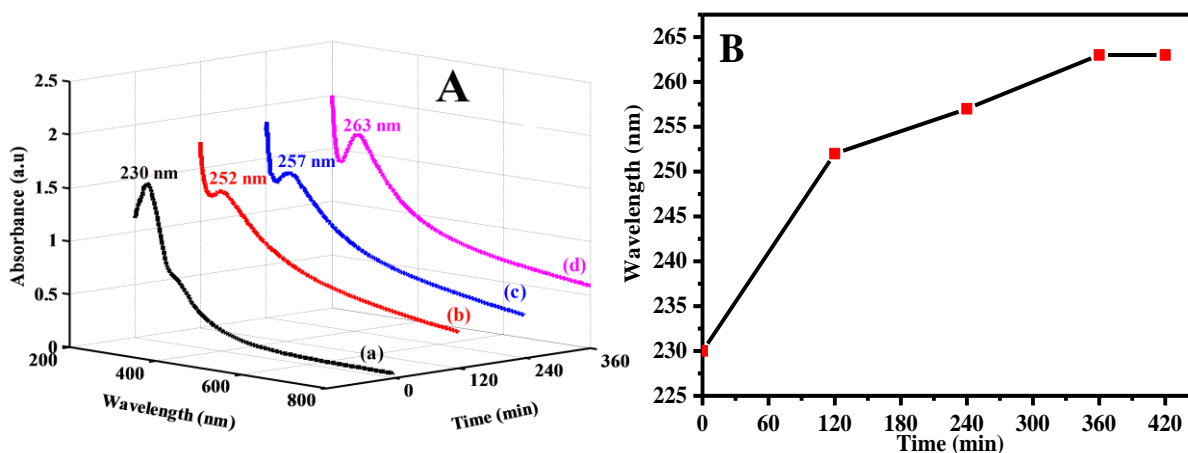


Fig. 3.4: 3D optical absorption spectra showing changes in the absorption peak of reaction mixture containing GO and malonic acid at pH 10.5 as a function of heating time - (panel A). Shift in the absorption maximum of GO with the heating time - (panel B).

3.1.3 Optimization of the pH

The pH of the reaction mixture was optimized by keeping the mass ratio of malonic acid:GO and heating time constant at 3.2:1 and 6 h, respectively. The pH of the reaction mixture was varied from 6.0 to 10.5 and the observed changes were monitored by using optical absorption spectroscopy. For the typical pH(s) of 6.0 and 10.5, the optical absorption maxima were observed at 253 and 263 nm, respectively (Fig. 3.5a and b). It evidently reveals that the reduction of GO is more effective at pH 10.5 and at pH 6.0 it remains incomplete. It may be mentioned here that at pH 6.0 it takes much longer time for accomplishing the effective reduction of GO. This aspect will be discussed later in the next chapter.

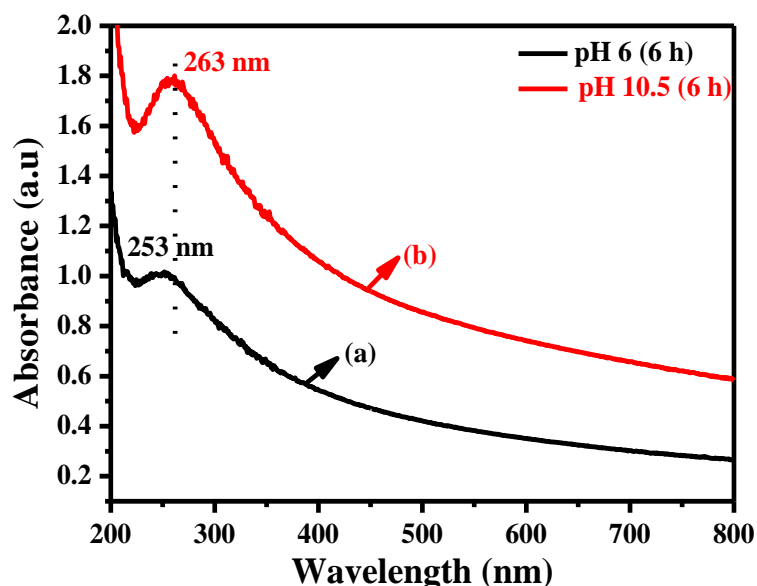


Fig. 3.5: The reduction of GO at pHs: 6.0 (a) and 10.5 (b) after 6 h of heating.

3.1.4 Synthesis of Graphene under Optimized Reaction Conditions

Based on the above optimized conditions for the reduction of GO, 80 mg (1.6 mg/mL or 15.38 mM) of malonic acid was mixed with 50 mL of GO dispersion containing 25 mg of GO (0.5 mg/mL) under vigorous stirring and the pH of the resulting solution was maintained at 10.5 by adding dilute NaOH. The reaction mixture was heated on a circulating water bath at 95 °C for 6 h. The resultant black suspension was centrifuged and washed with DIW from eight to nine times in order to remove any residual malonic acid. The product

thus obtained was dispersed into DIW maintaining the pH of the solution at 10.5 and is denoted as GRH-MA. Annealing of the as-synthesized GRH-MA was carried out at 300 °C for 1 h and is denoted as GRH-MA300.

In control experiments, the reduction of GO was also carried out by using oxalic acid and OH⁻ as reducing agent(s) under identical experimental conditions as mentioned above and the resulting product(s) are denoted as GRH-Ox and GRH-OH⁻, respectively.

3.2 Characterization of Graphene Sheets (GRH-MA)

The as-synthesized graphene has been analyzed by using a number of characterization techniques *viz.* UV-Vis, zetasizer, XRD, Raman, AFM, FESEM, TEM, FTIR, XPS, ¹³C NMR, TGA, I-V and CV and details of these investigations are described below:

3.2.1 Optical Studies

The optical absorption spectrum of GO exhibits a peak and a shoulder at 230 and 302 nm which can be attributed to π - π^* transition due to C=C and n- π^* transition corresponding to the C=O group, respectively (Fig. 3.6a). The heating of GO (0.5 mg/mL) in the presence of malonic acid (1.6 mg/mL) at pH 10.5 for 6 h results in the formation of blackish product exhibiting a red shifted absorption peak at 263 nm (Fig. 3.6b). It indicates the formation of graphene (GRH-MA) upon reduction of GO due to the restoration of sp² character. Digital photographs of GO and GRH-MA are shown in the inset of Fig. 3.6. The colloidal dispersion of GRH-MA was fairly stable as was revealed by its dynamic light scattering (DLS) measurement in which the value of ζ -potential was determined to be - 55 mV (Fig. 3.7). It may be mentioned that the ζ -potential value was obtained without adding any additional surfactant/stabilizer. It suggests that the malonic acid acts both as an effective reducing agent as well as stabilizer in the present case.

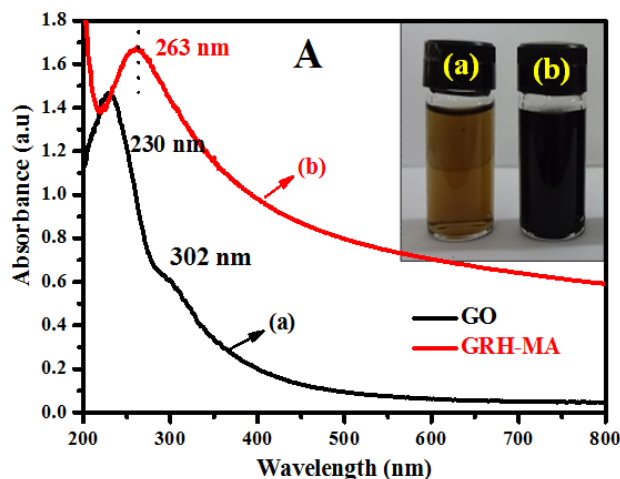


Fig. 3.6: Optical absorption spectra of GO (a) and GRH-MA (b) along with their digital photographs captured by dispersing them in water (inset).

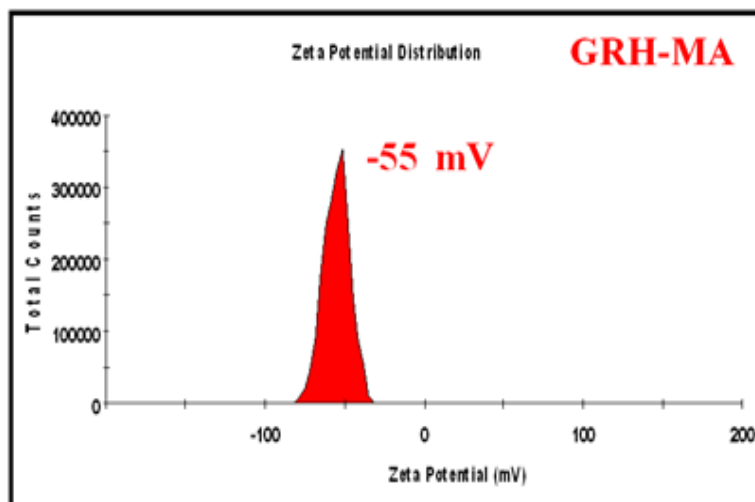


Fig. 3.7: ζ -potential of GRH-MA.

In a control experiment, the effect of OH^- at the used pH of 10.5 was also analyzed in the absence of malonic acid (GRH-OH^-). The absorption spectra of GRH-OH^- obtained after 6 h of heating is shown in Fig. 3.8a. It shows the absorption maximum at 257 nm, which is quite different to that obtained in the presence of malonic acid (263 nm) (Fig. 3.6b), suggesting that OH^- under these conditions does not result in the complete reduction of GO. The complete reduction of GO by OH^- takes place at relatively much longer period (~13 h) (Fig. 3.8b).

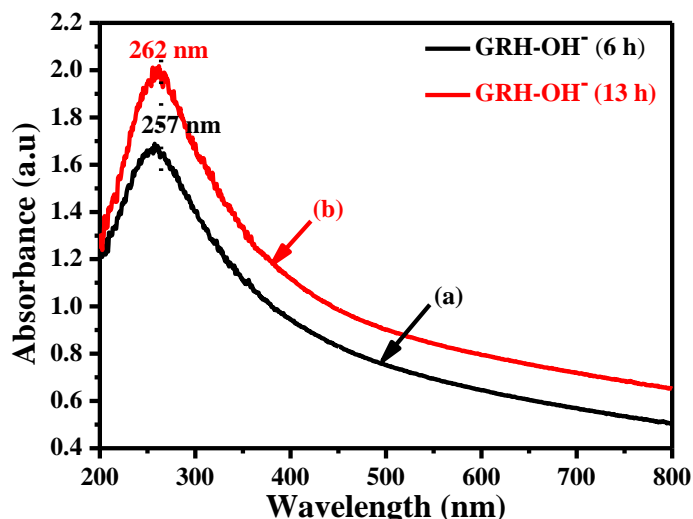


Fig. 3.8: Optical absorption spectra of GRH-OH⁻ after 6 h (a) and 13 h (b) of heating.

3.2.2 Raman Spectroscopy

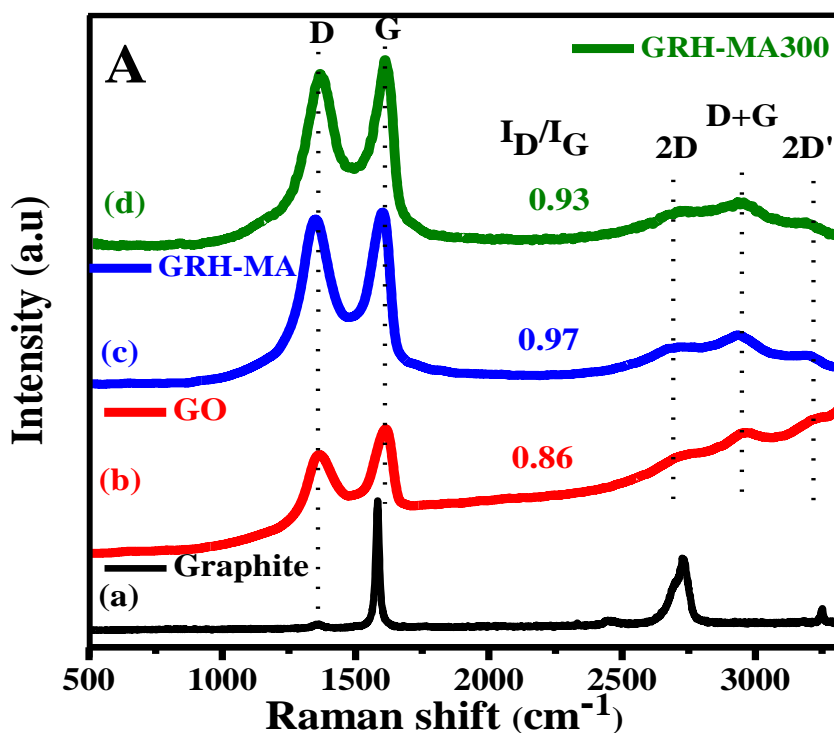
The Raman spectra of graphite, GO, GRH-MA and GRH-MA300 are shown in Fig. 3.9A and their spectral data have been summarized in Table 3.1. The Raman spectrum of graphite shows two characteristic bands (cm^{-1}) at 1359 (D band) and 1583 (G band) (Fig. 3.9A-a) as assigned earlier [383]. The D band has been attributed to the breathing mode of A_{1g} symmetry induced due to the defects and G band arising from the in-plane bond stretching of the sp^2 carbons and is assigned to E_{2g} symmetry [383,384]. On the other hand, GO exhibits D and G bands (cm^{-1}) at 1356 and 1606 (Fig. 3.9A-b), respectively matching fairly well to the previous report on GO [383]. A comparison of the Raman spectra of GO with graphite shows that the shape of the peaks due to D and G bands in case of GO become broad, and the G band is blue shifted from 1583 to 1606 cm^{-1} .

The change in the I_D/I_G ratio of GO in the presence of malonic acid at 95 °C was examined as a function of heating time (Fig. 3.9B). It showed a gradual increase in the I_D/I_G ratio from 0.86 to 0.97 after 6 h of heating at 95 °C indicating the reduction of GO to GRH-MA (Fig. 3.9A-b and c). GRH-MA also exhibits typical D and G bands (cm^{-1}) at 1353 and 1604, respectively. An increase in the I_D/I_G ratio of GRH-MA (0.97) as compared to that of GO (0.86) suggests the increased number of smaller sp^2 domains upon the removal of

Synthesis of ultra thin graphene sheets using malonic acid as a reducing agent for energy storage applications

oxygen functionalities in GO [324]. This aspect was further probed by calculating the in-plane crystallite size (L_a in nm) of the GO and GRH-MA, from which the value was worked out to be 19.48 and 17.27 nm, respectively.

The as-synthesized GRH-MA was annealed at a mild temperature of 300 °C (GRH-MA300) and the Raman spectrum due to this sample also shows D and G bands (cm^{-1}) at 1354 and 1596, respectively. It shows an interesting feature, the G band is red shifted from 1604 to 1596 cm^{-1} in the direction in which the graphitic (sp^2) character is increased (Fig. 3.9A-d) as has been reported previously upon annealing [385]. This finding suggests that the annealing process leads to the production of more ordered graphitic structure.



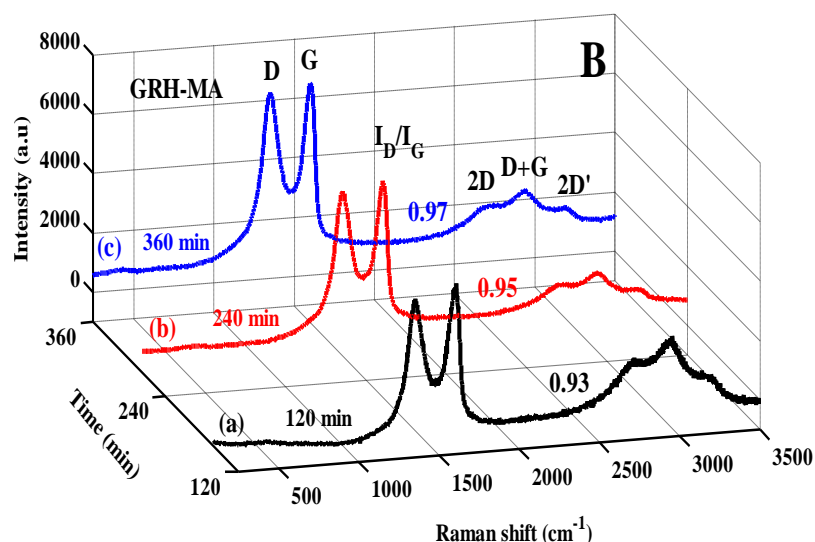


Fig. 3.9: Raman spectra of: graphite (a), GO (b), GRH-MA (c) and GRH-MA300 (d) - (panel A). Changes in the 3D Raman spectra of GO as a function of heating time - (panel B).

Table 3.1: Raman spectral data of graphite, GO, GRH-MA and GRH-MA300.

Sample(s)	D band (cm ⁻¹)	G band (cm ⁻¹)	I _D /I _G
Graphite	1359	1583	-
GO	1356	1606	0.86
GRH-MA	1353	1604	0.97
GRH-MA300	1354	1596	0.93

3.2.3 XRD Studies

The XRD patterns of graphite, GO, GRH-MA and GRH-MA300 are shown in Fig. 3.10. The XRD pattern of graphite exhibits a sharp peak at 26.2° corresponding to the (002) plane with a ‘d’ spacing of 0.339 nm (Fig. 3.10a), whereas, the XRD pattern due to GO shows a relatively broader peak at 10.2° corresponding to the reflection from (002) plane with a ‘d’ spacing of 0.865 nm (Fig. 3.10b) which has been assigned to the intercalation of the water molecules and oxygen containing functional groups between the layers of graphite. These observations are in agreement to the previous report [271]. In contrast to the precursors, graphite and GO, the peak due to GRH-MA is quite broad and is observed at 24.2° corresponding to the reflection from (002) plane with a reduced ‘d’ spacing of 0.36 nm (Fig. 3.10c), which is slightly higher than that of graphite (0.339 nm). To further analyze the slight difference in the obtained ‘d’ value of GRH-MA (0.36 nm) as compared to that of pristine graphite (0.339 nm), the as-synthesized sample was annealed at a mild temperature

of 300 °C (GRH-MA300). The XRD pattern due to this sample shows a relatively sharper peak with a reduction in the ‘d’ value to 0.35 nm (Fig. 3.10d), which is now more closer to that of pristine graphite. The sharpness of peak suggests an increased ordering of the as-synthesized graphene sheet upon annealing for a shorter period of time at mild temperature [386].

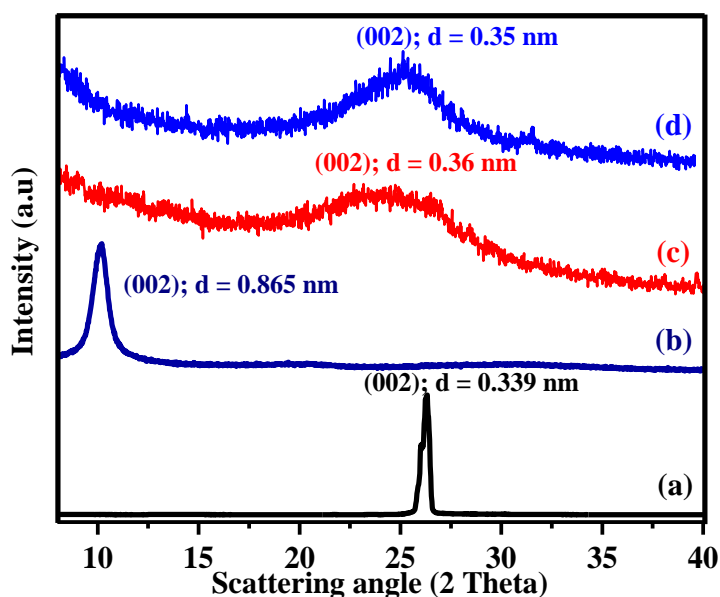


Fig. 3.10: XRD patterns of graphite (a), GO (b), GRH-MA (c) and GRH-MA300 (d).

3.2.4 AFM Analysis

The topography and surface heights of GO and GRH-MA were examined by performing AFM analyses (Fig. 3.11). AFM images of these samples show them to contain a sheet-like structure (Fig. 3.11a and b). The average surface height for GO and GRH-MA across several lines (all lines not shown) were estimated to be 1.12 ± 0.1 nm and 0.41 ± 0.03 nm, respectively (Fig. 3.11a' and b'). The observed GO thickness (1.12 ± 0.1 nm) has been earlier assigned to its single-layer [290]. On the other hand, the AFM image of GRH-MA shows it to contain fairly fine sheet structure, which clearly shows it to be a single-layer graphene sheet. It may be mentioned that in previous studies the thickness of the sheet ranging from 0.7 to 1.0 nm has been claimed for the single-layer graphene [387,290,388].

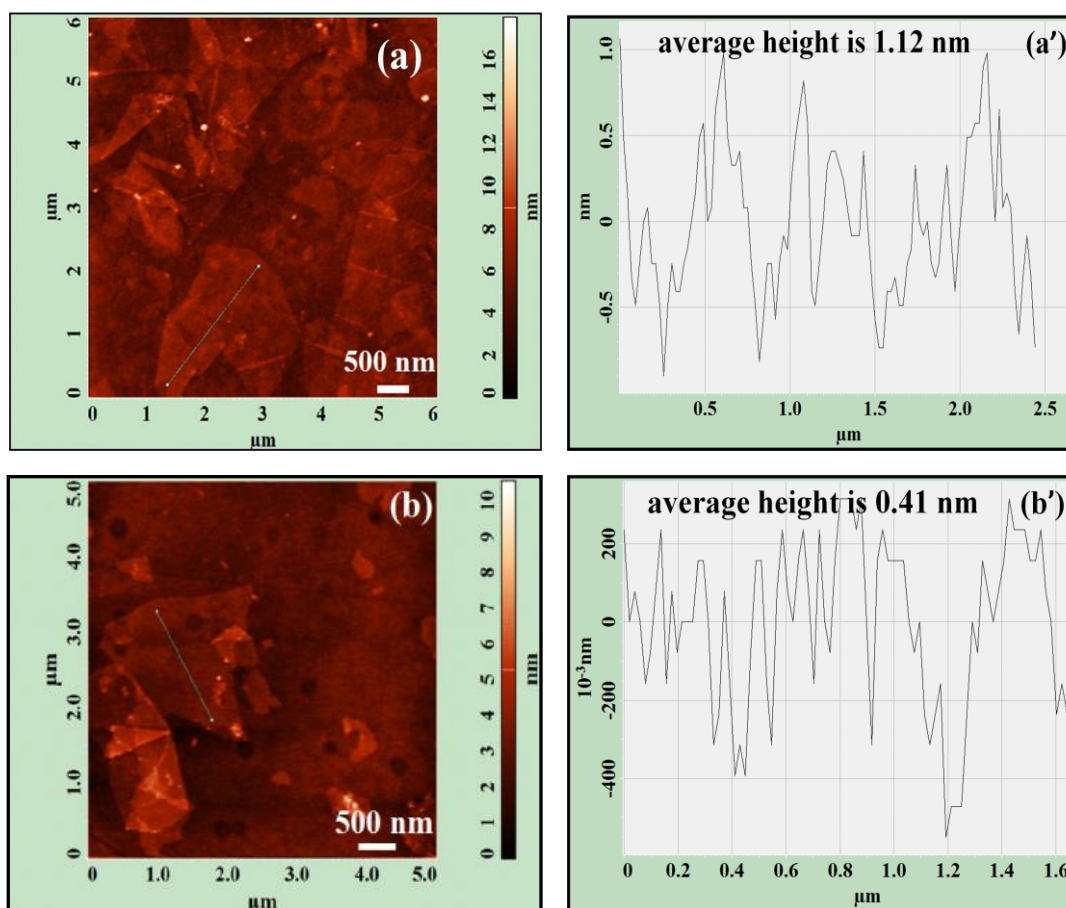


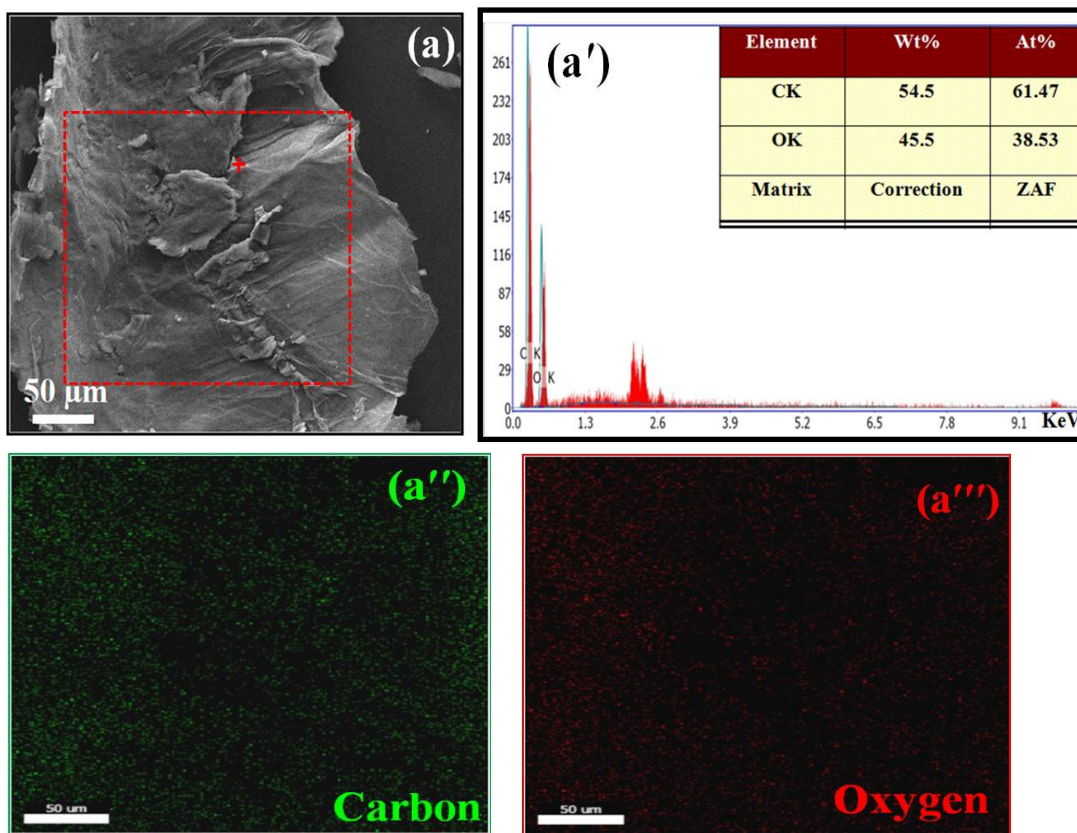
Fig. 3.11: AFM images and their height profile along a particular line indicated in these images: GO (a and a') and GRH-MA (b and b'), respectively.

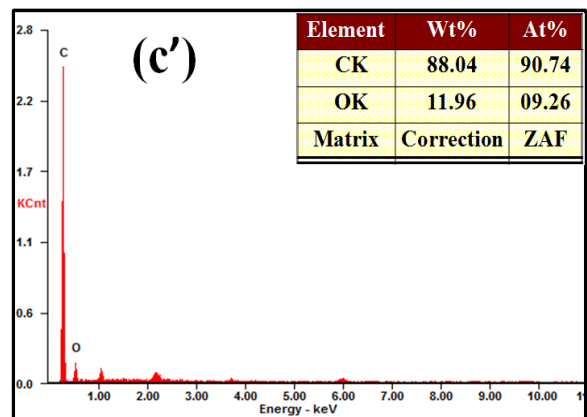
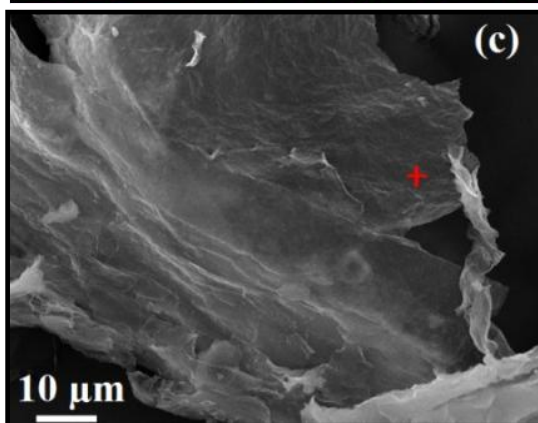
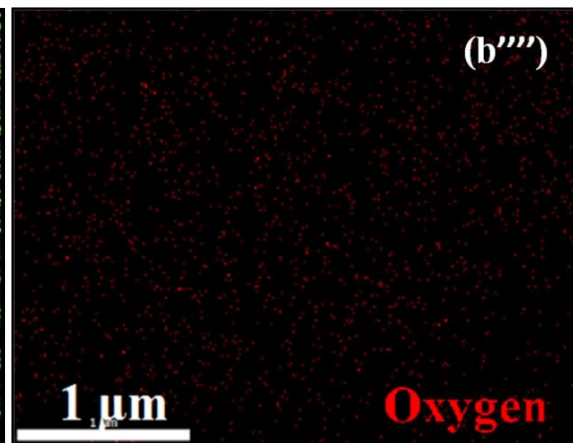
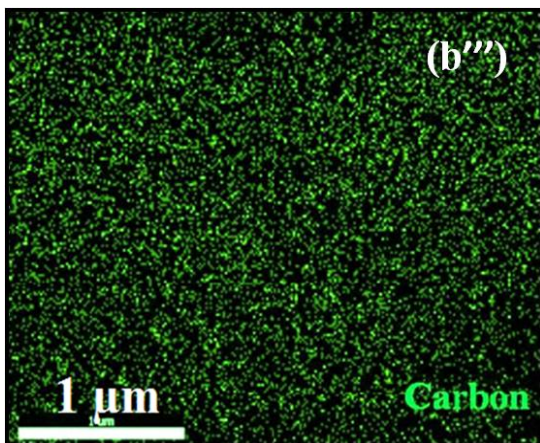
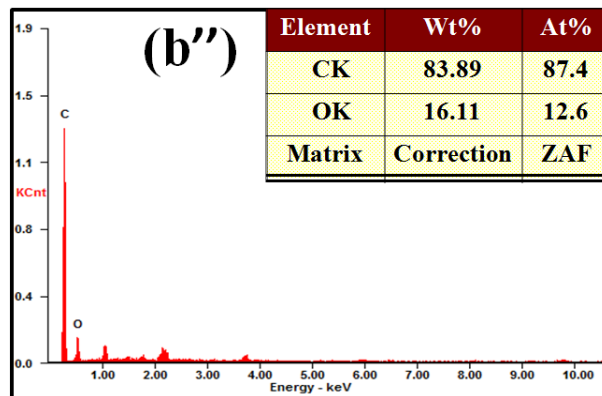
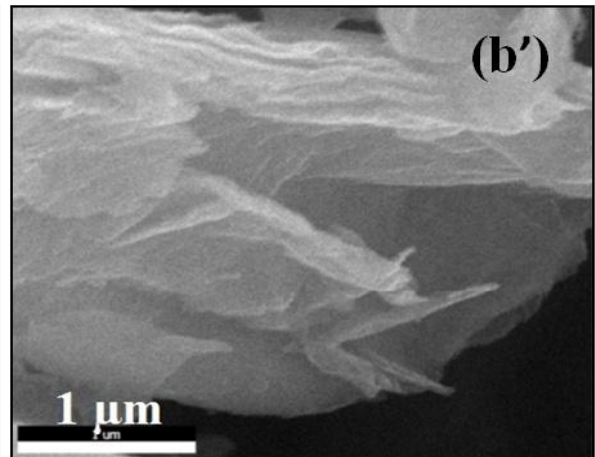
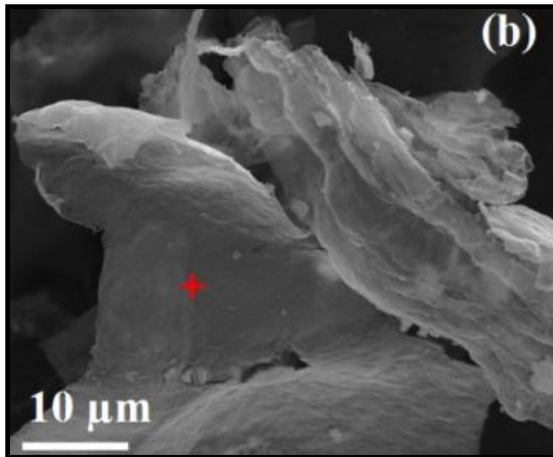
3.2.5 FESEM Analysis

The morphologies of the precursor GO and the products GRH-MA and GRH-MA300 were examined by recording their FESEM images (Fig. 3.12a, b and c). EDAX analyses of these image(s) at the location(s) marked by cross sign in red have been shown along with their respective image(s) (Fig. 3.12a', b' and c'). The FESEM image of GO appears to be agglomerated (Fig. 3.12a). EDAX analysis of this sheet at the marked location indicate the C/O ratio to be of the order of 1.59 (Fig. 3.12a'). The elemental mapping for a small area of this sheet shows the homogeneous distribution of carbon and oxygen (Fig. 3.12a'' and a'''). On the other hand, the FESEM image of GRH-MA at lower and higher magnifications shows it to be much finer sheet folded at places (Fig. 3.12b and b') with the estimation of its dimension to be 150 x 100 μm (not shown). EDAX analysis of the sheet

Synthesis of ultra thin graphene sheets using malonic acid as a reducing agent for energy storage applications

given in Fig. 3.12b shows C/O ratio of 6.93, which is more than 4 times higher to that of GO, indicating the reduction of GO (Fig. 3.12b" and d). This is also revealed by the elemental mapping of the GRH-MA image recorded at higher magnification (Fig. 3.12b'), which clearly shows the homogeneous distribution of carbon and oxygen with much higher density of carbon (Fig. 3.12b"" and b''"). FESEM image of GRH-MA300 and its line mapping are shown in Fig. 3.12c and c''. This sheet is extremely thin with fairly high C/O ratio of 9.8 (Fig. 3.12c' and d). Thus, a comparison of the C/O ratio for these samples exhibit the trend: GRH-MA300 > GRH-MA > GO. Interestingly, annealing of GRH-MA at relatively mild temperature (GRH-MA300) seems to bring the increasing removal of residual functionalities present on GRH-MA. It may be pointed out that the employed annealed temperature is much lower compared to those used for the preparation of graphene sheet(s) in which fairly higher temperature were employed [389].





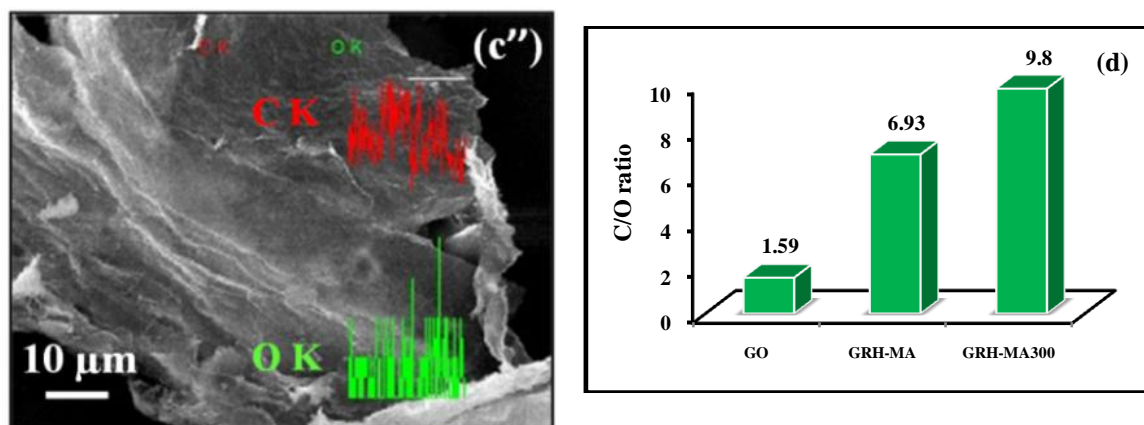
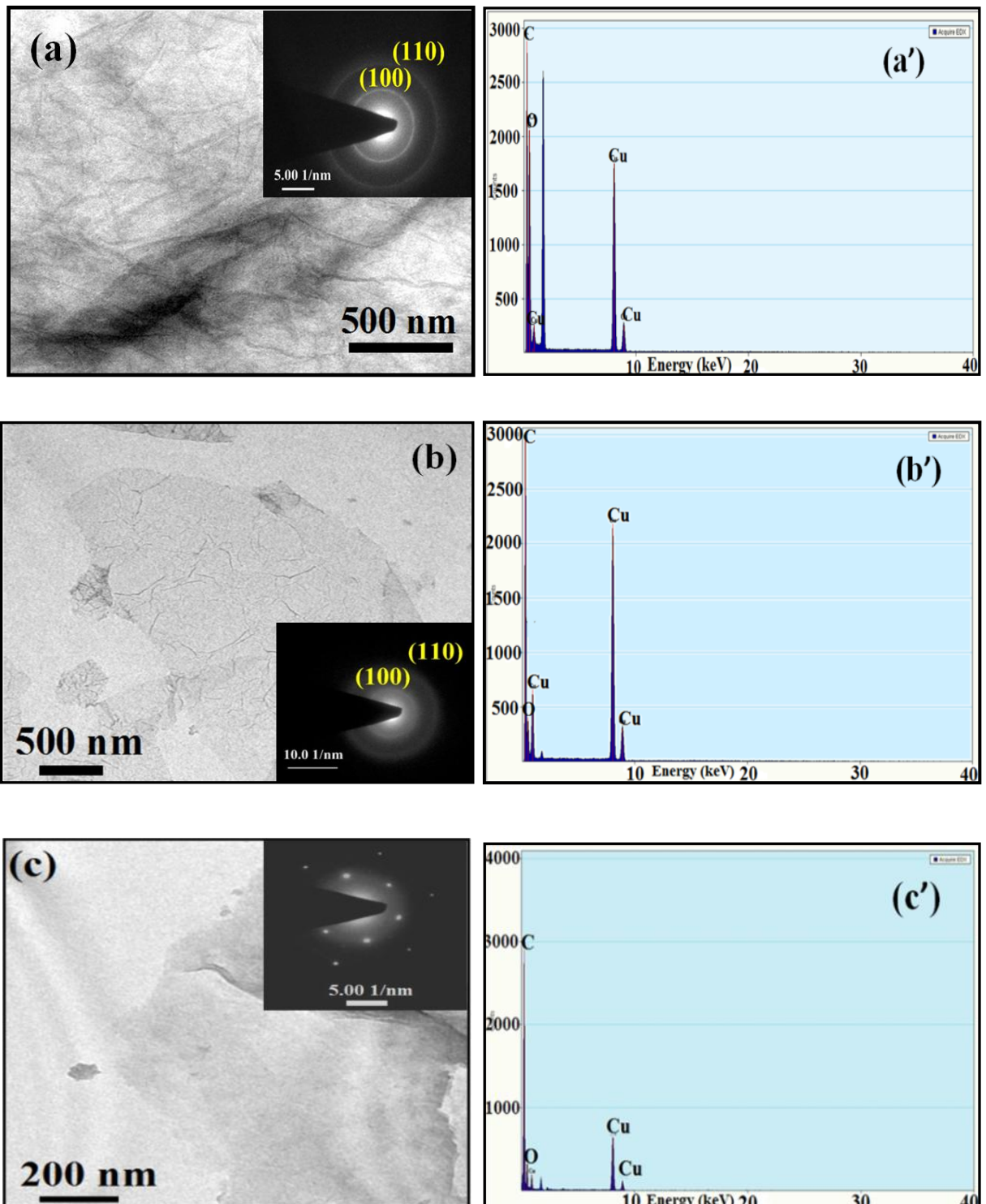


Fig. 3.12: FESEM images and their EDAX analyses on a particular location(s) marked by cross sign in red: GO (a and a'), GRH-MA (b, b' and b'') and GRH-MA 300 (c and c'), respectively; Elemental mapping of GO and GRH-MA: carbon (a'' and b''') and oxygen (a''' and b'''), respectively. Line mapping of GRH-MA300 (c''). C/O ratio of: GO, GRH-MA and GRH-MA300 (d).

3.2.6 TEM and SAED Analysis

TEM images of GO, GRH-MA and GRH-MA300 containing SAED patterns in the inset along with their EDAX spectra have been shown in Fig. 3.13. TEM image of GO exhibits the formation of sheet-like structure. SAED pattern of GO demonstrates it to be polycrystalline corresponding to the (100) and (110) planes of graphite having hexagonal structure matching with the JCPDS file no. 75-1621 (Fig. 3.13a-inset). On the other hand, the TEM images of GRH-MA and GRH-MA300 exhibit the formation of very thin sheets (Fig. 3.13b and c). The SAED pattern of GRH-MA shows the presence of diffused concentric rings indicating its amorphous nature matches to the (100) and (110) planes (Fig.3.13b-inset). Whereas, in the case of GRH-MA300, it exhibited the formation of crystalline hexagonal structure displaying six-fold symmetry (Fig. 3.13c-inset). The SAED pattern of GRH-MA300 shows the intensity of inner spots to be much stronger as compared to those of outer spots. The similar pattern has earlier been assigned to monolayer graphene [242]. EDAX analyses of these samples exhibit the C/O ratio to increase in the order: GO < GRH-MA < GRH-MA300 (Fig. 3.13a', b' and c'). In the HRTEM image of GRH-MA300,

lattice fringes are observed with an average 'd' spacing of 0.35 ± 0.01 nm (Fig. 3.13c'''), which is in agreement with the XRD results (Fig. 3.10).



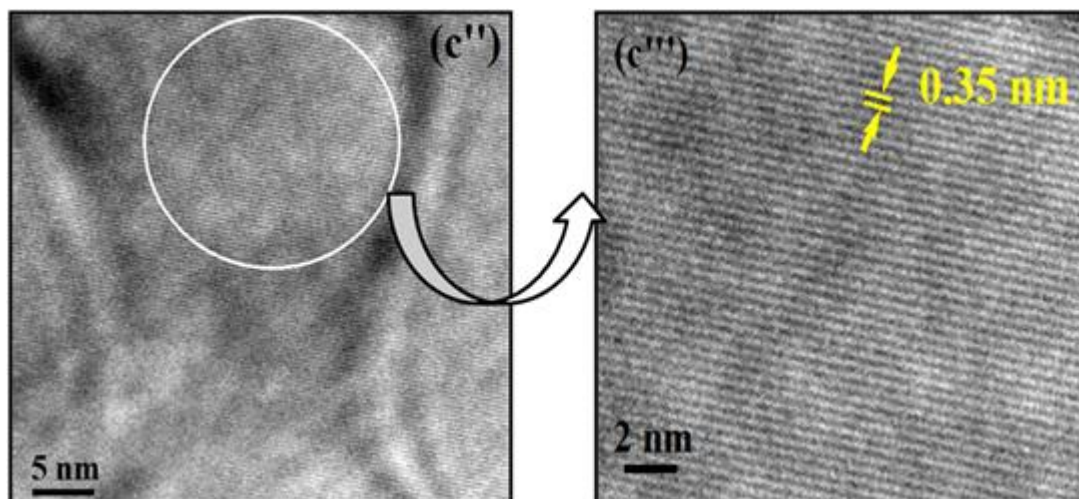


Fig. 3.13: TEM images containing SAED patterns in the inset along with their EDAX analyses: GO (a and a'), GRH-MA (b and b') and GRH-MA300 (dispersed in acetonitrile) (c and c'), respectively. HRTEM image of GRH-MA300 (c'') and its magnified image (c''').

3.2.7 FTIR Spectroscopy

IR spectra of GO, GRH-MA and GRH-MA300 in the mid IR range ($4000-500\text{ cm}^{-1}$) are shown in Fig. 3.14. The IR spectrum of GO (Fig. 3.14a) shows fairly intense bands (cm^{-1}) at 3425, 1718, 1632, 1222 and 1054 which could be assigned to $-\text{OH}$ stretching, $\text{C}=\text{O}$ ($-\text{COOH}$), $\text{C}=\text{C}$, $\text{C}-\text{O}-\text{C}$ (epoxy) and $\text{C}-\text{O}$ (alkoxy), respectively and matches with the previous report on GO [284]. In the IR spectrum of GRH-MA (Fig. 3.14b), the intensity of peaks due to $-\text{OH}$ stretching (3425 cm^{-1}) and $\text{C}-\text{O}$ (1054 cm^{-1}) are significantly reduced, peaks due to $\text{C}=\text{O}$ (1718 cm^{-1}) and $\text{C}-\text{O}-\text{C}$ (1222 cm^{-1}) are completely vanished, whereas the peak due to $\text{C}=\text{C}$ at 1632 cm^{-1} is still retained. These observations clearly indicate the reduction in oxygen functionalities of GO. The IR spectrum of GRH-MA300 (Fig. 3.14c) shows further reduction in the intensities of peaks due to $-\text{OH}$ stretching and $\text{C}-\text{O}$ groups suggesting the increased elimination of oxygen functionalities of GO.

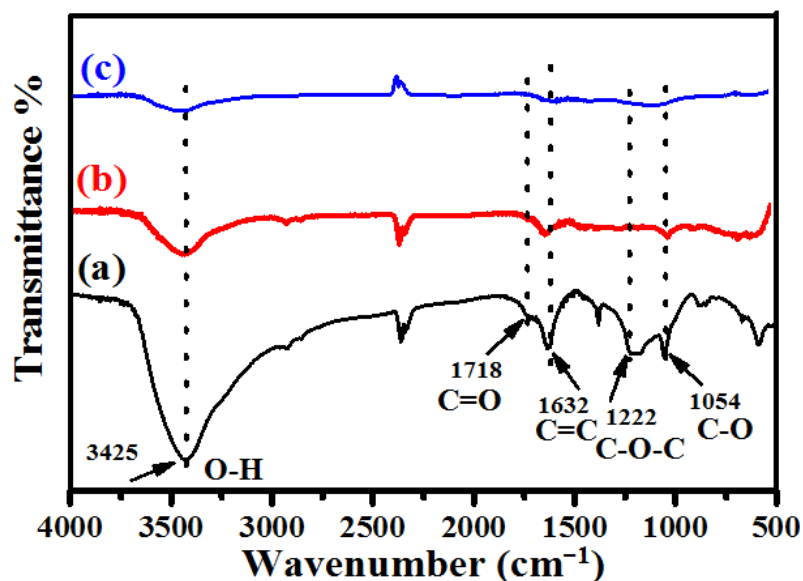


Fig. 3.14: IR spectra of: GO (a), GRH-MA (b) and GRH-MA300 (c).

3.2.8 XPS Studies

The survey scans for the surface analyses of precursor GO and product GRH-MA was carried out by using XPS in the binding energy range of 200-800 eV (Fig. 3.15A). The high resolution C 1s spectrum of GO is shown in panel B. It exhibits four different components of carbon with binding energies (eV) of 284.3, 286.0, 286.8 and 288.0. These bands have been assigned to C-C (sp^3 hybridized carbon)/C=C (aromatic sp^2 carbon), C-OH, C-O-C (epoxy) and C=O (carboxylic), respectively and matches to those reported previously for GO [390]. Whereas, the C 1s spectrum of GRH-MA (panel C) shows three different components of carbon at binding energies (eV) of: 284.4, 285.6 and 288.1 corresponding to C-C/C=C (sp^3/sp^2 hybridized carbon), C-OH and C=O (carboxylic), respectively. A comparison of the C 1s spectra of GO (panel B) and GRH-MA (panel C) clearly reveals that for GRH-MA, there is an increase in the intensity of C=C, decrease in the intensity of C-OH and the absence of the carbon component corresponded to C-O-C (286.8 eV). It suggests that after the reduction of GO the relative contribution of carbon singly and doubly bonded to oxygen is reduced significantly. A comparison of the O 1s spectra of GO with that of GRH-MA (panel D) shows that in case of GRH-MA the intensity of the peak is reduced by

more than a factor of 7. It thus suggests that the oxygen functionalities have been reduced largely upon the reduction of GO resulting in the enhancement of sp^2 character.

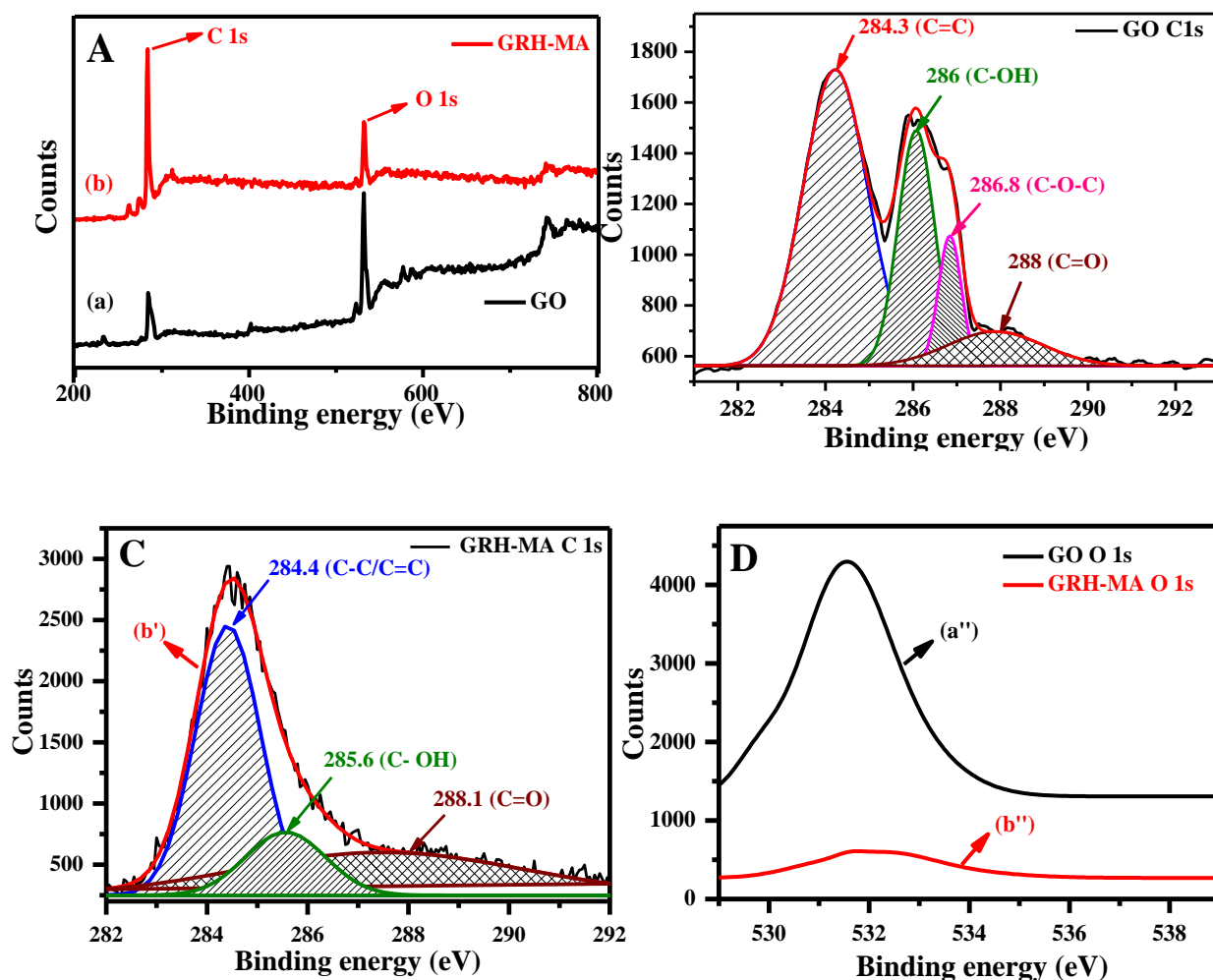


Fig. 3.15: XPS survey scan of: GO (a) and GRH-MA (b) - (panel A); GO C 1s (a') - (panel B); GRH-MA C 1s (b') - (panel C); GO O 1s (a'') and GRH-MA (b'') - (panel D).

3.2.9 Solid-State ^{13}C NMR Spectroscopy

The reduction of GO was further analyzed by recording the solid-state ^{13}C magic angle spinning (MAS) NMR spectra of GO, GRH-MA and GRH-MA300 (Fig. 3.16). The NMR spectrum of GO shows five different components of carbon (chemical shift (approx.) in ppm) namely, C-O-C (epoxide), C-OH (^{13}C nuclei in hydroxyl), graphitic sp^2 carbon, O-C=O (carbonyl carbon of ester) and C=O (ketone) at 61, 70, 100-140, 167 and 191, respectively which are very similar to those reported previously in the literature [253,324]. In contrast to GO, the NMR spectrum of GRH-MA exhibits almost complete elimination of

the peaks due to C-O-C, ketonic C=O and a tremendous decrease in the intensity of the peaks due to O-C=O and C-OH. Further, ^{13}C NMR spectrum of GRH-MA300 exhibits the elimination of all the oxygen functionalities corresponding to C-O-C, C-OH, O-C=O and C=O. These studies reveal that the reduction of GO into GRH-MA and GRH-MA300 results in the significant enhancement of the broad resonance peaks due to graphitic components (100-140 ppm) and follows the order: GO < GRH-MA < GRH-MA300, evidently demonstrates an increased graphitic (sp^2) character of the as-synthesized graphene sheets.

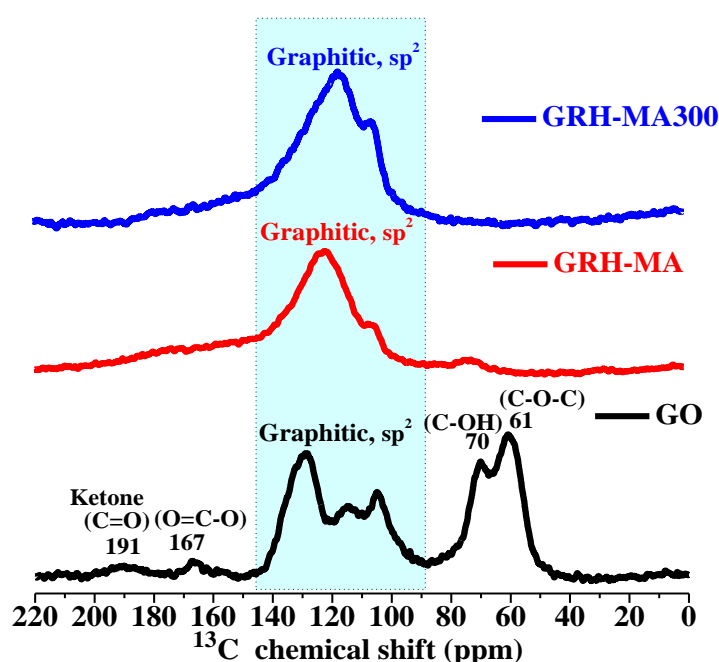


Fig. 3.16: Solid-state ^{13}C MAS NMR spectra of GO, GRH-MA and GRH-MA300 at 12 kHz.

3.2.10 TGA Measurements

The thermal stability of the precursors graphite, GO and malonic acid along with the reduction products, GRH-MA and GRH-MA300 was examined by TGA (Fig. 3.17). For graphite, the TGA curve was very similar to that reported earlier (Fig. 3.17a) [271]. The TGA curve for GO shows the specific weight losses in three stages at 115, 215 and 305 °C corresponding to weight losses (%) of: 19, 59 and 68.6, respectively (Fig. 3.17b). These losses have been attributed to the removal of adsorbed water, the decomposition of labile

oxygen functionalities (anhydride, carboxylic and lactone groups) and removal of relatively stable oxygen functionalities (phenols and carbonyl), respectively similar to those observed earlier [391]. However, for the GRH-MA significantly lower weight losses (%) of: 15, 23 and 33 were observed at 115, 215 and 305 °C, respectively (Fig. 3.17d). Further, the weight loss beyond 320 to 1100 °C is not significant (not shown). TGA analysis of GRH-MA300 shows further improved thermal stability in all respect (Fig. 3.17e). In this case the total extent of weight losses recorded up to 1100 °C (not shown) demonstrates this sample to be fairly stable.

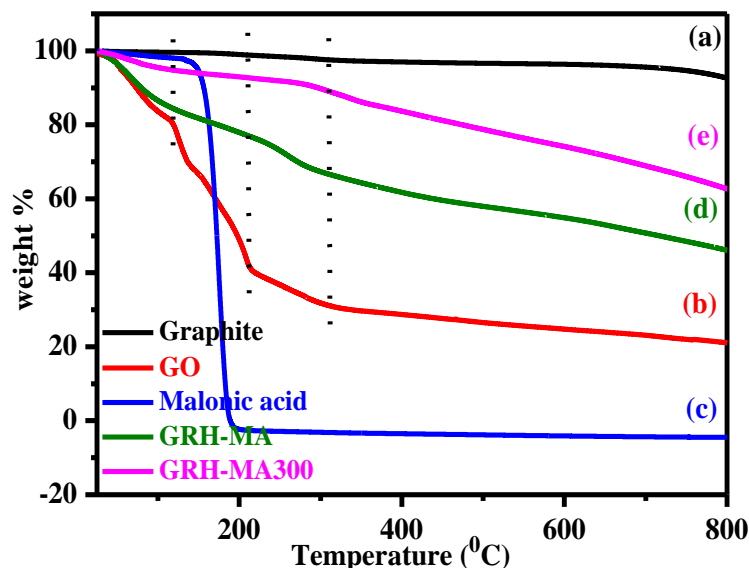


Fig. 3.17: TGA curves of graphite (a), GO (b), malonic acid (c) GRH-MA (d) and GRH-MA300 (e).

3.2.11 I-V Measurements

The extent of reduction of GO was further ascertained by recording the I-V plots for the precursor GO and its reduction products, GRH-MA and GRH-MA300 (Fig. 3.18). A comparison of their I-V curves evidently shows a tremendous increase in the conductivity of GRH-MA (4.4 S/cm) as compared to that of GO (3.05×10^{-4} S/cm). The value of conductivity is further enhanced to 18.1 S/cm for GRH-MA300, which is more than 4 times higher to that of GRH-MA (4.4 S/cm). Notably, this value of conductivity is even higher to that of graphene paper (17.14 S/cm), obtained by the reduction of GO paper by its

immersion into HI solution, annealed at 800 °C [385].

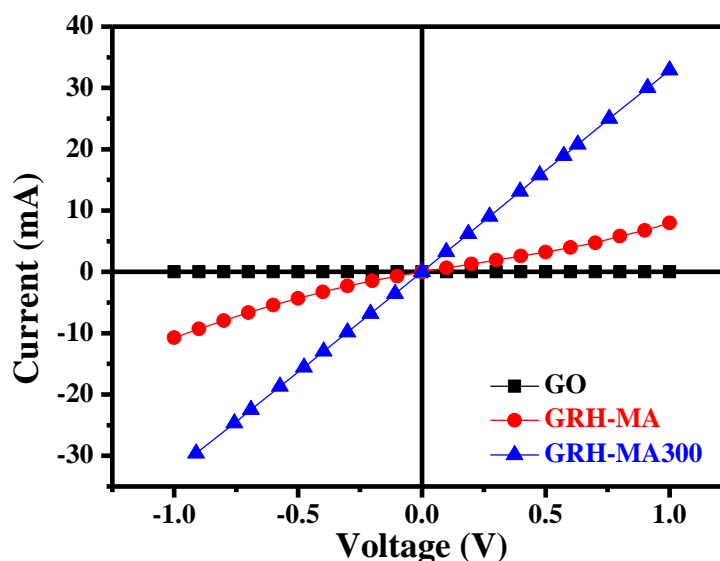


Fig. 3.18: I-V curves of GO (black), GRH-MA (red) and GRH-MA300 (blue).

3.2.12 Electrochemical Studies

The electrochemical behavior of GO and GRH-MA electrodes was investigated for energy storage applications. Cyclic voltammograms (CV) of GO and GRH-MA have been recorded in the voltage range of 0 to 0.8 V at different scan rates ranging from 5 to 100 mV/s. These curves show an increase in the current densities with increasing scan rates (Fig. 3.19A and B). From the CV curves the specific capacitance (C_s) for GO and GRH-MA at scan rates of 5, 10, 30, 50, 70 and 100 mV/s, were calculated to be 2.02, 1.65, 1.27, 1.12, 1.04 and 0.96; and 188, 151, 128, 100, 91 and 78 F/g, respectively (Fig. 3.19A-C). A comparison of the CV curves for GO and GRH-MA reveals that at different scan rates, the areas covered under the CV curves for GRH-MA were much higher as compared to those of GO (Fig. 3.19A and B). For a typical scan rate of 100 mV/s, the value of C_s for GRH-MA is much higher (78 F/g) as compared to that of GO (0.96 F/g) (Fig. 3.19D).

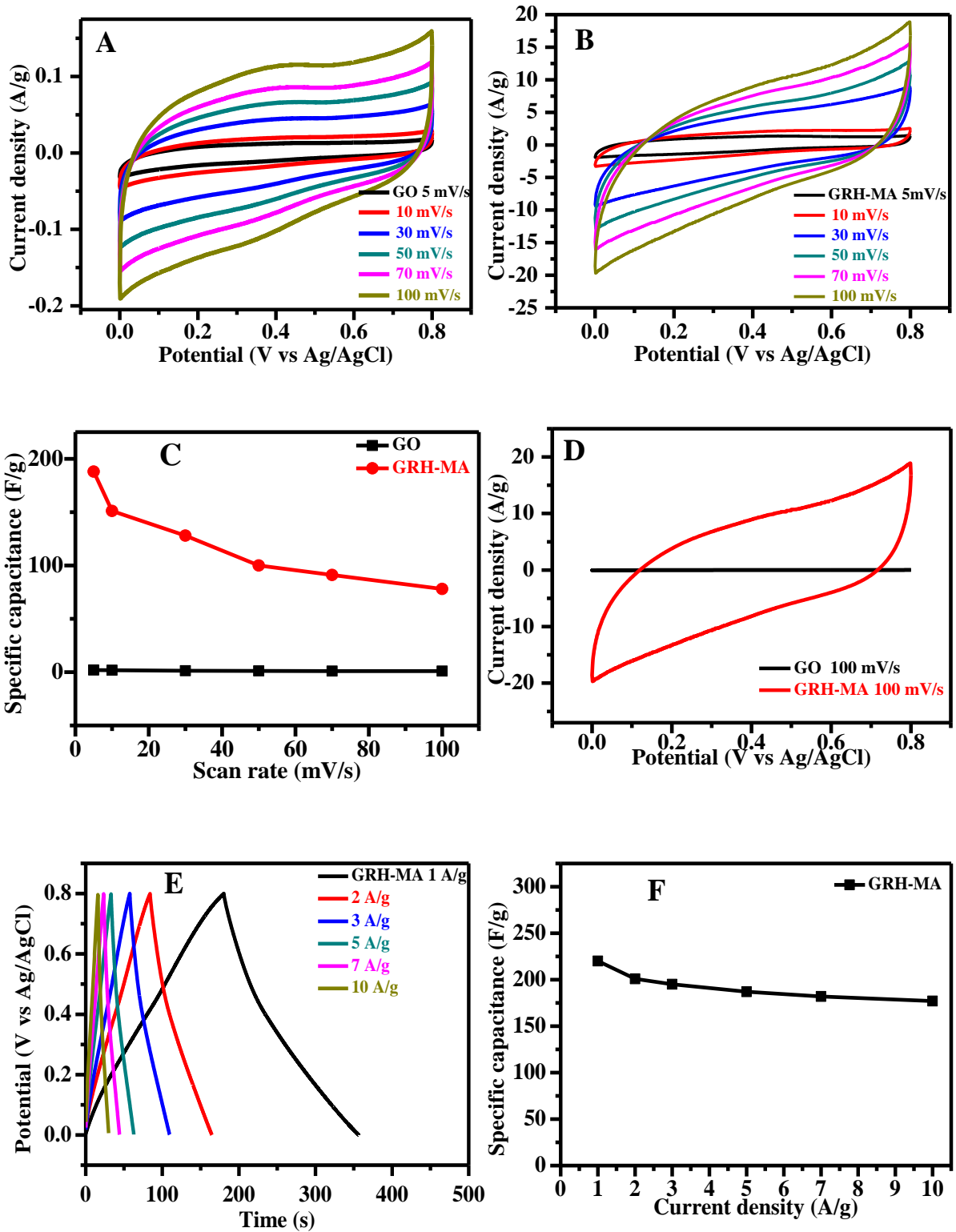
The capacitive behavior of GO and GRH-MA as electrode materials was also investigated by designing the galvanostatic charge-discharge (GCD) experiments in the same potential window of 0.0 to 0.8 V as was used for CV measurements. Fig. 3.19E shows the GCD curves for GRH-MA at different current densities (A/g): 1, 2, 3, 5, 7 and 10. From

Synthesis of ultra thin graphene sheets using malonic acid as a reducing agent for energy storage applications

these curves, the C_s (F/g) values were calculated to be 220, 201, 195, 187, 182 and 177, respectively. It may be mentioned that the shape of the charge-discharge curves is typically symmetrical triangular for all the recorded current densities. A change in the current densities from 1 to 10 A/g resulted in the reduction of C_s from 220 to 177 F/g (Fig. 3.19F). It is worth noting that even for the high current density of 10 A/g a fairly higher value of C_s is retained. For comparison purpose, the GCD curve for GO was also recorded at a current density of 1 A/g from which the C_s value was calculated to be 2.5 F/g, which is significantly lower to that of GRH-MA (220 F/g) (Fig. 3.19G).

The long term cycling stability for GRH-MA was examined at the highest used current density (10 A/g). The typical portions of these runs exhibiting the first and last three cycles are shown in Fig. 3.19H-inset. From these measurements, the C_s value for the first cycle was calculated to be 177 F/g which increased gradually to 186 F/g after 1000th cycle (Fig. 3.19H). A slight increase in the C_s value up to 1000 cycles might have been arisen due to the presence of small residual oxygen functionalities on GRH-MA, as was also indicated by its slightly higher thickness (0.41 ± 0.03 nm) (Fig. 3.11b') as compared to that of single layer graphene (0.34 nm). Moreover, a partial contribution to the increase in the C_s value might also have been possible due to the wetting of the electrode material. For 1000 cycles, the charging-discharging curves recorded at 10A/g exhibited the coulombic efficiency of 100-101% (Fig. 3.19H).

Fig. 3.20A shows the change in energy densities for the as-synthesized GRH-MA at various current densities. Fig. 3.20B shows the Ragone plot which exhibited the high energy density of 19.55 Wh/kg at a power density of 400 W/kg. Notably, even at a higher power density of 3947 W/kg, the energy density decreased to 15.35 Wh/kg only.



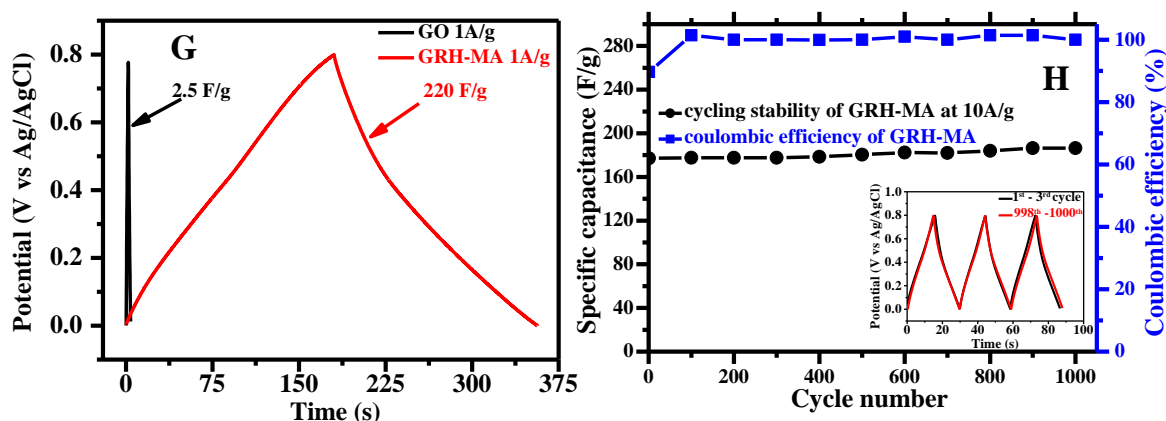


Fig. 3.19: CV curves of GO and GRH-MA at different scan rate(s) – (panels A and B). Variation in the specific capacitance (C_s) values as a function of scan rate(s) for: GO and GRH-MA – (panel C). A typical CV curve of GO and GRH-MA at a scan rate of 100 mV/s – (panel D). Galvanostatic charge-discharge (GCD) curves of GRH-MA at various current densities – (panel E). Variation in the C_s value obtained from the GCD curves for different current densities – (panel F). GCD curves of GO and GRH-MA at a current density of 1 A/g – (panel G). Variation in the C_s value and coulombic efficiency as a function of number of cycles (panel H) and the GCD curves for the first and last three cycles – (panel H-inset). All electrochemical measurements were performed in 1 M H_2SO_4 as an aqueous supporting electrolyte.

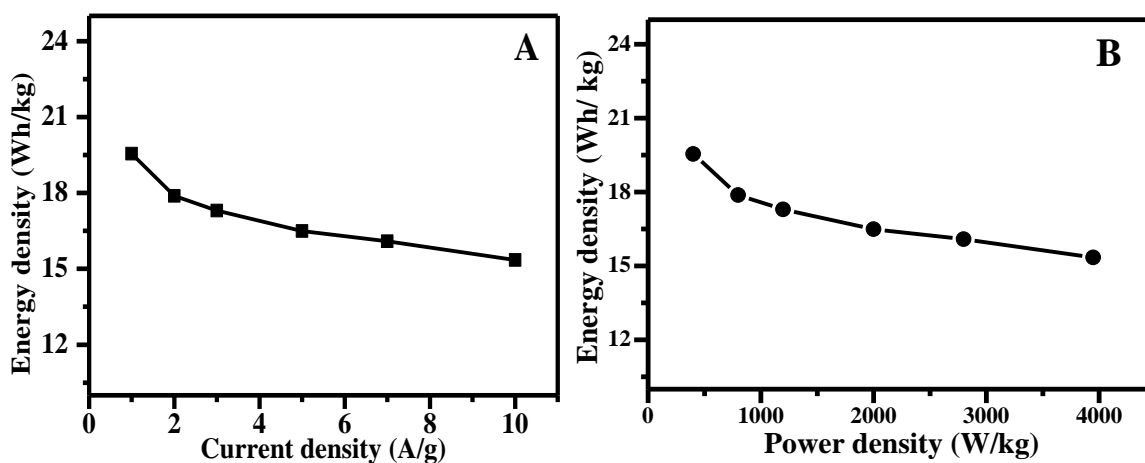


Fig. 3.20: Change in the energy densities of GRH-MA electrode in aqueous electrolyte with current densities (A) and Ragone plot for GRH-MA (B).

3.3 Discussion

It is interesting to observe that the malonic acid at mild pH (10.5) results in the effective reduction of GO into graphene (GRH-MA) as was evident by its optical absorption, XRD, Raman, and microscopic techniques (Fig. 3.6, 3.9-3.13). The effective reduction of GO at mild pH is understood by the increased nucleophilicity of relatively

stable malonate ion formed under these conditions having active methylene group, which is stabilized by the presence of electron withdrawing carbonyl groups (Fig. 3.2). The malonic acid is known to have $pK_a(s)$ of 2.83 and 5.69 and at pH 10.5 both the $-COOH$ groups would largely exist as $-COO^-$. Therefore, it might also be considered that the reduction of GO is occurring through COO^- . This aspect was further probed in a control experiment by employing oxalic acid, containing two carboxyl groups but lacks the presence of active methylene group, as a reducing agent under identical conditions of pH (GRH-Ox). The complete reduction of GO to GRH-Ox takes relatively much longer time (9 h), as was evidenced by recording its optical absorption spectra at different times (Fig. 3.21). The fact that oxalic acid has lower $pK_a(s)$ of 1.25 and 4.14 as compared to that of malonic acid, but still is less effective as a nucleophile in mild basic pH conditions (pH 10.5), clearly suggests the participation of active methylene group in malonic acid which makes it more effective nucleophile (Scheme 3.1). The higher efficiency of reduction of GO by malonic acid is also supported by Raman spectroscopy in which the I_D/I_G ratio for GRH-MA (0.97) (Fig. 3.9) was found to be higher as compared to that of GRH-Ox (0.95) after complete reduction (Fig. 3.22). The higher I_D/I_G ratio has earlier been suggested due to the increased number of smaller sp^2 domains upon reduction of GO [324].

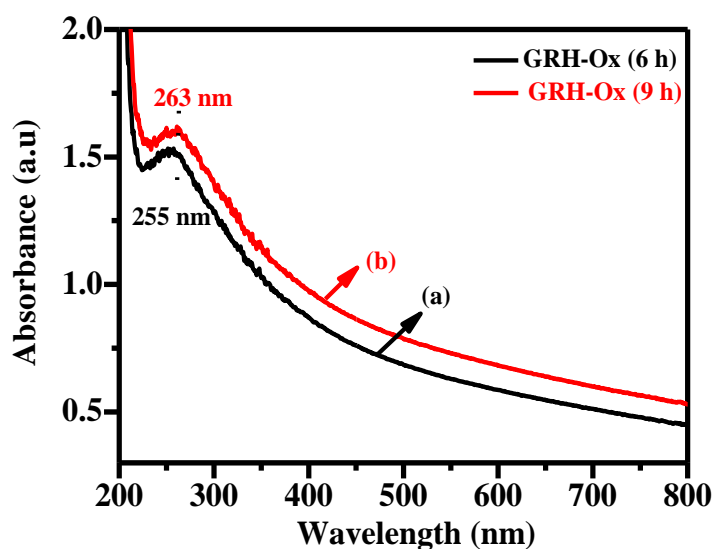


Fig. 3.21: Optical absorption spectra of GRH-Ox after: 6 h (a) and 9 h (b) of heating.

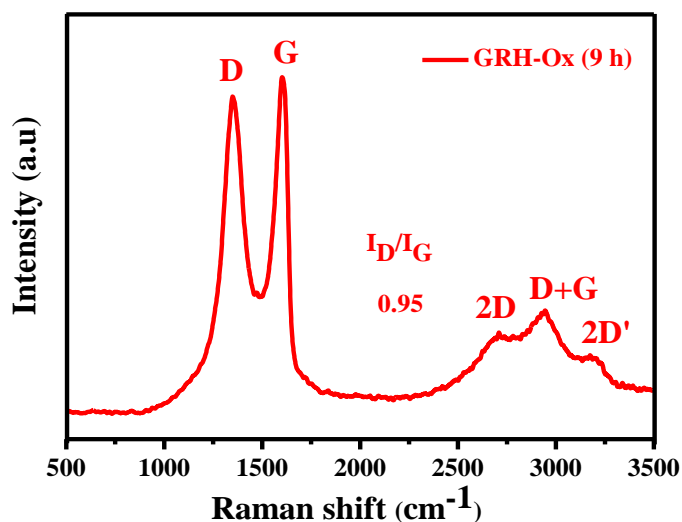
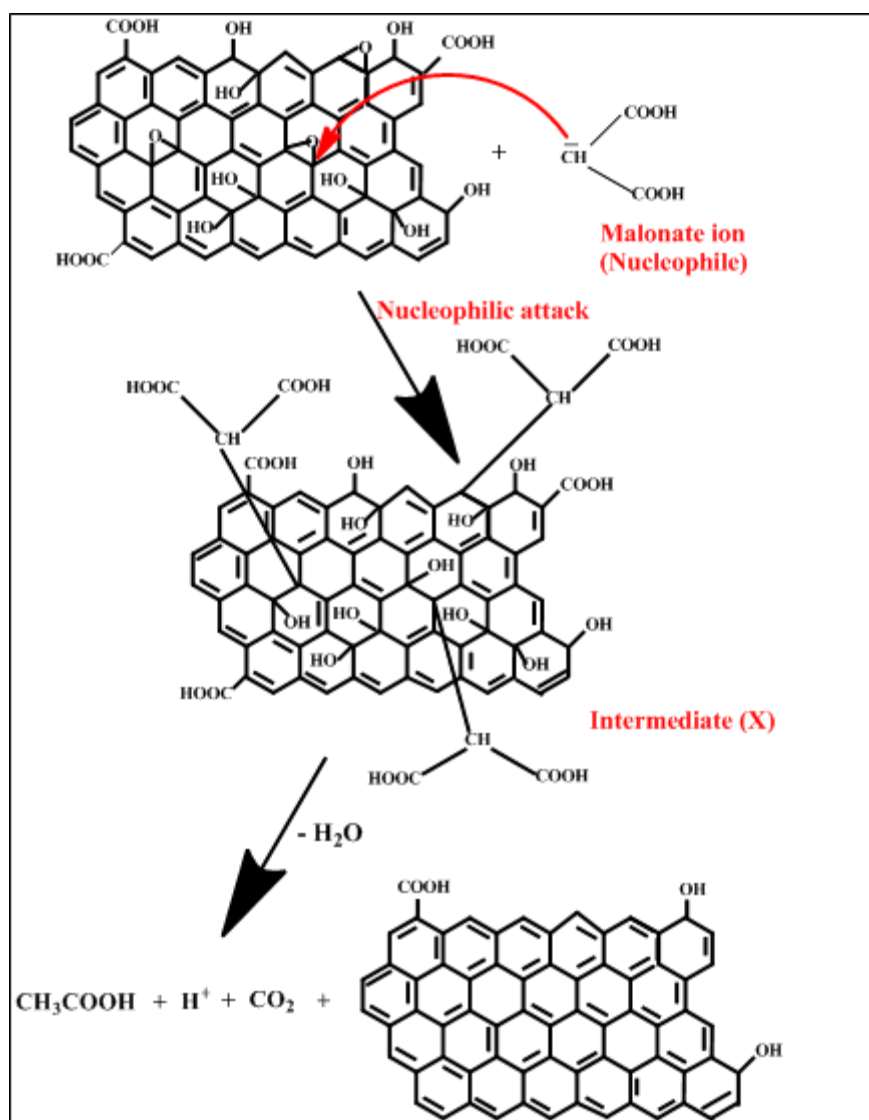


Fig. 3.22: Raman spectrum of GRH-Ox after 9 h of heating.



Scheme 3.1: Mechanism showing nucleophilic attack of malonate ion on the epoxy group of GO and resulting in the formation of graphene.

The effect of pH was further analyzed by performing the reduction of GO at lower pH (6.0) employing malonic acid as a reductant. At this pH, the canonical structures of malonic acid are relatively less stabilized and would act as a nucleophile with a limited capability. It was evident by the optical absorption and Raman spectrum obtained upon the reduction of GO at pH 6.0 after 6 h of heating at 95 °C (GRL-MA) (Fig. 3.23A and B). At this pH (6.0), the optical absorption spectrum shows blue shifted peak (253 nm) (Fig. 3.23A) as compared to that at pH 10.5 (263 nm) (Fig. 3.8) and the I_D/I_G ratio from the Raman spectrum was found to be 0.92 (Fig. 3.23B), which is less than that observed at pH 10.5 (0.97) (Fig. 3.9A-c) during the same period of heating. It took much longer time (10 h) for the completion of reduction of GO, as was seen by recording their optical absorption and Raman spectrum (Chapter 4). It thus suggests that the more effective reduction of GO takes place at pH 10.5 within a short duration of 6 h.

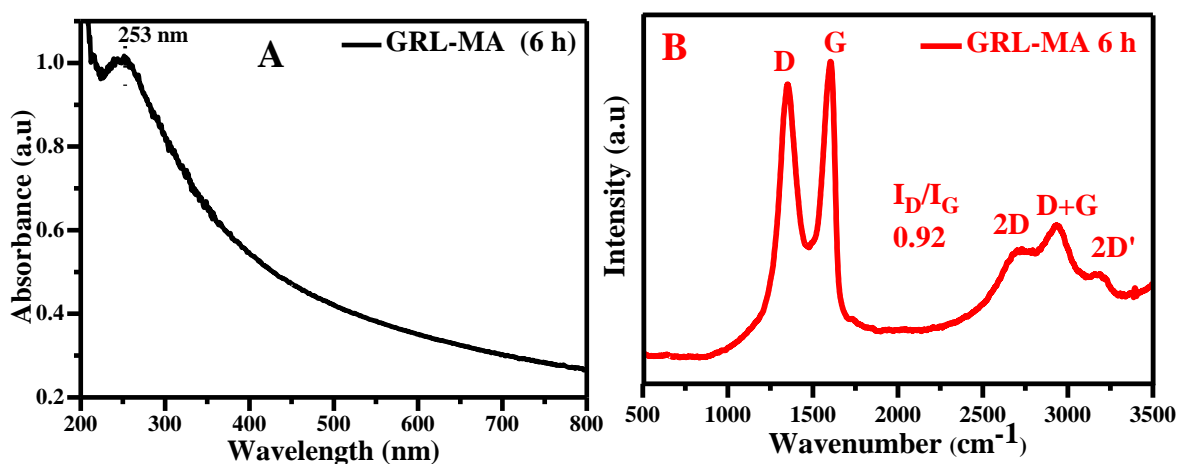


Fig. 3.23: Optical absorption spectrum of GRL-MA (a) and Raman spectrum of GRL-MA (b) after 6 h of reaction.

The effective reduction of GO was further indicated by the EDAX analyses using FESEM, which showed more than four times increase in C/O ratio (6.93) of GRH-MA as compared to that of GO (1.56) (Fig. 3.12). The disappearance of the peaks due to C=O and C-O-C, and retaining of the C=C peak in IR spectroscopy (Fig. 3.14); the absence of the peak due to C-O-C (epoxy), reduction in the intensity of C-OH and increase in the intensity

of C=C peak in XPS evidently suggests the enhanced sp^2 character in GRH-MA (Fig. 3.15). These findings are very well supported by the solid-state ^{13}C NMR spectrum which showed almost complete elimination of the peaks due to C-O-C and ketonic C=O groups in GRH-MA along with the enhancement in the graphitic sp^2 resonance peak (Fig. 3.16). I-V measurements show four orders of magnitude higher conductivity for GRH-MA (4.4 S/cm) as compared to that of GO (3.05×10^{-4} S/cm) confirming the restoration of π - conjugation in GRH-MA (Fig. 3.18). Moreover, the value of conductivity of GRH-MA is about two orders of magnitude higher to that of GRH-Ox (1.03×10^{-2} S/cm) (Fig. 3.24). It clearly demonstrates that the observed conductivity for GRH-MA is not only higher to that of similar reducing agent, oxalic acid, but also of the same magnitude to those of other effective reducing agents, reported earlier like NaBH_4 [264] and L-ascorbic acid [292].

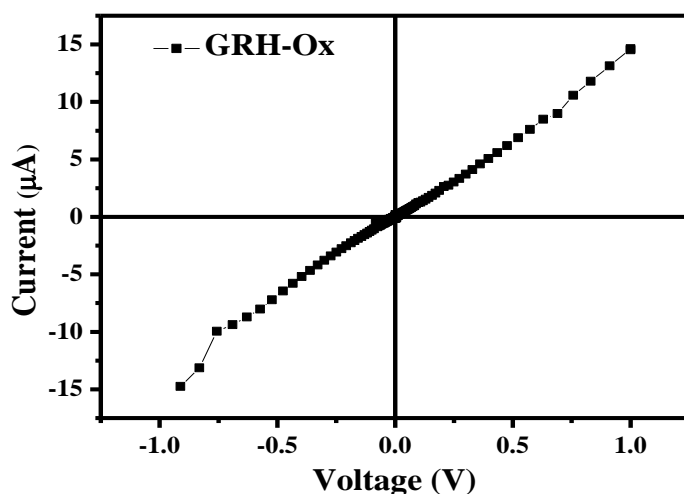


Fig. 3.24: I-V curve of GRH-Ox.

The effectiveness of reduction by malonic acid at pH 10.5 is further revealed by the AFM data in which the thickness of GRH-MA was estimated to be 0.41 ± 0.03 nm (Fig. 3.11b'), which is slightly higher to that of the single-layer graphene (0.34 nm), as has been estimated for the spacing between the two adjacent layers of graphite. In contrast to GRH-MA the thickness of GO sheet was determined to be 1.23 nm, from which it is quite apparent that the functionalities of GO has been reduced to a large extent by malonic acid

reduction at this pH. A little higher thickness of graphene sheet as compared to that of the single-layer graphene has possibly arisen due to the small residual oxygen functionalities present on the reduced GO. On the contrary, the thickness of GRH-Ox was found to be 0.75 nm (Fig. 3.25), which is significantly higher to that of GRH-MA (0.41 ± 0.03 nm). Thereby, suggesting the effectiveness of malonic acid in producing ultrathin graphene sheet due to the involvement of active methylene group.

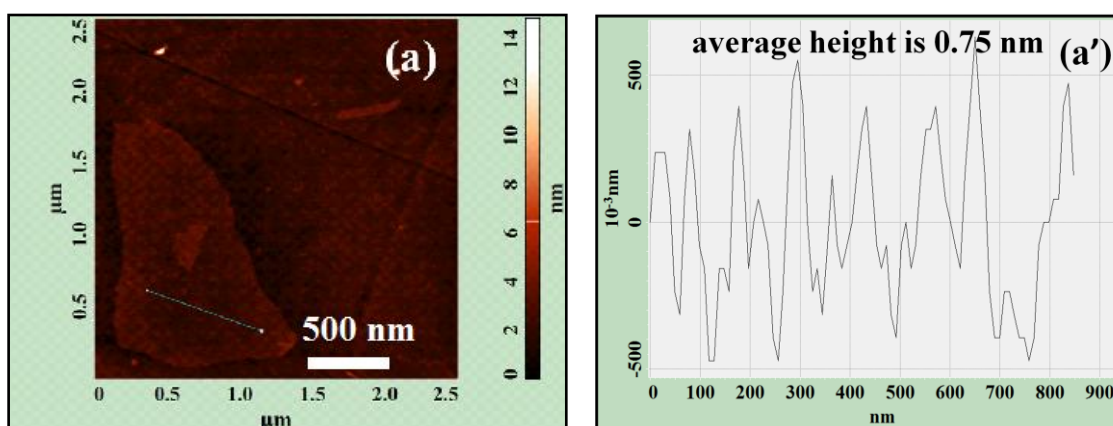


Fig. 3.25: AFM image of GRH-Ox (a) and its height profile along a particular line (a').

Annealing of the GRH-MA at a mild temperature of $300\text{ }^{\circ}\text{C}$ (GRH-MA300) for a shorter period (1 h) induces the transformation of amorphous graphene into crystalline graphene with hexagonal structure displaying six-fold symmetry. The observed difference in the intensity of spots in SAED pattern of the annealed sample indicates the presence of monolayer in this case (Fig. 3.13c-inset) [242]. Its HRTEM image shows the lattice fringes with an average ‘d’ spacing of 0.35 ± 0.01 nm suggesting the production of more ordered structure of graphene upon annealing (Fig. 3.13c'''). This was also evidenced by XRD data, where the peak corresponding to (002) plane became relatively less broad (Fig. 3.10d). For this sample, a further reduction in the intensities of the peaks due to $-\text{OH}$ and $-\text{C}-\text{O}$ groups in IR suggests the increased removal of remaining oxygen functionalities (Fig. 3.14c) which is also manifested by its solid-state ^{13}C NMR, which showed complete elimination of all the oxygen functionalities due to $\text{C}-\text{O}-\text{C}$, $\text{C}-\text{OH}$, $\text{O}=\text{C}-\text{O}$ and $\text{C}=\text{O}$ (Fig. 3.16). This aspect was

further evidenced by a significant increase in the conductivity of GRH-MA300 (Fig. 3.18), suggesting the increased restoration of sp^2 hybridized carbon upon annealing.

The CV measurements of GRH-MA exhibit the C_s value of 78 F/g at 100 mV/s, which is significantly higher to that of GO (0.96 F/g) (Fig. 3.19D). The lower value of C_s for GO electrode as compared to that of GRH-MA may be attributed to the poor conductivity of GO (Fig. 3.18). This observation is understood by the presence of sp^3 hybridization and low faradic rate of reaction in GO besides its lower surface area ($38.9 \text{ m}^2/\text{g}$). CV curves of GRH-MA exhibits nearly rectangular shape, in contrast to that of distorted shape of GO, arising from electrical double layer capacitance (EDLC) behavior involving non-faradic storage of charge through reversible adsorption of ion, thus suggesting its good capacitive performance (Fig. 3.19D).

This behavior is also revealed by the GCD measurements in which the C_s value at a current density of 1.0 A/g was observed to be 220 F/g which is much higher than that of GO (2.5 F/g) (Fig. 3.19G). It may be mentioned that the value of C_s for GRH-MA is even higher to those measured earlier for chemically reduced graphene(s) as well as for some of the N-doped graphene(s) (Table 3.2). The high value of C_s (186 F/g) at a current density of 10 A/g after 1000 cycles suggests the fairly high cycling stability of as-synthesized GRH-MA. Moreover, the energy density value of GRH-MA (19.55 Wh/kg) at a power density of 400 W/kg is much higher to that reported earlier [280] and is significantly higher to those reported for available commercial supercapacitors (3-4 Wh/kg at 3-4 kW/kg) [382]. These findings suggest that the immense potential of GRH-MA as an efficient energy storage material.

Table 3.2: A Comparison of the specific capacitance (C_s) value of GRH-MA with the previously reported chemically reduced graphene(s) and some of the N-doped graphene(s).

Reducing agent(s)	Specific Capacitance (C_s) obtained from GCD curves	Ref.
Malonic acid reduced GO	220 F/g at 1 A/g	This Work
Caffeic acid reduced GO	136 F/g at 1 A/g	274
Microbial reduction of GO by Shewanella	117 F/g at 1 A/g	287
Trigol reduced GO	130 F/g at 1 A/g	379
Dimethyl ketoxime reduced GO	141 F/g at 3 A/g	387
Double microwave assisted exfoliation of expandable graphite	189 F/g at 1 A/g	392
Hydrazine monohydrate reduced GO	133 F/g at 1 A/g	393



Chapter 4

***ONE-STEP CHEMICALLY
CONTROLLED WET SYNTHESIS OF
GRAPHENE NANORIBBONS FROM
GRAPHENE OXIDE FOR HIGH
PERFORMANCE SUPERCAPACITOR
APPLICATIONS***

4. ONE-STEP CHEMICALLY CONTROLLED WET SYNTHESIS OF GRAPHENE NANORIBBONS FROM GRAPHENE OXIDE FOR HIGH PERFORMANCE SUPERCAPACITOR APPLICATIONS

In recent years, a control of the dimensionality of graphene using wet chemical approach has been considered to be a challenging task as it may allow manipulating their physicochemical properties by changing the surface functionalities. Among different dimensionalities of carbon nanostructures, two-dimensional graphene nanoribbons (GNRs) have found significant importance due to its width and edge dependent characteristic features. In literature, a number of methods have been employed for the synthesis of GNRs [3,200,309,310]. The solution-based production of GNRs has been carried out by oxidative unzipping of MWNTs to produce GO nanoribbons followed by its reduction using different reducing agents [200,309,311,312], but most of the reducing agents used for the reduction of GO nanoribbons are hazardous. We have come across only one research article employing the wet chemical route for the synthesis of GNRs by the direct reduction of GO, but it involved five steps of synthesis [316]. However, it would be interesting to produce GNRs by reducing the number of steps for its synthesis employing mild reducing agent(s).

In the present chapter, we have carried out one-step chemically controlled wet synthesis of GNRs by the reduction of GO using malonic acid as a reducing agent. Specifically, the concentration of malonic acid and the pH of the medium have been optimized for performing the reduction of GO as regards to the controlled nucleation and growth of graphene with desired dimensionality and physicochemical properties. At mild concentration of malonic acid (1.6 mg/mL) and low pH (~ 6.0), the initial grown carbon nanostructures undergo folding to produce nanoribbons involving supramolecular interactions, whereas at higher concentrations (≥ 2.6 -3.6 mg/mL) and pH(s) ($> \sim 8$ -11) nanosheets are formed. Interestingly, it presents a novel approach to bring a transformation in the morphology of carbon nanostructures by changing the

pH of the reaction mixture. The as-synthesized GNRs exhibit fairly high conductivity, specific capacitance and long-term cyclic stability, suggesting its potential for high performance supercapacitor application.

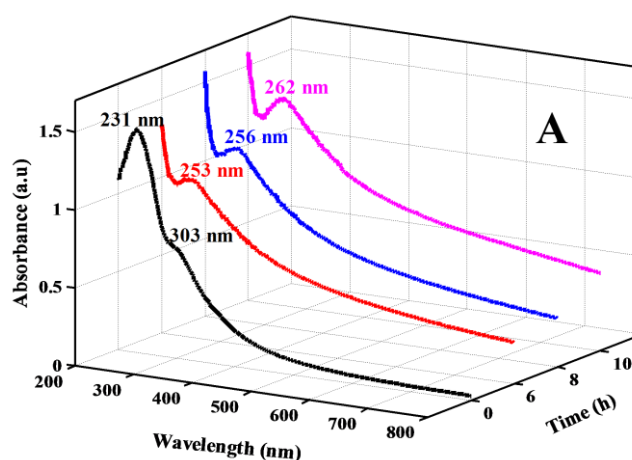
4.1 Optimization of Various Parameters for the Reduction of GO to Produce Graphene Nanoribbons

4.1.1 Amount of Malonic Acid

In the present chapter, the amount of malonic acid was fixed at 1.6 mg/mL (mass ratio of malonic acid:GO to be 3.2:1), as was found to be the optimum for the effective reduction of GO to produce graphene sheets in Chapter 3.

4.1.2 Optimization of the Heating Time

The heating time of the reaction mixture containing malonic acid and GO was varied up to 12 h by keeping the mass ratio of malonic acid:GO and pH constant at 3.2:1 and 6.0, respectively. The change in the absorption peak of the reaction mixture as a function of heating time up to 10 h is shown in Fig. 4.1A. It clearly shows that the absorption maximum is gradually red shifted from 231 to 262 nm associated with the regular change in the color from yellowish-brown to black. After 10 h, the reaction mixture did not show any shift in the absorption maximum and increase in absorbance (Fig. 4.1B). Therefore, the heating time of the reaction mixture was kept to be 10 h.



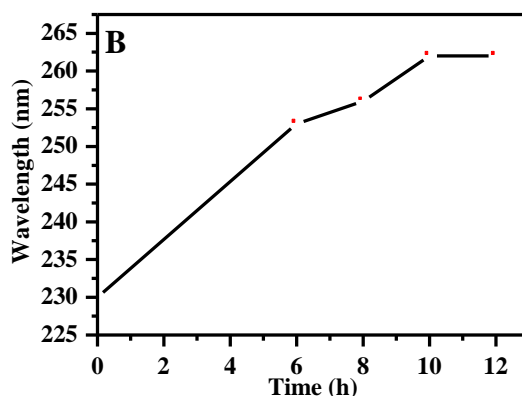


Fig. 4.1: 3D optical absorption spectra showing changes in the absorption peak of reaction mixture containing GO and malonic acid at pH 6.0 as a function of heating time – (panel A). Shift in the absorption maximum of GO with the time of heating – (panel B).

4.1.3 Optimization of the pH

The optimum pH for the reaction mixture was analyzed by keeping the mass ratio of malonic acid:GO and heating time constant at 3.2:1 and 10 h, respectively and varying the pH from 6.0 to 10.5. The observed changes were monitored by recording their optical absorption spectra and performing FESEM analyses. For the typical pH(s) of 6.0, 7.5 and 8.2, the optical absorption maximum were observed at 262 nm with a slight variation in the absorption coefficient in the entire recorded UV-Vis range (Fig. 4.2), indicating the reduction of GO for all the samples. In FESEM analyses, the morphologies for pH(s) of 6.0, 7.5 and 8.2 were found to be curl-shaped nanoribbons, aggregated stacked nanoribbons and sheets, respectively (*vide infra*). The desired morphology was achieved at a pH of 6.0. Therefore, the pH of the reaction mixture throughout the present study was kept at 6.0.

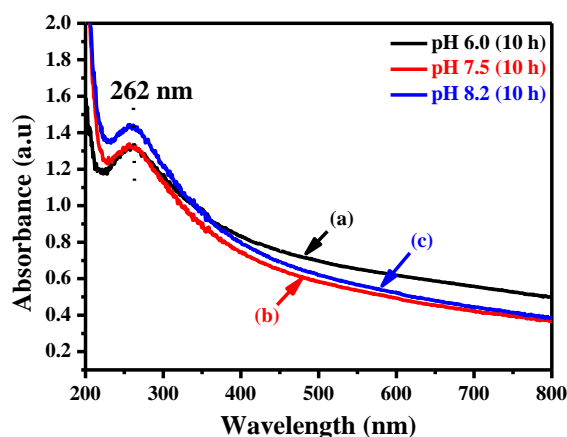


Fig. 4.2: The reduction of GO at pHs: 6.0 (a), 7.5 (b) 8.2 (c) after 10 h heating.

4.1.4 Synthesis of Graphene Nanoribbons under Optimized Reaction Conditions

Based on the above optimized conditions for the reduction of GO to produce GNRs, 40 mg (1.6 mg/mL or 15.38 mM) of malonic acid was mixed with 25 mL of GO dispersion containing 12.5 mg of GO (0.5 mg/mL) under vigorous stirring and the pH of the resulting mixture was maintained at 6.0 by adding dilute NaOH. The resulting solution was heated in a circulating water bath at 95 °C for 10 h and the black suspension thus obtained was repeatedly washed with DIW for several times in order to remove any unreacted malonic acid. The product was then separated by centrifugation and dispersed into DIW at a pH of 6.0 and has been denoted as GNRs. Annealing of the as-synthesized GNRs was carried out at 300 °C for 1 h and has been represented by GNRs-300.

In control experiments the reduction of GO was also carried out by using oxalic acid and OH⁻ as reducing agent(s) under identical experimental conditions as mentioned above and the resulting product(s) are denoted as GRL-Ox and GRL, respectively.

4.2 Characterization of Graphene Nanoribbons (GNRs)

The as-synthesized GNRs have been characterized by using a number of spectroscopic and microscopic techniques such as UV-Vis, zetasizer, XRD, Raman, AFM, FESEM, TEM, FTIR, XPS, ¹³C NMR, TGA, I-V and CV and details of these investigations are described below:

4.2.1 Optical Spectra

Fig. 4.3 shows the optical absorption spectra of precursor GO and product GNRs, obtained by the reduction of GO at pH 6.0 using malonic acid as reductant. The absorption spectrum of GO exhibits a peak at 231 nm and a shoulder at 303 nm, which has been attributed to C=C bonds (π - π^* transition) and C=O bonds (n - π^* transition), respectively (Fig. 4.3a). On the contrary, the absorption spectrum of GNRs show a red shifted broad absorption peak at 262 nm after 10 h of heating (Fig. 4.3b) suggesting the restoration of

conjugated structure upon reduction of GO. Digital photographs of GO and GNRs were captured by dispersing them in water (Fig. 4.3-inset). The appearance of dark black color in vial 'b' as compared to that of yellowish-brown color in vial 'a' clearly indicates the effective reduction of GO yielding GNRs.

The stability of the colloidal dispersion of GNRs was analyzed by performing DLS measurements. Its ζ -potential was found to be -45.1 mV, suggesting it to be fairly stable (Fig. 4.4).

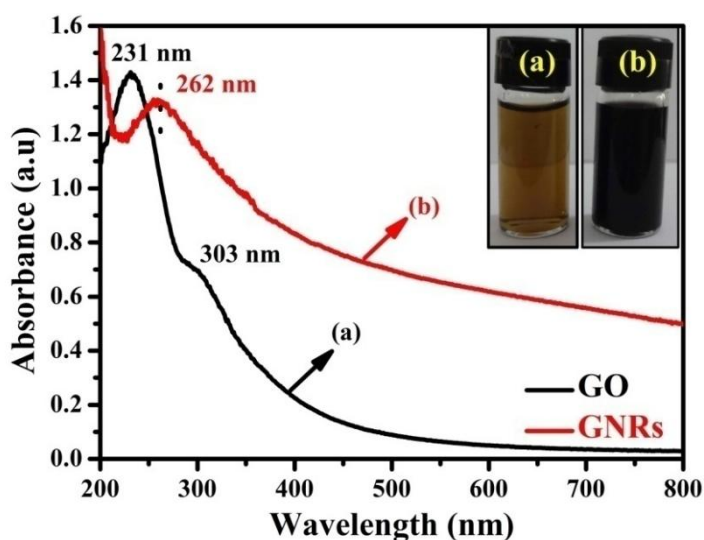


Fig. 4.3: Optical absorption spectra of GO (a) and GNRs (b) along with their digital photographs captured by dispersing them in water (inset).

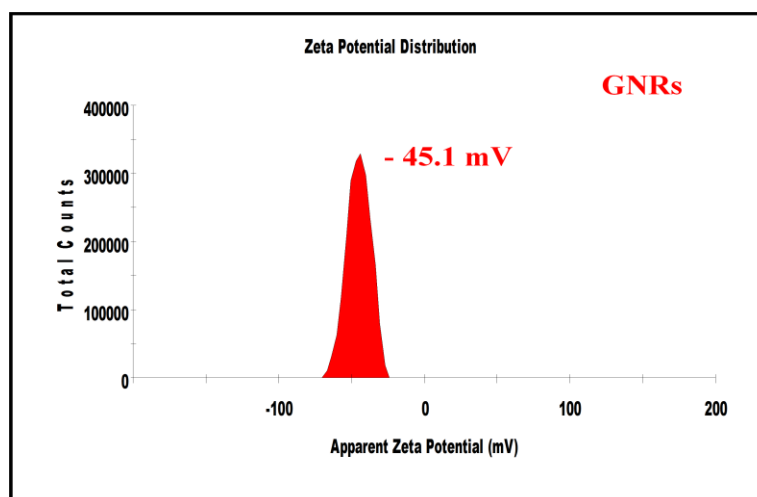


Fig. 4.4: ζ -potential of GNRs in aqueous medium.

4.2.2 XRD Studies

The XRD patterns of graphite, GO, GNRs and its annealed sample at 300 °C (GNRs-300) are shown in Fig. 4.5. The XRD pattern of graphite exhibits a sharp peak at 26.2° matching to the reflection from (002) plane with a ‘d’ spacing of 0.339 nm (Fig. 4.5a). Whereas, GO exhibits slightly broader peak at 10.59° with a ‘d’ spacing of 0.835 nm corresponding to the (002) plane (Fig. 4.5b). These patterns were very similar to those reported earlier [257]. Unlike to those of precursors, graphite and GO, the XRD pattern of GNRs shows a broader peak at 24.74° corresponding to the reflection from (002) plane with a ‘d’ spacing of 0.360 nm (Fig. 4.5c), clearly demonstrating the reduction of GO. In contrast to the XRD pattern of GNRs, GNRs-300 shows a relatively sharper peak at 25.2° again matching to the reflection from (002) plane with a ‘d’ spacing of 0.353 nm (Fig. 4.5d). The reduction in the value of ‘d’ spacing from 0.360 nm (GNRs) to 0.353 nm (GNRs-300) suggests that the crystallinity of GNRs is increased upon annealing at mild temperature.

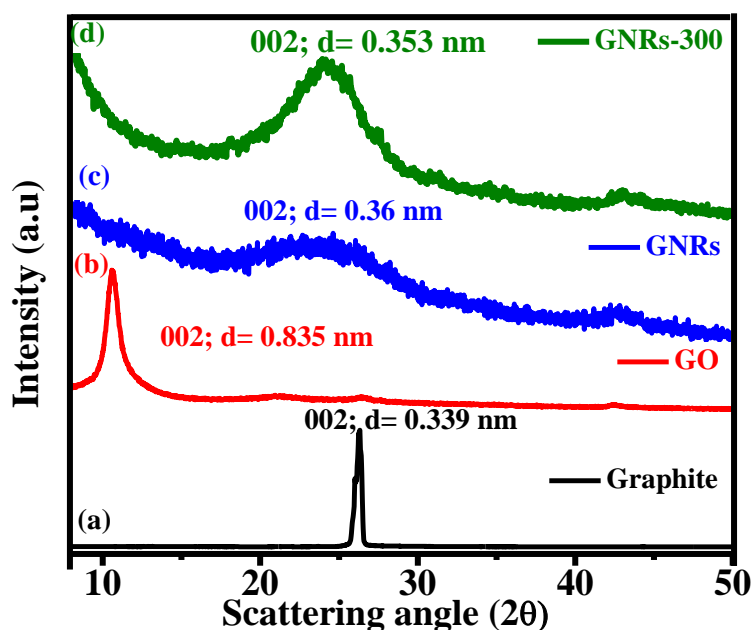
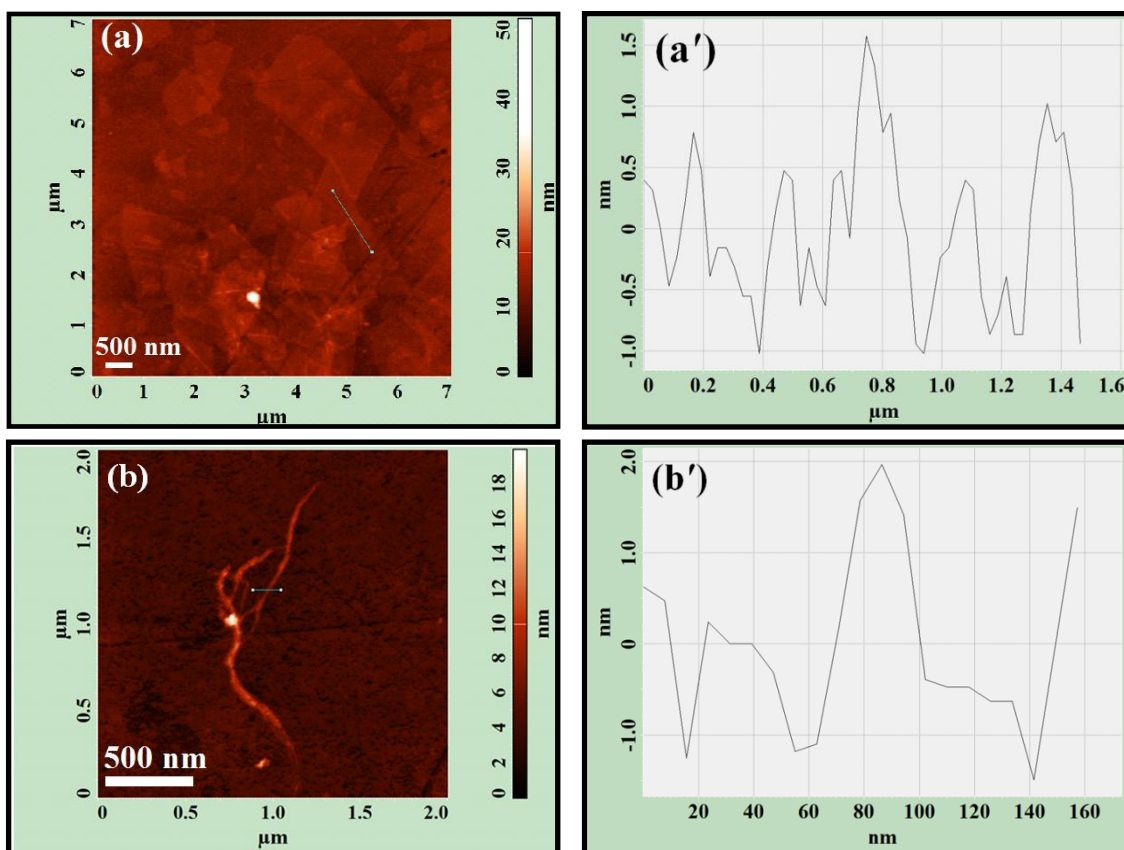


Fig. 4.5: XRD patterns of graphite (a), GO (b), GNRs (c) and GNRs-300 (d).

4.2.3 AFM Analysis

AFM was used to analyze the surface topography of GO and GNRs and to determine their surface heights. The AFM image of GO shows the presence of ~ 1.4 nm thick sheets suggesting it to be single-layer [394] (Fig. 4.6a and a'). The surface height of GNRs was measured at several locations by recording the line profile and was found to be 3.3 ± 0.2 nm (Fig. 4.6b and b'). However, their surface height was monitored for several such synthesized samples and was computed to be 3.0 ± 0.5 nm. These data evidently suggest that the nanoribbons are produced by folding of reduced GO to a few layers. The 2D images of GNRs annealed at 300°C (GNRs-300) are shown in Fig. 4.6c and c'. The line profile analysis of a small portion of the image given in Fig. 4.6c' has been shown in Fig. 4.6c''. The average height of these nanoribbons was estimated to be 1.1 ± 0.5 nm, which indicates that they contain about 3 to 4 layers.



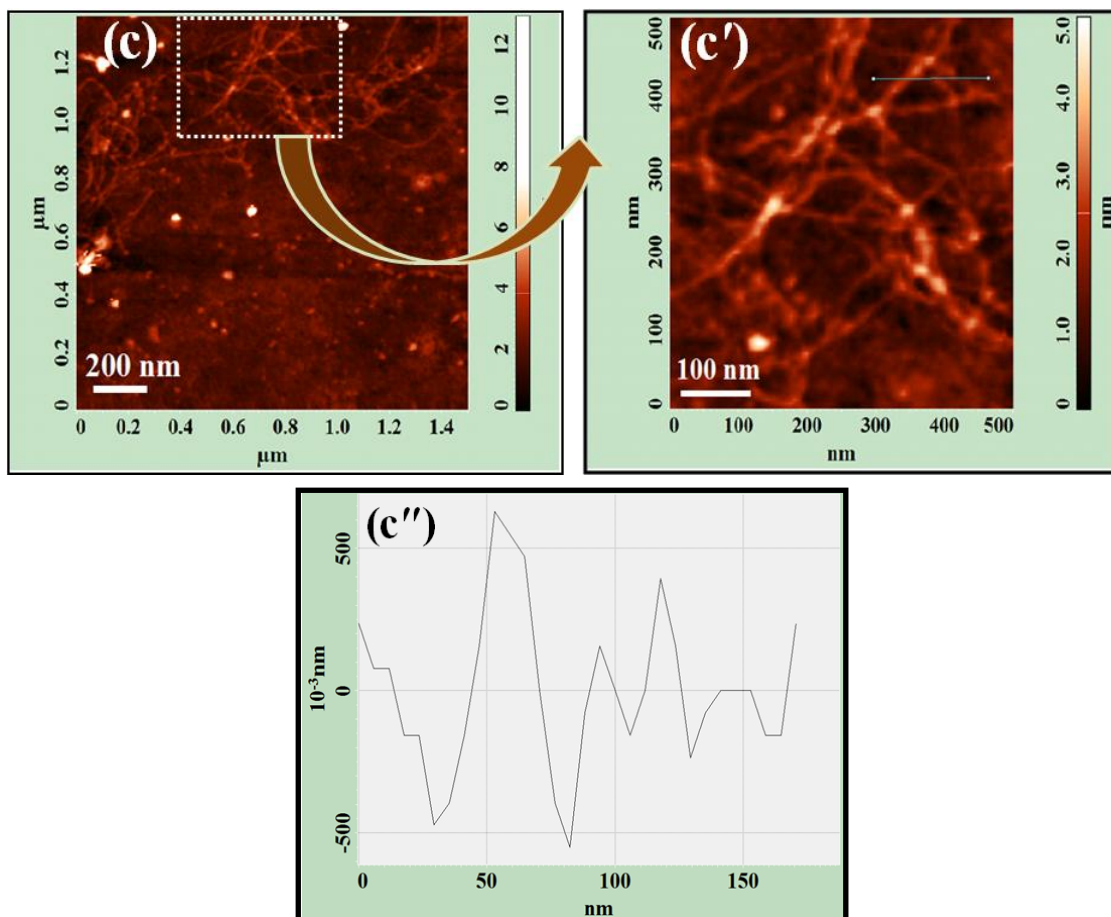
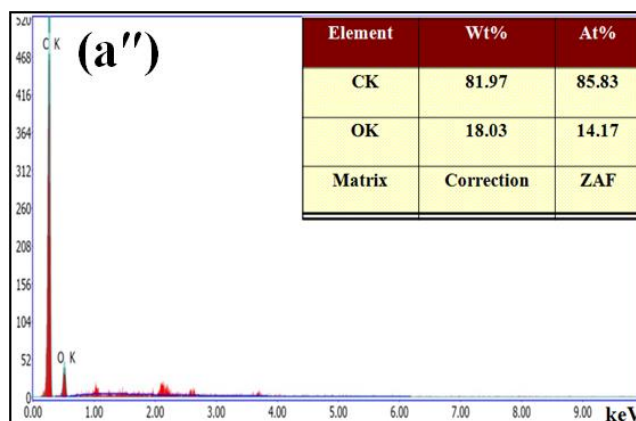
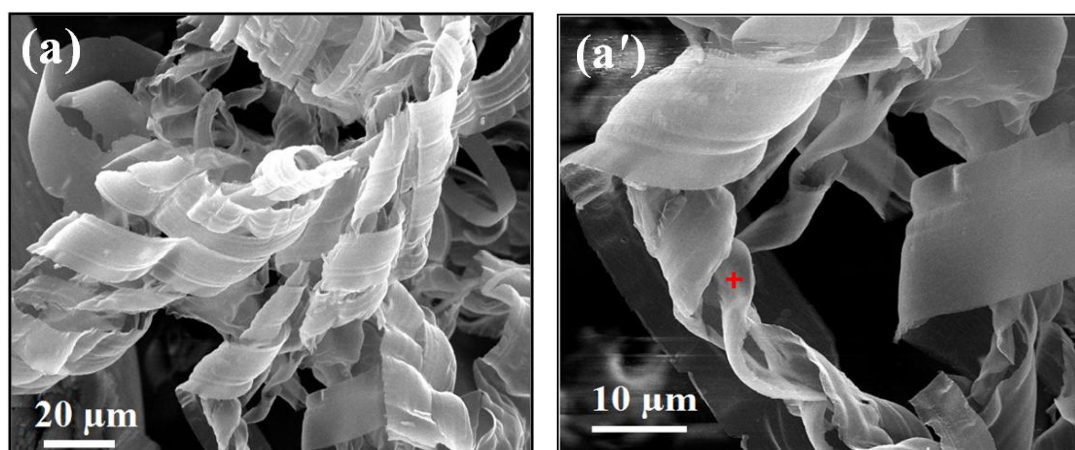


Fig. 4.6: AFM images and their height profile along a particular line: GO (a and a') and GNRs (b and b'), respectively (the surface height of GNRs at the typical indicated location measured by its line profile comes out to be 3.15 nm); GNRs-300 image at lower and higher magnifications (c and c') and its height profile along a particular line (c'').

4.2.4 FESEM Analysis

The morphologies of the reduction products GNRs and its annealed sample at 300 °C (GNRs-300) have been analyzed by using FESEM (Fig. 4.7). The EDAX spectra of these FESEM image(s) were recorded at the location(s) marked by (+) sign in red. As mentioned in the previous chapter, the FESEM image of GO exhibited the formation of agglomerated sheet with the C/O ratio of 1.59. Whereas, the FESEM images of the reduction product of GO, recorded at both lower and higher magnifications, show the formation of curl-shaped nanoribbons-like morphology (Fig. 4.7a and a'). EDAX analyses of these nanoribbons, recorded at higher magnification, shows C/O ratio to be 6.05 (Fig. 4.7a''), which is more than 3 times to that of GO (1.59) indicating the effective reduction of GO. This observation

is also supported by the elemental mapping of another image of GNRs recorded at lower magnification (image not shown), which showed the homogeneous distribution of carbon and oxygen with a much higher density for carbon (Fig. 4.7a''' and a'''). These nanoribbons are entangled with each other exhibiting their multiple folding, and for this reason it was not possible to determine the width and length of individual nanoribbons accurately. Although from some of the FESEM images captured at low resolutions (Fig. 4.7a'''' and a'''''), the length of these curl-shaped nanoribbons could be estimated and was found to vary in the range from 0.15 to 1 mm. On the other hand, the morphology of GNRs-300 reveals more of the unfolding of GNRs with the higher C/O ratio of 8.21 (Fig. 4.7b and b'). A comparison of the EDAX analyses of these samples exhibits C/O ratio to follow the order: GO (1.59) < GNRs (6.05) < GNRs-300 (8.21).



One-step chemically controlled wet synthesis of graphene nanoribbons from graphene oxide for high performance supercapacitor applications

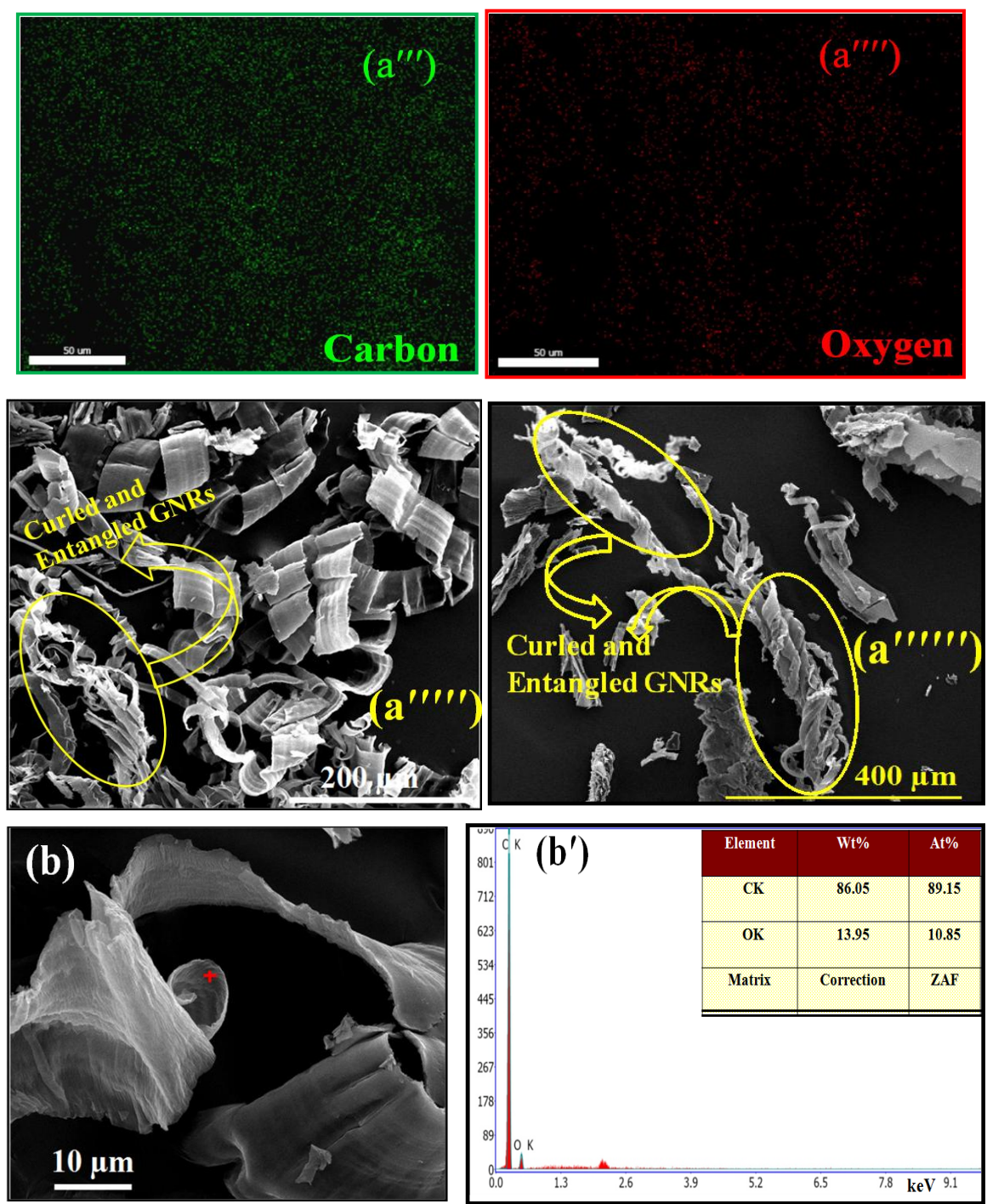


Fig. 4.7: FE-SEM images and their EDAX analyses at a particular location marked by (+) sign in red: GNRs (a, a' and a''), respectively. Elemental mapping of GNRs: Carbon (a''') and oxygen (a'''); FESEM images of GNRs at lower magnifications (a''') and (a''').

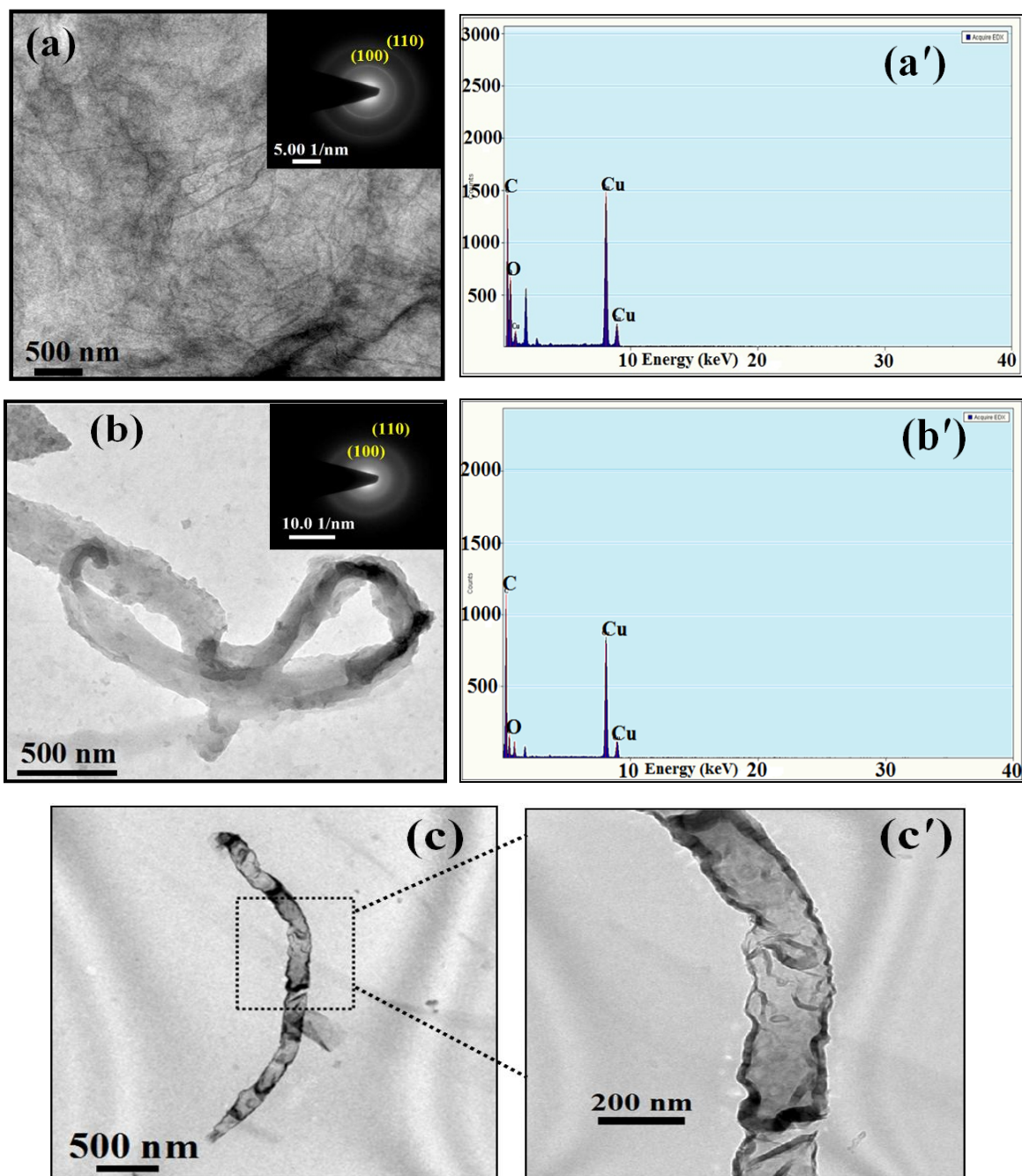
FE-SEM image of GNRs-300 (b) and its EDAX analysis at a particular location marked by cross sign in red (b').

4.2.5 TEM and SAED Analysis

Fig. 4.8 shows the TEM images of GO, GNRs and GNRs-300 along with their SAED patterns and EDAX spectra. TEM image of GO exhibits the formation of sheet-like morphology (Fig. 4.8a). Its SAED pattern indicating it to be polycrystalline and corresponds to the (100) and (110) planes of graphite having a hexagonal structure matching with the JCPDS file no. 75-1621 (Fig. 4.8a-inset). On the other hand, the TEM image of GNRs clearly shows the formation of coiled nanoribbons (Fig. 4.8b). The width of these nanoribbons from their several TEM images, prepared at different times, was estimated to vary in the range of ~ 150 -300 nm. Its SAED pattern shows diffused concentric rings matches to the (100) and (110) planes (Fig. 4.8b-inset), indicating their amorphous nature. HRTEM analysis of this sample did not show any fringes. Annealing of GNRs at a mild temperature of 300 °C (GNRs-300) produces more of unfolded nanoribbons as has been revealed by its images recorded at lower and higher magnifications (Fig. 4.8c and c'). GNRs-300 shows relatively smaller width ranging from about 140-200 nm unlike to that of GNRs. SAED image of GNRs-300, however, exhibits its polycrystalline nature displaying a ring pattern containing largely binary and ternary spots, thereby, indicating that it arises from bilayer and trilayer GNRs (Fig. 4.8c''). C/O ratio of these samples follows the order: GO < GNRs < GNRs-300 (Fig. 4.8a', b' and c'). In the case of GNRs-300 we could, however, obtain the lattice fringes (Fig. 4.8c''') and from these fringes the number of layers could be counted at different locations. At places multiple layers were stacked on each other, emerging as bundles and entangled with each other very similar to that observed in its AFM image (Fig. 4.6c and c'). The locations, where there was no entanglement, it exhibited the presence of 3-4 layers, which matches well with the observations made from its AFM analysis (Fig. 4.6). But, at the locations where entanglement was evident the number of layers was found to vary from 10-24 layers (Fig. 4.8c'''). The average 'd' spacing from these fringes were estimated to be 0.35 ± 0.01 nm (Fig. 4.8c''''-inset), and this value is very

One-step chemically controlled wet synthesis of graphene nanoribbons from graphene oxide for high performance supercapacitor applications

similar to that observed in the previous report on GNRs in which they were produced by the pyrolysis of the solvothermal product obtained from propanol and sodium [315], as well as with the XRD data (Fig. 4.5). The observation about the number of layers upon annealing in the GNRs-300, however, became more evident from the AFM images, where it could become possible to estimate the surface height of individual nanoribbons (Fig. 4.6c").



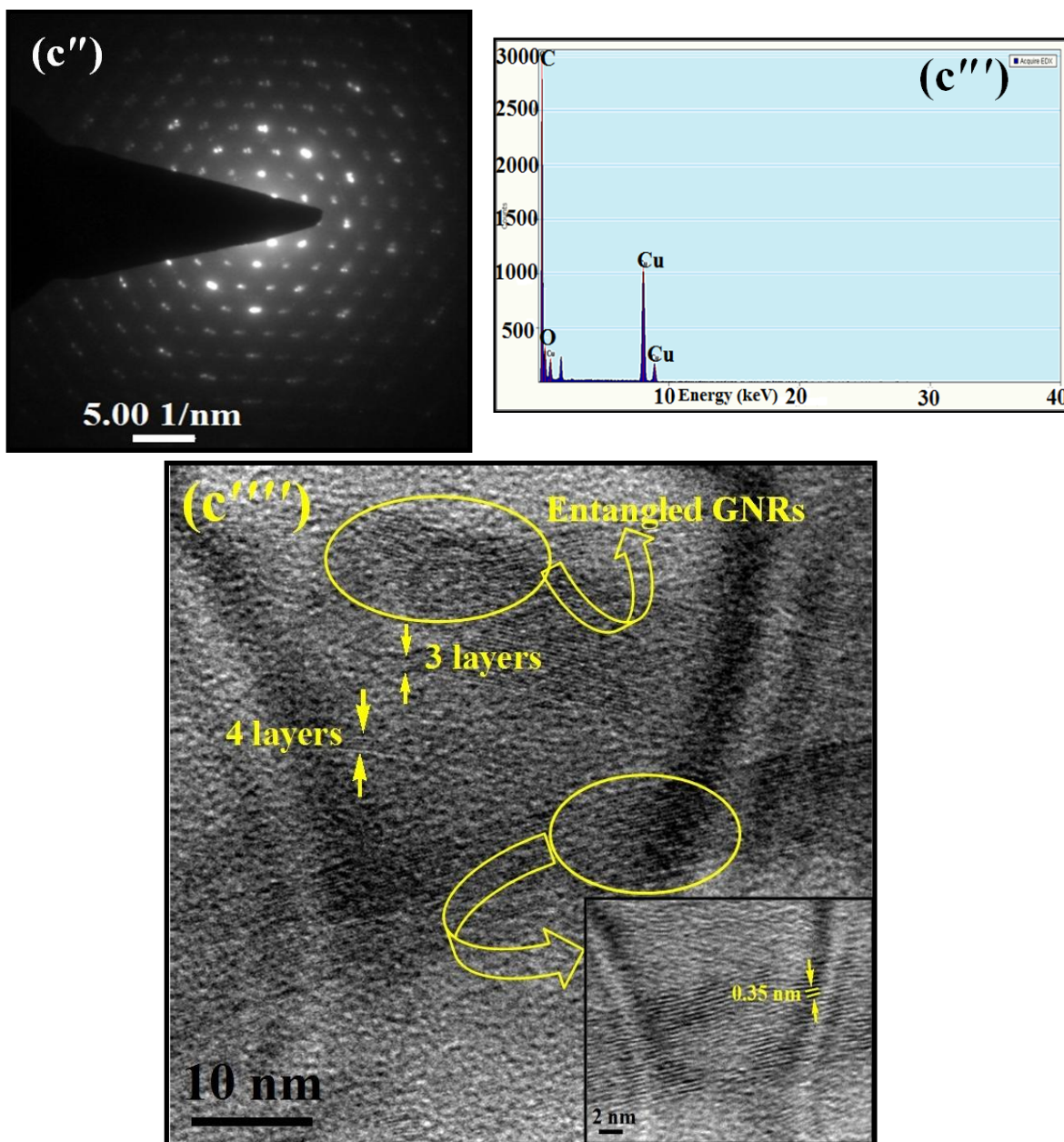


Fig. 4.8: TEM images containing SAED patterns in the inset and their EDAX analyses: GO (a and a') and GNRs (b and b'), respectively. TEM images of GNRs-300 at lower (c) and higher magnifications (c'); SAED pattern (c'') and EDAX analysis (c'). HRTEM image of GNRs-300 (c''') and its magnified image showing the 'd' spacing (c'''-inset).

4.2.6 FTIR Spectroscopy

In order to ascertain the reduction of GO, FTIR spectra of GO, GNRs and GNRs-300 were recorded in the mid-IR range ($4000\text{-}500\text{ cm}^{-1}$) (Fig. 4.9). The IR spectrum of GO exhibits several vibrational bands (cm^{-1}) at 3423, 1727, 1631, 1223, and 1058, which have been attributed to -OH stretching, C=O (COOH), C=C , C-O-C (epoxy) and C-O (alkoxy), respectively [284]. On the other hand, the IR spectrum of GNRs was fairly different to that

of GO in which the intensities of the peaks (cm^{-1}) due to $-\text{OH}$ (3431), $\text{C}=\text{O}$ (1745) and $\text{C}-\text{O}$ (1093) are reduced along with the slight blue shift and the peak due to $\text{C}-\text{O}-\text{C}$ (1223) has vanished completely. Apart from this, the bands due to symmetric and asymmetric stretching of $\text{C}-\text{H}$ at 2923 and 2857 cm^{-1} have become fairly intense and the peak due to $\text{C}=\text{C}$ is still retained. These observations indicate that the reduction of GO has been largely effective but some residual functionalities are still remains on GNRs. The IR spectrum of GNRs-300 shows further reduction in the intensities of the peaks due to $-\text{OH}$ stretching, $\text{C}-\text{O}$ (alkoxy), and the peak due to $\text{C}=\text{O}$ (COOH) is almost vanished. However, the bands due to symmetric and asymmetric stretching of $\text{C}-\text{H}$ and the peak due to $\text{C}=\text{C}$ are still retained. From these observations it is evident that sp^2 character is significantly enhanced for both GNRs and GNRs-300 as compared to that of GO. Notably, in case of GNRs-300 the residual oxygen functionalities have reduced to a greater extent.

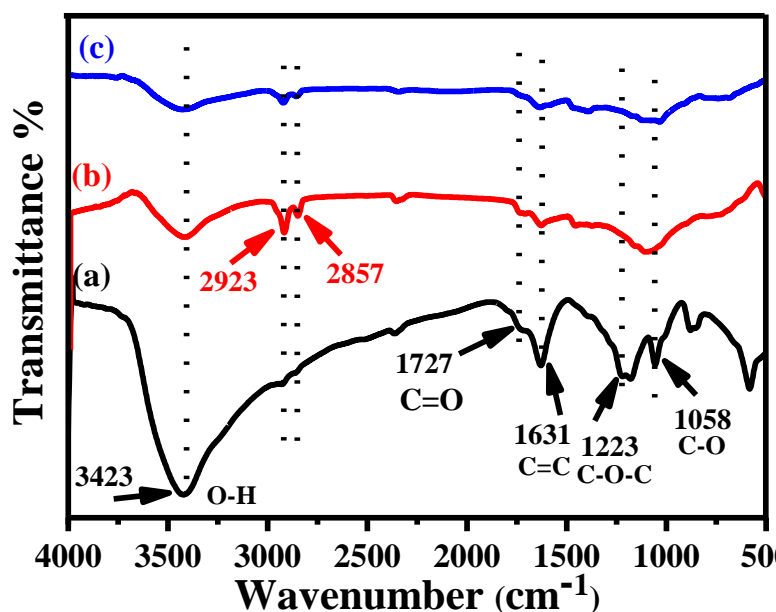
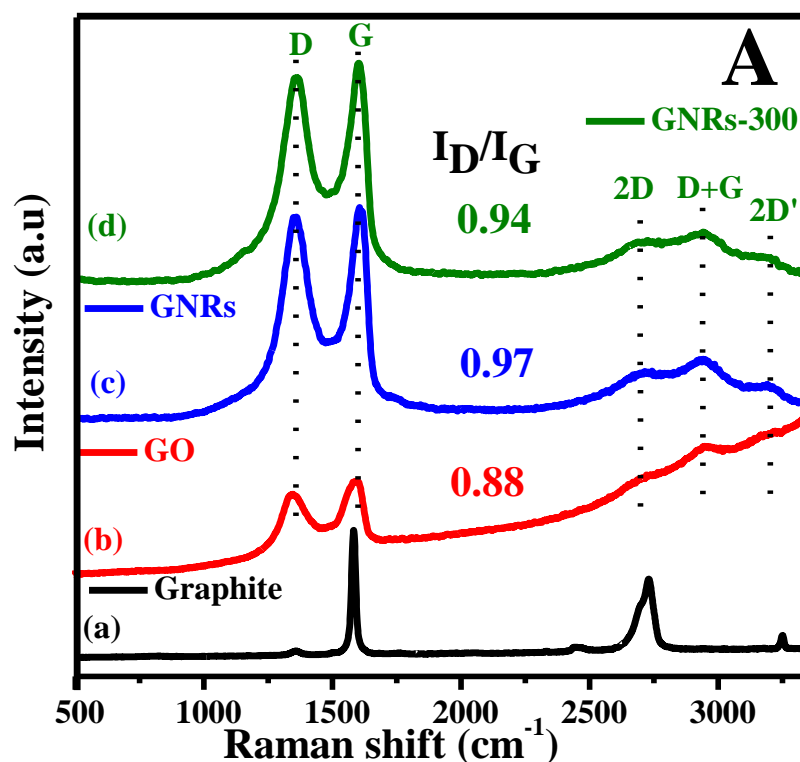


Fig. 4.9: FTIR spectra of: GO (a), GNRs (b) and GNRs-300 (c).

4.2.7 Raman Spectroscopy

The electronic structures of graphite, GO, GNRs and GNRs-300 were examined by Raman spectroscopy (Fig. 4.10) and their spectral data have been summarized in Table 4.1. The Raman spectra of graphite and GO exhibit the spectral features very similar to those

reported previously [383] (Fig. 4.10A-a and b). A careful examination of the Raman spectrum of GNRs shows the higher intensity of D band associated with the higher I_D/I_G ratio of 0.97 (Fig. 4.10A-c) as compared to that of GO (0.88) (Fig. 4.10A-b), indicating an increase in the number of smaller sp^2 domains [324]. This aspect was further manifested by calculating the in-plane crystalline size (L_a in nm) of the GO and GNRs, from which the values were calculated to be 19.03 and 17.27, respectively. Moreover, an additional D' band is noted in GNRs at 1623 cm^{-1} (Fig. 4.10C-c''), suggesting the presence of additional disordered/defects created due to residual functionalities in GNRs. The annealing of this sample at mild temperature of $300\text{ }^\circ\text{C}$ (GNRs-300) resulted in the decrease in the intensity of D band associated with the decrease in the I_D/I_G ratio to 0.94 along with the elimination of the D' band (Fig. 4.10A-d and C-d''). Moreover, the G band is red shifted (Fig. 4.10B-d') in this case. These features suggest an increase in the structural order in GNRs-300.



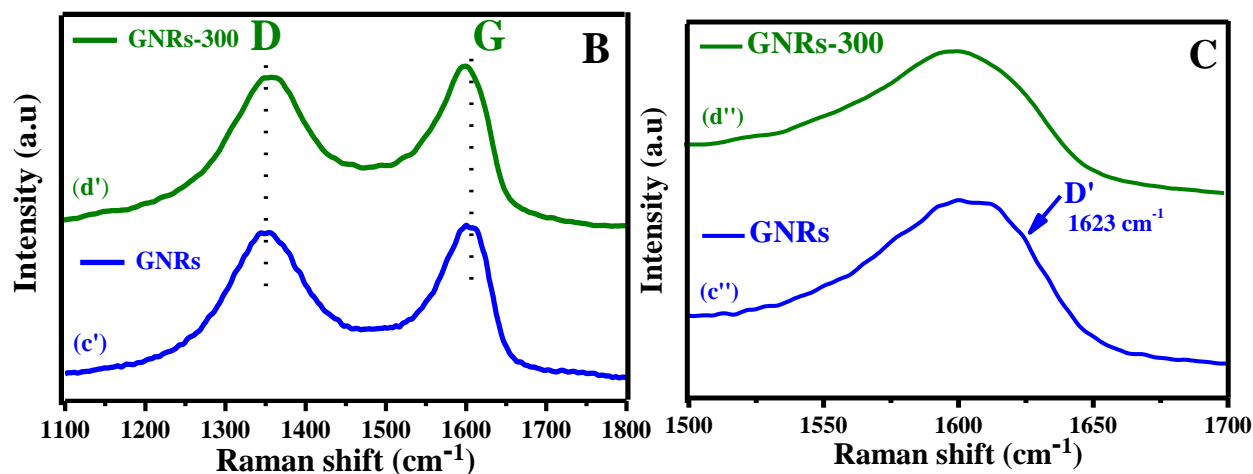


Fig. 4.10: Raman spectra of graphite (a), GO (b), GNRs (c) and GNRs-300 (d) – (panel A); expanded Raman spectra of GNRs (c') and GNRs-300 (d') in the wavenumber range of 1100-1800 cm^{-1} – (panel B); D' band of GNRs (c'') and GNRs-300 (d'') in the wavenumber range of 1500-1700 cm^{-1} – (panel C).

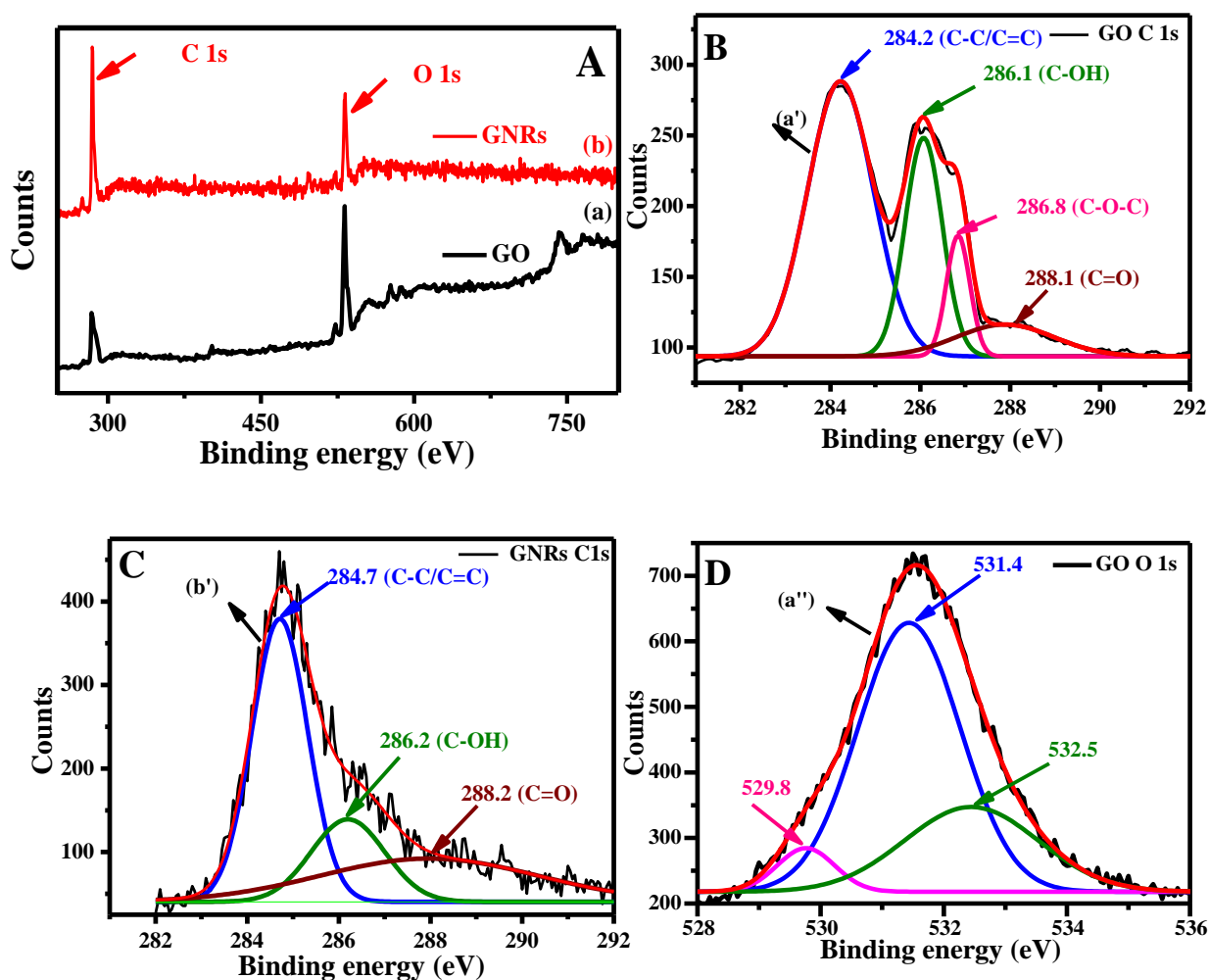
Table 4.1: Raman spectral data of graphite, GO, GNRs and GNRs-300.

Sample(s)	D band (cm^{-1})	G band (cm^{-1})	I_D/I_G
Graphite	1359	1582	-
GO	1355	1604	0.88
GNRs	1351	1605 (D' 1623)	0.97
GNRs-300	1359	1599	0.94

4.2.8 XPS Analysis

In order to analyze the surface of GO and GNRs, their survey scans were recorded by using XPS and are shown in Fig. 4.11A. The analyses of these spectra reveals that the C/O ratio is significantly increased in GNRs as compared to that of GO (Fig. 4.11A). The high resolution C 1s spectrum of GO contains four different components of carbon corresponding to the, C-C/C=C bonds due to the sp^3/sp^2 hybridized carbon (284.2 eV), C-OH (286.1 eV), C-O-C from epoxy (286.8 eV) and C=O from carboxyl group (288.1 eV) (Fig. 4.11B) [390]. In contrast to GO, C 1s spectrum of GNRs exhibits three different components of carbon arising from C-C/C=C (284.7 eV), C-OH (286.2 eV) and C=O (288.2 eV) (Fig. 4.11C). Moreover, in GNRs the intensity due to C=C component is enhanced whereas, the intensity of the peak due to C-OH is reduced. The high resolution O 1s spectrum of GO shows three different components of oxygen at binding energies (eV) of

529.8, 531.4 and 532.5, which have been assigned to lattice oxygen, carbon double bonded to oxygen (C=O) and carbon single bonded to oxygen (epoxide and hydroxyl), respectively. In case of GNRs, the O 1s spectrum also exhibits three different components of oxygen at binding energies (eV) of 531.8, 533.2 and a broad peak at 535.0 which have been attributed to C=O, physisorbed water and due to charging effect, respectively [395,396]. Further, a comparison of the O 1s spectra of GO and GNRs in panels D and E clearly reveals that the intensity due to O 1s band is reduced by about 2-fold in the case of GNRs as compared to that of GO. These data clearly indicate the effective reduction of GO into GNRs.



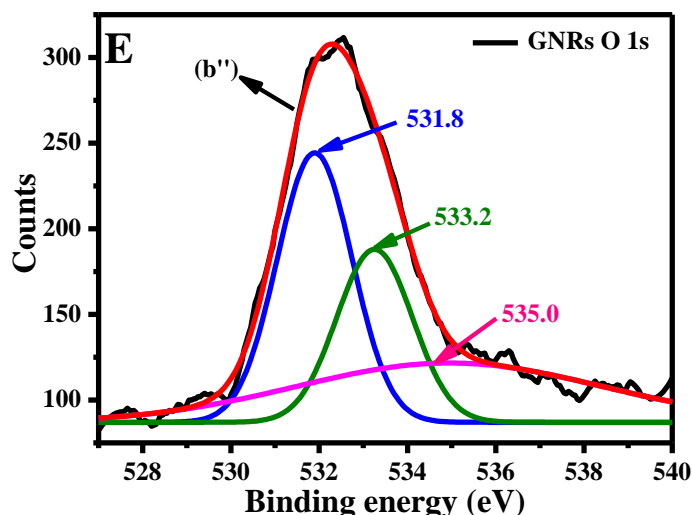


Fig. 4.11: XPS survey scans of GO (a) and GNRs (b) – (panel A); GO C 1s (a') – (panel B); GNRs C 1s (b') – (panel C); GO O 1s (a'') – (panel D) and GNRs O 1s (b'') – (panel E).

4.2.9 Solid-State ^{13}C NMR Spectroscopy

The reduction of GO into GNRs was further scrutinized by recording solid-state ^{13}C MAS NMR spectra of GO, GNRs and GNRs-300 (Fig. 4.12). The NMR spectrum of GO shows the presence of five different components of carbon (chemical shift (approx.) in ppm) namely, C-O-C (61), C-OH (70), graphitic sp^2 carbon (100-140), O-C=O carbonyl carbon of ester (167) and ketonic C=O group (190) [253]. In contrast to GO, the NMR spectrum of GNRs exhibits significant elimination of the carbon components due to C-O-C and ketonic C=O and a tremendous decrease in the intensity of the peaks due to C-OH and O-C=O. Whereas, the NMR spectrum of GNRs-300 exhibits the elimination of almost all the functionalities: C-O-C, C-OH, O-C=O and C=O. Interestingly, the reduction of GO into GNRs results in the enhancement of the broad resonance peaks due to graphitic components (100-140 ppm) and follows the order: GNRs-300 > GNRs > GO, suggesting the increasing graphitic (sp^2) character of the as-synthesized nanoribbons.

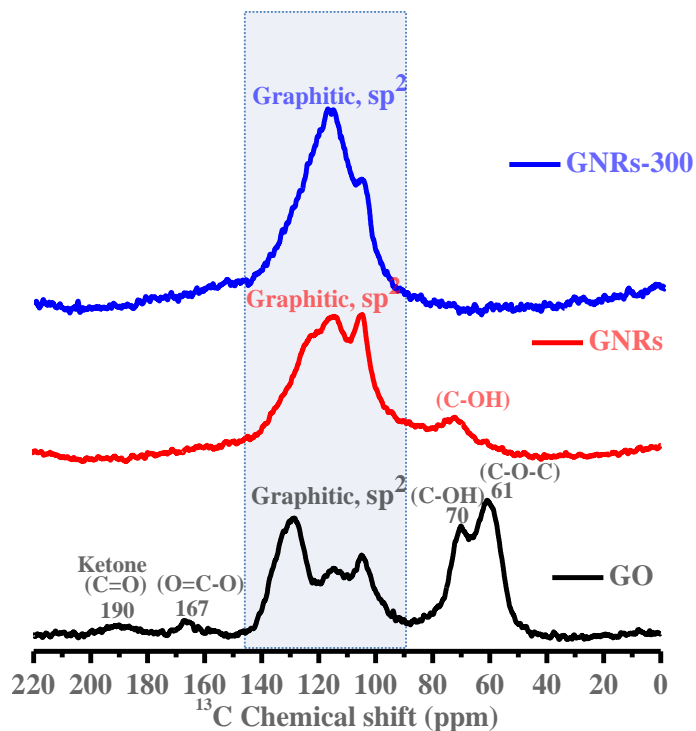


Fig. 4.12: Solid state ^{13}C MAS NMR spectra of GO, GNRs and GNRs-300 at 12 kHz.

4.2.10 I-V Measurements

The extent of reduction of GO into GNRs was further verified by recording the I-V curves for the precursor GO and its reduction products GNRs and GNRs-300 (Fig. 4.13). I-V curve for GO shows the conductivity value of 2.7×10^{-4} S/cm, whereas, the values of conductivity for GNRs and GNRs-300 increased significantly to 2.85 S/cm and 14.7 S/cm, respectively.

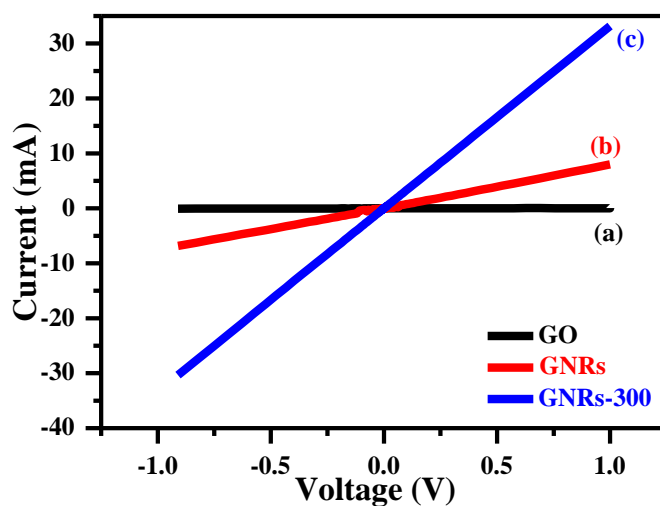


Fig. 4.13: I-V curves of GO (a), GNRs (b) and GNRs- 300 (c).

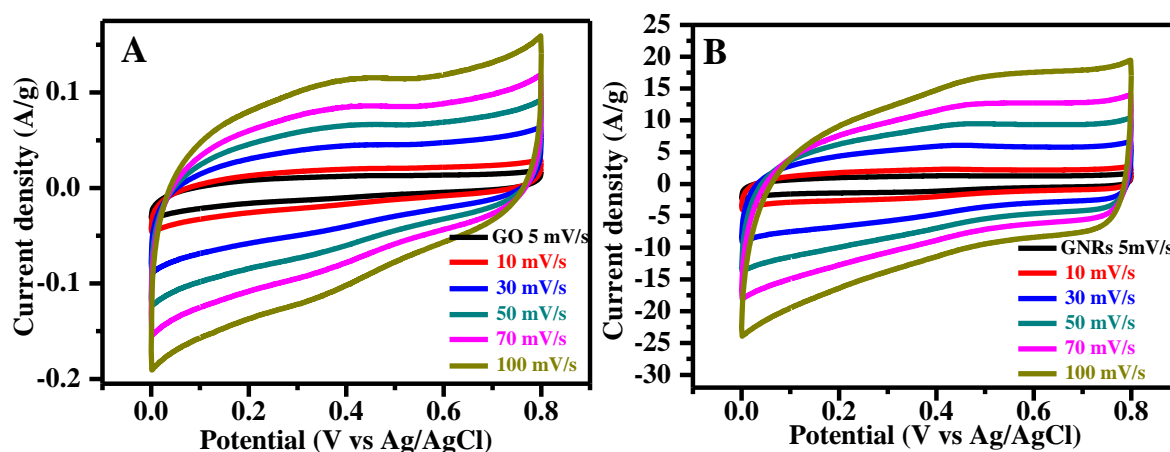
4.2.11 Electrochemical Measurements

The electrochemical behavior of GO, GNRs and GNRs-300 were investigated for the supercapacitor applications (Fig. 4.14). Cyclic voltammetry (CV) curves of GO, GNRs and GNRs-300 were recorded in the voltage range of 0.0 to 0.8 V at different scan rate(s) ranging from 5 to 100 mV/s. These curves exhibited an increase in current densities with increasing scan rates (Fig. 4.14A-C). The values of specific capacitance (C_s (F/g)) for GO, GNRs and GNRs-300 at the scan rates of 5, 10, 30, 50, 70 and 100 mV/s were calculated to be 2.02, 1.65, 1.27, 1.12, 1.04 and 0.96; 210, 189, 161, 145, 134 and 122; and 185, 147, 121, 113, 99 and 91, respectively (Fig. 4.14A-D). For a typical scan rate of 100 mV/s, GNRs (122 F/g) and GNRs-300 (91 F/g) shows much higher C_s values as compared to that of GO (0.96 F/g) (Fig. 4.14E). The lower value of C_s for GO as compared to those of GNRs and GNRs-300 may be attributed to the poor conductivity of GO (Fig. 4.13). This observation is also supported by the presence of sp^3 hybridization and low faradic rate of reaction in GO besides its lower surface area ($38.9 \text{ m}^2/\text{g}$). Interestingly, the CV curves for GNRs were almost rectangular in shape with a small redox hump, which indicates it to have major contribution arising from EDLC and a minor contribution from the pseudo-capacitance due to the residual functionalities similar to those reported previously [397,231]. In contrast to GNRs, the shape of the CV curves in case of GNRs-300 was almost rectangular suggesting the elimination of residual functionalities largely upon annealing at mild temperature of 300 °C.

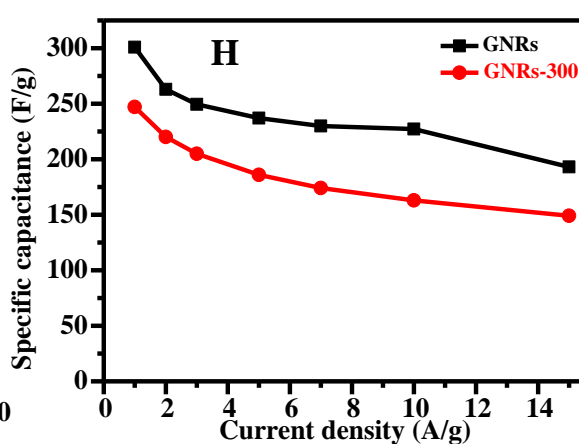
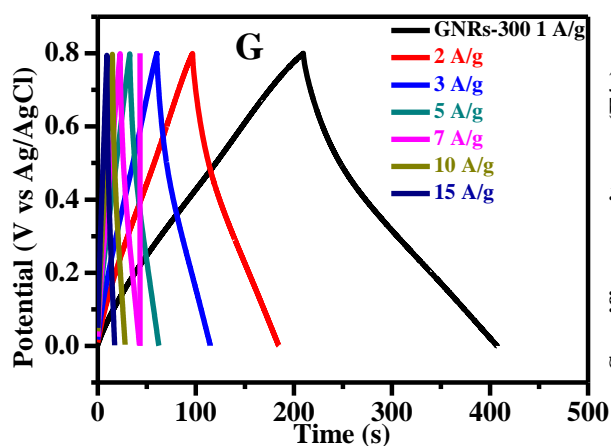
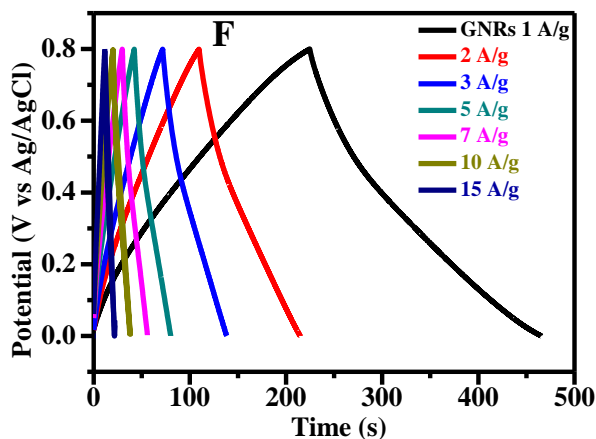
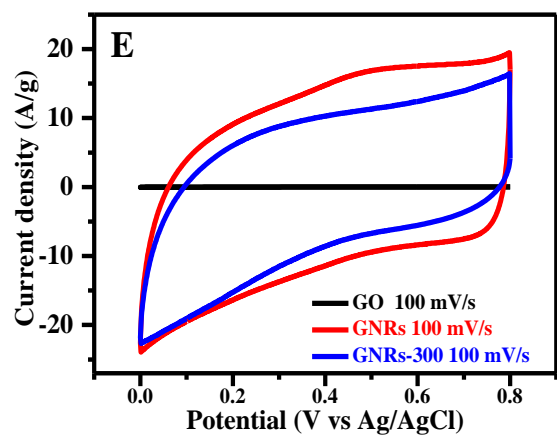
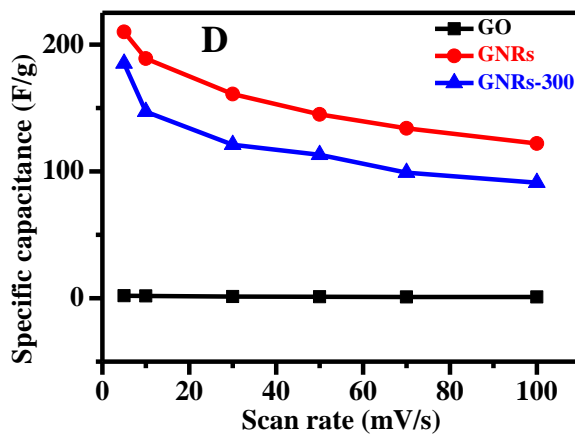
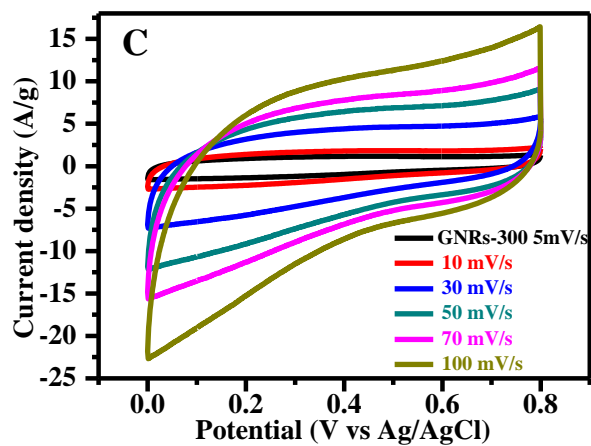
The electrochemical capacitive performance for GO, GNRs and GNRs-300 as electrode materials was also determined by GCD measurements in the potential window of 0.0 to 0.8 V similar to that used for CV measurements. Fig. 4.14F and G shows the charge-discharge curves for GNRs and GNRs-300 at various current densities of 1, 2, 3, 5, 7, 10 and 15 A/g from which the C_s values (F/g) were calculated to be 301, 263, 250, 237, 230, 227 and 193; and 247, 220, 205, 186, 174,

163 and 149, respectively. The shape of these curves is nearly symmetrical triangle. An increase in the current densities from 1 to 15 A/g results in the reduction of C_s values for GNRs and GNRs-300 from 301 to 193 F/g and 247 to 149 F/g (Fig. 4.14H), respectively. It is worth mentioning that even at a high current density of 15 A/g, the C_s values for GNRs and GNRs-300 are fairly high. A comparison of the C_s values obtained from GCD curve of GO (2.5 F/g at 1 A/g) with those of GNRs (301 F/g at 1A/g) and GNRs-300 (247 F/g at 1A/g) shows it to be considerable lower (Fig. 4.14I). Notably, the C_s value even for GRH-MA (220 F/g at 1A/g) (reported in Chapter 3) is fairly lower as compared to those of GNRs and GNRs-300.

For GNRs, the long term cycling stability was examined for 4000 cycles at the highest used current density of 15 A/g (Fig. 4.14J). The inset of Fig. 4.14J shows the typical first three and last three cycles of these runs. The C_s for the first cycle was calculated to be 193 F/g, which remains constant up to about 80 cycles and is increased gradually to 210 F/g up to 4000th cycle. After 80th cycle, the increase in the value of C_s may be attributed to the presence of residual functionalities on GNRs (Fig. 4.9, 4.11 and 4.12). Similar observations about the role of residual functionalities have been made in previous studies [231,277]. For 4000 cycles, the coulombic efficiency was estimated to be 100% from charging-discharging curves at 15 A/g (Fig. 4.14J).



One-step chemically controlled wet synthesis of graphene nanoribbons from graphene oxide for high performance supercapacitor applications



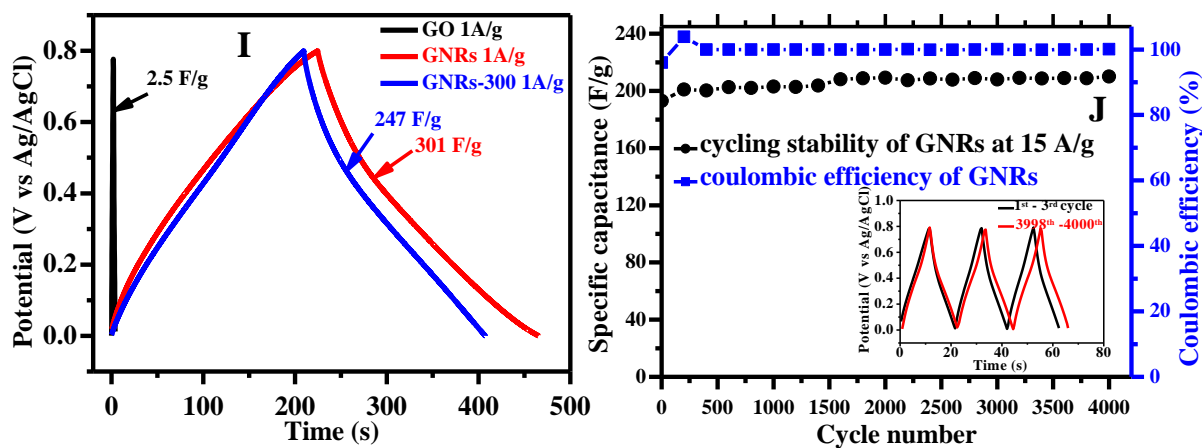


Fig. 4.14: CV curves of GO, GNRs and GNRs-300 at different scan rates – (panels A, B and C). Variation in the values of specific capacitance (C_s) as a function of scan rate for GO, GNRs and GNRs-300 – (panel D). A typical CV curve of GO, GNRs and GNRs-300 at a scan rate of 100 mV/s – (panel E). Galvanostatic charge-discharge (GCD) curves of GNRs and GNRs-300 at various current densities – (panel F and G). Variation in the value of C_s obtained from the GCD curves at different current densities – (panel H). GCD curves of GO, GNRs and GNRs-300 at a current density of 1 A/g – (panel I). Variation in the C_s and coulombic efficiency as a function of number of cycles (panel J) and the GCD curves for the first and last three cycles – (panel J-inset). All electrochemical measurements were performed in 1 M H_2SO_4 as an aqueous supporting electrolyte.

Fig. 4.15A shows the change in energy densities for the as-synthesized GNRs and GNRs-300 at various current densities. Fig. 4.15B shows the Ragone plots for GNRs and GNRs-300 exhibiting the high energy densities (Wh/kg) of 26.76 and 21.95 at a power density of 400 W/kg, respectively. Under identical experimental conditions, the value of energy density for GRH-MA was found to be 19.55 Wh/kg (reported in Chapter 3). Notably, even at a higher power density of 5944 W/kg, the energy density for GNRs decreased to 16.84 Wh/kg only. These results evidently suggest the tremendous potential of the as-synthesized GNRs as electrode material for energy storage devices.

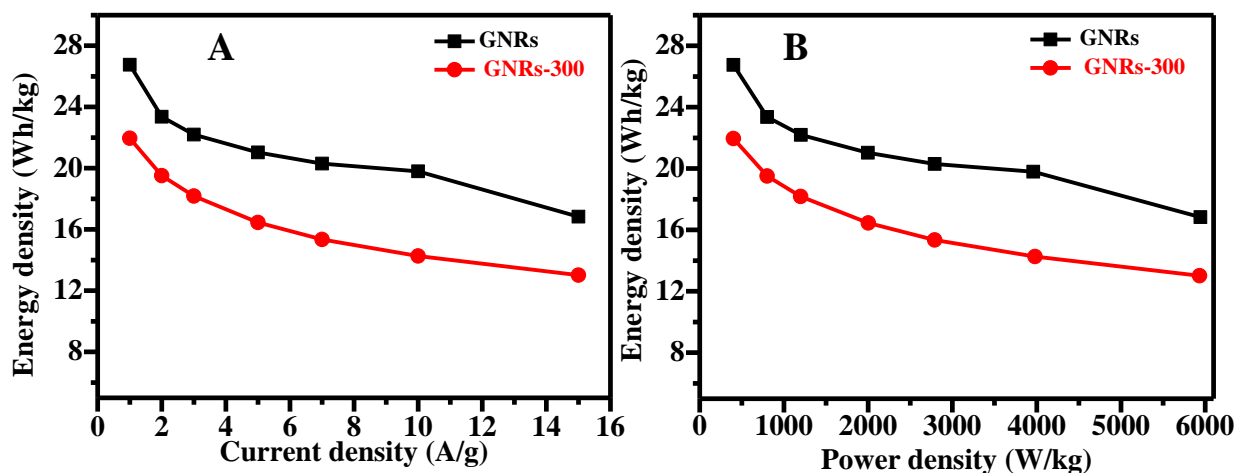


Fig. 4.15: Change in the energy density of GNRs and GNRs-300 electrodes in an aqueous electrolyte with current density (A) and Ragone plots for GNRs and GNRs-300 (B).

4.3 Discussion

The reduction of GO by employing malonic acid as a reductant at pH 6.0 was confirmed by the optical absorption spectroscopy and XRD (Fig. 4.3 and 4.5). It was exciting to observe that the reduction of GO at pH 6.0 resulted in the formation of GNRs (Fig. 4.6-4.8), unlike that at pH \sim 7.5 and 10.5, which produced stacked aggregated GNRs (Fig. 4.16) and ultrathin graphene sheets (Chapter 3), respectively. The lowering of pH below 6.0, however, caused this solution to undergo aggregation possibly because of relatively lower negative ζ -potential. It is worth mentioning that for pH (\geq 8) the reduction of GO resulted in the formation of graphene sheets only (not shown). These observations suggest that the pH of the solution plays a crucial role in producing carbon nanostructures with different morphologies. In control experiments, the reduction of GO was also examined at low pH (6.0) using OH⁻ at 95 °C in the absence of additional reducing agent (GRL) as well as by employing oxalic acid as reducing agent (GRL-Ox), which does not contain active methylene group. The absorption spectrum of GRL obtained after 10 h of heating exhibited the absorption maximum at 253 nm (Fig. 4.17). Under similar experimental conditions, GRL-Ox

showed the absorption maximum at 258 nm (Fig. 4.18a). It clearly shows that neither GRL nor GRL-Ox exhibits the effective reduction of GO in 10 h duration unlike that for GNRs, which showed the effective reduction of GO (Fig. 4.3). However, the complete reduction of GRL-Ox was observed to take place in about 15 h (Fig. 4.18b). These experiments clearly reveal that the reduction of GO with malonic acid containing an active methylene group is more effective than that of OH^- and oxalic acid.

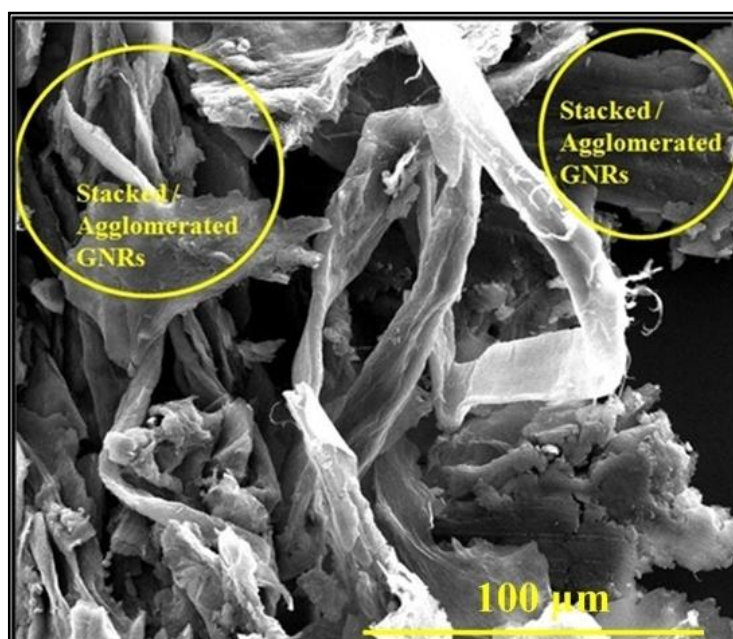


Fig. 4.16: FESEM image of GNRs at pH \sim 7.5 showing the stacked agglomerated GNRs.

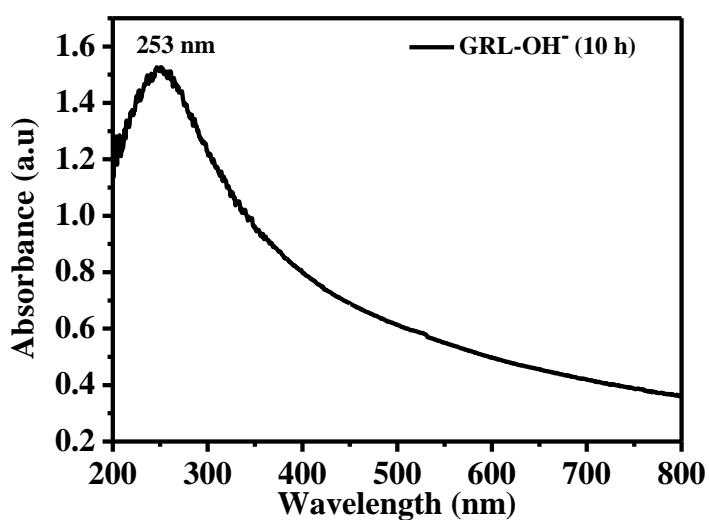


Fig. 4.17: Optical absorption spectrum of GRL after 10 h of heating.

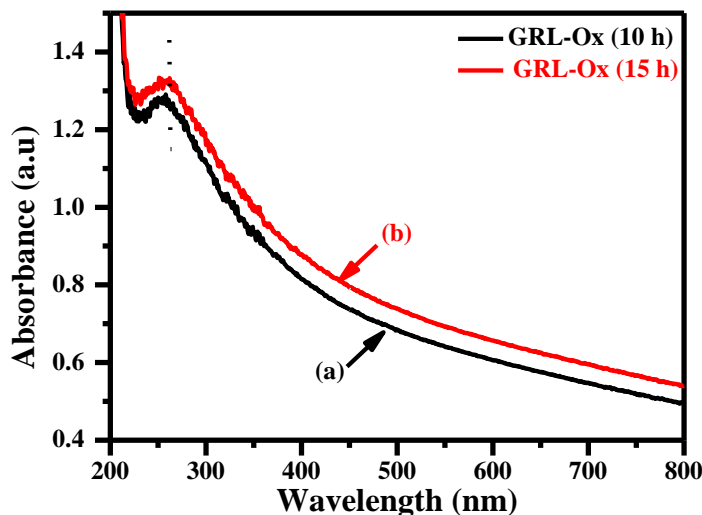


Fig. 4.18: Optical absorption spectra of GRL-Ox after 10 h (a) and 15 h (b) of heating.

In Raman spectroscopy, an increase in the intensity of D band (I_D/I_G ratio) indicates large number of small sp^2 domains as was supported by the decrease in the in-plane crystallite size. The presence of D' band suggests the existence of defects in GNRs, which might have arisen possibly due to the presence of edges [398], structural disorder/residual functionalities (Fig. 4.10). The as-synthesized GNRs had a thickness of about 3.3 ± 0.2 nm (Fig. 4.6b and b') and were found to be ~ 0.15 to 1 mm long (Fig. 4.7a'''' and a''''') with the width varying in the range of about 150 to 300 nm (Fig. 4.8b), as was revealed by AFM, FESEM and TEM analyses, respectively.

The formation of GNRs at pH 6.0 can be analyzed in terms of the $pK_a(s)$ of malonic acid (2.83 and 5.69), which suggest that at this pH the carboxyl ($-\text{COOH}$) groups of malonic acid are partially unionized (Fig. 4.19). It was also evidenced by ζ -potential measurements at pH 6.0, which shows relatively low value of ζ -potential (-45 mV) as compared to that at pH 10.5 (-55 mV) (Chapter 3). Obviously, the equilibrium between different resonating structures remains shifted towards the partial ionized form at pH 6.0 (Fig. 4.19).

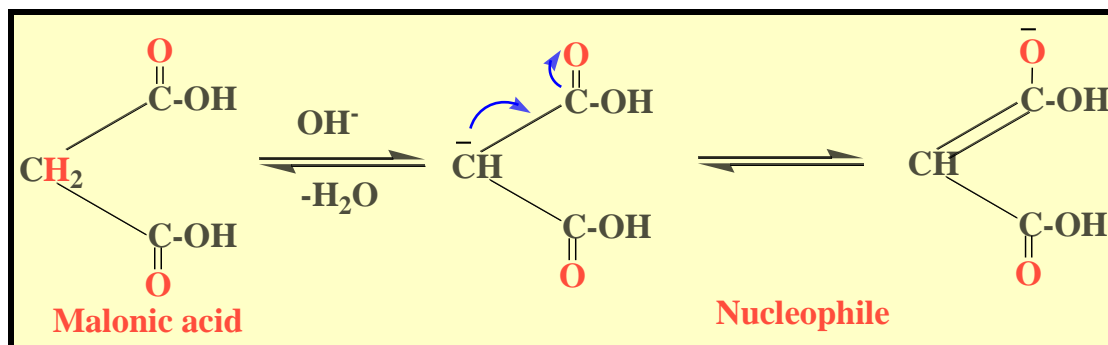
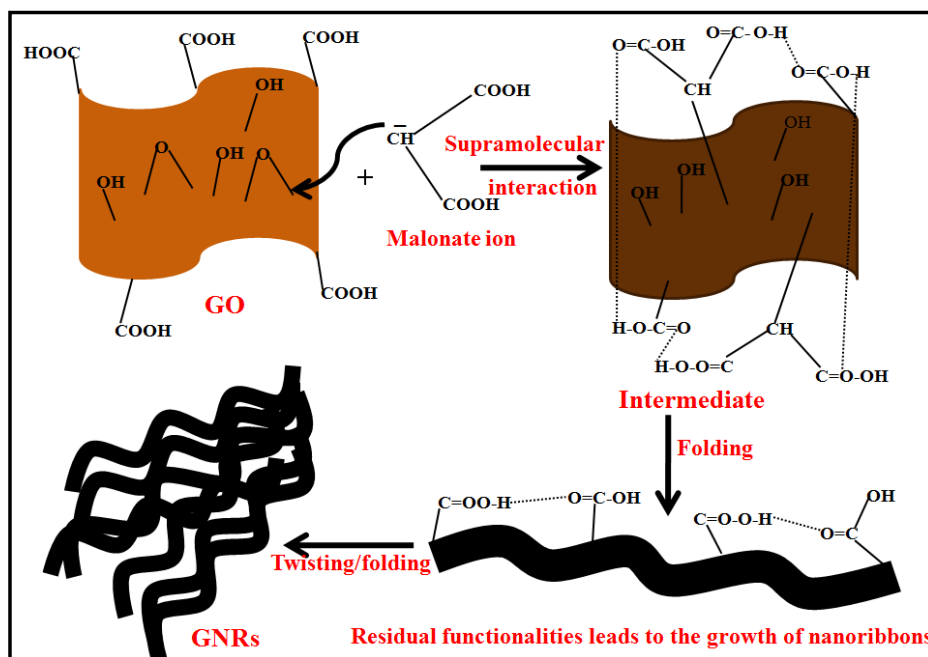


Fig. 4.19: Resonating structures of malonic acid in mild acidic condition.

GO exhibits the formation of a sheet-like structure having various oxygen containing functional groups like -OH, C-O-C and -COOH, which in the presence of malonic acid at pH 6.0 are reduced to form GNRs with relatively lesser residual functionalities (mainly -COOH groups) as was evidenced by IR, XPS and solid-state ^{13}C NMR studies (Fig. 4.9, 4.11 and 4.12). The difference in the morphology at pH 6.0, to that at pH 10.5 (Chapter 3), possibly arises because of the formation of an intermediate(s) between GO and malonic acid that might have caused its folding to form the nanoribbons-like structure (Scheme 4.1). It is understood to occur through supramolecular interactions involving -COOH groups of malonic acid and residual -COOH groups present on various edges of the reduced GO. The growth of the carbon nanostructures, thereafter takes place through weak non-covalent interactions involving several such micron-sized intermediates in the process of self-assembly. It leads to their folding and eventually results in the formation of ~ 0.15 to 1 mm long curled and entangled GNRs. The folding of sheet by AFM was also apparent which resulted an increase in the thickness to 3.3 ± 0.2 nm in the present chapter as compared to that of sheet observed earlier (Chapter 3) at pH 10.5 (0.41 ± 0.03 nm).

One-step chemically controlled wet synthesis of graphene nanoribbons from graphene oxide for high performance supercapacitor applications



Scheme 4.1: The nucleophilic attack of malonate ion on the epoxy group of GO and resulting in the formation of graphene nanoribbons (GNRs).

The significant reduction in the intensities of C-OH and O-C=O groups and almost complete elimination of C-O-C and ketonic C=O functionalities in GNRs are clearly evidenced by solid-state ^{13}C NMR (Fig. 4.12). These findings are also supported by the XPS analyses (Fig. 4.11). In contrast to GNRs, the solid-state ^{13}C NMR spectrum of GNRs-300 shows nearly complete elimination of all the oxygenated groups namely, C-OH and O=C-O (Fig. 4.12) which is understood by the removal of residual functionalities on GNRs. This observation is also indicated by its IR spectroscopic data (Fig. 4.9). This aspect is also manifested by the morphological changes of GNRs-300, observed by FESEM and TEM, which showed the straightening of the folded GNRs and is explained by the decreased extent of supramolecular interaction through $-\text{COOH}$ groups (Fig. 4.7b and 4.8c). AFM analysis of GNRs-300 showed the reduced surface height of 1.1 ± 0.5 nm as compared to those of GNRs (3.3 ± 0.2) (Fig. 4.6), evidently validates the removal of remaining functionalities on GNRs. These observations are also supported by the significant increase in the BET surface area of GNRs-300 ($470 \text{ m}^2/\text{g}$) as compared to those of GNRs ($129 \text{ m}^2/\text{g}$).

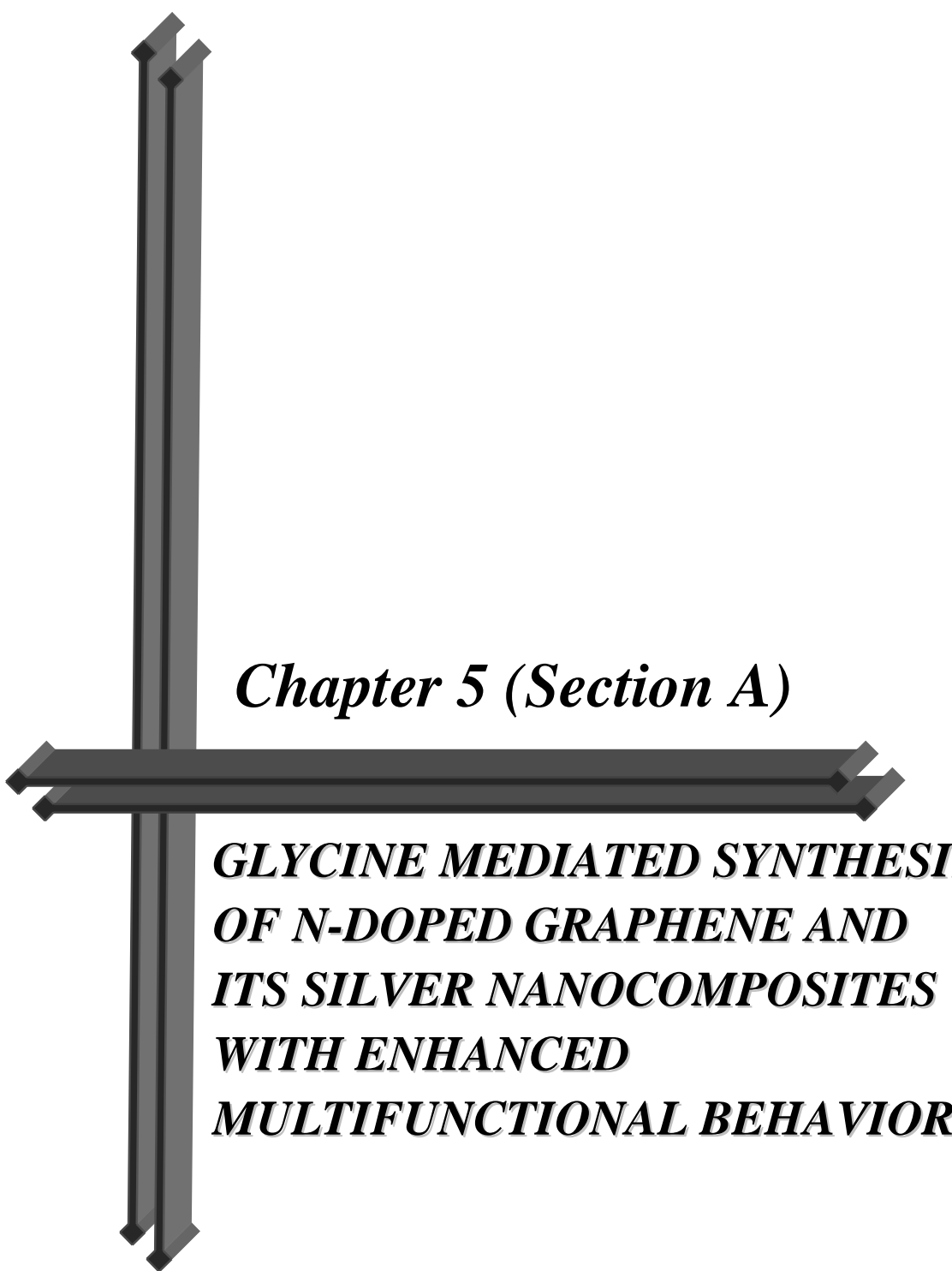
The annealing of GNRs at a mild temperature of 300 °C (GNRs-300) resulted in the occurrence of crystallinity in GNRs-300, as was evidenced by its XRD, SAED and HRTEM analyses (Fig. 4.5 and 4.8). The extent of reduction of GO to GNRs and GNRs-300 is revealed by the I-V measurements which showed more than four orders of magnitude higher conductivity for GNRs (2.85 S/cm) as compared to that of GO (2.7×10^{-4} S/cm) (Fig. 4.13) confirming the restoration of sp^2 character in GNRs upon reduction. Interestingly, the conductivity for GNRs-300 (14.7 S/cm) is more than five times that of GNRs, which clearly demonstrates that the annealing at a mild temperature of 300 °C further enhances the sp^2 character in as-synthesized GNRs (Fig. 4.13). The linearity in the I-V curves for both GNRs and GNRs-300 displays their metallic behavior. The observed ohmic nature indicates that they have sp^2 hybridized domains [399]. The value of current observed in the entire recorded range of voltage is more than an order of magnitude higher to those reported for reduced GO obtained by thermal exfoliation and reduction of GO at a much higher temperature of 1100 °C [399].

In the present case the shape of the CV curves for GNRs evidently suggests that the C_s value (122 F/g at 100 mV/s) is largely contributed due to EDLC involving non-faradic storage of charge through reversible adsorption of ions. A partial contribution to the C_s value also arises due to the pseudo-capacitance involving faradic reaction between residual oxygen functionalities on GNRs at the edge planes, as was evidenced by IR, XPS and ^{13}C NMR (Fig. 4.9, 4.11 and 4.12), and H^+ ions of electrolyte (Fig. 4.14B). Apart from this the hydrophilic nature of the residual functionalities on GNRs might facilitate the increased permeability of the electrolytic solution, resulting in the faster wetting of the electrode [400,267] contributing to the C_s . The observed decrease in the C_s value for GNRs-300 (91 F/g at 100 mV/s) has been attributed to the loss in pseudo-capacitive functionalities from the edge plane(s) of GNRs (Fig. 4.14C) as is also reflected by the increased conductivity of

GNRs-300 (Fig. 4.13c). It thus suggests that the C_s value is now largely contributed due to EDLC.

The C_s value for GNRs, calculated from GCD curves (301 F/g at 1 A/g) (Fig. 4.14F), is fairly high in comparison to that of GRH-MA (220 F/g at 1 A/g) (Chapter 3), as well as graphene sheets synthesized by employing other different reducing agents such as tin powder (152 F/g at 1.5 A/g) [278], trigol (130 F/g at 1 A/g) [379], tartaric/malic/oxalic acid (100.8/112.4/147 F/g at 0.1 A/g) [269], caffeic acid (136 F/g at 1 A/g) [274] and from bio-reduction (137 F/g at 1.3 A/g) [283]; and even higher than those of some N-doped graphene sheets involving reducing agents such as hydrazine (133 F/g at 1 A/g) [401] and ammonia (233.3 F/g at 0.5 A/g) [402]. For GNRs obtained by the electrochemical exfoliation of graphite using an aqueous electrolyte, the C_s value was found to be (140 F/g at 1 A/g) [310]. Whereas, for GNRs synthesized by unzipping of pristine MWCNTs/CNTs different values of C_s were obtained from the following methods: employing H_3PO_4 as the reducing agent (150 F/g at 1A/g) [403]; using hydroiodic acid as reductant (147 F/g at 0.5 A/g) [404]; heat treatment in Ar at 600 °C of: oxidized CNTs (130 F/g at 1 mV/s) [378] and graphene oxide nanoribbons obtained from MWCNTs (115.6 F/g at 1.7 A/g) [308]. Further, the high value of C_s (210 F/g) at a current density of 15 A/g after 4000 cycles suggests the high stability of this system. Moreover, the energy density (Wh/kg) values for GNRs (23.36) and GNRs-300 (19.52) calculated at a power density of 800 W/kg (Fig. 4.15B) are much higher to those reported for thermally reduced graphene oxide nanoribbons (15.06 Wh/kg at 807 W/kg) [308], and are significantly higher to those of the available commercial supercapacitors (3-4 Wh/kg at 3-4 kW/kg) [382].

The above features suggest the potential of this material for application in high performance supercapacitors.



Chapter 5 (Section A)

***GLYCINE MEDIATED SYNTHESIS
OF N-DOPED GRAPHENE AND
ITS SILVER NANOCOMPOSITES
WITH ENHANCED
MULTIFUNCTIONAL BEHAVIOR***

5A. GLYCINE MEDIATED SYNTHESIS OF N-DOPED GRAPHENE AND ITS SILVER NANOCOMPOSITES WITH ENHANCED MULTIFUNCTIONAL BEHAVIOR

In literature, a number of reducing agents have been employed for the reduction of GO to synthesize N-doped graphene but most of these reagents (such as hydrazine [324], hydroxylamine [331], ammonia [335], hexamethyltetramine [337] and dicyandiamide [338]) are corrosive. In the recent past, a number of environmental friendly reducing agents including amino acids have also been investigated for the reduction of GO to produce N-doped graphene [273,339-342]. Lately, two contradictory reports have appeared in the literature about the use of glycine (Fig. 5.1) as a reducing agent [273,339]. These reports make use of different concentrations of glycine (10 and 16.6 mM), which resulted in different observations from two laboratories. In one of the reports, glycine has been reported to be inefficient reducing agent at its concentration of 10 mM for the reduction of GO upon 6 h of heating at 95 °C and maintaining the pH of the solution at about ~ 10 [273]. In another report, 16.6 mM concentration of glycine have been employed for performing the reduction of GO, which required about 12 h of stirring at room temperature followed by its heating for 24 h at 95 °C [339]. However, the later report has established the glycine to be an effective reducing agent.

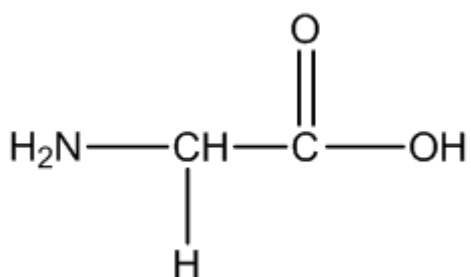


Fig. 5.1: Structure of glycine.

As regards to the amino acid mediated synthesis of N-doped graphene-Ag nanocomposites, we have come across two reports employing glycine [371] and arginine [354] as reducing agents. Mayavan *et al.* [371] have employed glycine as a reducing agent for the reduction of GO and Ag⁺ containing GO:Gly:Ag in the mass ratio (1:2:2) in aqueous medium. The resulting mixture was sonicated for 2 h followed by its gradual heating from room temperature to 500 °C under Ar atmosphere at 2 °C/min and was maintained at this temperature for 2 h. In another report [354] using arginine as a reducing agent, microwave induced (2.45 GHz, 900 W) reduction of GO was performed employing high concentration of Ag⁺ (100 mM). However, in none of these reports, N-doped graphene-Ag nanocomposites thus produced was investigated for their electrical and electrochemical behavior.

In the present section, we have synthesized glycine mediated N-doped graphene by exploring the effect of various parameters on the reduction efficiency of GO such as the concentration of glycine, pH and heating time and also examined its formation mechanism. In the subsequent work, the N-doped graphene was modified by decorating its surface with Ag NPs by simultaneous reduction of GO and Ag⁺ using glycine as an environmental benign reducing agent. These nanocomposites were prepared under mild conditions of temperature and pH in aqueous medium as optimized above for N-doped graphene. The as-synthesized nanocomposites exhibit fairly high surface area with enhanced conductivity and electrochemical features as compared with that of N-doped graphene and also showed relatively high SERS activity for the detection of 4-ATP as a probe molecule. In comparison to the previous report on arginine mediated synthesis of graphene-Ag nanocomposites, the present system employs fairly low concentration of Ag⁺ and has demonstrated very similar SERS activity. To the best of our knowledge, this is the first report on these nanocomposites using environmentally benign conditions for the synthesis, analyzing

the nature of interaction among different components and exploring their multifunctional features.

5A.1 Optimization of Various Parameters for the Effective Reduction of GO to Produce N-doped Graphene

5A.1.1 Optimization of the Amount of Glycine

The mass ratio of glycine to GO was optimized by monitoring its optical absorption spectra (Fig. 5.2). The mass ratio(s) of glycine:GO were varied from 2.6-5.2:1 by keeping the time of heating and pH of the reaction mixture constant at 3 h and 10.5, respectively (Fig. 5.2). For the mass ratios of glycine:GO ranging from 2.6-5.2:1, it resulted in a gradual increase in the absorption in the entire UV-Vis range. At lower mass ratios of glycine:GO (2.6:1 and 4.0:1) it exhibited the absorption maxima at 257 and 260 nm, respectively, indicating the incomplete reduction of GO. The efficient reduction of GO was obtained for the mass ratio of 5.2:1 (glycine:GO) showing the absorption maximum at 263 nm. Thereafter, any increase in the mass ratio of glycine:GO did not result any change in the absorption maximum and absorbance (not shown). Therefore, the mass ratio of glycine:GO was kept at 5.2:1.

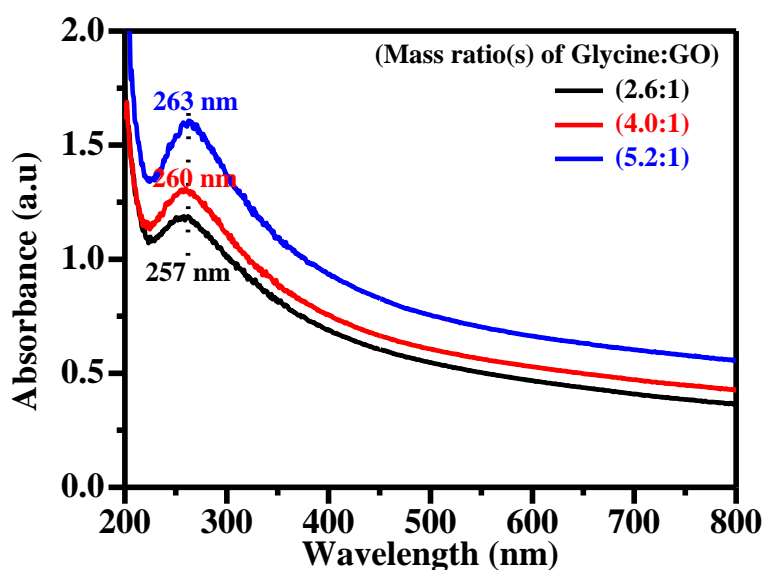


Fig. 5.2: Optical absorption spectra for the reduction of GO as a function of mass ratio(s) of glycine:GO varying from 2.6-5.2:1.

5A.1.2 Optimization of the Heating Time and pH

The heating time of the reaction mixture containing GO and glycine was varied from 1 to 4 h by keeping the mass ratio of glycine:GO and pH constant at 5.2:1 and 10.5, respectively. The changes in the absorption peak of the reaction mixture as a function of heating time up to 3 h is shown in Fig. 5.3A. It clearly shows that the absorption maximum is gradually red shifted from 254 to 263 nm. After 3 h, the reaction mixture did not show any shift in the absorption maximum (Fig. 5.3B). Therefore, the heating time of the reaction mixture was kept to be 3 h by keeping mass ratio of glycine:GO and pH constant at 5.2:1 and 10.5, respectively and this sample is denoted as GRH-Gly. It may be mentioned that the optimum heating time for the reduction of GO using glycine at pH 4.5 keeping all other conditions constant was found to be 10 h (details not shown) and is denoted as GRL-Gly. It shows the absorption maximum at 263 nm (Fig. 5.4A). The Raman spectrum of this sample showed I_D/I_G ratio of 1.01 (Fig. 5.4B), which is very similar to that of GRH-Gly (*vide infra*).

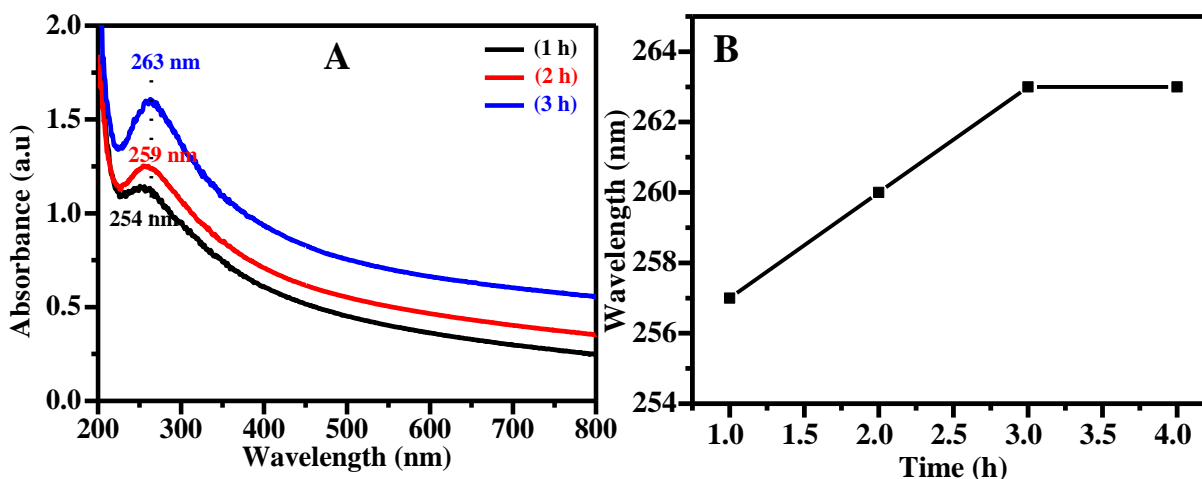


Fig. 5.3: Changes in the absorption peak of reaction mixture containing GO and glycine at pH 10.5 as a function of heating time – (panel A). Shift in the absorption maximum of the reaction mixture with heating time – (panel B).

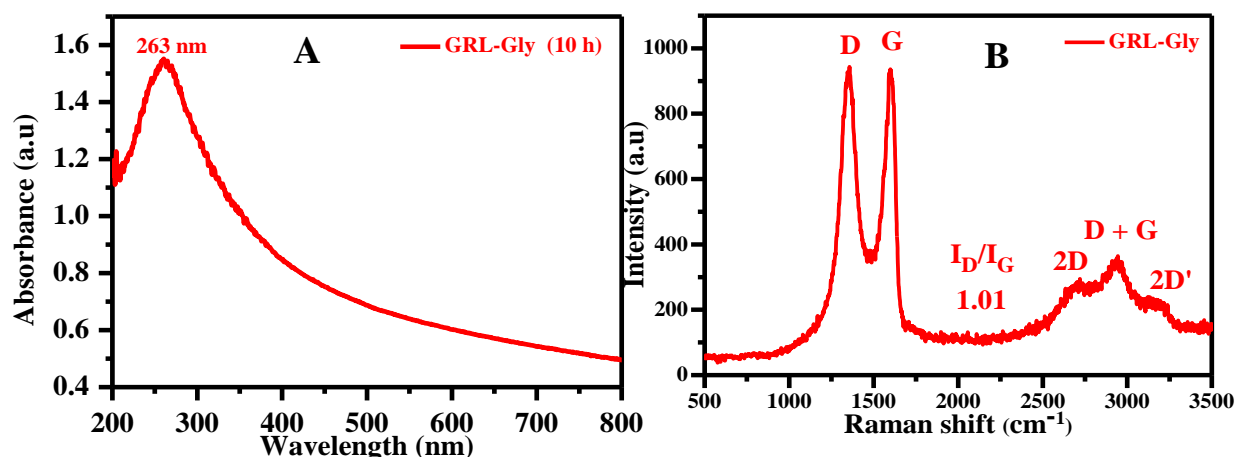


Fig. 5.4: Optical absorption spectrum of GRL-AIB – (panel A) and its Raman spectrum – (panel B).

5A.1.3 Synthesis of N-doped Graphene (GRH-Gly) under Optimized Reaction Conditions

Based on the above optimized conditions for the reduction of GO, 52 mg of glycine (34.6 mM or 2.6 mg/mL) was mixed with 20 ml of GO dispersion containing 10 mg of GO (0.5 mg/ml) under stirring and the pH of the resulting solution was maintained at 10.5 by adding dilute NaOH. The completion of the reaction takes about 3 h at 95 °C. The resultant black solid was centrifuged and washed with DIW from five to six times in order to remove any residual glycine as it is soluble in water. The product obtained was re-dispersed in DIW maintaining the pH of the solution at 10.5.

5A.2 Optimization of Various Parameters for the Simultaneous Reduction of GO and Ag⁺ to Synthesize N-doped Graphene-Ag Nanocomposites

5A.2.1 Optimization of the Amount of Silver Nitrate

For the synthesis of N-doped graphene-Ag nanocomposites the amount of Ag⁺ was optimized by varying its concentration and keeping the mass ratio of glycine:GO, pH and heating time of reaction mixture constant at 5.2:1, 10.5 and 3 h, respectively. At low concentration of Ag⁺ containing the mass ratio of AgNO₃:GO (1:10), a peak at 259 nm in UV region and a broad peak at about 410 nm in visible region was observed (Fig. 5.5a). An

increase in this mass ratio to 2:10 resulted in the red shifted peak at 262 nm associated with an increase in absorption in the visible region peaking at about 413 nm (Fig. 5.5b). This observation was also supported by the change in color from yellow-brown to black at this concentration (*vide Infra*). A further increase in the mass ratio(s) of AgNO₃:GO (3-9:10) caused the optical absorption in UV region to get gradually blue shifted associated with a reduction in its intensity. However, the peak at 413 nm becomes increasingly more intense with increasing Ag⁺ (Fig. 5.5c to e). This clearly indicates that glycine is now mainly involved in reducing Ag⁺ and GO partially. This observation was also supported by the change in color from dark black to greenish black at higher Ag⁺ concentration (not shown). Therefore, for the simultaneous reduction of Ag⁺ and GO the mass ratio of AgNO₃:GO was kept to be 2:10.

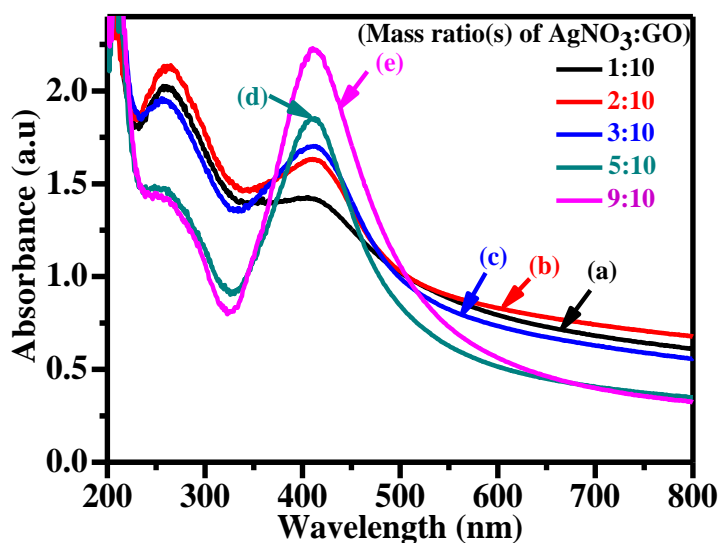


Fig. 5.5: Optical absorption spectra for the simultaneous reduction of Ag⁺ and GO as a function of mass ratio(s) of AgNO₃:GO (1-9:10).

5A.2.2 Optimization of the Heating Time

The heating time of the reaction mixture containing glycine, Ag⁺ and GO was varied from 1 to 4 h by keeping the amount of glycine, mass ratio of AgNO₃:GO and pH constant at 2.6 mg/mL, 2:10 and 10.5, respectively. The changes in the absorption peak of the reaction mixture as a function of heating time up to 3 h is shown in Fig. 5.6A. It clearly

shows that with increased heating time from 1-3 h, the absorption in the UV and visible regions are observed to red shift from 255 to 262 nm and 402 to 413 nm, respectively associated with an increase in their absorbance. Any prolonged heating, did not result in any shift in the absorption maximum (Fig. 5.6B). Therefore, the heating time of reaction mixture was kept to be 3 h.

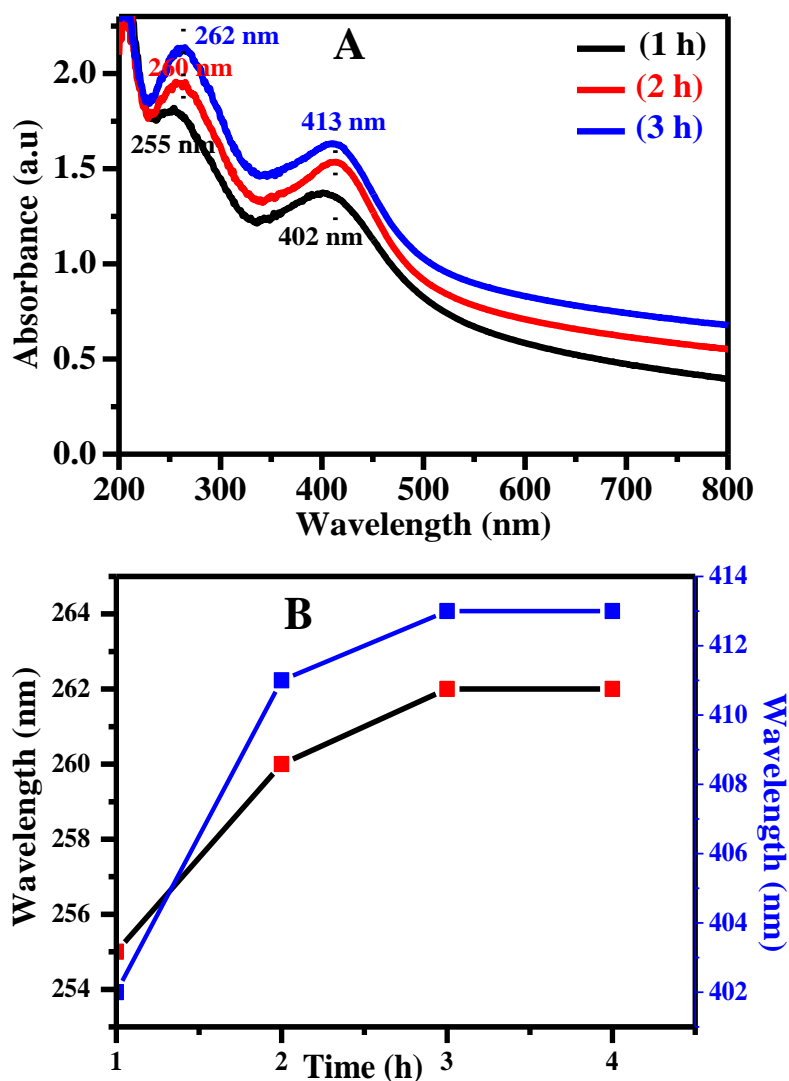


Fig. 5.6: Changes in the absorption peak of reaction mixture containing glycine, GO and Ag^+ at pH 10.5 as a function of heating time – (panel A). Shift in the absorption maxima of GO and plasmonic band due to Ag NPs with the time of heating – (panel B).

5A.2.3 Synthesis of N-doped Graphene-Ag Nanocomposites under Optimized Reaction Conditions

For the synthesis of N-doped graphene-Ag nanocomposites using above mentioned optimized conditions, 52 mg of glycine (34.6 mM) was mixed with 20 ml of GO dispersion containing 10 mg of GO (0.5 mg/ml) followed by the addition of 2 mg of AgNO₃ (0.59 x 10⁻³ M) under stirring and the pH of this solution was maintained at 10.5. The resulting reaction mixture was heated for 3 h on water bath at 95 °C. The resultant black solution was centrifuged and washed with DIW from five to six times in order to remove any residual glycine. The product thus obtained was re-dispersed in DIW maintaining the pH of the solution at 10.5 and is denoted as GRH-GlyAg.

For the comparison purpose, the control experiment was performed in the absence of reducing agent under the similar experimental conditions. In brief, 2 mg of AgNO₃ was mixed with 20 ml of GO dispersion containing 10 mg of GO (0.5 mg/ml) and the pH of the solution was maintained at 10.5 and heated for 3 h at 95 °C. This sample has been denoted as GO-Ag. In other control experiment bare Ag NPs was also synthesized following the similar procedure as mentioned above in the absence of GO and it has been denoted as Gly-Ag.

5A.2.4 Electrochemical Measurements

The GCE electrodes were polished sequentially by making slurry from alumina powder of size 1 μm followed by 0.5 and 0.03 μm using microcloth pad. The electrodes were rinsed thoroughly in an ultrasonic bath sequentially using DIW and ethanol for about 10-15 min, respectively. GCE electrodes were then dried under the flow of N₂. GRH-Gly and GRH-GlyAg dispersions were prepared by suspending them in DMF (0.5 mg/mL) by ultrasonication for about 20-30 min. These homogeneously prepared solutions (6 μL) were drop-casted repeatedly in the aliquot of 2 μL after drying each time onto the surface of GCE electrode. The electrode surfaces were then allowed to dry overnight at room temperature.

The loading mass on the working electrodes were estimated to be (0.042 mg/cm²). All electrochemical measurements were performed at room temperature in 2 M KNO₃ as an aqueous supporting electrolyte. The electrolyte was purged strongly with N₂ for about 5 min in order to remove any dissolved oxygen prior to performing electrochemical measurements.

5A.2.5 SERS Measurements

The SERS activity of GRH-GlyAg nanocomposites was measured by using 4-aminothiophenol (4-ATP) as a probe molecule. 50 µl of the as-synthesized GRH-GlyAg (1 mg/ml) in ethanol was taken and it was mixed with the different concentrations of 4-ATP ($1 \times 10^{-3} - 5 \times 10^{-8}$ M) to make the total volume of 200 µl. The resultant mixture was shaken for 1 h and was allowed to equilibrate for 3 h. In a control experiment a typical concentration of 4-ATP (1×10^{-7} M) was adsorbed on GRH-Gly and bare Ag NPs by using the same procedure as was adopted for the adsorption of the 4-ATP on GRH-GlyAg. An aliquot of about 10 µl of these solutions was applied on the glass plate and dried prior to recording the Raman spectra.

5A.3 Characterization of N-doped Graphene (GRH-Gly) and N-doped Graphene-Ag (GRH-GlyAg) Nanocomposites

The as-synthesized GRH-Gly and GRH-GlyAg nanocomposites have been analyzed by using a number of characterization techniques *viz.* UV-Vis, zetasizer, XRD, Raman, AFM, FESEM, TEM, FTIR, XPS, ¹³C NMR, TGA, I-V and CV and details of these investigations are described below:

5A.3.1 Optical Studies

Optical absorption spectra of GO, N-doped graphene (GRH-Gly) and Ag coated N-doped graphene (GRH-GlyAg) are shown in Fig. 5.7. The optical absorption spectrum due to GO exhibit the peaks at 230 and 301 nm corresponds to π - π^* and n - π^* transitions, respectively (Fig. 5.7a). On the other hand, the reduction of GO using glycine in the absence of Ag⁺ at pH 10.5 (GRH-Gly) shows a red shifted

peak at 263 nm indicating the restoration of graphitic character (Fig. 5.7b). The GRH-GlyAg nanocomposites were obtained by the reduction of GO in the presence of Ag^+ using glycine as a reducing agent at pH 10.5. For GRH-GlyAg, the development of peak in UV region (262 nm) along with the peak in visible region (413 nm) has been assigned to the simultaneous reduction of GO to graphene and plasmonic absorption arising due to the formation of Ag NPs, respectively (Fig. 5.7c). The digital images of GO, GRH-Gly and GRH-GlyAg exhibiting a change in color from yellowish-brown to black in case of the later two samples are shown in the inset of Fig. 5.7.

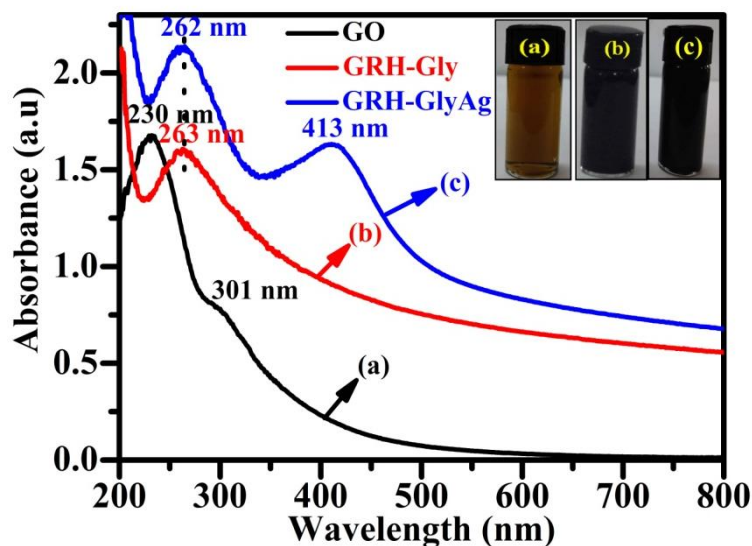


Fig. 5.7: Optical absorption spectra of GO (a), GRH-Gly (b) and GRH-GlyAg (c) along with their digital images (inset).

The stability of as-synthesized nanocomposites was revealed by performing the DLS measurement in which the value of ζ -potential was found to be -49.6 mV (Fig. 5.8). It suggests the fairly high stability of GRH-GlyAg nanocomposites.

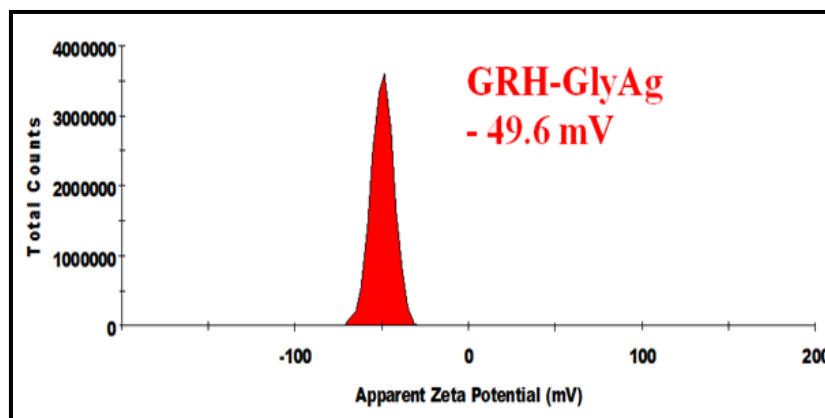


Fig. 5.8: ζ -potential of GRH-GlyAg in aqueous medium.

5A.3.2 XRD Studies

Fig. 5.9 presents the XRD patterns of GO, GRH-Gly and GRH-GlyAg. The XRD pattern of GO shows peaks at 10.14° and 42.34° with the 'd' spacing of 0.872 and 0.214 nm, which corresponds to the reflection from (002) and (100) planes, respectively. This is very similar to the data reported previously for GO [257,281]. XRD pattern of GRH-Gly shows relatively broader peaks with high and low intensities at 2 theta values of 25.5° and 42.70° with the 'd' spacing of 0.349 and 0.212 nm corresponding to the reflection from (002) and (100) planes, respectively matching with the previous reports on N-doped graphene [405]. On the other hand, the GRH-GlyAg shows a broad peak along with several sharp peaks at 2 theta values of 24.55° , 38.13° , 44.27° , 64.51° , 77.46° and 81.68° analogous to the (002) plane of graphene and (111), (200), (220), (311) and (222) planes of Ag NPs matching to the face-centered cubic (fcc) structure (JCPDS card no. 04-0783) with the 'd' spacing values of 0.362, 0.236, 0.205, 0.144, 0.123 and 0.118 nm, respectively [347]. Using the Scherrer equation [375], the average crystallite size of Ag NPs was determined to be about 17 nm from the two highest intense reflections.

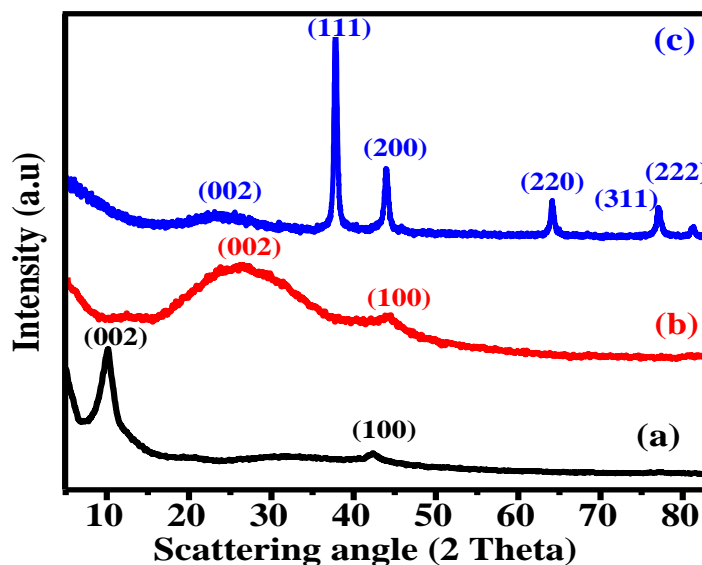


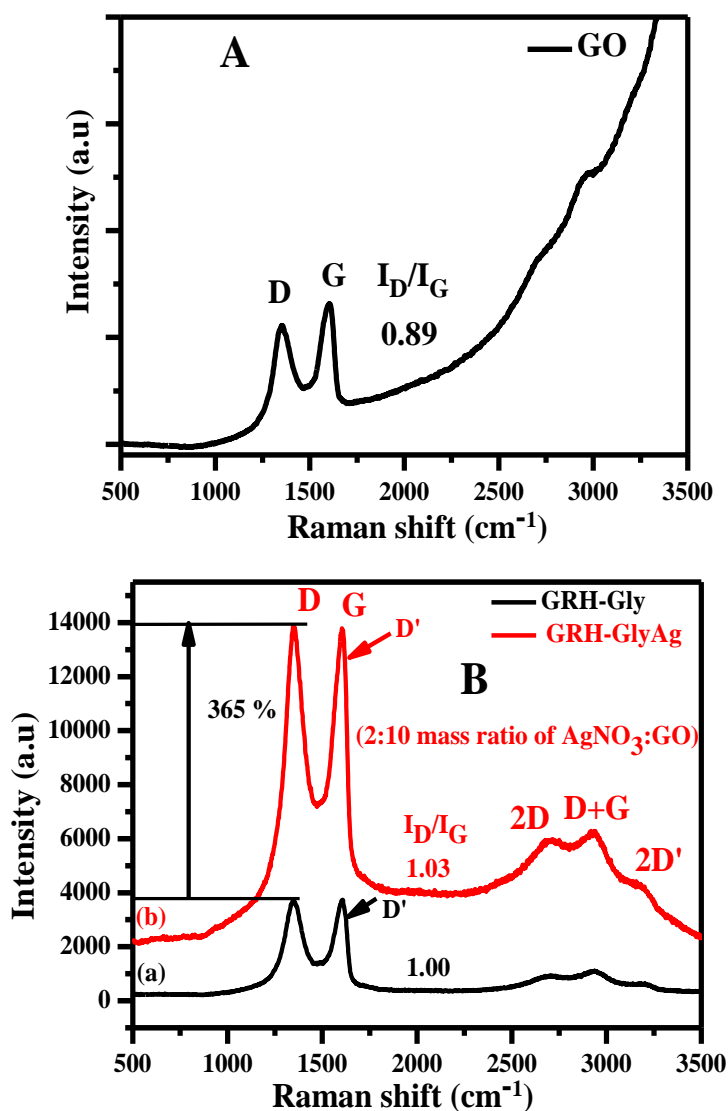
Fig. 5.9: XRD patterns of GO (a), GRH-Gly (b) and GRH-GlyAg (c).

5A.3.3 Raman Spectroscopy

Raman spectroscopy was used to study the electronic structures of GO, GRH-Gly and GRH-GlyAg (Fig. 5.10). Their spectral data have been summarized in Table 5.1. The Raman spectrum of GO is shown in Fig. 5.10A. It exhibits typical D and G bands at 1354 and 1605 cm^{-1} similar to those observed previously [383] and its I_D/I_G ratio was worked out to be 0.89. The Raman spectrum of GRH-Gly also exhibited D and G bands at 1349 and 1604 cm^{-1} , respectively along with an additional D' band at 1623 cm^{-1} (Fig. 5.10B-a) possibly arising due to the doping of N. Moreover, in this case the I_D/I_G ratio is increased to 1.00 as compared to that of GO (0.89) similar to those observed earlier for N-doped graphene [318,324]. The increase in the I_D/I_G ratio for GRH-Gly suggests the effective reduction of GO accounting for the increased number of smaller sp^2 domains.

The Raman spectrum of the optimized GRH-GlyAg sample as was arrived by optical absorption spectroscopy for the mass ratio of 2:10 (AgNO_3 :GO) was recorded in Fig. 5.10B-b. It shows that the peak intensities of D and G bands are enhanced by about 365 % as compared to that of GRH-Gly upon decoration with Ag NPs. It also exhibited the D' band at 1623 cm^{-1} , suggesting the effective doping of N has taken place in GRH-GlyAg similar to

that of GRH-Gly (Fig. 5.10C). A further increase in the I_D/I_G ratio for this sample (1.03) suggests the increased defects formation on the surface of GRH-Gly upon the decoration by Ag NPs. This aspect was further probed by calculating the in-plane crystallite size (L_a in nm) which comes out to be 20.18, 16.75 and 16.26 nm for GO, GRH-Gly and GRH-GlyAg, respectively. The value of L_a follows the order: GO > GRH-Gly > GRH-GlyAg supporting the increased defects formation upon doping of N and its further functionalization by Ag. These features suggest the effective reduction of GO/Ag⁺ to GRH-GlyAg under these conditions, as has also been observed earlier for N-doped graphene decorated by Ag using other reducing agents [359,406].



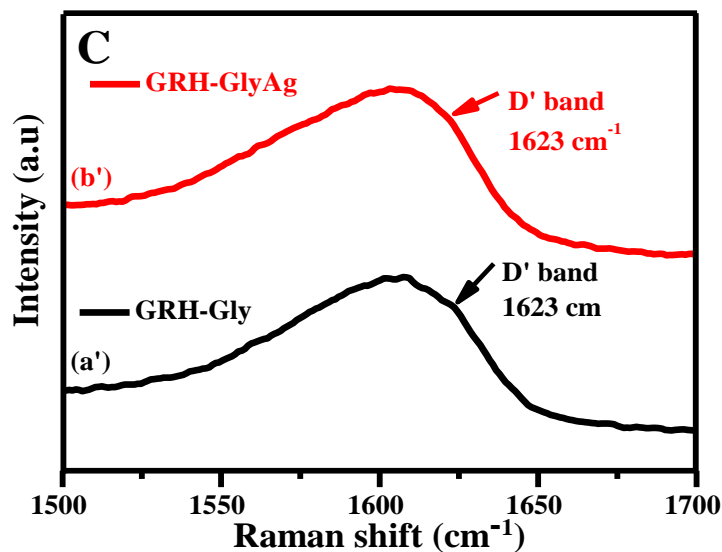


Fig. 5.10: Raman spectra of GO – (panel A); GRH-Gly (a) and GRH-GlyAg (b) – (panel B); expanded D' band of: GRH-Gly (a') and GRH-GlyAg (b') in the wavenumber range of 1500-1700 cm^{-1} – (panel C).

Table 5.1: Raman spectral data of GO, GRH-Gly and GRH-GlyAg.

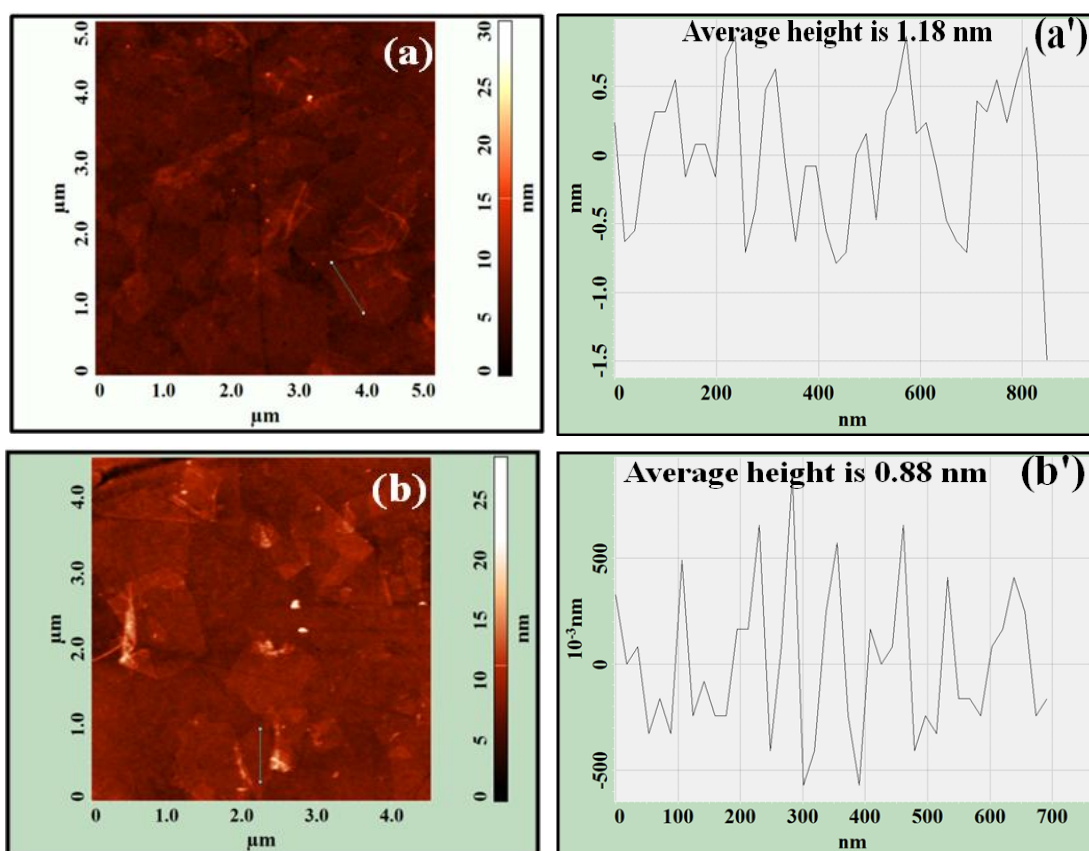
Sample(s)	D band (cm^{-1})	G band (cm^{-1})	I_D/I_G
GO	1354	1605	0.89
GRH-Gly	1349	1604 (D' 1623)	1.00
GRH-GlyAg	1351	1606 (D' 1623)	1.03

5A.3.4 AFM Analysis

The surface topography of the precursor GO and the products, GRH-Gly, and GRH-GlyAg, was examined by AFM and their 2D images are shown in Fig. 5.11. The surface roughness of GO sheet along a particular line marked in its 2D image (Fig. 5.11a) was found to be 1.18 nm, which has been reported previously corresponding to single-layer [290]. On the other hand, the average surface height of GRH-Gly sheet along a particular marked line as well as from several other locations on this sheet was computed to be 0.88 ± 0.15 nm (Fig. 5.11b), which is smaller than that of GO. This decrease in average surface height is attributed to the removal of functionalities from the surface of GO. It may be noted that the

surface heights for GO and GRH-Gly were recorded at the locations, where the folding was not apparent.

The AFM image of GRH-GlyAg shows that the entire GRH-Gly sheet is uniformly decorated by Ag NPs and the average particle size (size distribution) of Ag NPs over the entire graphene sheet was estimated to be 18 nm (10-32 nm) (Fig. 5.11c). For a typical case, the surface height along a particular line marked in Fig. 5.11c, where Ag NPs were present in a continuous array shows the average size of Ag NPs to be 16 nm (Fig. 5.11c'). Moreover, the nature of graphene sheet seems to be modified in GRH-GlyAg upon the decoration of Ag NPs since its folding is not apparent unlike to the bare graphene sheet in GRH-Gly. It suggests that the binding of Ag NPs does not allow the folding of the graphene sheet.



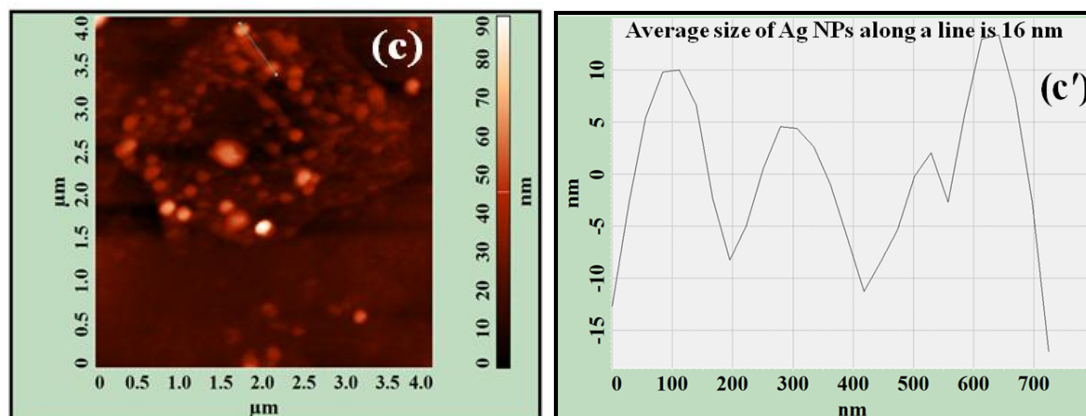
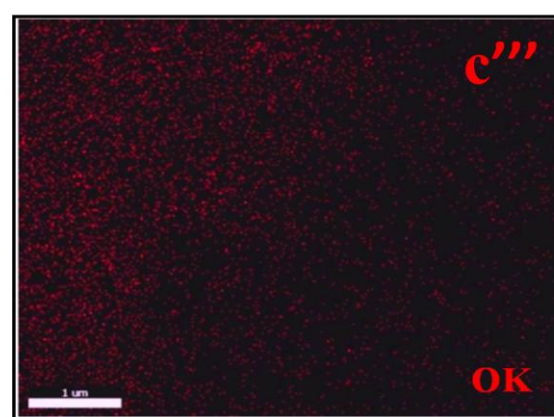
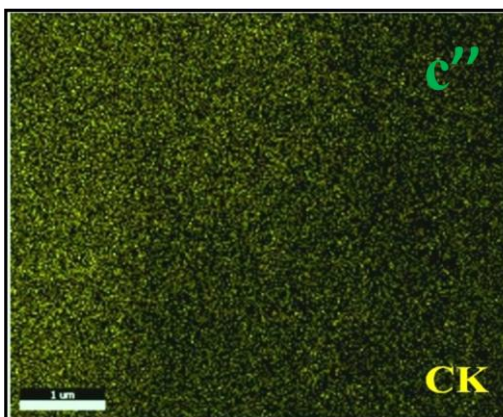
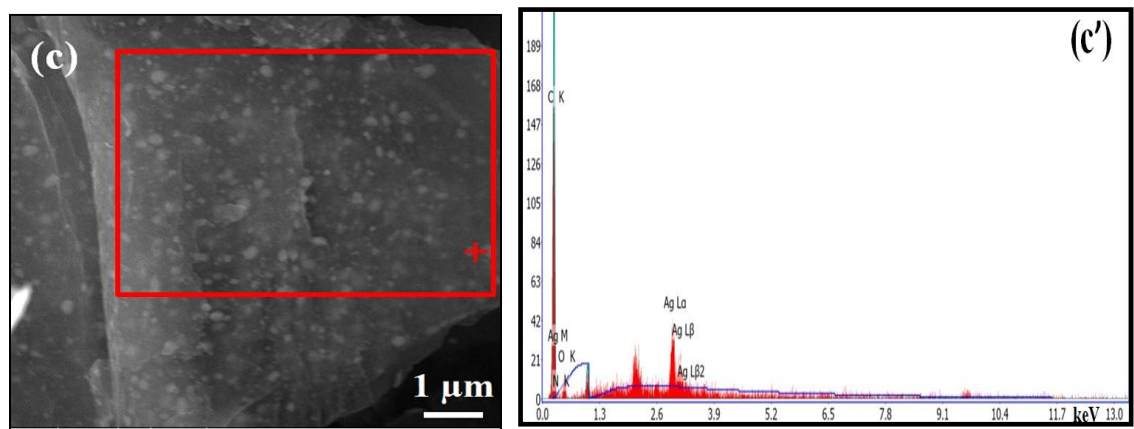
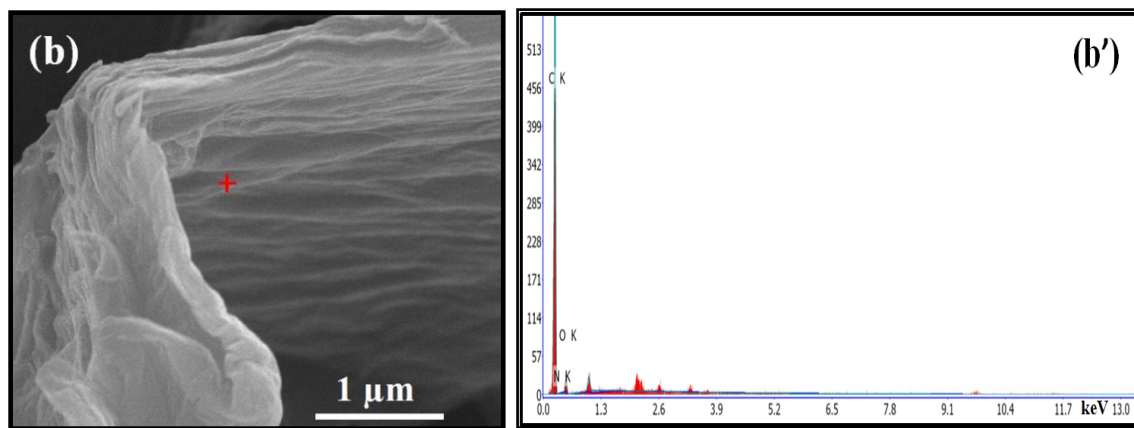
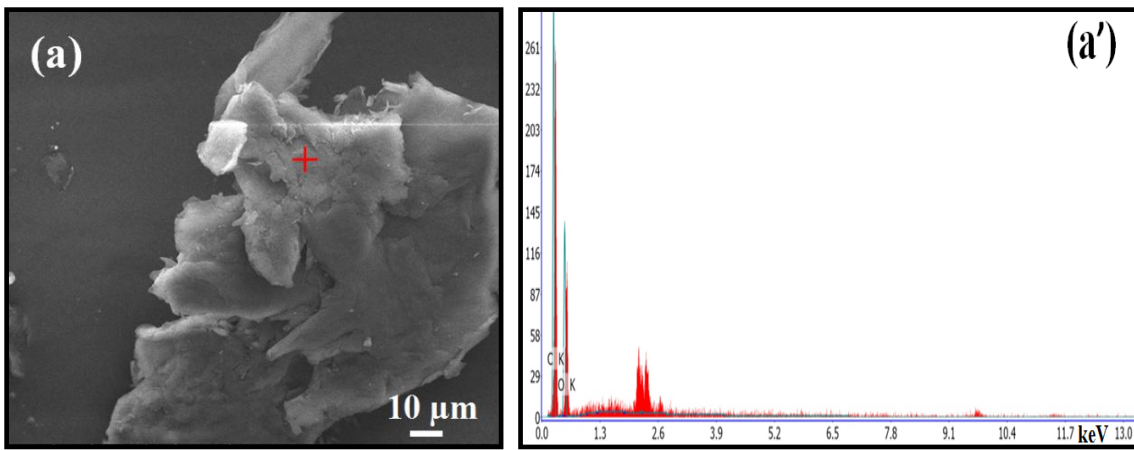


Fig. 5.11: AFM images and their height profile along a particular line: GO (a and a'), GRH-Gly (b and b') and GRH-GlyAg (c and c'), respectively.

5A.3.5 FESEM Analysis

The morphologies of GO, GRH-Gly and GRH-GlyAg were further examined by FESEM analyses (Fig. 5.12). EDAX spectra of the FESEM image(s) were recorded at the location(s) marked by (+) sign in red. FESEM image of GO indicates it to contain aggregated sheets consisting of C and O elements (Fig. 5.12a and a'). FESEM image of GRH-Gly exhibits relatively a very thin and crumpled sheet and its EDAX analysis shows the presence of N apart from C and O (Fig. 5.12b and b'). On the other hand, the FESEM image of GRH-GlyAg exhibits fairly high density of spherical Ag NPs on the surface of GRH-Gly sheet (Fig. 5.12c). Its EDAX analysis shows the presence of C, N, O along with the presence of Ag in GRH-GlyAg (Fig. 5.12c'). The elemental mapping of a portion of this sheet indicated by the red square in this image shows the homogeneous distribution of C, N, O along with Ag. These results clearly support the uniform distribution of Ag NPs on the graphene sheet in GRH-GlyAg.



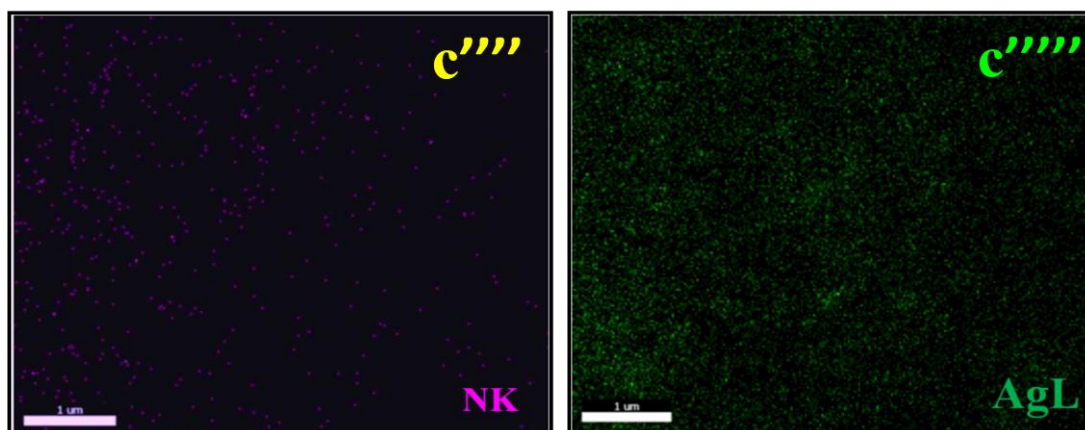
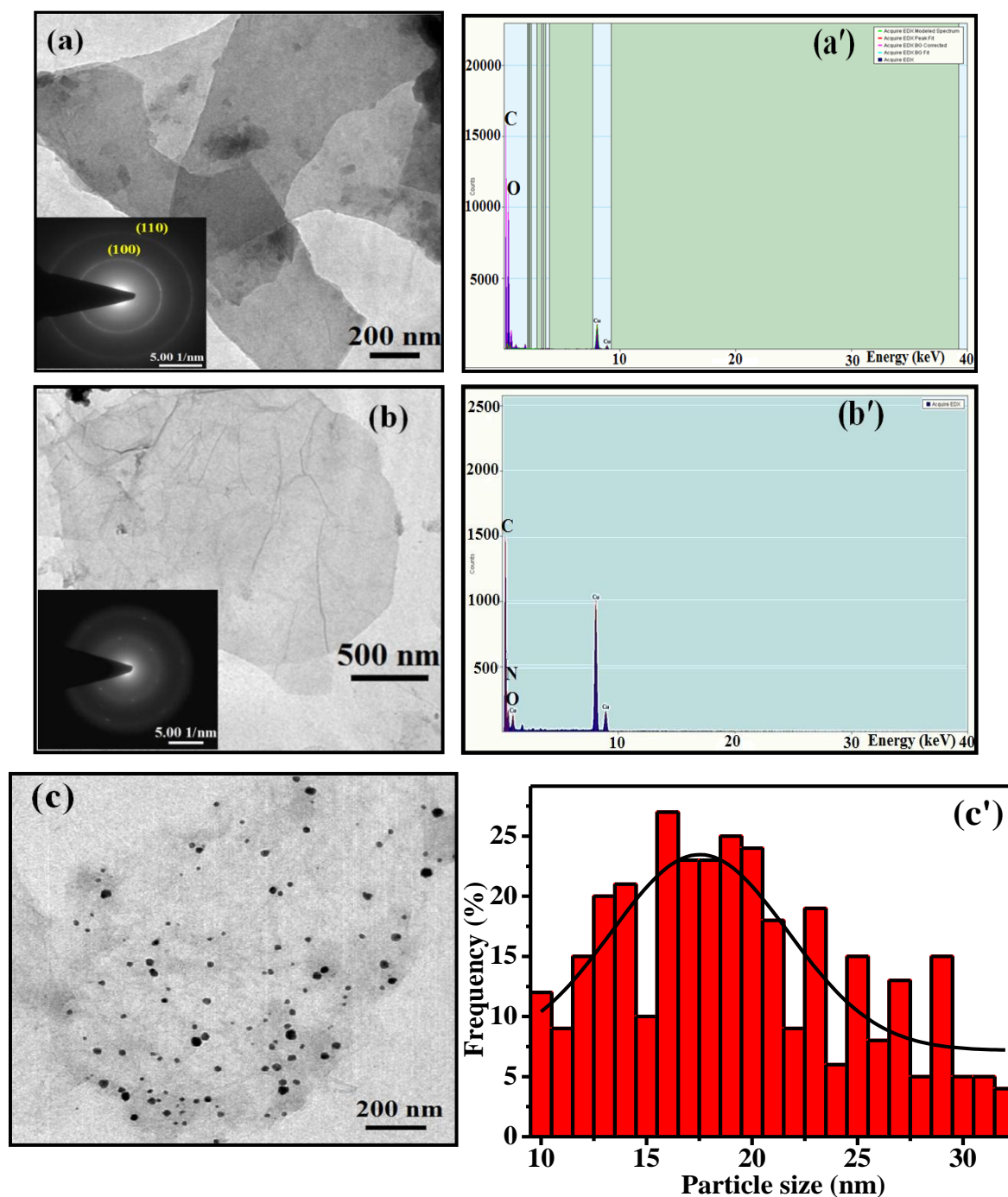


Fig. 5.12: FESEM and EDAX images of GO (a and a'), GRH-Gly (b and b') and GRH-GlyAg (c and c'), respectively. Elemental mapping images of GRH-GlyAg showing: C (c"), O (c'''), N (c''''') and Ag (c''''') elements.

5A.3.6 TEM and SAED Analysis

TEM images of GO, GRH-Gly and GRH-GlyAg along with their SAED patterns and EDAX analyses are shown in Fig. 5.13. TEM images of these samples exhibit sheet-like structure (Fig. 5.13a, b and c). GO sheets appeared to be relatively thicker (Fig. 5.13a) as compared to that of GRH-Gly (Fig. 5.13b). Whereas, GRH-Gly, sheet shows wrinkles and folding at various locations (Fig. 5.13b). On the other hand, TEM image of GRH-GlyAg exhibits the surface of the sheet without folding and wrinkles, which is uniformly decorated with Ag NPs (Fig. 5.13c). The average particle size of Ag NPs (size distribution) on the surface of GRH-Gly sheet was estimated from various such images prepared at different times and found to be 17.5 nm (10-32 nm) (Fig. 5.13c'). SAED pattern of GO exhibits the ring pattern displaying polycrystallinity (Fig. 5.13a-inset). Whereas, the SAED pattern of GRH-Gly clearly shows it to be crystalline with six-fold symmetry (Fig. 5.13b-inset). On the other hand, the SAED pattern of GRH-GlyAg also exhibits ring pattern with bright spots displaying polycrystallinity corresponding to the (111), (200), (220), (311), (222) and (420) planes matching to the fcc structure of Ag NPs (JCPDS file no. 04-0783) (Fig. 5.13c''). From HRTEM image of GRH-GlyAg, the 'd' spacing was calculated to be 0.236 nm which matches to the most intense reflection from (111) plane of Ag NPs matching to the fcc

structure (Fig. 5.13c'''). EDAX analyses of these samples clearly shows the presence of C and O in GO; C, O, and N in GRH-Gly and C, O, N and Ag in case of GRH-GlyAg (Fig. 5.13a', b' and c''').



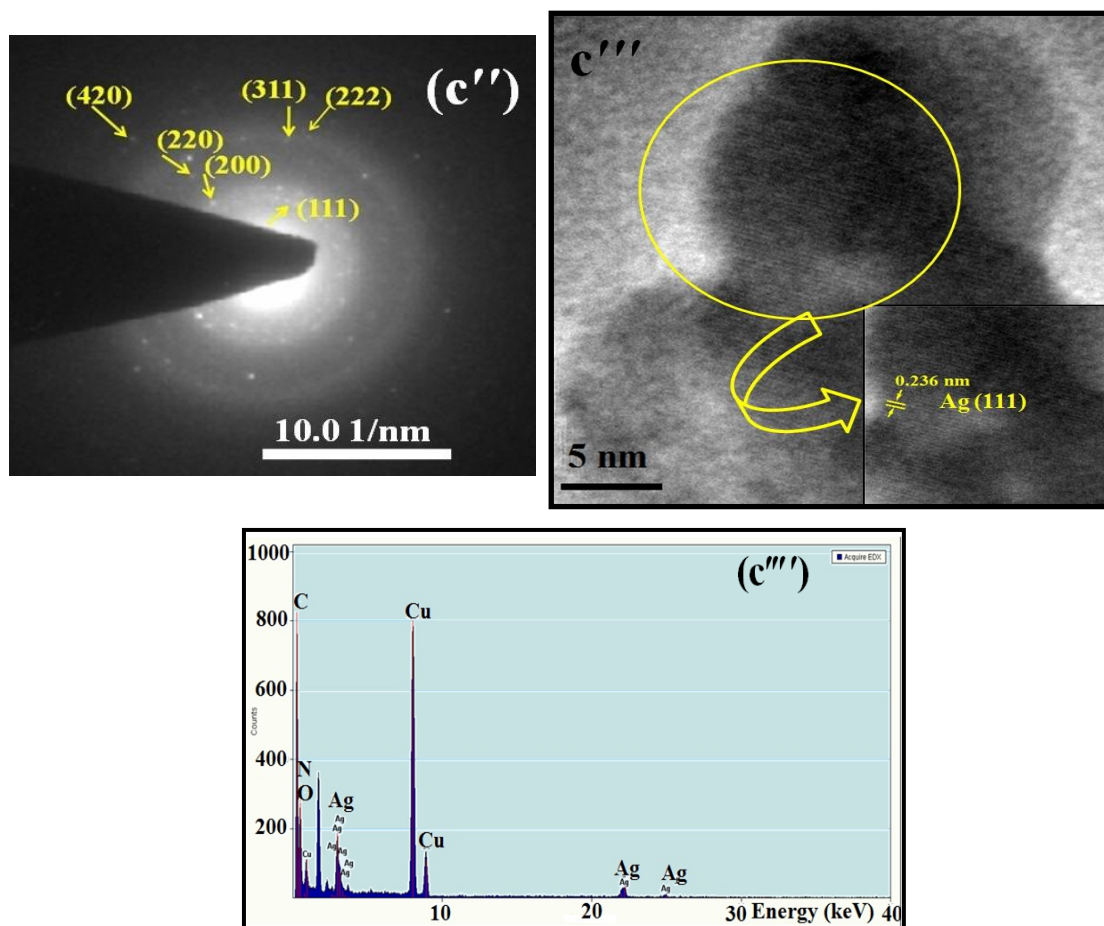


Fig. 5.13: TEM images and EDAX analyses of GO (a and a') and GRH-Gly (b and b') along with their SAED patterns in the inset, respectively. TEM micrograph, particle size distribution and SAED pattern of GRH-GlyAg (c, c' and c''); HRTEM image of GRH-GlyAg (c''') and its magnified image showing a 'd' spacing corresponding to Ag (111) plane (c'''-inset); EDAX analysis of GRH-GlyAg (c''').

5A.3.7 FTIR Spectroscopy

FTIR spectra of GO, GRH-Gly and GRH-GlyAg are shown in Fig. 5.14. The various prominent vibrational bands (cm^{-1}) for GO were observed at 3435, 2925, 2853, 1730, 1629, 1382, 1221 and 1054, which have been assigned to $-\text{OH}$ stretching, symmetrical and unsymmetrical C-H stretching, C=O (carboxylic), C=C, C-OH stretching/deformation, C-O-C (epoxy) and C-O (alkoxy) functionalities, respectively and matches to the previously reported data on GO [284]. The reduction of GO into GRH-Gly results in the reduction of intensity of vibrational band due to $-\text{OH}$ stretching. It also results in the complete disappearance of the peaks due to C=O and C-O-C functionalities (panels A and B). However, the peaks due to C-O and C-OH become fairly weak and broad. Furthermore, a

weaker and less intense bands due to $-\text{CH}$ stretching were observed as compared to that for GO, which might have occurred due to the doping of N as also has been noted previously [407]. The doping of N is further indicated by the appearance of a new broad peak in the vicinity of 1580 cm^{-1} , which is likely to arise from co-contribution of both aromatic $\text{C}=\text{C}$ and $-\text{N}-\text{H}$ bending. Apart to this, a weak and broad peak is also observed at 1340 cm^{-1} , which has been assigned to $\text{C}-\text{N}$ stretching. The *in situ* generation of Ag NPs on the surface of GRH-Gly (GRH-GlyAg) does not bring any change in the vibrational spectrum of GRH-Gly, except that a broad peak due to $\text{C}=\text{C}$ stretching, the band due to $-\text{N}-\text{H}$ bending and $\text{C}-\text{N}$ stretching are slightly shifted to lower wavenumber (cm^{-1}) from 1629 to 1621 , 1580 to 1573 , and 1340 to 1280 - 1245 , respectively.

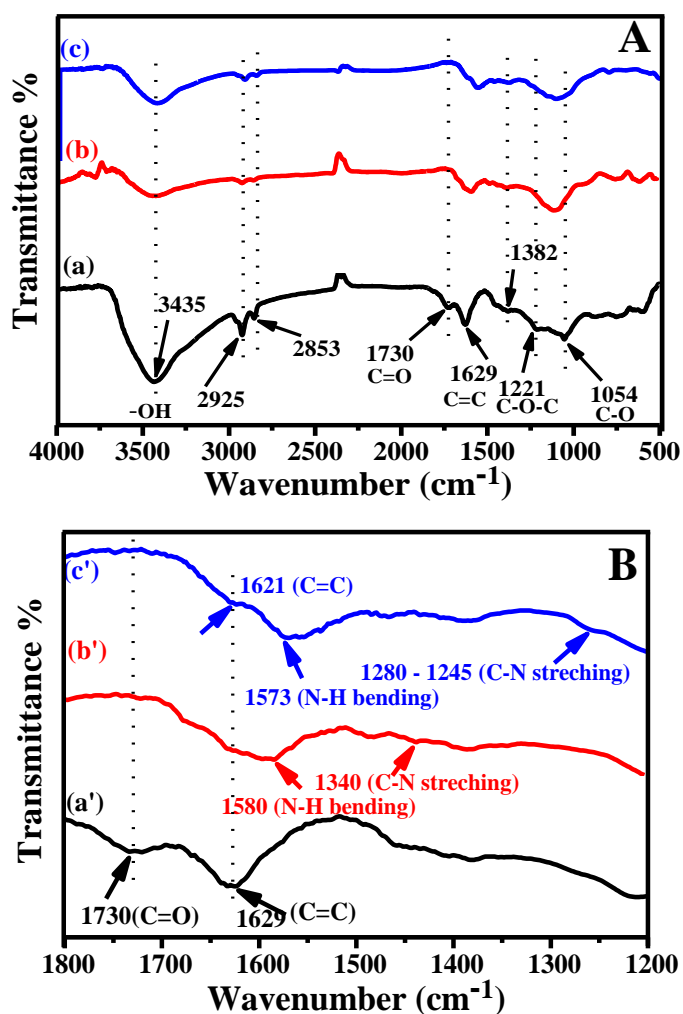


Fig. 5.14: FTIR spectra of: GO (a), GRH-Gly (b) and GRH-GlyAg (c) – (panel A); expanded FTIR spectra of: GO (a') GRH-Gly (b') and GRH-GlyAg (c') in the range of 1800 - 1200 cm^{-1} – (panel B).

5A.3.8 Solid-State ^{13}C NMR Spectroscopy

The reduction of GO and doping of N into GRH-Gly and GRH-GlyAg was also examined by using solid-state ^{13}C MAS NMR spectroscopy (Fig. 5.15). The ^{13}C spectrum of GO exhibits various peaks at about 61, 70, 105, 115, 129, 167 and 190 ppm, which have been assigned to epoxy (C-O-C), C-OH (^{13}C nuclei in hydroxyl), sp^2 carbon with graphitic structure in different environments, carbonyl carbon of ester (O-C=O) and ketonic carbon (C=O), respectively which is very similar to the previous reports [253,324]. Interestingly, in GRH-Gly sample, the functionalities like C-O-C is completely eliminated and the peak due to C-OH functionality is significantly reduced along with its broadening. The graphitic sp^2 carbon peaks has now become more intense, broadened and up-shifted. It suggests an increase in the graphitic nature of the GRH-Gly as observed earlier [253]. The ^{13}C NMR spectrum of GRH-GlyAg remains unchanged except that the sp^2 carbon peak has further shifted to upfield and broadened, which clearly indicates that the sp^2 character is further increased in GRH-GlyAg. As a matter of fact, a new peak was developed in both the samples (GRH-Gly and GRH-GlyAg) at about 172 and 174 ppm, respectively which is attributed to the formation of imine (C=N) functionality as reported earlier [408].

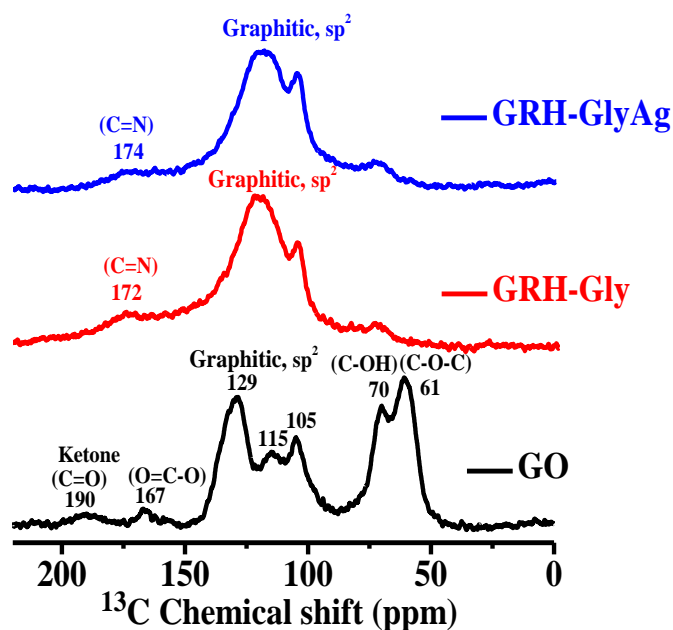
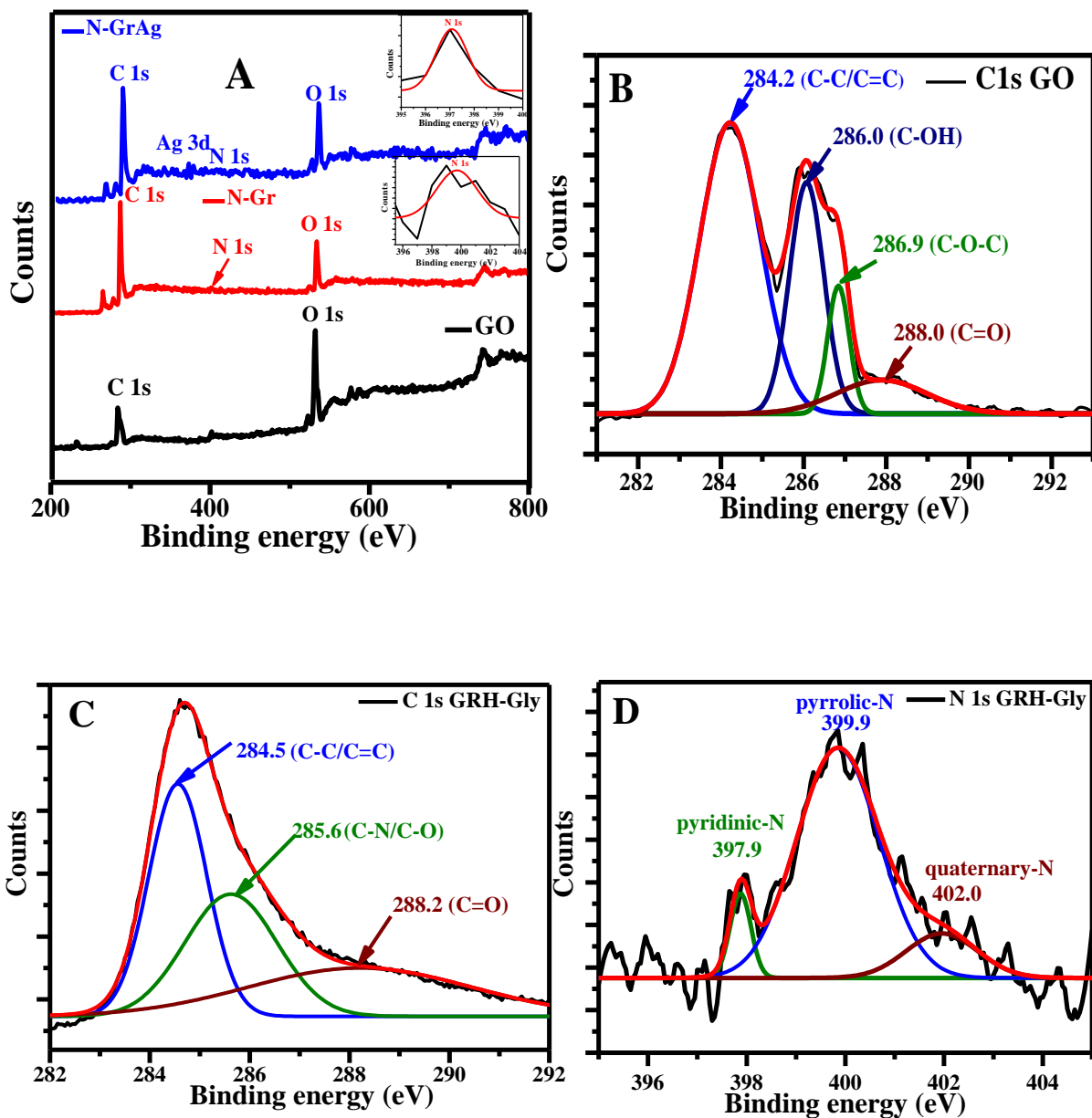


Fig. 5.15: Solid-state ^{13}C NMR spectra of GO, GRH-Gly and GRH-GlyAg.

5A.3.9 XPS Measurements

The surface analyses of GO, GRH-Gly and GRH-GlyAg nanocomposites were performed by using XPS (Fig. 5.16). The survey scans of these samples in the range of 200-800 eV are presented in Fig. 5.16A indicating the presence of C 1s and O 1s in GO; C 1s, N 1s and O 1s in GRH-Gly; C 1s, N 1s, O 1s and Ag 3d in GRH-GlyAg. The high resolution C 1s spectrum for GO, C 1s and N 1s spectra for GRH-Gly and C 1s, N 1s and Ag 3d for GRH-GlyAg are shown in Fig. 5.16B-G. The C 1s spectrum of GO depicts four deconvoluted peaks (eV) at 284.2, 286.0, 286.9 and 288.0 which have been assigned to C-C/C=C (sp^3/sp^2 carbon), C-OH, C-O-C (epoxy) and C=O (carboxylic) groups, respectively (Fig. 5.16B). On the other hand, the C 1s spectrum of GRH-Gly is deconvoluted into three different components of carbon at binding energies (eV) of 284.5, 285.6 and 288.2 corresponding to C-C/C=C, C-N (carbon singly bonded to nitrogen) and C=O, respectively (Fig. 5.16C). Interestingly, a new peak is observed in GRH-Gly at 285.6 eV (Fig. 5.16C) which is slightly shifted to lower binding energy than to that of GO (286.0 eV) (Fig. 5.16B) and may be assigned to C-N. However, it is difficult to isolate the presence of C-O/C-N at this binding energy as these binding energies are fairly close [359]. The N 1s spectrum of GRH-Gly has been deconvoluted into three components of N: pyridinic-N (397.9 eV), pyrrolic-N (399.9 eV) and quaternary-N (402.0 eV) (Fig. 5.16D). It is apparent from the area under these peaks that the major component among these N moieties corresponded to the pyrrolic-N. The high resolution C 1s spectrum of GRH-GlyAg also exhibits three different components of carbon at (eV): 284.5, 285.7 and 288.0 very similar to that observed in GRH-Gly (Fig. 5.16E). N 1s spectrum of this sample also exhibited three different components of N: pyridinic-N (398.5 eV), pyrrolic-N (400.0 eV) and quaternary-N (401.7 eV), but the binding energies corresponding to pyridinic and pyrrolic-N were slightly shifted to higher energies as compared to that present in case of GRH-Gly (Fig. 5.16F). For this sample also the major component corresponded to the pyrrolic-N. Ag 3d doublet spectrum

for GRH-GlyAg is shown in panel G. It shows two peaks at 368.4 and 374.4 eV which could be assigned to characteristic Ag 3d doublet corresponding to Ag 3d_{5/2} and Ag 3d_{3/2}, respectively (Fig. 5.16G). These peaks are present at slightly higher binding energies by about 0.5 eV as compared to that of bulk metallic Ag [359]. This shift to higher energies could be attributed to the binding of Ag to GRH-Gly. The elemental composition for GRH-GlyAg shows C (80.3 %), N (1.91 %), O (17.4 %) and Ag (0.309 %). This clearly indicates the doping/effective functionalization of graphene sheets by N and their decoration by the Ag NPs.



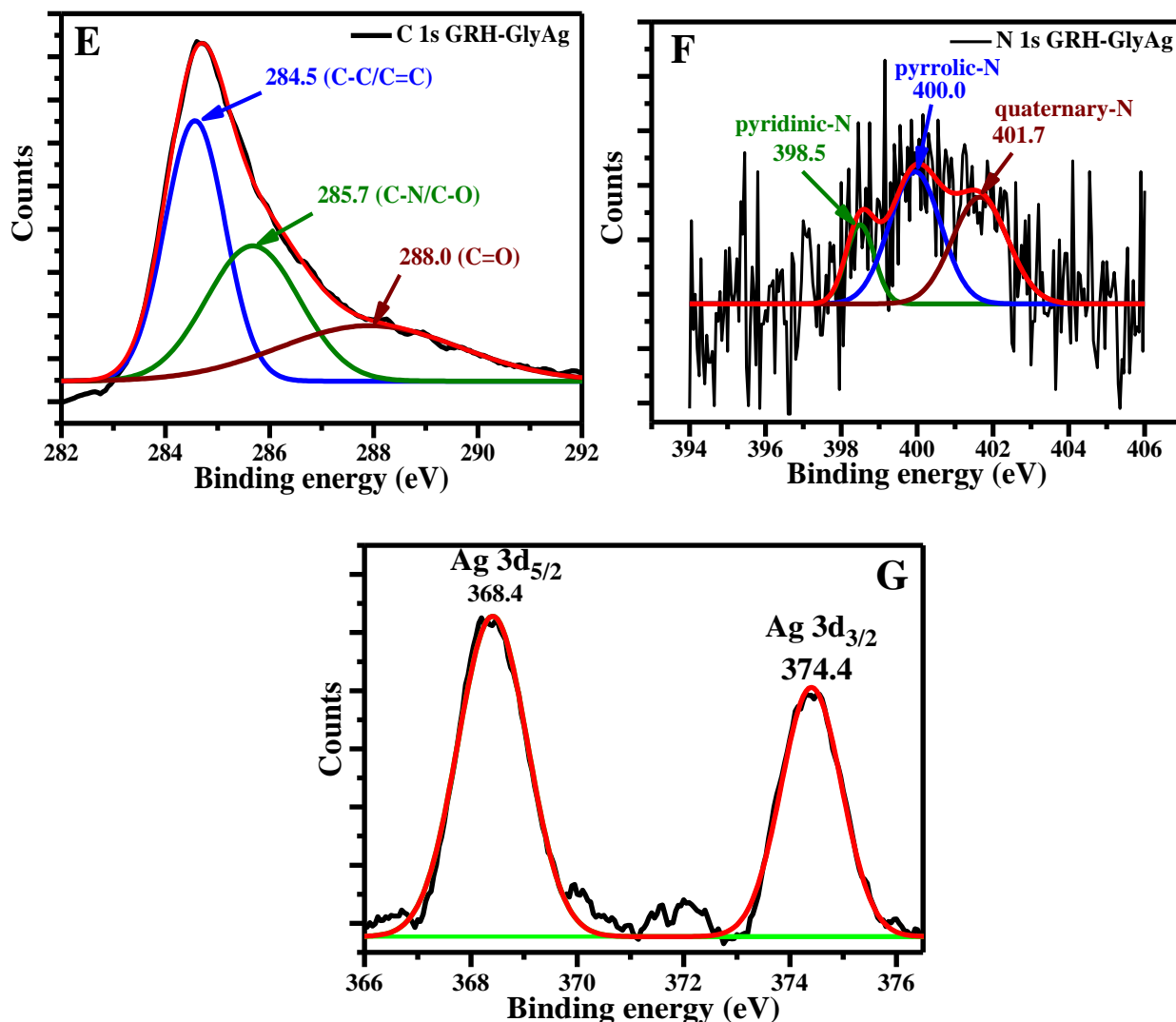


Fig. 5.16: XPS survey scans of GO (a), GRH-Gly (b) and GRH-GlyAg (c) – (panel A), N 1s of GRH -Gly and GRH-GlyAg (panel A-inset); C 1s spectrum of GO – (panel B); C 1s and N 1s spectra of GRH-Gly – (panels C and D); C 1s, N 1s and Ag 3d spectra of GRH-GlyAg – (panels E-G).

5A.3.10 TGA Measurements

The thermal stability of the precursor GO and the products, GRH-Gly and GRH-GlyAg, was examined by recording their TGA curves (Fig. 5.17). The TGA curve of GO exhibits 14% weight loss at about 100 °C, which is assigned to the removal of adsorbed water and the second major weight loss of 29% occurred at about 195 °C and has been attributed to the decomposition of labile oxygen functionalities such as carboxylic, anhydride and lactone groups as observed in previous report [391]. Whereas, in case of

GRH-Gly there is about 8% of weight loss at around 100 °C and only 14% of weight loss occurs at about 200 °C. The third slow but steady major loss started from about 430 °C, which was followed by a steep loss in weight up to 540 °C amounting to be about 90%. Thereafter, it becomes almost constant. The weight loss in this range corresponds to the removal of stable oxygen functionalities (phenols and carbonyl) [391]. Whereas, in case of GRH-GlyAg the weight loss at 100 and 200 °C are reduced to about 6 and 10%, respectively. In this case the third major weight loss started at about 430 °C and unlike GRH-Gly occurred up to 500 °C only, which has been estimated to be about 68%. These nanocomposites were found to be fairly stable up to 800 °C. It clearly shows that the as-synthesized nanocomposites are apparently more stable as compared to those of GO and GRH-Gly.

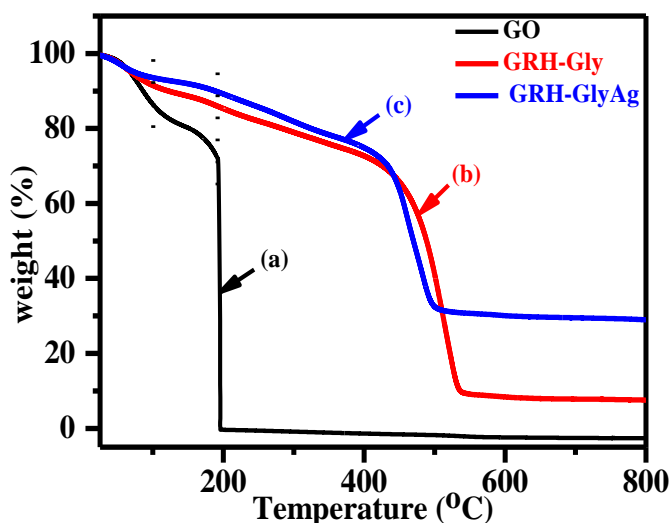


Fig. 5.17: TGA curves of GO (a), GRH-Gly (b) and GRH-GlyAg (c).

5A.3.11 I-V Studies

The I-V curves of GRH-Gly and GRH-GlyAg are presented in Fig. 5.18. These plots showed linearity over the entire voltage range (-1 to +1 V) suggesting them to follow the ohmic behavior. In case of GRH-Gly, a drastic increase in conductivity (11.4 S/cm) is observed as compared to that of GO (2.7×10^{-4} S/cm) (Chapter 4). This value is about four orders of magnitude higher as compared to that of GO and could be attributed to the

removal of the oxygen functionalities from its surface. The decoration of Ag NPs on the surface of GRH-Gly sheet (GRH-GlyAg) further enhances its conductivity to 25.9 S/cm which is more than two-fold higher to that of GRH-Gly. The increase in conductivity for GRH-GlyAg possibly arises due to the increased delocalization of the π electrons in the presence of Ag on GRH-Gly. It also prevents the aggregation of graphene sheet in GRH-GlyAg as is evident from its AFM/TEM images (Fig. 5.11 and 5.13), which might have contributed to its higher conductivity.

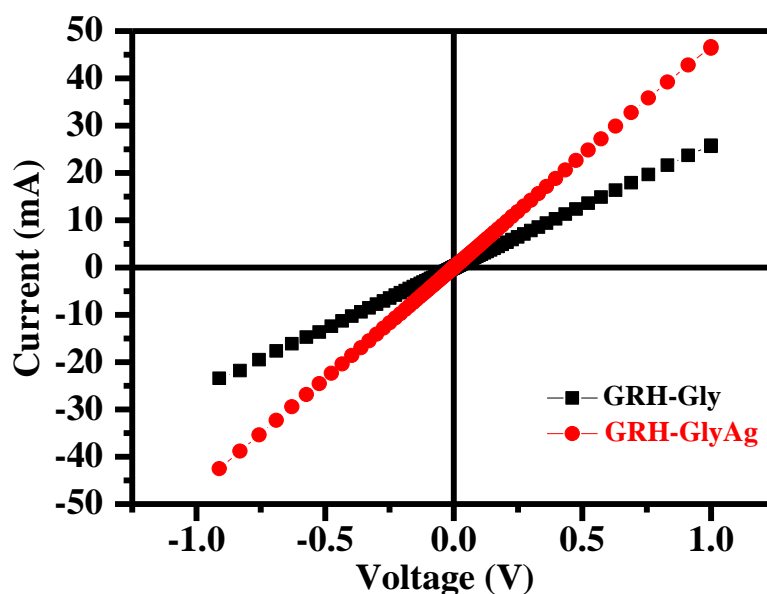


Fig. 5.18: I-V curves of GRH-Gly (black) and GRH-GlyAg (red).

5A.3.12 Electrochemical Measurements

The electrochemical behavior of GRH-Gly and GRH-GlyAg was analyzed by using cyclic voltammetry (CV) in 2 M KNO_3 as an aqueous supporting electrolyte (Fig. 5.19A). The CV measurements were recorded in the potential window of 0-0.8 V at a scan rate of 100 mV/s. GRH-Gly exhibits almost rectangular shape arising from electric double layer capacitance (EDLC) along with the contribution from pseudo-capacitance developed due to the different moieties of N (pyridinic/pyrrolic/quaternary). Whereas, in the case of GRH-GlyAg a pair of fairly well separated redox peaks were observed at 0.45 and 0.29 V corresponding to the anodic and cathodic peaks, respectively. A careful examination of this curve indicates that the anodic peak is relatively sharper than that of cathodic peak.

Moreover, these peaks are broad and asymmetrical which might be arising because of the existence of the multiple redox involving the interaction of Ag and GRH-Gly functionalities. From these curves, the specific capacitance (C_s in F/g) values for GRH-Gly and GRH-GlyAg were calculated to be 130 and 346, respectively. The C_s value for GRH-GlyAg (346 F/g) is more than 2.6 times higher as compared to that of GRH-Gly (130 F/g). Moreover, the observed value of C_s for GRH-GlyAg in the present case is much higher to that reported earlier for Ag/RGO (220 F/g) [356].

Electrochemical impedance spectroscopy (EIS) was performed to further analyze the resistance characteristic of GRH-Gly and GRH-GlyAg (Fig. 5.19B). The Nyquist plots (imaginary (Z'') Vs real (Z') component) for both the samples did not show any semi-circle in the high frequency region indicating the low resistance. However, a careful examination of these curves reveal that the GRH-Gly exhibit slightly higher resistance as compared to that of GRH-GlyAg in the higher frequency region. The low frequency region for both the samples exhibit linear curve variation with a steeper slope for GRH-GlyAg which suggest the faster ion transport diffusion for GRH-GlyAg. Thus, the curve for GRH-GlyAg displays good capacitive behavior in both the frequency regions.

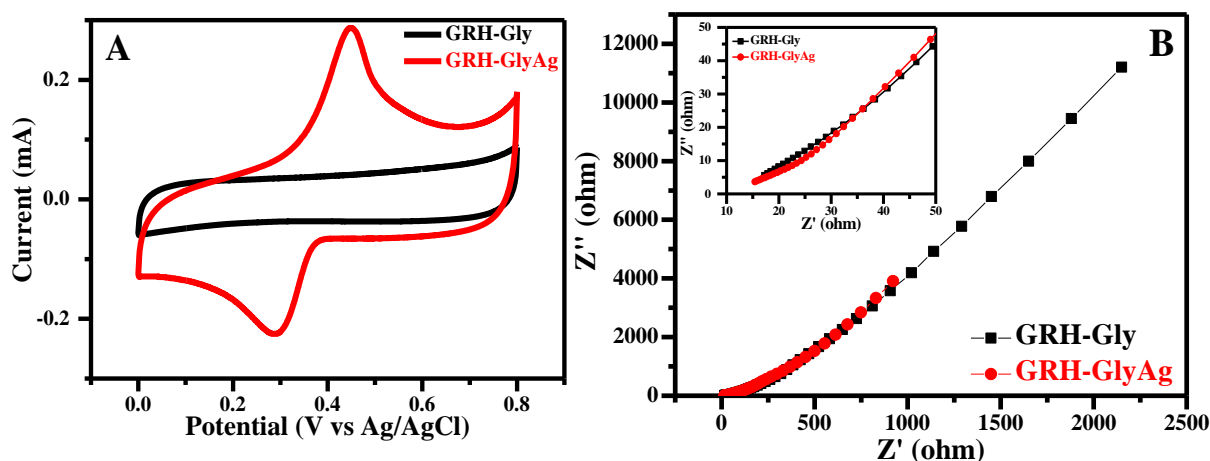
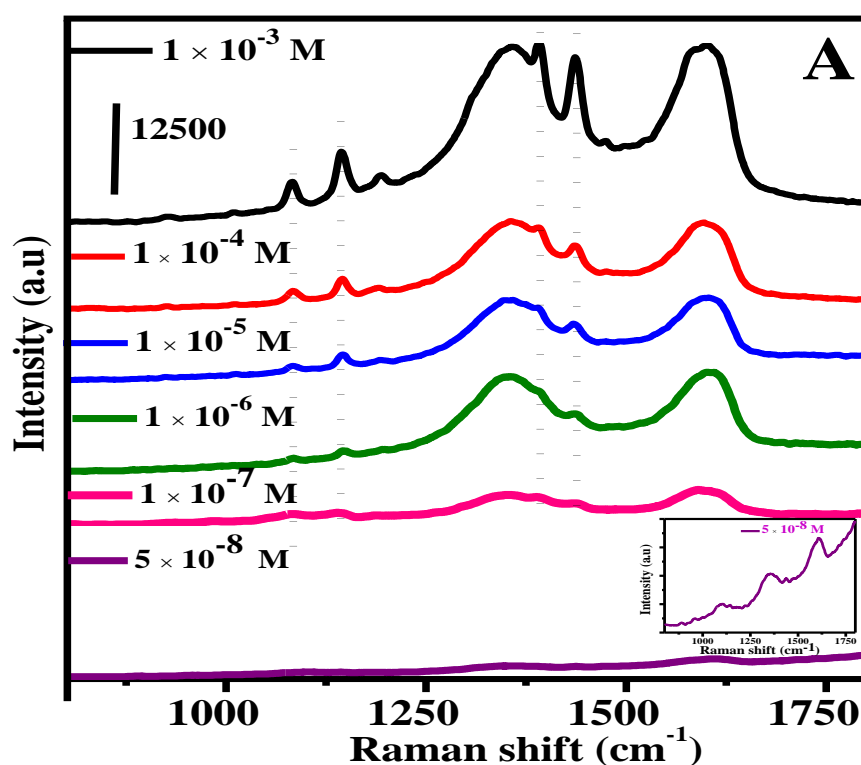


Fig. 5.19: CV curves of GRH-Gly and GRH-GlyAg at a scan rate of 100 mV/s in 2 M KNO_3 as an aqueous supporting electrolyte – (panel A). Nyquist plots of GRH-Gly and GRH-GlyAg in the frequency range of 0.1 Hz – 10 kHz at amplitude of 10 mV – (panel B); expanded high frequency region of GRH-Gly and GRH-GlyAg – (panel B-inset)

5A.3.13 SERS Measurements

The SERS activity of GRH-GlyAg nanocomposites was evaluated by using 4-aminothiophenol (4-ATP) as a probe molecule (Fig. 5.20). The SERS spectra of 4-ATP adsorbed on GRH-GlyAg nanocomposites at its various concentrations (1×10^{-3} – 5×10^{-8} M) have been shown in Fig. 5.20A. The Raman spectrum of solid 4-ATP exhibits several distinctive (strong and medium) bands (cm^{-1}) at: 1091, 1172, 1598, 1120, 1208, 1482 (Fig. 5.20B-a). For a typical 4-ATP concentration (1×10^{-7} M) adsorbed on GRH-GlyAg, these bands (cm^{-1}) are observed at about 1081, 1139, 1186, 1388, 1434, and 1589 (Fig. 5.20B-b) in the present work, which are very similar to those observed earlier for Ag NPs-graphene nanocomposites [353]. A comparison of the Raman spectra of blank 4-ATP (Fig. 5.20B-a) with that obtained after its adsorption on GRH-GlyAg (Fig. 5.20B-b) clearly reveal the distinctive shifts in the frequencies of 4-ATP (cm^{-1}) from 1091 to 1081 and 1598 to ~ 1589 which have been assigned to the formation of carbon-sulphur (C-S) bond and Ag-S bond formed between Ag NPs and –SH group of 4-ATP, respectively [353]. These shifts are indicative of the interaction of 4-ATP with Ag NPs present on the surface of GRH-Gly.



In control experiments, the SERS activity of GRH-Gly and bare Ag NPs for 4-ATP adsorbed on their surface at its typical concentration of 1×10^{-7} M have been shown in Fig. 5.20B-c and d. For the 4-ATP (1×10^{-7} M) adsorbed on the GRH-Gly sheets and bare Ag NPs, the intensities of the bands were, however, very weak. The much higher intensity of Raman bands in case of GRH-GlyAg clearly reveals its excellent SERS activity.

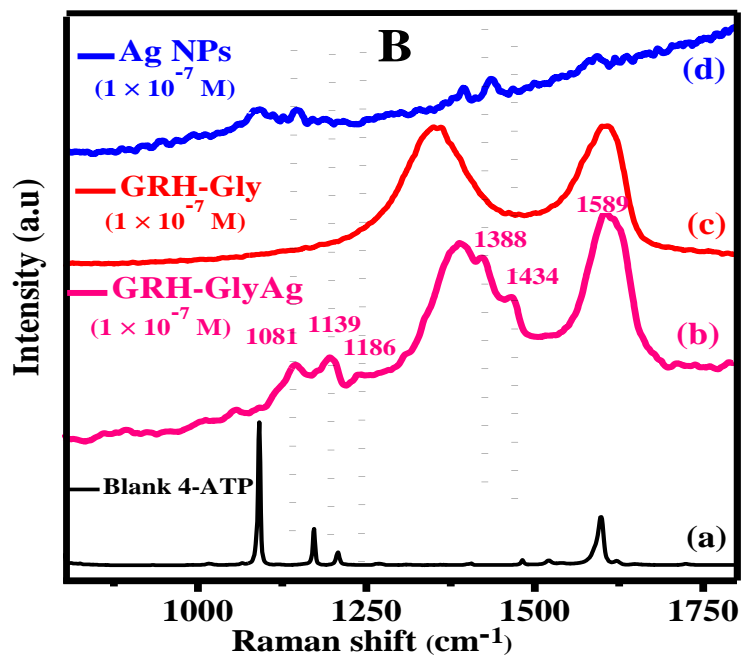


Fig. 5.20: SERS spectra of 4-ATP adsorbed on GRH-GlyAg nanocomposites at its various concentrations (1×10^{-3} – 5×10^{-8} M) – (panel A). Raman spectrum of solid 4-ATP (a) and SERS spectra of typical concentration of 4-ATP (1×10^{-7} M) adsorbed on GRH-GlyAg (b), GRH-Gly (c) and bare Ag NPs (d) – (panel B).

5A.4 Discussion

The reduction of GO and GO/Ag⁺ to GRH-Gly and GRH-GlyAg, respectively by employing glycine as a reducing agent was indicated by the optical absorption spectroscopy (Fig. 5.7). In the reaction mixture containing GO, glycine and Ag⁺, there would be the competition between GO and Ag⁺ for glycine along with the possibility of direct reaction between GO and Ag⁺ as has been reported earlier [361]. The formation of GRH-GlyAg was monitored by following the reduction of GO/Ag⁺ as a function of the concentration of Ag⁺ (Fig. 5.5). At low concentration of Ag⁺ containing Ag⁺:GO mass ratio of 1:10, a part of GO remains unreacted as was revealed by optical spectroscopy (Fig. 5.5a), whereas at a little

higher concentration of Ag^+ having 2:10 mass ratio of $\text{Ag}^+:\text{GO}$, the reduction of GO was observed to be the maximum (Fig. 5.5b). A further increase in the concentrations of Ag^+ containing mass ratio(s) of $\text{Ag}^+:\text{GO}$ (3-9:10) possibly results in the reduction of Ag^+ at a much faster rate rather than accomplishing the reduction of GO, which became evident by the increasing strong plasmonic absorption of Ag NPs (Fig. 5.5c to e). Thus, at varied mass ratios of $\text{Ag}^+:\text{GO}$, the resultant optical absorption spectra arises due to the formation of graphene, Ag NPs and unreacted GO if any. In control experiments, the reaction between glycine and Ag^+ (Gly-Ag) and GO and Ag^+ (GO-Ag) in the absence of glycine were performed at 95°C at pH 10.5 for 3 h. For Gly-Ag sample, the appearance of plasmonic band at about 417 nm is attributed to the formation of Ag NPs (Fig. 5.21a'). In case of GO-Ag, the optical absorption spectrum exhibited a broad absorption peak in the range of 230 - 260 nm peaking at 247 nm along with a plasmonic band at around 407 nm (Fig. 5.21b). It could be understood in terms of the partial reduction of GO under alkaline conditions [409] and formation of Ag NPs, respectively. Raman spectroscopy shows an increase in the $I_{\text{D}}/I_{\text{G}}$ ratio for GO-Ag to 0.97 (Fig. 5.22) as compared to that of GO (0.89), which clearly suggests the production of more disordered state for GO-Ag nanocomposites, and is assigned to the chemical interaction between GO and Ag NPs [410]. The XRD data however, shows that a part of Ag^+ remains unreacted under these conditions and corresponds to Ag_2O (Fig. 5.23). The IR spectroscopy for GO-Ag showed the presence of relatively strong C=O stretching frequency, as observed in IR spectrum of GO (Fig. 5.24). These features are quite different to those observed in the present system, i.e. for GRH-Gly/GRH-GlyAg. Thus, ruled out the contribution of Gly-Ag and GO-Ag in the present system.

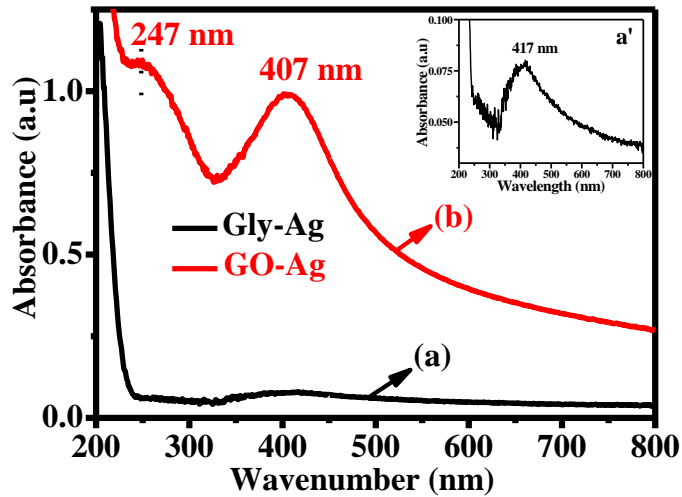


Fig. 5.21: Optical absorption spectra of Gly-Ag (a) and GO-Ag (b). Magnified optical absorption spectrum of Gly-Ag (b').

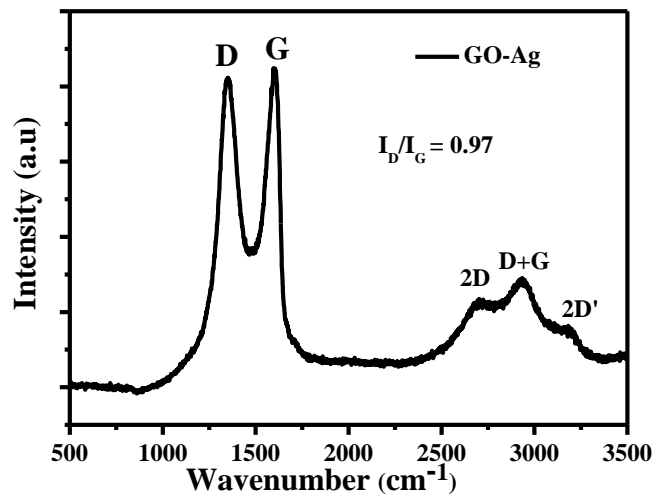


Fig. 5.22: Raman spectrum of GO-Ag.

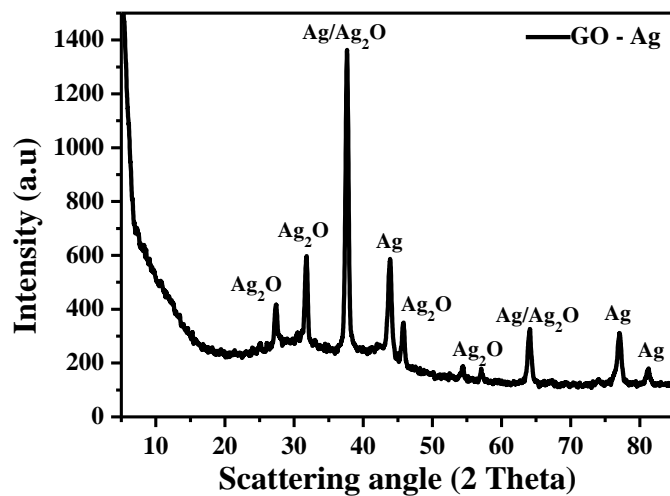


Fig. 5.23: XRD spectrum of GO-Ag.

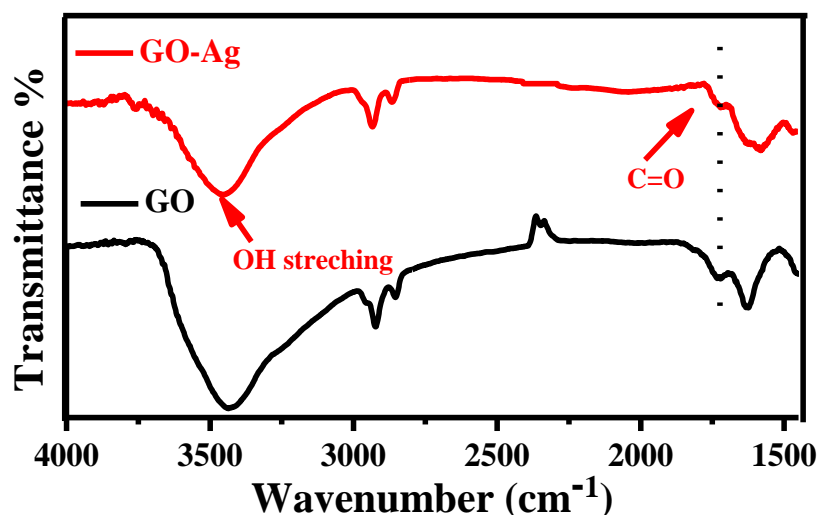


Fig. 5.24: IR spectra of GO (shown for comparison) and GO-Ag.

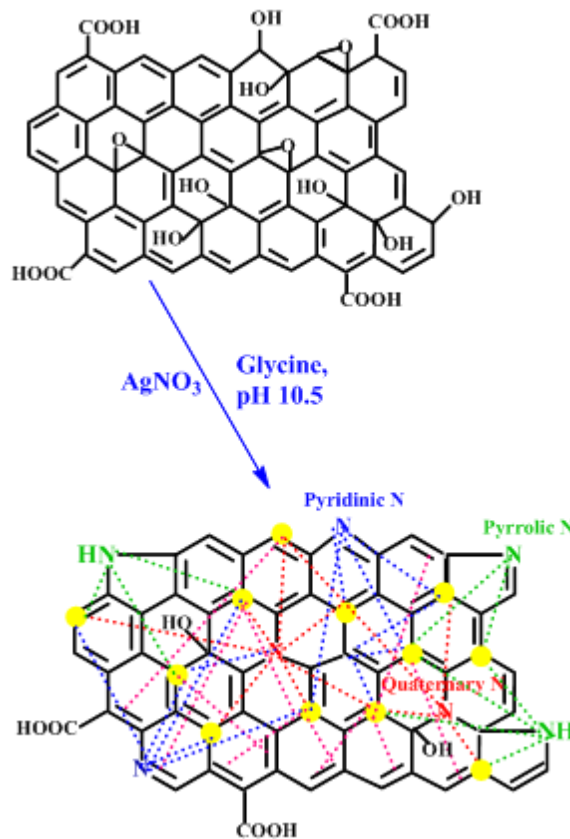
The effective reduction of GO by glycine to produce GRH-Gly and *in situ* generation of Ag NPs on the surface of GRH-Gly was evident by XRD pattern of GRH-GlyAg (Fig. 5.9) which exhibited Ag to be present in fcc structure as was also revealed by its SAED analysis (Fig. 5.13c"). The I_D/I_G ratio in the Raman spectra followed the order: GO (0.89) < GRH-Gly (1.00) < GRH-GlyAg (1.03) (Fig. 5.10). It suggested an increase in the number of smaller sp^2 domains for both GRH-Gly and GRH-GlyAg, as was supported by the decrease in-plane crystallite size which followed the order: GO > GRH-Gly > GRH-GlyAg. The appearance of D' band for the later two samples is indicative of the creation of additional defects due to the doping of N and functionalization by Ag NPs. The decoration of Ag NPs in GRH-Gly (GRH-GlyAg) was also suggested by the enhancement in the intensities of D and G bands (Fig. 5.10B).

The morphologies of GRH-Gly and GRH-GlyAg were examined by AFM, FESEM and TEM analyses (Fig. 5.11-5.13) which showed the thin and crumpled sheet for the former and relatively unfolded sheet for GRH-GlyAg, the surface of which is homogeneously decorated with Ag NPs with an average particle size (size distribution) of 17.5 nm (10-32 nm) (Fig. 5.13). The size of Ag NPs was also supported by XRD analysis (Fig. 5.9).

In XRD pattern of GRH-GlyAg, a weak and broad peak with a slight increase in the value of 'd' spacing to 0.362 nm as compared to that of GRH-Gly (0.349 nm) was observed (Fig. 5.9). This is explained due to the weak interaction of Ag NPs produced on its surface through different nitrogen moieties generated upon doping of N, resulting into the weakening and broadening of (002) plane of GRH-Gly [406]. The doping of N in both GRH-Gly and GRH-GlyAg is also indicated by IR spectroscopy which showed the appearance of new peaks due to C-N stretch and N-H bending (Fig. 5.14). These peaks were shifted slightly to lower wavenumber(s) in GRH-GlyAg as compared to that of GRH-Gly, which is understood due to the binding of N with Ag NPs. The doping of N in GRH-Gly and GRH-GlyAg is also examined by the ^{13}C solid-state NMR spectra, where the appearance of new broad peaks was noted at about 172 and 174 ppm, respectively corresponding to the formation of C=N bond (Fig. 5.15).

The formation of C-N bond was further corroborated by XPS analyses of GRH-Gly and GRH-GlyAg, which exhibited the new bands at 285.6 and 285.7 eV, respectively in their C 1s spectra (Fig. 5.16C and E). The N 1s spectrum of GRH-Gly shows three different components of N at 397.9, 399.9 and 402.0 eV (Fig. 5.16D) corresponding to pyridinic, pyrrolic and quaternary-N, respectively which are shifted to 398.5, 400.0 and 401.7 eV, in case of N 1s spectrum of GRH-GlyAg (Fig. 5.16F). The shift of these peaks could be attributed to the binding of Ag NPs with different N moieties. The enhanced stability of GRH-GlyAg nanocomposites revealed by TGA analysis (Fig. 5.17) also suggested the interaction of Ag NPs with N of graphene as well as their supramolecular interactions with π electrons of the graphene. These observations are in line with the IR data (Fig. 5.14). These interactions are also manifested by the change in morphology of GRH-GlyAg as compared to that of GRH-Gly, which shows relatively much less folding of sheet upon decorating its surface with Ag NPs (Fig. 5.13).

Based on the different interactions observed by IR, ^{13}C NMR and XPS and discussed above, the formation of N-doped graphene sheet decorated with Ag NPs is presented below in Scheme 5.1.



Scheme 5.1: Scheme for the formation of GRH-GlyAg depicting the interaction of Ag NPs with different domains of N and π bond containing moieties present on the surface of GRH-Gly.

The high conductivity of GRH-Gly can be appreciated due to the effective reduction of GO and its simultaneous functionalization with N (Fig. 5.18). A further increase in the conductivity of GRH-Gly (11.4 S/cm) upon decorating its surface by Ag NPs in GRH-GlyAg (25.9 S/cm) can be attributed to the presence of conducting Ag NPs and its increased surface area ($523 \text{ m}^2/\text{g}$) than to that of GRH-Gly ($360 \text{ m}^2/\text{g}$). A comparison of the value of conductivity for GRH-GlyAg (25.9 S/cm) observed in the present work is 150 times higher to that reported previously (0.1667 S/cm) for reduced graphene decorated with Ag NPs (Ag-rGO) by using electron beam radiation (350 kGy irradiation) [411] and is also more than

two-fold higher to that of GRH-Gly (11.4 S/cm). It clearly indicates the importance of functionalization by N as well as incorporation of Ag in enhancing the conductivity.

The high value of specific capacitance (C_s) observed in the present case for GRH-GlyAg (346 F/g) than to that of GRH-Gly (130 F/g) (Fig. 5.19A) is attributed to the high electrical conductivity (25.9 S/cm), high surface area (523 m²/g) and prevention of the aggregation of GRH-Gly due to the presence of Ag NPs on its surface. This observation is also supported by the EIS measurements where GRH-GlyAg exhibited less resistance in both low and high frequency region as compared to GRH-Gly. Both of these studies suggest the better electrochemical behavior of GRH-GlyAg (Fig. 5.19B).

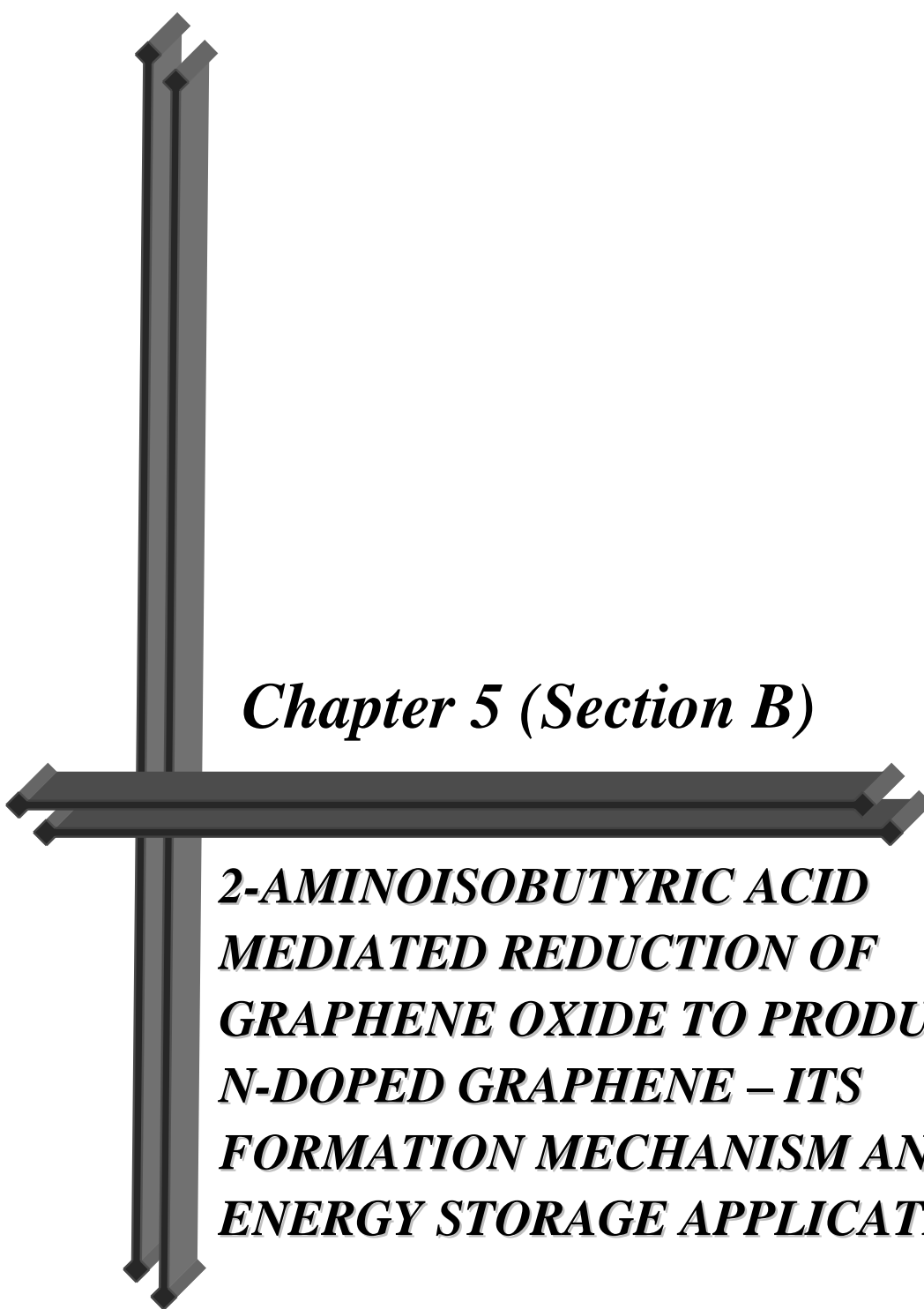
SERS measurements further manifested the interaction of Ag with N in GRH-GlyAg (Fig. 5.20). SERS effect has been generally argued to occur through either electromagnetic (EM) or chemical (CM) enhancement mechanisms [132,345]. The excitation of localized surface plasmons in EM results in enormous enhancement of the Raman signal (10^{12}), whereas the CM enhancement has been considered to arise through the formation of charge transfer (CT) complexes between excited Ag and the SERS substrate resulting in relatively lower enhancement ($10^1 - 10^2$). Therefore, in GRH-GlyAg, the observed enhancement of Raman signal by about 3-4 times to that of GRH-Gly, has been considered to arise through chemical interaction between Ag and GRH-Gly. It might have been contributed by the change in polarizability occurring due to the charge-transfer interaction between the pyridinic/pyrrolic moieties of GRH-Gly and Ag NPs because Ag having relatively low electronegativity than to that of nitrogen.

The SERS activity of GRH-GlyAg was further investigated by using 4-ATP as a probe molecule. The observed SERS activity of as-synthesized nanocomposites containing the moderate average size (size distribution) of Ag NPs 17.5 nm (10-32 nm), demonstrated the fairly high detection limit for 4-ATP (5×10^{-8} M) and is very similar to that of Ag/rGO nanocomposites containing Ag NPs having the size in the range of 21.4 ± 10.5 nm, prepared

by using arginine as a reducing agent [354]. However, in this work, extremely high concentration of AgNO₃ (100 mM) was employed [354] which is more than two orders of magnitude lower, to that used in the present work (0.59 mM). It thus makes the present system environmentally benign. These and some other important features of the previously reported similar system(s) have been summarized in Table 5.2. In fact the SERS activity in the present case could further be improved significantly by using Ag NPs of bigger size [354]. The enhanced electrical conductivity, surface area, specific capacitance and SERS of as-synthesized nanocomposites suggest their potential for multifunctional applications.

Table 5.2: A comparison of the synthetic details and the characteristic features of previously reported amino acid mediated system(s) for the synthesis of N-doped graphene-Ag nanocomposites.

Reducing Agent(s) (its concentration in mM)	[Ag ⁺] (mM)/ Mass ratio (GO:Amino acid:AgNO ₃)	Ag (wt. %) (surface at.%)	Method; Temperature; Time	Size (size distribution) of Ag NPs	Surface area (m ² /g)	Electrical conductivity (S/cm)	Detection limit (nM) by SERS	Ref.
Glycine (34.6)	0.59/1:5.2:0.2	0.3 (surface at.%)	Thermal; 95 °C; 3 h	17.5 (10-32 nm)	523	25.9	50	This work
Glycine	- /1:2:2	-	Thermal; Temperature increased gradually from room temperature to 500 °C and maintained for 2 h	15-20 nm	Not Reported	Not Reported	Not Reported	371
Arginine (38.3)	100/1:13.3:3.8	69.6	Microwave (4 Cycles); (2.45 GHz, 900 W); 600 s (50 s 'on' and 10 s 'off' for three times in each cycle)	21.4 ± 10.5 nm	Not Reported	Not Reported	10	354



Chapter 5 (Section B)

***2-AMINOISOBUTYRIC ACID
MEDIATED REDUCTION OF
GRAPHENE OXIDE TO PRODUCE
N-DOPED GRAPHENE – ITS
FORMATION MECHANISM AND
ENERGY STORAGE APPLICATIONS***

5B. 2-AMINOISOBUTYRIC ACID MEDIATED REDUCTION OF GRAPHENE OXIDE TO PRODUCE N-DOPED GRAPHENE – ITS FORMATION MECHANISM AND ENERGY STORAGE APPLICATIONS

Amino acids and its derivatives have specific advantages because of their non-toxic and biocompatible nature. In the previous Section 5A, we have explored the usage of glycine as a reducing agent by optimizing its different parameters to accomplish the effective reduction of GO. In the present Section, we have examined the use of 2-aminoisobutyric acid (AIB) (Fig. 5.25), a derivative of glycine, as a reducing agent in order to investigate the effect of methyl substituent on glycine. It results in the simultaneous reduction and functionalization of GO to produce N-doped graphene. Its formation mechanism has been analyzed. The energy storage applications for N-doped graphene, employing AIB and glycine as reducing agents, have also been investigated.

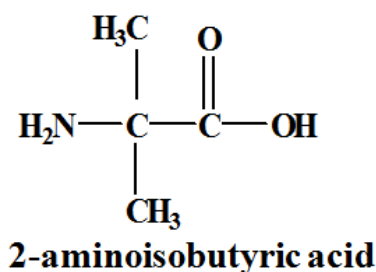


Fig. 5.25: Structure of 2-aminoisobutyric acid.

5B.1 Optimization of Various Parameters for the Reduction of GO to Synthesize N-doped Graphene

5B.1.1 Optimization of the Amount of AIB

The mass ratio of AIB to GO was optimized by monitoring its optical absorption spectra (Fig. 5.26). The mass ratio(s) of AIB:GO were varied from 2.6-5.2:1 by keeping the time of heating and pH of the reaction mixture constant at 3 h and 10.5, respectively (Fig. 5.26). For the mass ratio(s) of AIB:GO ranging from 2.6-5.2:1, it resulted in a gradual increase in absorption in the entire UV-Vis range. At lower mass ratio(s) of AIB:GO (2.6:1 and 4.0:1), it exhibited the absorption maxima at 257 and 260 nm, respectively, indicating the incomplete reduction of GO. The efficient reduction of GO was obtained for the mass ratio of 5.2:1 (AIB:GO) showing the absorption maximum at 263 nm. Thereafter, any increase in the mass ratio of AIB:GO did not result any change in the absorption maximum and absorbance (not shown). Therefore, the mass ratio of AIB:GO in all the experiments was fixed at 5.2:1.

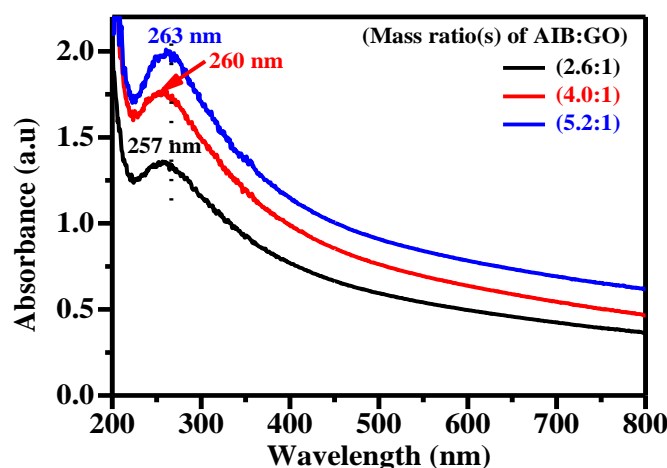


Fig. 5.26: Optical absorption spectra for the reduction of GO as a function of mass ratio(s) of AIB:GO varying from 2.6 - 5.2:1.

5B.1.2 Optimization of the Heating Time and pH

The heating time of the reaction mixture containing AIB and GO, by keeping the mass ratio of AIB:GO and pH constant at 5.2:1 and 10.5 respectively, was varied from 1 to

4 h. The change in the absorption peak of the reaction mixture as a function of heating time upto 3 h is shown in Fig. 5.27A. It shows that the absorption maximum is gradually red shifted from 256 to 263 nm. After 3 h, the reaction mixture did not show any shift in the absorption maximum (Fig. 5.27B). Therefore, the heating time for the reaction mixture was fixed at 3 h by keeping mass ratio of AIB:GO and pH constant at 5.2:1 and 10.5, respectively and this sample is denoted as GRH-AIB. At low pH of 4.5 keeping all other reaction conditions constant, the optimum heating time for the reduction of GO was found to be 7 h which shows the absorption maximum at 263 nm (Fig. 5.28). This sample is denoted as GRL-AIB.

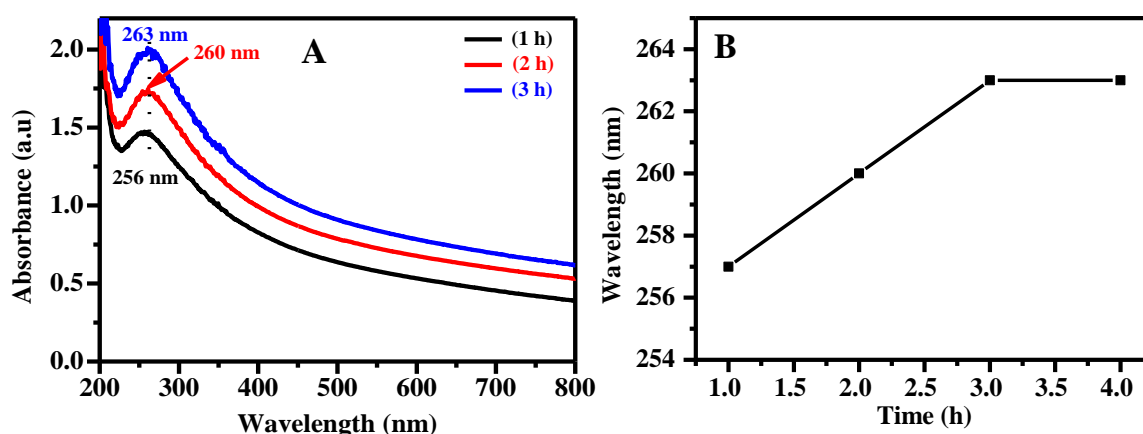


Fig. 5.27: Changes in the absorption peak of reaction mixture containing GO and AIB at pH 10.5 as a function of heating time – (panel A). Shift in the absorption maximum of reaction mixture with the time of heating – (panel B).

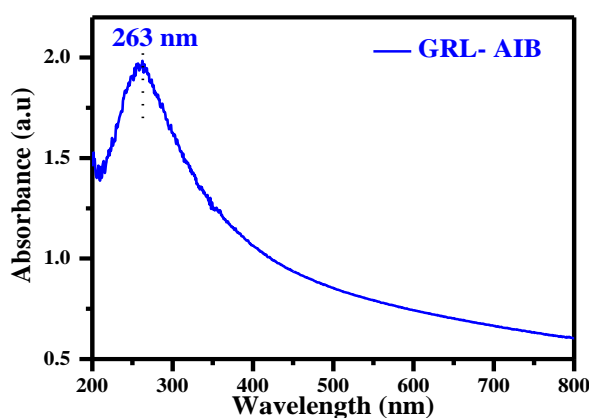


Fig. 5.28: Optical absorption spectrum of GRL-AIB.

5B.1.3 Synthesis of N-doped Graphene (GRH-AIB) under Optimized Reaction Conditions

Based on the above optimized conditions for the reduction of GO, 52 mg of AIB (25 mM or 2.6 mg/mL) was mixed with 20 ml of GO dispersion containing 10 mg of GO (0.5 mg/mL) under stirring and the pH of the resulting solution was maintained at 10.5 by adding dilute NaOH. This reaction was performed using a circulating water bath as well as on a heating plate equipped with stirrer and temperature sensor. The completion of the reaction on water bath takes about 3 h at 95 °C, whereas on heating plate it required only about 1 h at 100 °C. The resultant black solid was centrifuged and washed with DIW from five to six times in order to remove any residual AIB as it is soluble in water.

In a control experiment, the reduction of GO was also performed by using NaOH as a reducing agent at pH 10.5 under identical experimental conditions as mentioned above and the resulting product is denoted as GRH-OH.

5B.2 Characterization of N-doped Graphene

The as-synthesized N-doped graphene has been analyzed by using a number of characterization techniques *viz.* UV-Vis, zetasizer, XRD, Raman, AFM, FESEM, TEM, FTIR, XPS, ¹³C NMR, TGA, I-V and CV and details of these investigations are described below:

5B.2.1 Optical Studies

The optical absorption spectrum of GO displays a peak at 230 nm and a shoulder at 302 nm, and these peaks have been assigned to π - π^* transition corresponding to C=C and n- π^* transition due to the C=O group (Fig. 5.29a). The reduction of GO using AIB at pH 10.5 shows a change in color from yellowish-brown to black. The black product (GRH-AIB) thus obtained depicted a red shifted absorption peak at 263 nm (Fig. 5.29b). This red shift has been attributed to the

increase in the electron density and structural reorganisation in GO suggesting its reduction into graphene. Digital images of precursor GO and product GRH-AIB obtained by dispersing them in water is shown in Fig. 5.29 - inset.

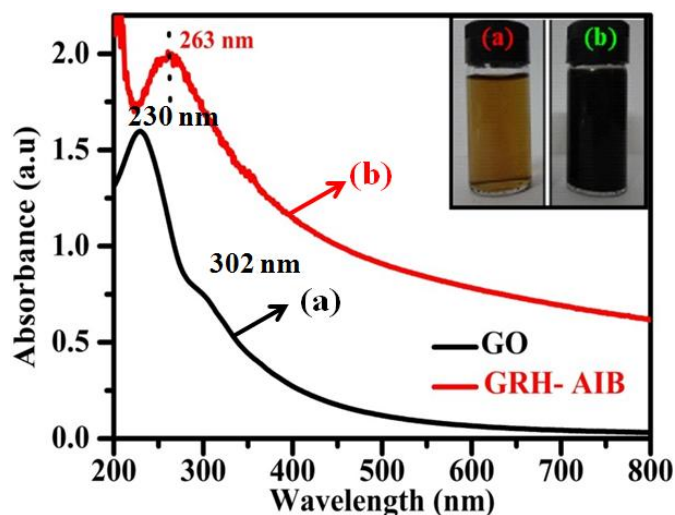


Fig. 5.29: Optical absorption spectra of: GO (a) and GRH-AIB (b) along with their digital photographs captured by dispersing them in water (inset).

The stability of as-synthesized GRH-AIB was examined by performing the DLS measurement in which the value of ζ -potential was found to be -48.1 mV (Fig. 5.30). It suggests the fairly high stability of GRH-AIB.

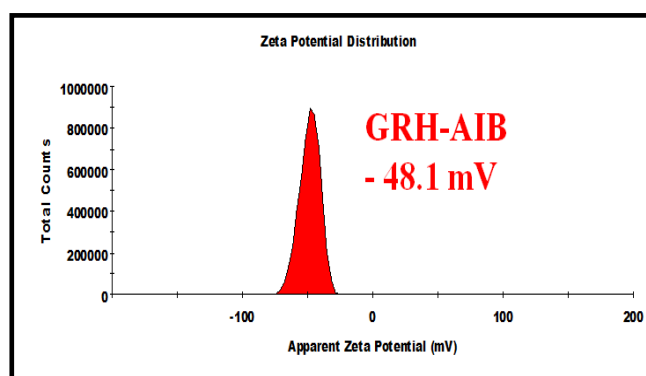


Fig. 5.30: ζ -potential of GRH-AIB in aqueous medium.

5B.2.2 Raman Spectroscopy

In order to work out the electronic structure of the as-synthesized graphene, Raman spectroscopy was used to analyze the precursors (graphite and GO) along

with the reduction products GRH-AIB and GRL-AIB. The corresponding spectral data are summarized in Table 5.3. The Raman spectrum due to graphite (Fig. 5.31A-a) is very similar to those reported earlier [383]. The Raman spectrum of GO (Fig. 5.31A-b) exhibits D and G bands (cm^{-1}) at 1357 and 1601 matching fairly well to the previous reports on GO [383]. In this case the ratio of I_D/I_G was computed to be 0.89.

The Raman spectrum of GRH-AIB exhibits D and G bands (cm^{-1}) at 1351 and 1598 (Fig. 5.31A-c). A close examination of these bands reveals that the intensity of D band at 1351 cm^{-1} is increased and G band is shifted to lower energy by 3 cm^{-1} as compared to that of GO and a new shoulder is developed at 1623 cm^{-1} (D' band) in case of GRH-AIB (Fig. 5.31B-c'). All these features suggest that the reduced GO may be N-doped in the present case similar to that reported previously [318,324]. The increase in the I_D/I_G ratio for GRH-AIB (1.02) compared to that of GO (0.89) suggests an increased number of smaller sp^2 domains. This aspect was further used to calculate the in-plane crystallite size (L_a in nm) of the N-doped graphene, from which the value of L_a was worked out to be 16.5 nm for GRH-AIB. This value is fairly small compared to that of GO (18.9 nm) suggesting that the reduction/doping leads to a decrease in crystallite size.

Raman spectrum of GRL-AIB is shown in Fig. 5.31A-d. It exhibits all the features as regards to the different Raman bands very similar to that observed in GRH-AIB. An analysis of this spectrum also showed the characteristic D' band (Fig. 5.31B-d') and a similar I_D/I_G ratio of 1.03. It clearly indicates that the nature of the product at this pH is also the same as obtained at pH 10.5 but it takes longer time (7 h) for the reduction of GO (Fig. 5.28). For this reason, in other experiments only GRH-AIB has been characterized.

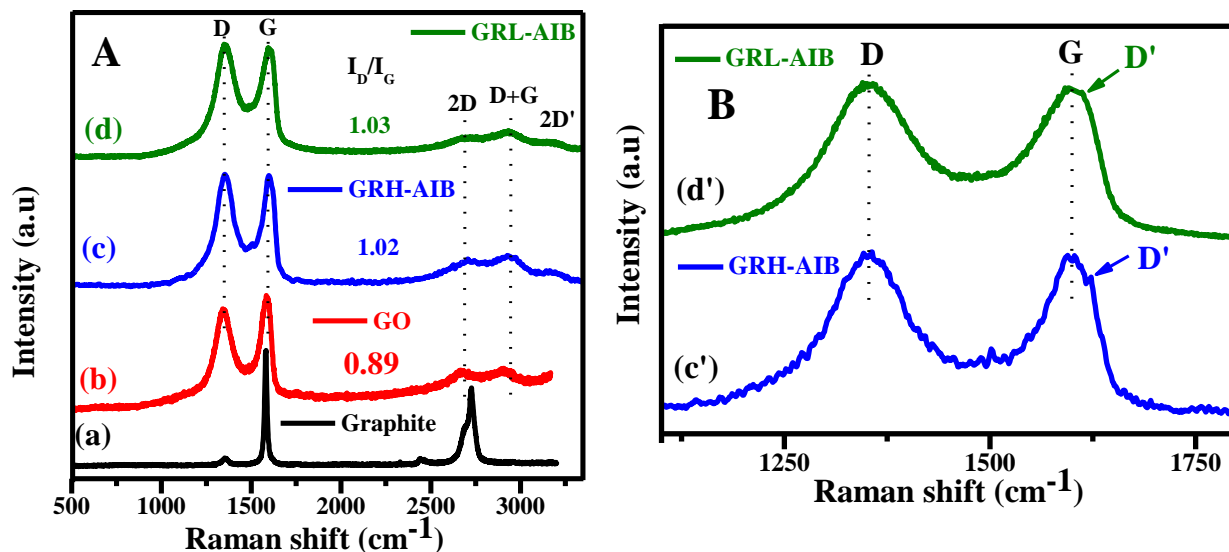


Fig. 5.31: Raman spectra of graphite (a), GO (b), GRH-AIB (c) and GRL-AIB (d) – (panel A); expanded Raman spectra of: GRH-AIB (c') and GRL-AIB (d') in 1100-1800 cm^{-1} range (panel B).

Table 5.3: Raman spectral data of graphite, GO, GRH-AIB and GRL-AIB.

Sample(s)	D (cm^{-1})	G (cm^{-1})	I_D/I_G
Graphite	1357	1575	-
GO	1357	1601	0.89
GRH-AIB	1351	1598 (1623 D')	1.02
GRL-AIB	1351	1595 (1617 D')	1.03

5B.2.3 XRD Analysis

The XRD patterns of graphite, GO and GRH-AIB are shown in Fig. 5.32. The graphite flakes depicts the characteristic sharp and intense peak at 26.3° corresponding to the (002) plane with a 'd' spacing value of 0.338 nm (Fig. 5.32a). The XRD pattern of GO obtained by the oxidation of graphite shows (002) reflection at much lower angle of 10.4° with a fairly high 'd' spacing value of 0.85 nm as compared to that of graphite which has been assigned to the intercalation of water molecule and oxygen containing functional groups between the layers of the graphite (Fig. 5.32b). XRD pattern due to GRH-AIB is fairly different to both of its precursors

and exhibit a broad peak at 23.1° with a 'd' spacing of 0.385 nm corresponding to the (002) reflection (Fig. 5.32c).

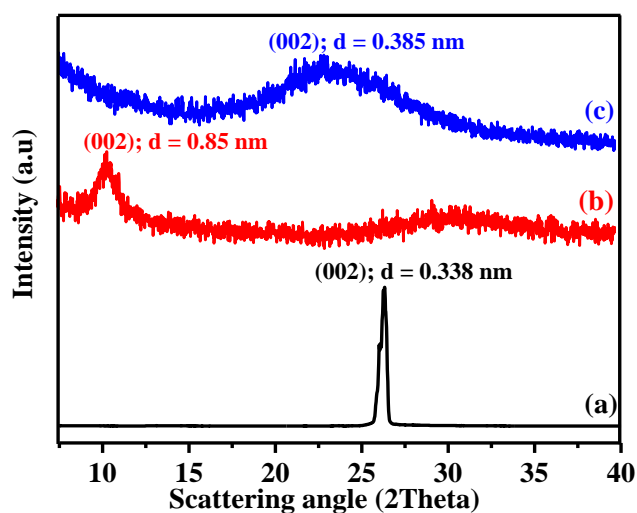


Fig. 5.32: XRD patterns of: graphite (a), GO (b) and GRH-AIB (c).

5B.2.4 AFM Measurements

AFM was used to analyze the surface topography of precursor GO and as-synthesized GRH-AIB, their 2D images are shown in Fig. 5.33. It exhibits the formation of sheet-like structure in both the cases. Using NOVA software, the thickness of these sheets was examined along several line(s) at various location(s) and are shown at a particular marked location in Fig. 5.33a' and b'. From the height profiles, the average surface height for GO and GRH-AIB along the marked line was measured to be 1.25 and 0.83 nm, respectively. The smaller average height for GRH-AIB as compared to that of GO might have resulted due to the removal of oxygenated groups from the surface of GO. The observed variation in the surface heights of GO and GRH-AIB, suggests the GO sheet to be 1 layer thick and GRH-AIB sheet to be 1-2 layers thick [290].

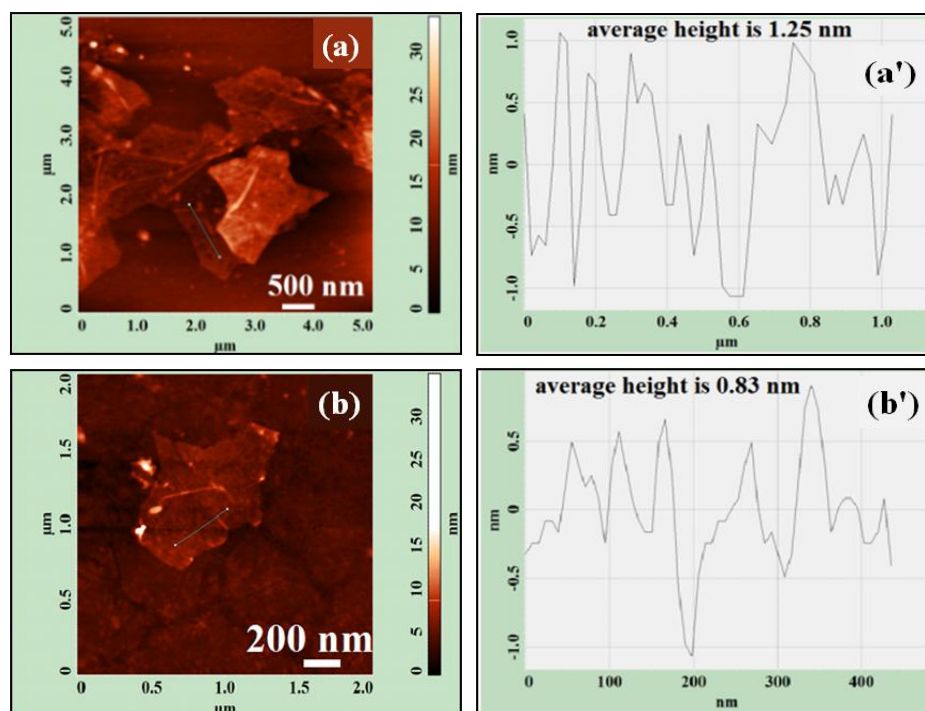


Fig. 5.33: AFM images and their height profiles along a particular marked line: GO (a and a') and GRH-AIB (b and b'), respectively.

5B.2.5 FESEM Analysis

FESEM image of GRH-AIB and its EDAX spectrum recorded at a particular location marked by cross sign in red is shown in Fig. 5.34. The FESEM image of GO shows it to be layered structure as reported in Chapter 3. Whereas, the FESEM image due to GRH-AIB consists of folded transparent sheets (Fig. 5.34a). The dimension of this sheet was estimated from its other image recorded at low resolution (Fig. 5.34a'), and was found to be about $20 \times 20 \mu\text{m}$.

An analysis of elemental composition of GO and GRH-AIB shows the later to have C/O ratio of 8.4 (Fig. 5.34b) which is more than 5 times higher to that of GO (1.59) (Chapter 3) and it also shows the presence of N (3.23 at.%).

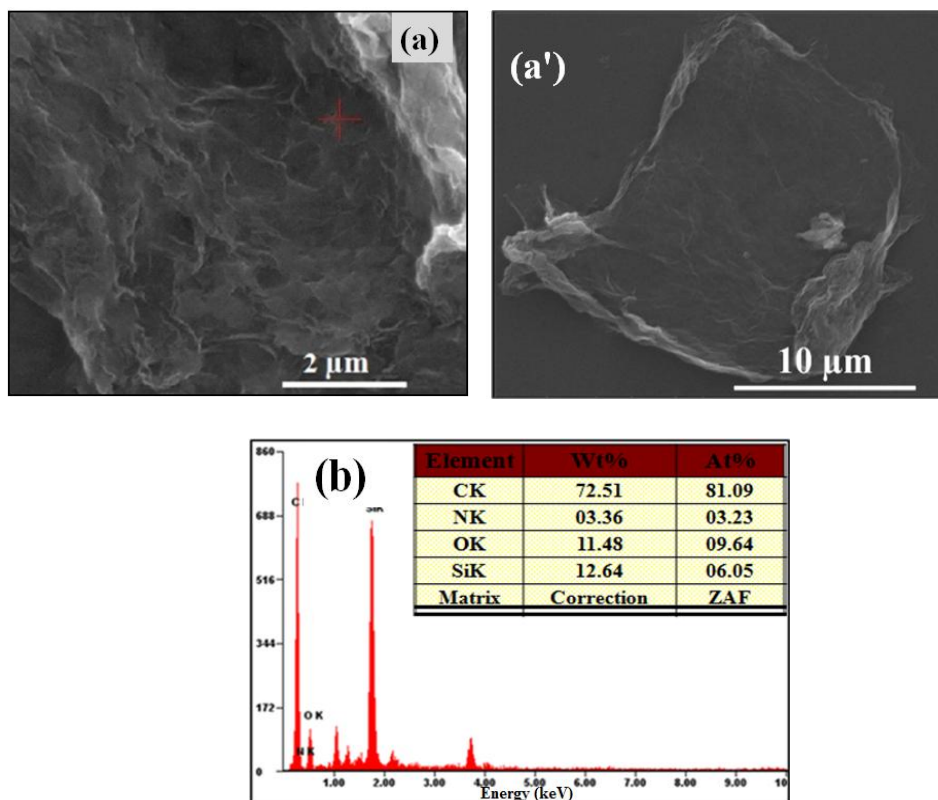


Fig. 5.34: FE-SEM image of GRH-AIB at higher (a) and lower magnifications (a'); EDAX spectrum (b). (The contribution due to Si has arisen from the used glass substrate).

5B.2.6 TEM and SAED Analysis

The TEM image of GO exhibits a sheet-like structure (Fig. 5.35a) and its HRTEM image shows some fringes on the edges (Fig. 5.35a'). An analysis of these fringes gives 'd' spacing of 0.80 ± 0.05 nm corresponding to (002) plane, which is higher to that of graphite (0.338 nm). It may be mentioned that the observed 'd' spacing value matches very well with XRD data (Fig. 5.32). Its SAED pattern (Fig. 5.35a-inset) shows concentric rings masked with bright spots indicating it to be of polycrystalline nature. TEM image of GRH-AIB (Fig. 5.35b) indicates it to consist of wrinkled nanosheets. Its SAED analysis clearly exhibits the nature of graphene sheets to be crystalline with six-fold symmetry (Fig. 5.35b-inset). The HRTEM image of GRH-AIB exhibits fringes all along the sheet from which the value of 'd' spacing was estimated to be 0.38 nm (Fig. 5.35b'). It may be noted that the measured 'd'

spacing of 0.38 nm is higher than that of graphite (0.338 nm). It has possibly arisen because of an increase in microstructural disorder of graphene by the incorporation of nitrogen. Such an increase in the 'd' spacing has also been reported earlier for the synthesis of graphene using hydrazine as reducing agent [412].

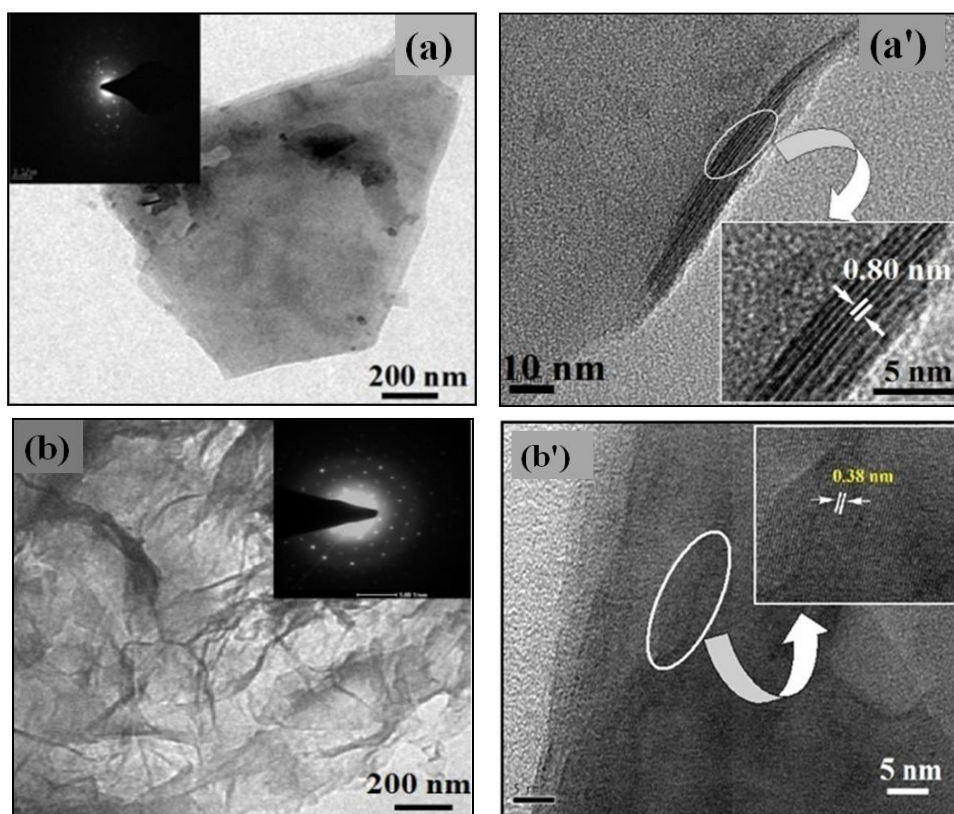


Fig. 5.35: TEM image of GO (a) and GRH-AIB (b) along with their SAED patterns in inset. HRTEM image of GO (a') and GRH-AIB (b').

5B.2.7 FTIR Studies

The FTIR spectra of GO and GRH-AIB are shown in Fig. 5.36. The precursor, GO, exhibits various prominent vibrational bands (cm^{-1}) at 3425, 1727, 1628, 1221, 1054 which have been assigned to -OH stretching, C=O (carboxylic), C=C, C-O-C (epoxy) and C-O (alkoxy) groups, respectively (Fig. 5.36A-a). In the IR spectrum of GRH-AIB, the peak due to free -OH stretching is reduced significantly and new bands appeared at 2924 and 2851 cm^{-1} due to symmetric and asymmetric stretching of the C-H, respectively (Fig. 5.36A-b). IR spectra of GO and GRH-AIB on the

expanded scale (1800-1300 cm^{-1}) are presented in Fig. 5.36B. A comparison of the IR spectra of GO with GRH-AIB depicts a significant difference in their vibrational bands. In case of GRH-AIB, the peaks due to C=O (1727 cm^{-1}) and C-O-C (1221 cm^{-1}) have vanished completely and the peaks due to C-O (1054 cm^{-1}) and -OH (3425 cm^{-1}) have also become fairly weak and broad. Whereas, the peak at 1628 cm^{-1} due to the C=C bonds is still retained. Interestingly, some new peaks with poor absorption have appeared in the wavenumber range (cm^{-1}) from 1580-1542 and 1367, which may be assigned to N-H bending and C-N stretching, respectively. Similar observations were earlier made by Lee *et al.* in the case of glycine as a reducing agent [339]. These observations suggests the reduction of GO and its simultaneous doping with N.

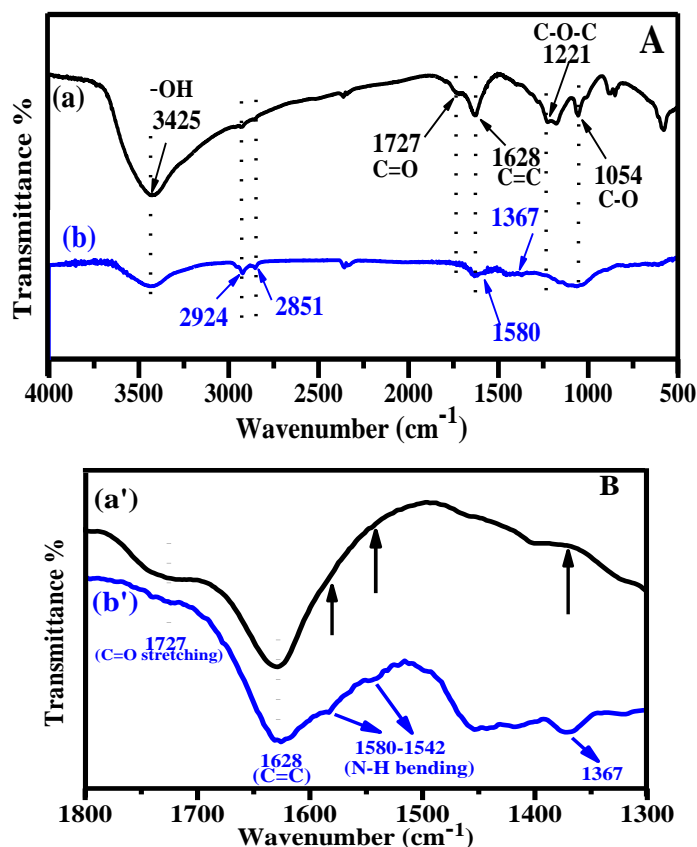


Fig. 5.36: FTIR spectra of: GO (a) and GRH-AIB (b) – (panel A); expanded FTIR spectra of: GO (a') and GRH-AIB (b') in the range of 1800-1300 cm^{-1} – (panel B).

5B.2.8 ^{13}C Solid-State NMR Spectroscopy

The reduction of GO and doping of N was further examined by performing solid-state ^{13}C MAS NMR spectroscopy (Fig. 5.37). The ^{13}C NMR spectrum of GO exhibits five different components of carbon at about 61, 70, 105, 115, 129, 167 and 190 ppm corresponding to C-O-C (epoxy), C-OH (^{13}C nuclei in hydroxyl), sp^2 carbon with graphitic structure in different environments, O-C=O (carbonyl carbon of ester) and C=O (ketonic carbon), respectively similar to those reported previously for GO [253,324]. Interestingly, in the NMR spectrum of GRH-AIB, the functionality like C-O-C is almost completely eliminated and the peak due to C-OH is reduced significantly along with its broadening. The graphitic sp^2 carbon peaks has now become more intense, broadened and up-shifted. It suggests an increase in the graphitic nature of the GRH-AIB as observed earlier [253,324]. Apart from this, a new and broad peak is also developed at about 176 ppm which is attributed to the formation of imine (C=N) functionality as reported earlier [408].

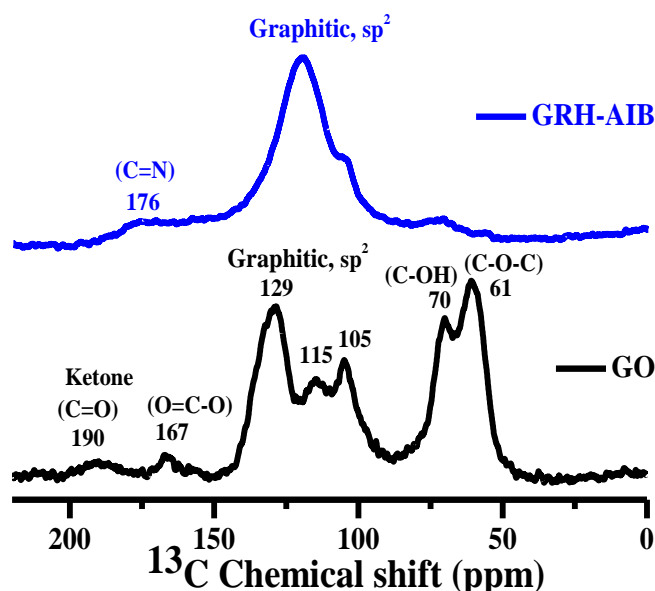


Fig. 5.37: Solid-state ^{13}C NMR spectra of GO and GRH-AIB.

5B.2.9. XPS Analysis

The surface analyses of GO and GRH-AIB were performed by using XPS. The survey scans of these samples were recorded in the binding energy range of 0-800 eV (Fig.

5.38A). Panel B shows the high resolution C 1s spectrum of GO which depicts four different components of carbon (eV) at 284.2, 286, 286.7 and 287.9 which have been assigned to C=C/C-C due to sp^2/sp^3 hybridized carbon, C-OH, C-O of epoxy/alkoxy and C=O of carboxylic groups, respectively. Similarly, high resolution C 1s spectrum of GRH-AIB consists of four different bands (eV) at 284.4, 285.6, 286.4, 288.1 which have been assigned to C=C/C-C, C-N (carbon singly bonded to nitrogen), C-O and C=O, respectively (panel C). A comparison of C 1s spectra due to GO and GRH-AIB reveals that in case of GRH-AIB the peak due to C=C is enhanced, whereas peaks due to C-O and C=O corresponding to epoxy/alkoxy and carboxylic groups are reduced. In addition to this, a new peak owing to C-N (285.6 eV) is developed which is slightly shifted to lower binding energy than to that of GO (286 eV). However, it is difficult to isolate the presence of C-OH/C-N at this binding energy as these binding energies are fairly close [359]. These changes in GRH-AIB are understood due to an increase in graphitic character and doping of N. To further examine the doping of N and its different moieties, the N 1s spectrum (panel D) has been deconvoluted into various peaks having different binding energies, which can be assigned to pyridinic-N at 398.1 eV, pyrrolic-N at 399.3 eV and quaternary-N at 400.3 eV. It is indicated from the area under these curves that the major component among these N moieties corresponded to quaternary-N (Fig. 5.38D). GO and GRH-AIB exhibits O 1s peaks (eV) at 531.7 and 532, respectively (panel E). The intensity of O 1s peak is decreased in GRH-AIB as compared to that of GO. The formation of different N configurations in graphene has been indicated in the figure given in panel F. It may be mentioned that, the observation about doping of N in the present system is similar to that reported by Lee *et al.* [339] who have employed glycine as a reducing agent.

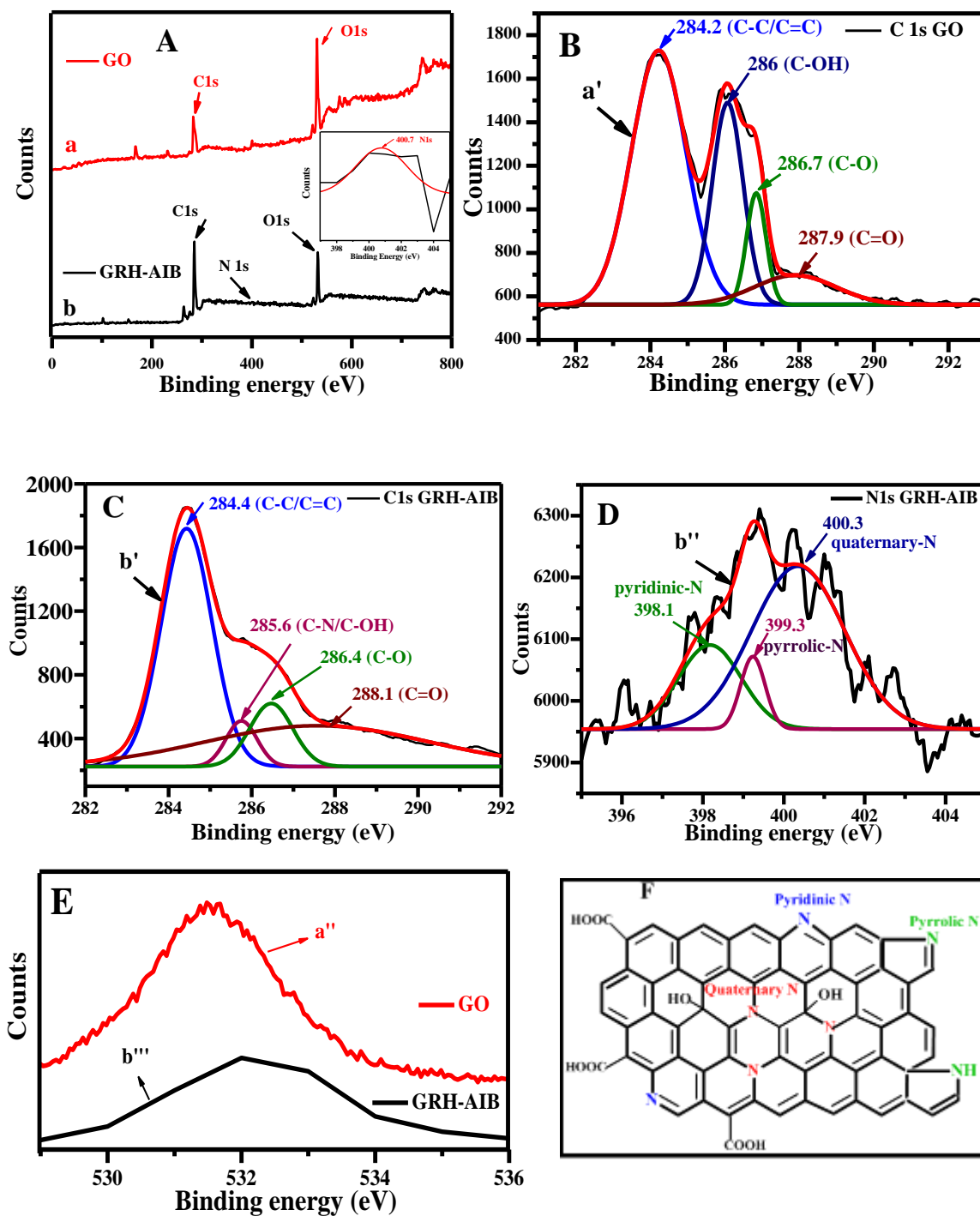


Fig. 5.38: XPS spectra of GO (a) and GRH-AIB (b), inset N 1s – (Panel A); C 1s spectra of GO (a') and GRH-AIB (b') – (panels B and C); N 1s spectrum of GRH-AIB (b'') – (panel D); O 1s spectra of GO (a'') and GRH-AIB (b''') – (panel E); Schematic presentation of N-doped graphene – (panel F).

5B.2.10. TGA Analysis

The thermal stability of the precursors, graphite and GO, along with the as-synthesized GRH-AIB was examined by recording their TGA curves from ambient temperature to 700 °C and are shown in Fig. 5.39. The TGA curve of graphite shows behavior very similar to that observed previously [271]. The TGA curve due to GO exhibits a weight loss of about 15% at around 100 °C and 43% at around 235 °C and have been assigned to the removal of adsorbed water and labile oxygen containing functional groups CO, CO₂, respectively. The third process starts at about 450 °C and a major loss in this process occurs up to 600 °C corresponds to about 54% weight loss. Whereas, the TGA curve due to GRH-AIB under similar conditions shows only about 10% of weight loss up to 100 °C and 18% loss up to 235 °C. The third major loss of weight starts at around 450 °C and the loss up to 600 °C comes out to be about 31%. Moreover, this behaviour is very similar to that observed in a previous study on N-doped graphene [413]. After 650 °C virtually there was no further loss, which suggests relatively higher stability of GRH-AIB as compared to that of GO.

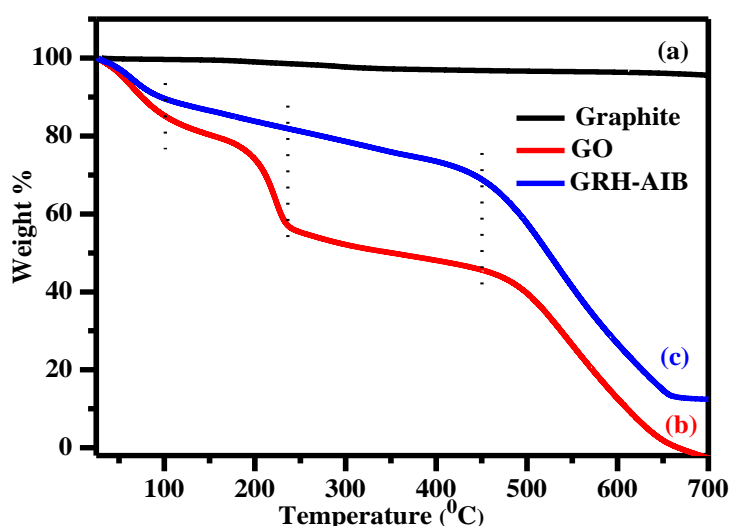


Fig. 5.39: TGA curves of graphite (a), GO (b), and GRH-AIB (c).

5B.2.11 I-V Measurements

The I-V curve of GRH-AIB (Fig. 5.40) shows linearity over the entire recorded voltage range from -1 to +1 V, suggesting it to follow the ohmic behavior. Moreover, it exhibits drastic increase in conductivity (6.3 S/cm) as compared to that of GO (2.7×10^{-4} S/cm) (Chapter 4). The high conductivity of GRH-AIB has been attributed to the removal of the oxygen functionalities from its surface and doping of N.

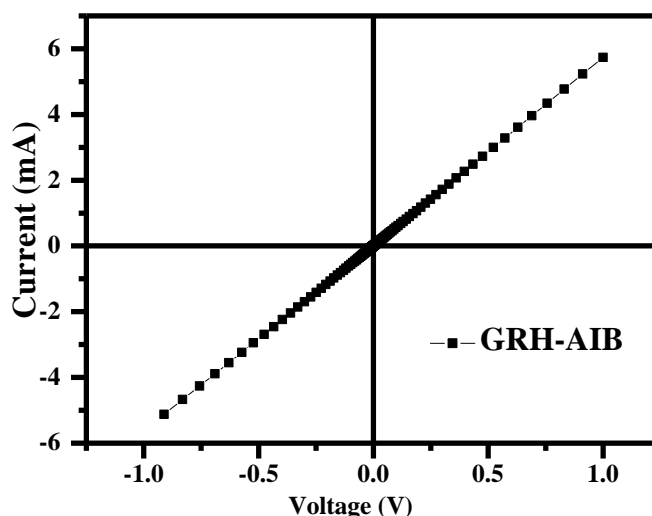


Fig 5.40: I-V curve of GRH-AIB.

5B.2.12 Electrochemical Measurements

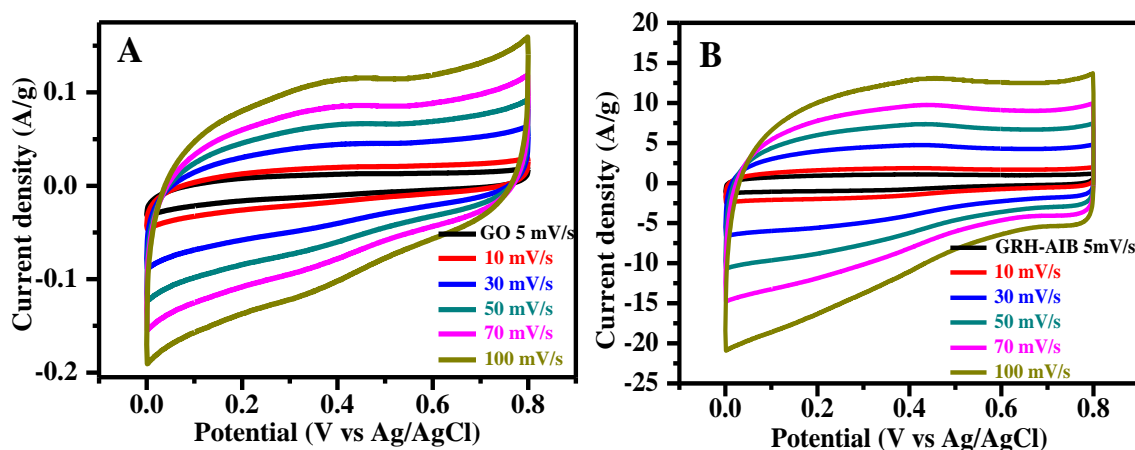
The electrochemical behavior of GO, GRH-AIB and GRH-Gly were investigated for the supercapacitor applications (Fig. 5.41). Cyclic voltammetry (CV) curves of GO, GRH-AIB and GRH-Gly were recorded in the voltage range of 0.0 to 0.8 V at different scan rate(s) ranging from 5 to 100 mV/s. These curves exhibited an increase in the current densities with increasing scan rates (Fig. 5.41A-C). The values of specific capacitance (C_s (F/g)) for GO, GRH-AIB and GRH-Gly at the scan rates of 5, 10, 30, 50, 70 and 100 mV/s were calculated to be 2.02, 1.65, 1.27, 1.12, 1.04 and 0.96; 161, 148, 132, 123, 117 and 110; and 231, 216, 198, 188, 181 and 173, respectively (Fig. 5.41A-D). For a typical scan rate of 100 mV/s, GRH-AIB (110 F/g) and GRH-Gly (173 F/g) shows much higher C_s values to that of GO (0.96 F/g) (Fig. 5.41E). The lower value of C_s for GO as compared to those of

GRH-AIB and GRH-Gly may be attributed to the poor conductivity of GO (Fig. 5.40). This observation is also understood by the presence of sp^3 hybridization and low faradic rate of reaction in GO besides its lower surface area ($38.9 \text{ m}^2/\text{g}$). Interestingly, the CV curves of GRH-AIB were almost rectangular in shape (Fig. 5.41B) which is characteristic of EDLC with a small redox hump arising from the pseudo-capacitance due to the presence of different N moieties (pyridinic-N, pyrrolic-N and quaternary-N) with the major component corresponded to quaternary-N as has been revealed by its XPS analysis (Fig. 5.38). In contrast to GRH-AIB, the shape of the CV curves for GRH-Gly (Fig. 5.41C) were approximately rectangular in shape with well distinguished redox hump arising due to the contribution of pseudo-capacitive N functionalities with the major component corresponded to pyrrolic-N as was arrived from XPS studies (Fig. 5.16D).

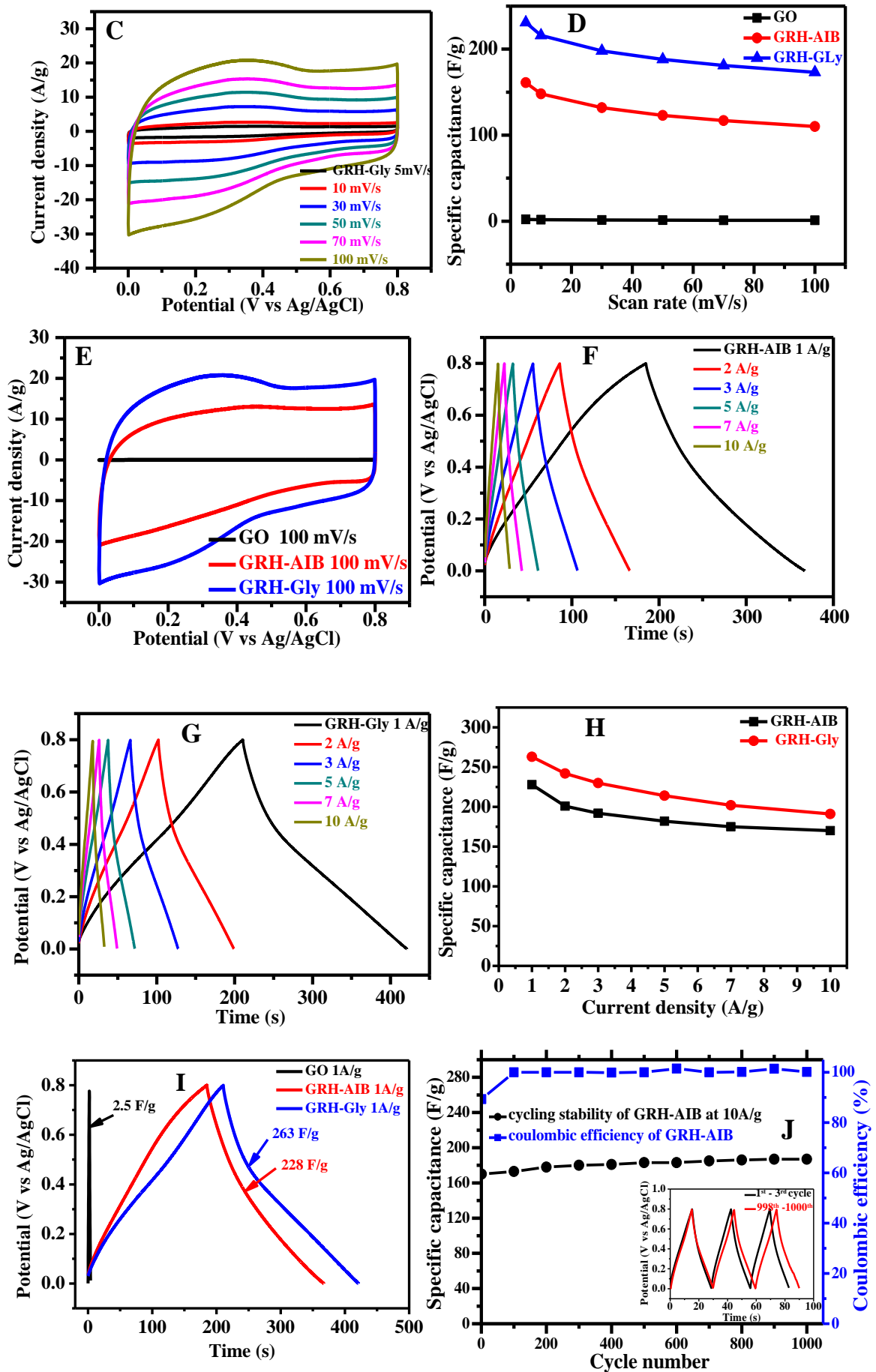
The electrochemical capacitive performance for GO, GRH-AIB and GRH-Gly as electrode materials was also determined by GCD measurements in the potential window of 0.0 to 0.8 V similar to that used for CV measurements. Fig. 5.41F and G show the charge-discharge curves for GRH-AIB and GRH-Gly at various current densities of 1, 2, 3, 5, 7, and 10 A/g from which the C_s values (F/g) were calculated to be 228, 201, 192, 182, 175 and 170; and 263, 242, 230, 214, 202 and 191, respectively. The shape of these curves is nearly symmetrical triangle which shows the good capacitive behavior. An increase in the current densities from 1 to 10 A/g results in the reduction of C_s values for GRH-AIB and GRH-Gly from 228 to 170 F/g and 263 to 191 F/g (Fig. 5.41H), respectively. It is noteworthy that even at high current density of 10 A/g, the C_s values for GRH-AIB and GRH-Gly are fairly high. A comparison of the C_s values of GRH-AIB (228 F/g at 1A/g) and GRH-Gly (263 F/g at 1A/g) obtained from GCD curves to that of GO (2.5 F/g at 1 A/g) shows them to be much higher (Fig. 5.41I).

For GRH-AIB, the long term cycling stability was examined for 1000 cycles at the highest used current density of 10 A/g (Fig. 5.41J). The inset of Fig. 5.41J shows the typical first three and last three cycles of these runs. The C_s for the first cycle was calculated to be 170 F/g which is increased gradually to 187 F/g up to 1000th cycle. This increase in the value of C_s may be attributed to the presence of different N-moieties. Similar observations about the role of N functionalities have been made in previous studies [340,414]. For 1000 cycles, the charging-discharging curves recorded at 10 A/g exhibited coulombic efficiency of 100-101% (Fig. 5.41J).

For GRH-Gly, the long term cycling stability was examined for 1000 cycles at the current density of 10 A/g (Fig. 5.41K) and the inset of this figure shows the typical first three and last three cycles of these runs. The C_s value for the first cycle was calculated to be 191 F/g which increased gradually to 209 F/g up to 1000th cycle. This increase in the C_s value has been attributed to the different N-moieties contributing to the pseudo-capacitance similar to those reported earlier [340,414]. For 1000 cycles, the charging-discharging curves recorded at 10 A/g exhibited coulombic efficiency of 100-102.6% (Fig. 5.41K).



2-aminoisobutyric acid mediated reduction of graphene oxide to produce N-doped graphene – its formation mechanism and energy storage applications



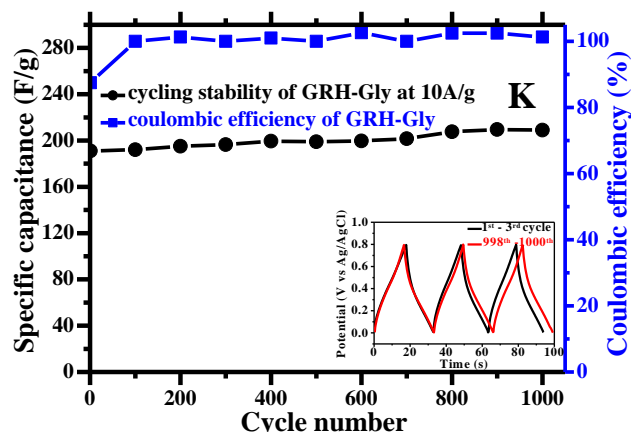


Fig. 5.41: CV curves of GO, GRH-AIB and GRH-Gly at different scan rates – (panels A, B and C). Variation in the value(s) of specific capacitance (C_s) as a function of scan rate(s) for GO, GRH-AIB and GRH-Gly – (panel D). A typical CV curve of GO, GRH-AIB and GRH-Gly at a scan rate of 100 mV/s – (panel E). Galvanostatic charge-discharge (GCD) curves of GRH-AIB and GRH-Gly at various current densities – (panels F and G). Variation in the value of C_s obtained from the GCD curves for different current densities – (panel H). GCD curves of GO, GRH-AIB and GRH-Gly at a typical current density of 1 A/g – (panel I). Variation in the C_s values of GRH-AIB and GRH-Gly and their coulombic efficiencies as a function of number of cycles (panels J and K) and their GCD curves for the first and last three cycles – (panels J and K-inset). All electrochemical measurements were performed in 1 M H_2SO_4 as an aqueous supporting electrolyte.

Fig. 5.42A and B shows the change in energy densities at various current densities and Ragone plots for GRH-AIB and GRH-Gly, respectively. The Ragone plots for these samples exhibits the high energy densities of 20.26 and 23.37 Wh/kg at a power density of 400 W/kg, respectively. Notably, even at higher power densities of 3963 and 3941 W/kg, the energy densities for GRH-AIB and GRH-Gly decreased to 14.75 and 16.42 Wh/kg only, respectively. These results evidently suggest the tremendous potential of the as-synthesized GRH-AIB and GRH-Gly as electrode materials for energy storage devices.

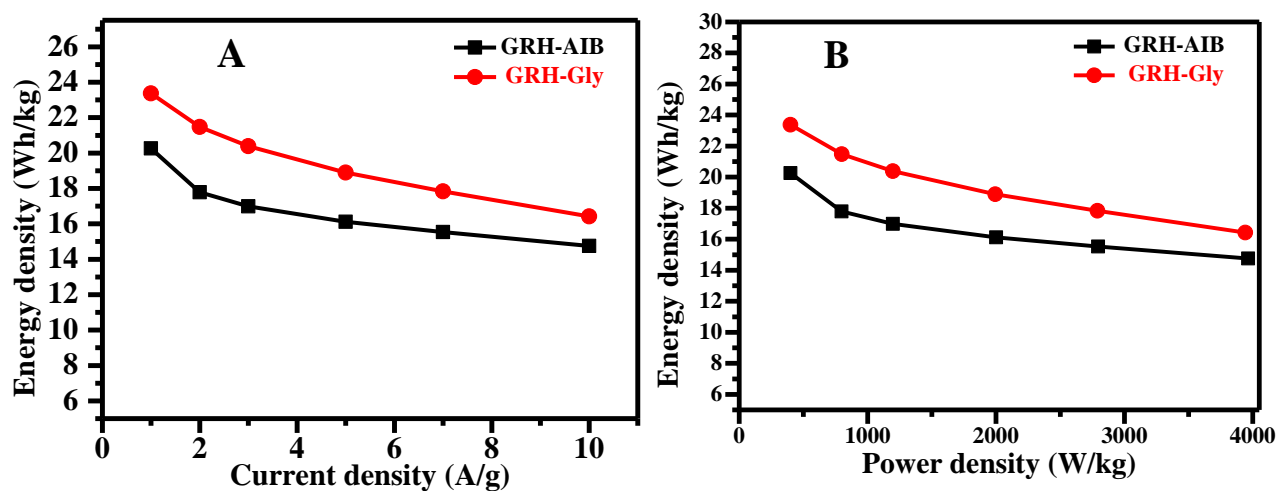


Fig. 5.42: Change in the energy densities of GRH-AIB and GRH-Gly electrodes with current densities (A) and Ragone plots for GRH-AIB and GRH-Gly (B).

5B.3 Discussion

The reduction of GO by AIB at high (10.5) as well as low (4.5) pHs clearly indicates the efficient reduction of GO to graphene, as was evidenced by the observed changes in the optical absorption (Fig. 5.29 and 5.28). These observations are also very well supported by Raman spectroscopic measurements made at high and low pHs, respectively (Fig. 5.31) and are understood in terms of the I_D/I_G ratio. For the typical case of AIB, the values of I_D/I_G at high (1.02) and low (1.03) pHs were very similar and fairly higher to that of GO (0.89) suggesting an increase in disorder in microstructures of reduced GO. The fact that the time taken for the reduction of GO by AIB at low pH was slightly higher compared to that at high pH, (Section 5B.1.2) suggests the involvement of basic $-NH_2$ and $-COO^-$ groups in the reduction at high pH, whereas at low pH since $-NH_2$ group will be largely protonated it reduces the efficiency of reduction. A Comparison of the efficiency of reduction of GO by AIB (present section) and glycine (Chapter 5 (Section A)) at low pH shows the later to be relatively less efficient, as was revealed by the longer time taken by glycine (10 h) as compared to AIB (7 h). This is understood by the difference in the structure of AIB (Fig. 5.25) and glycine (Fig. 5.1).

In a control experiment, the reduction of GO was also performed by using NaOH as a reductant maintaining the pH of the solution at 10.5. The complete reduction of GO into graphene using NaOH took more than about 13 h (Chapter 3), which is fairly longer as compared to that of GRH-AIB, which gets completed in 3 h (Fig. 5.29b). It is even longer to that of GRL-AIB, which gets completed within 7 h (Fig. 5.28). During 3 h, we could not find any significant conversion of GO to graphene by OH^- at pH 10.5 which was confirmed by recording its optical absorption (Fig. 5.43). It clearly rules out the participation of OH^- in the reduction of GO. Therefore, the reduction of GO at high and low pHs is understood due to the involvement of mainly $-\text{NH}_2$ and COO^- and $-\text{COOH}$ groups, respectively. This finding is in line with the earlier observation of Lee *et al.* [339] in which they observed glycine to be effective reducing agent for GO.

Thus the reduction of GO using AIB at high pH (GRH-AIB) is more efficient to that at low pH (GRL-AIB).

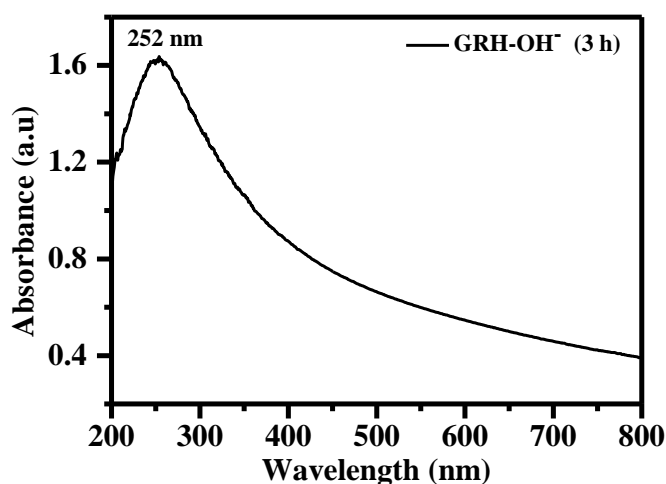


Fig. 5.43: Optical absorption spectrum of GRH-OH⁻ after 3 h of heating.

The formation of graphene in GRH-AIB was evidenced by XRD, SAED and HRTEM analyses (Fig. 5.32 and 5.35). The formation of folded transparent sheets for GRH-AIB is quite apparent by AFM, FESEM and TEM images (Fig. 5.33-5.35). From the AFM study, the average thickness of GRH-AIB sheet (0.83) was found to be less than that of GO (1.23), suggesting it to be about 1-2 layers thick (Fig. 5.33). GRH-AIB also exhibited the high C/O ratio (8.4) compared to that of GO (1.59), indicating the GRH-AIB to have more sp^2 character (Fig. 5.34). The presence of hexagonal sp^2 carbon features is also revealed by SAED analysis (Fig. 5.35b- inset).

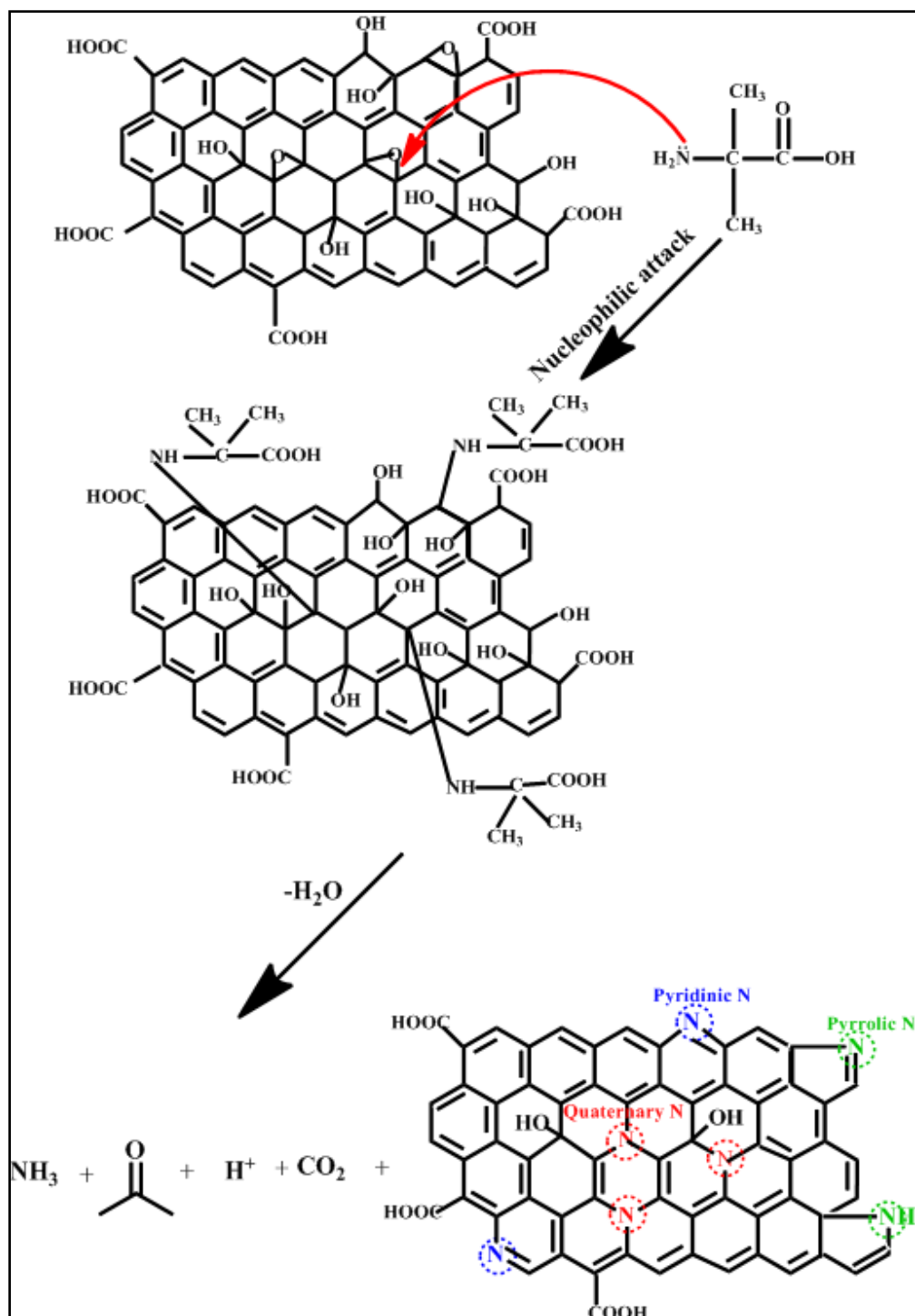
The reduction of GO was also associated with a significant reduction in the intensity of peaks due to C=O of carboxylic and C-O of epoxy groups in its XPS spectrum (Fig. 5.38). Graphene interacts with AIB mainly through $-NH_2$ group is indicated by IR analysis (Fig. 5.36), in which the weak peaks due to C-N stretching and N-H bending were observed at 1376 and 1580-1542 cm^{-1} , respectively, suggesting the possibility of N-doping. The doping of N is also indicated by Raman spectroscopy in which a new band (shoulder) is developed at 1623 cm^{-1} (D' band), which is associated with an increase in the $I_{D'}/I_G$ ratio (Fig. 5.31B-c'). The doping of N is also supported by ^{13}C NMR studies, where the appearance of a new broad peak was noted at about 176 ppm corresponding to the formation of C=N bond (Fig. 5.37). It is further confirmed by XPS analysis which exhibited the development of a new peak corresponding to C-N bond at 285.6 eV (Fig. 5.38C). Based on the deconvoluted N 1s spectrum, the presence of different N configurations in graphene could be assigned to: pyridinic-N at 398.1 eV, pyrrolic-N at 399.3 eV and quaternary-N at 400.3 eV, respectively (Fig. 5.38D). Moreover, it is apparent from the area under the curve that the major component corresponded to quaternary-N.

The observed effect of pH in the two cases, AIB and glycine, can be appreciated in terms of the $pK_a(s)$ of these substrates. AIB and glycine has two

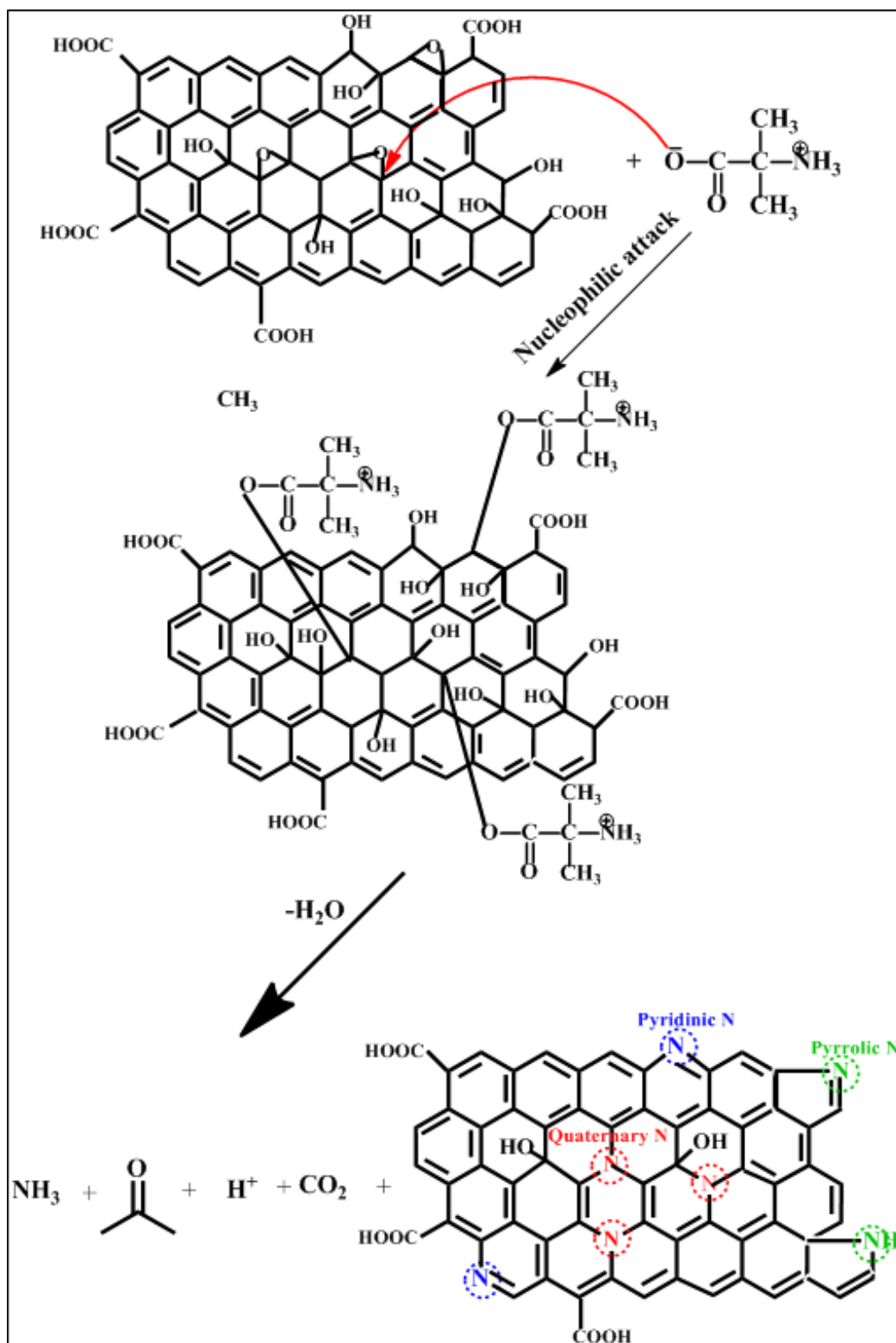
$pK_a(s)$: 2.36 (pK_1) and 10.21 (pK_2); 2.34 (pK_1) and 9.6 (pK_2), respectively. Both AIB as well as glycine exhibit very similar reduction efficiency at high pH. At pH 10.5, it is estimated that about 66% of AIB will be in the basic form, it is likely that the basic AIB acts as a nucleophile through $-NH_2$ and $-COO^-$ groups and attacks the epoxy/hydroxyl group of GO to form an intermediate X, which upon the loss of water at 95/100 °C yield graphene along with other decarboxylation products (Scheme 5.2 and 5.3), respectively. However, from the pK_2 of glycine it is estimated that at pH 10.5, glycine will be more basic (89%), and, therefore, it could act more effectively as nucleophile through $-NH_2$ to that of AIB. But the similar efficiency in the two cases can be understood by a difference in their electronic structure (Fig. 5.25 and 5.1). The +I effect of methyl groups in AIB results in the increased electron density at $-NH_2$ group, which may be contributing to the observed difference. It also explains the same duration of reduction in cases of AIB and glycine at high pH despite of the higher percentage of basic glycine. On the other hand, the pK_1 being similar for the two, at low pH (4.5), the reduction prominently takes place by nucleophilic attack through COO^- (Scheme 5.3), and more time is taken by glycine as compared to that of AIB. It is understood to the electronic effect of two methyl groups in AIB. At low pH it is likely that protonated amino group ($-NH_3^+$) interacts with GO involving cationic- π interaction (Scheme 5.4) as has been earlier reported by J. Wang *et al.* [415].

The formation of acetone and formaldehyde in cases of AIB/glycine along with graphene (Scheme 5.2) were confirmed by performing their chemical analysis. Acetone formation was analyzed by preparing its 2,4-dinitrophenyl hydrazone [416] and the formation of formaldehyde was tested by its characteristic spot test with chromotropic acid [417]. Their formation in the present systems was verified with their respective authentic sample.

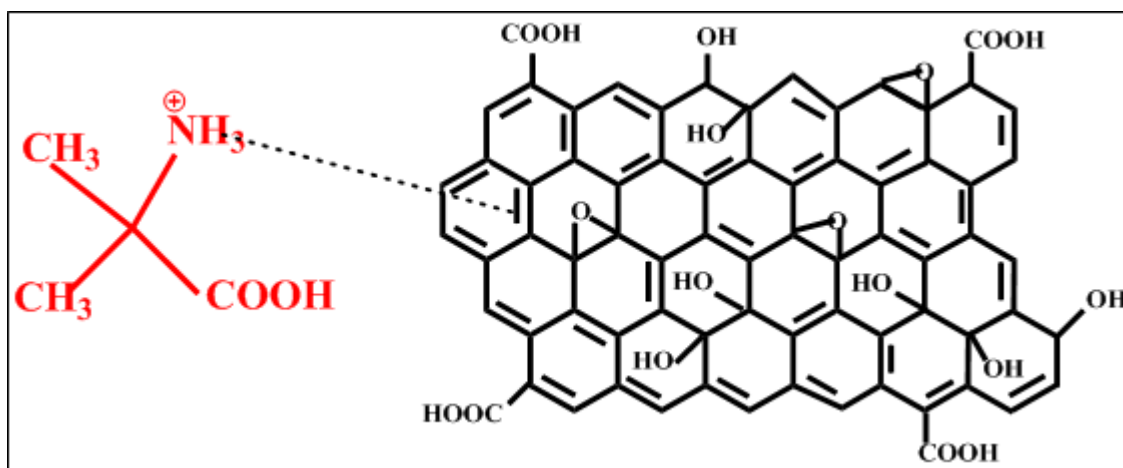
2-aminoisobutyric acid mediated reduction of graphene oxide to produce N-doped graphene – its formation mechanism and energy storage applications



Scheme 5.2: Mechanism showing the nucleophilic attack of $-\text{NH}_2$ group of AIB on the epoxy group of GO and resulting in the formation of N-doped graphene.



Scheme 5.3: Mechanism showing the nucleophilic attack of carboxylic group of AIB on the epoxy group of GO and resulting in the formation of N-doped graphene.



Scheme 5.4: Schematic representation indicating cationic- π interaction of GO with the protonated amino group of AIB.

The high conductivity of GRH-AIB can be explained due to the effective reduction of GO and its functionalization with N (Scheme 5.2). The conductivity of GRH-AIB (6.3 S/cm) is four orders of magnitude higher as compared to that of GO (2.7×10^{-4} S/cm) (Chapter 4). It is worth noting that this value of conductivity is also higher to some of the undoped graphene(s) [272,275,292] as well as N-doped graphene(s) reported previously [326,336,341]. A comparison of the value of conductivity for N-doped graphene (6.3 S/cm) obtained in the present case is much higher to those of N-doped graphene(s) reported earlier by employing reducing agents such as hydrazine (1.13 S/cm) [326], pyrrole (0.45 S/cm) [336] and comparable to that obtained by using aspartic acid as a reducing agent (7 S/cm) [341].

In the present work, the shape of the CV curves for GRH-AIB suggests that the C_s value is mainly contributed due to the EDLC with a minor contribution of pseudo-capacitance arising from the doping of N. Whereas, the CV curves for GRH-Gly shows higher pseudo-capacitance effect contributed by the N-doping which eventually leads to the higher specific capacitance (C_s) in this case. The difference in the values of C_s in two cases is understood in terms of the contribution of different N-moieties. In case of GRH-AIB, the major N-species was observed to be quaternary-N

(Fig. 5.38D), which has been reported to enhance the electron transport through the carbon materials [418]. On the other hand, in case of GRH-Gly the major component corresponded to pyrrolic-N (Fig. 5.16D), which has been considered to provide pseudo-capacitance through the redox reaction between N and proton of electrolyte (H^+) contributing to the overall enhanced C_s possibly by improving the wettability of electrode [340,418]. The previous work on similar system(s) has reported higher C_s in case of N-doped graphene containing major component as pyrrolic-N [419,420]. This is in accordance with the present work employing AIB and glycine as reducing agents, the higher C_s value was observed for GRH-Gly which contains pyrrolic-N as the major contributing species to that of GRH-AIB.

The C_s values of GRH-AIB and GRH-Gly measured from GCD curves is much higher as compared to some of the undoped graphene(s) as well as N-doped graphene(s) synthesized by employing different amino acid(s) as well as other reducing agent(s). A comparison of the C_s values observed in the present work with earlier reported system(s) have been summarized in Table 5.4.

Table 5.4: A Comparison of the specific capacitance (C_s) values of GRH-AIB/GRH-Gly with some previously reported undoped graphene(s) and N-doped graphene(s) produced by employing different amino acids along with other reducing agent(s).

Reducing agent(s)	Specific Capacitance (C_s) from GCD measurements	Ref.
2-Aminoisobutyric acid reduced GO (GRH-AIB)	228 F/g at 1 A/g	This Work
Glycine reduced GO (GRH-Gly)	263 F/g at 1 A/g	This Work
Caffeic acid reduced GO	136 F/g at 1 A/g	274
Microbial reduction of GO by <i>Shewanella</i>	117 F/g at 1 A/g	287
Trigol reduced GO	130 F/g at 1 A/g	379
Double microwave assisted exfoliation of expandable graphite	189 F/g at 1 A/g	392
Ammonia assisted Hydrothermal method to reduce GO	109.9 F/g at 1 A/g	335
Hexamethylenetetramine reduced GO	161 F/g at 0.5 A/g	337
Glycine reduced GO to produce N-doped hydrogel (NGgly)	161 F/g at 3 A/g	340
Arginine reduced GO to produce N-doped hydrogel (NGarg)	105 F/g at 3 A/g	340
Aspartic acid reduced GO to produce N-doped hydrogel (NGasp)	246 F/g at 3 A/g	340
Dimethyl ketoxime reduced GO	141 F/g at 3 A/g	387
Hydrazine monohydrate reduced GO	133 F/g at 1 A/g	393

The high values of C_s for GRH-AIB and GRH-Gly at a current density of 10 A/g after 1000 cycles evidently suggests these systems to be fairly stable. Moreover, the energy density (Wh/kg) values for GRH-AIB (20.26) and GRH-Gly (23.37) are much higher to those reported earlier for some of the N-doped graphene(s) [419,421] and are significantly higher to those of the available commercial supercapacitors [382]. These findings suggest the superior electrochemical properties of GRH-AIB/GRH-Gly and its immense potential for efficient energy storage materials.



Chapter 6

CONCLUSIONS

6. CONCLUSIONS

We have successfully synthesized graphene nanostructures by the reduction of GO employing malonic acid, glycine and 2-aminoisobutyric acid as a mild/environmental benign reducing agents. The effect of various parameters such as concentrations of precursor(s), pH of the media considering its effect on the nucleophilicity of reducing agent(s) and heating time have been investigated systematically by performing the reduction of GO at relatively lower temperature. The effect of changing of these parameters on the morphology and functionalization has also been examined.

The conclusions of the results presented in Chapters 3 to 5 have been furnished below:

In **Chapter 3**, the use of malonic acid as a reducing agent results in the formation of ultrathin graphene sheets under mild experimental conditions of pH (10.5) and temperature (95 °C) in aqueous medium. The presence of active methylene group in malonic acid makes it an effective nucleophile, resulting in its enhanced reducing capability as compared to other dibasic acids, which did not contain active methylene group. IR, Raman, XPS and ¹³C NMR studies indicate the increased graphitic character in reduced GO. These observations are also supported by the significantly higher conductivity of GRH-MA as compared to that of GO. The crystallinity in GRH-MA could be induced under mild thermal conditions of annealing (GRH-MA300) as was revealed by its XRD, Raman, SAED and HRTEM analyses. This sample exhibited further restoration of sp² character and four times higher conductivity with that of GRH-MA. The observation of rectangular shape cyclic voltammogram for GRH-MA covering large area under the curves as compared to that of GO clearly demonstrate it to be a good capacitor with EDLC behavior. The symmetrical triangular shape in GCD

measurements with high value of C_s (177 F/g) at a high current density of 10 A/g suggests it to be a fairly good energy storage material. Moreover, this material exhibits long cycling stability with fairly high coulombic efficiency (100-101%) and energy density/power density (19.55 Wh/kg/400 W/kg).

In **Chapter 4**, we have developed for the first time a one-step wet chemical environmental friendly synthetic route for the production of curl-shaped graphene nanoribbons (GNRs) from GO. GO is reduced to yield GNRs employing malonic acid as a reducing agent in aqueous medium under mild conditions of pH (6.0) and temperature (95 °C). The reduction of GO to GNRs is evidenced by optical, XRD, Raman, IR, XPS and ^{13}C MAS NMR. The entangled nanoribbons are ~ 0.15 to 1 mm long and ~ 150-300 nm wide as was estimated by FESEM and TEM analyses. The residual functionalities on GNRs is revealed by IR, XPS and ^{13}C MAS NMR, which assisted in the process of the growth of carbon nanostructures to yield GNRs involving weak non-covalent bonding. AFM analysis indicates the formation of a few layer GNRs and annealing reduces its thickness to about $1/3^{\text{rd}}$, which is also manifested by more than 3.5 times increase in surface area of GNRs-300 as compared to that of GNRs. The removal of residual functionalities upon annealing at mild temperature of 300 °C (GNRs-300), associated with the development of polycrystallinity, results in their unfolding due to the reduction in supramolecular interactions associated with increased sp^2 character of GNRs. Solid-state ^{13}C NMR spectra of as-synthesized samples demonstrated that the graphitic character follows the order: GNRs-300 > GNRs > GO, which is clearly evidenced by I-V analyses. GNRs modified electrode material exhibited high: specific capacitance (301 F/g at 1A/g), cycling ability (4000 cycles), coulombic efficiency (100%) and energy density (26.76 Wh/kg) at a power density of 400 W/kg.

The **Chapter 5, Section A** reports a one-pot method to synthesize N-doped graphene-Ag (GRH-GlyAg) nanocomposites employing environmental benign reducing agent, glycine in aqueous medium under mild conditions. The *in situ* generation of Ag NPs on the surface of GRH-Gly sheet prevents its aggregation through supramolecular interactions of Ag NPs with different domains of N and π bond containing moieties. These nanocomposites demonstrated its potential for SERS for the detection of 4-ATP at 50 nM. Thus, GRH-GlyAg nanocomposites having high surface area (523 m²/g), conductivity (25.9 S/cm), specific capacitance (346 F/g at 100 mV/s) and SERS activity have been synthesized employing green precursors using relatively low temperature (95 °C) in aqueous medium as compared to those used in previous studies.

The **Chapter 5, Section B** presents an efficient and environmental friendly method for the preparation of N-doped graphene employing thermal approach in both acidic (4.5) as well as basic (10.5) pH range using AIB as functionalizer and reducing agent in aqueous medium. The reduction of GO with AIB has been monitored by UV-Vis, IR, Raman spectroscopy, ¹³C NMR and C/O ratio has been estimated by EDAX analyses. For AIB at a pH of 10.5 (GRH-AIB), it takes less than half the time (3 h) to that in the acidic medium (7 h) (GRL-AIB) for accomplishing the reduction of GO, which are significantly shorter as compared to previous reports on similar system (~ 24 h). GRH-AIB produces a few-layer thick crystalline graphene sheets having six-fold symmetry. Functionalization of reduced GO by AIB introduces N in graphene as was evidenced by IR, ¹³C NMR and XPS analyses. The appearance of D' band in Raman spectrum for GRH-AIB suggests an increase in defects in the reduced GO, possibly involving the introduction of some sp³ defects upon functionalization in sp² graphitic structure. The doping possibly takes place through nucleophilic attack of -NH₂ and -COO⁻ groups of AIB on the epoxy/ hydroxyl group(s) of GO *via* the

formation of an intermediate to yield graphene along with other decarboxylation products. N-doped graphene synthesized by using AIB exhibits fairly high: conductivity (6.3 S/cm), specific capacitance (228 F/g at 1 A/g), cyclic stability (1000 cycles), coulombic efficiency (100 – 101%) and energy density/power density (20.26 Wh/kg/400 W/kg). The reduction efficiency of AIB has been compared with glycine at both pH(s). However, the N-doped graphene synthesized by using glycine exhibits high specific capacitance value than GRH-AIB which is understood due to the difference in the major contributing N-moiety. Thus, the synthesized N-doped graphene sheets by employing amino acid(s) as reducing agent(s) demonstrate their significant potential for supercapacitor applications.

To conclude, in the present thesis we have successfully employed mild/environmental friendly reducing agents for the effective reduction of GO to produce graphene under mild experimental conditions in aqueous medium. The higher nucleophilicity of the malonic acid is observed to be more effective for the efficient reduction of GO to produce thin graphene sheets. The judicious control of pH of the reaction mixture brings a change in the morphology of graphene involving supramolecular interactions among the residual functionalities of reduced GO and malonic acid besides controlling the nucleophilicity of the later. In these systems the annealing of the graphene nanostructures at a mild temperature has been found to be effective for removing the residual functionalities. The changed morphology of graphene exhibit improved characteristic features for the high performance supercapacitor applications.

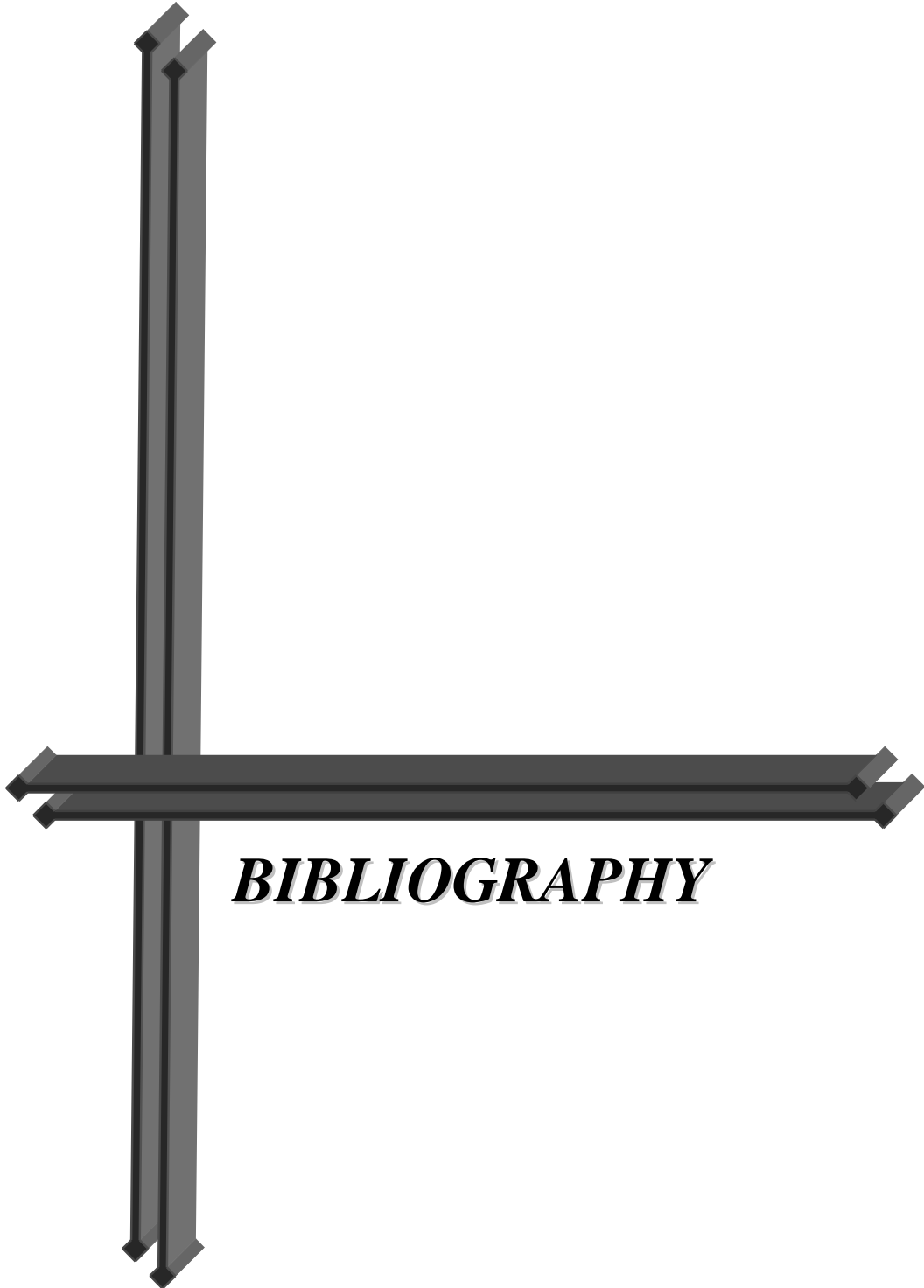
Further, the simultaneous reduction of GO and doping with N has been achieved by using environmental benign amino acids (glycine and AIB) as reducing agents in aqueous medium under acidic and basic pHs. The basic pH has been found to be more effective for the reduction of GO. The doping enhances the characteristic

features of graphene electrode as regards to the conductivity and energy storage capacity. The functionalization of N-doped graphene (GRH-Gly) with Ag NPs further enhanced the multifunctional features as regards to its conductivity, surface area and SERS.

Among the different studied system(s), the supercapacitor efficiencies obtained from the GCD measurements are found to follow the order: GNRs > GRH-Gly > GNRs-300 > GRH-AIB > GRH-MA > GO.

It suggests that the optimization of synthetic protocols in conjunction with the functionalization by suitable dopant(s), and controlling of different factors such as pseudo-capacitance and EDLC are needed to be judiciously worked out for achieving the higher supercapacitor efficiencies.

As regards to the future directions, there is tremendous scope for the development of economical and environmental friendly synthetic protocols for producing graphene in bulk quantities with a precise control on the size, shape and thickness. More research has to be focused on graphene composites for enhancing their physicochemical properties and practical utilization. In particular the synergistic effect of different components of composite(s) might lead to yield high performance supercapacitors.



BIBLIOGRAPHY

Bibliography

1. Feynman, R.P., "There's plenty of room at the bottom," (reprint from speech given at annual meeting of the west of the American Physical Society), *Eng. Sci.*, **23**, 22 (1960).
2. Klabunde, K.J. and Richards, R.M., "Nanoscale materials in chemistry," 2nd Edition, John Wiley & Sons (2009).
3. Georgakilas, V., Perman, J.A., Tucek, J. and Zboril, R., "Broad family of carbon nanoallotropes: classifications, chemistry, and applications of fullerenes, carbon dots, nanotubes, graphene, nanodiamonds and combined superstructures," *Chem. Rev.*, **115**, 4744 (2015).
4. Cao, G., "Nanostructures & nanomaterials synthesis, properties and applications," Imperial College Press (2004).
5. Daniel, M.-C. and Astruc, D., "Gold nanoparticles: assembly, supramolecular chemistry, quantum-size-related properties, and applications toward biology, catalysis, and nanotechnology," *Chem. Rev.*, **104**, 293 (2004).
6. Tiwari, J.N., Tiwari, R.N. and Kim, K.S., "Zero-dimensional, one-dimensional, two-dimensional nanostructured materials for advanced electrochemical energy devices," *Prog. Mater. Sci.*, **57**, 724 (2012).
7. Salata, O.V., "Applications of nanoparticles in biology and medicine," *J. Nanobiotechnol.*, **2**, 3 (2003).
8. Zhang, Y., Zhang, L. and Zhou, C., "Review of chemical vapor deposition of graphene and related applications," *Acc. Chem. Res.*, **46**, 2329 (2013).
9. Bo, Z., Yang, Y., Chen, J., Yu, K., Yan, J. and Cen, K., "Plasma-enhanced chemical vapour deposition synthesis of vertically oriented graphene nanosheets," *Nanoscale*, **5**, 5180 (2013).

Bibliography

10. Subrahmanyam, K.S., Panchakarla, L.S., Govindaraj, A. and Rao, C.N., "Simple method of preparing graphene flakes by an arc-discharge method," *J. Phys. Chem. C Lett.*, **113**, 4257 (2009).
11. Park, S. and Ruoff, R.S., "Chemical methods for the production of graphenes," *Nat. Nanotechnol.*, **4**, 217, (2009).
12. Chua, C.K. and Pumera, M., "Chemical reduction of graphene oxide: a synthetic chemistry viewpoint," *Chem. Soc. Rev.*, **43**, 291 (2014).
13. Xu, Y., Chen, L., Wang, X., Yao, W. and Zhang, Q., "Recent advances in noble metal based composite nanocatalysts: colloidal synthesis, properties, and catalytic applications," *Nanoscale*, **7**, 10559 (2015).
14. Tiano, A.L., Koenigsmann, C., Santulli, A.C. and Wong, S.S., "Solution-based synthetic strategies for one-dimensional metal containing nanostructures," *Chem. Comm.*, **46**, 8093 (2010).
15. Patete, J.M., Peng, X., Koenigsmann, C., Xu, Y., Karn, B. and Wong, S.S., "Viable methodologies for the synthesis of high quality nanostructures," *Green Chem.*, **13**, 482 (2011).
16. Sharma, N., Ojha, H., Bharadwaj, A., Pathak, D.P. and Sharma, R.K., "Preparation and catalytic applications of nanomaterials: a review," *RSC Adv.*, **5**, 53381 (2015).
17. Ghandi, K., Findlater, A.D., Mahimwalla, Z., Macneil, C.S., Awoonor-Williams, E., Zahariev, F. and Gordon, M.S., "Ultra-fast electron capture by electrosterically-stabilized gold nanoparticles," *Nanoscale*, **7**, 11545 (2015).
18. Cho, Y.S., Glicksman, H.D. and Amarakoon, V.R.W., "Encyclopedia of nanoscience and nanotechnology," Ed. Nalwa H.S., American Scientific Publishers, Valencia, California, **1**, 727 (2004).
19. Wu, H., Pan, W., Lin, D. and Li, H., "Electrospinning of ceramic nanofibers: fabrication, assembly and applications," *J. Adv. Ceram.*, **1**, 2 (2012).

Bibliography

20. Basu, B. and Balani, K., "Advanced structural ceramics," John Wiley & Sons (2004).
21. Chao, S. and Fatih, D., "Processing and dielectric properties of TiO₂ thick films for high-energy density capacitor applications," *Int. J. Appl. Ceram. Technol.*, **8**, 1363 (2011).
22. Changchun, Z., Hong, Y. and Zhang, X., "Applications of nanostructures calcium phosphate in tissue engineering," *Biomater. Sci.*, **1**, 1012 (2013).
23. Shi, L., Naik, A.J.T., Goodall, J.B.M, Tighe, C., Gruar, R., Binions, R., Parkin, I. and Darr, J., "Highly sensitive ZnO nanorod- and nanoprism-based NO₂ gas sensors: size and shape control using continuous hydrothermal pilot plant," *Langmuir*, **29**, 10603 (2013).
24. Sutradhar, N., Sinhamahapatra, A., Pahari, S.K., Pal, P., Bajaj, H.C., Mukhopadhyay I. and Panda, A.B., "Controlled synthesis of different morphologies of MgO and their use as solid base catalysts," *J. Phys. Chem. C*, **115**, 12308 (2011).
25. Gaur, U.K., Kumar, A. and Varma, G.D., "Fe-induced morphological transformation of 1-D CuO nanochains to porous nanofibres with enhanced optical, magnetic and ferroelectric properties," *J. Mater. Chem. C*, **3**, 4297 (2015).
26. Joo, J.B., Dahl, M., Li, N., Zaera, F. and Yin, Y., "Tailored synthesis of mesoporous TiO₂ hollow nanostructures for catalytic applications," *Energy Environ. Sci.*, **6**, 2082 (2013).
27. Xiang, J.Y., Tu, J.P., Zhang, L., Zhou, Y., Wang, X.L. and Shi, S.J., "Self-assembled synthesis of hierarchical nanostructured CuO with various morphologies and their application as anodes for lithium ion batteries," *J. Power Sources*, **195**, 313 (2010).
28. Zhang, Q., Zhang, K., Xu, D., Yang, G., Huang, H., Nie, F., Liu, C. and Yang, S., "CuO nanostructures: synthesis, characterization, growth mechanism, fundamental properties, and application," *Prog. Mater. Sci.*, **60**, 208 (2014).

Bibliography

29. Wang, C., Li, Q., Wang, F., Xia, G., Liu, R., Li, D., Li, N., Spendelow, J.S. and Wu, G., "Morphology-dependent performance of CuO anodes via facile and controllable synthesis for lithium-ion batteries," *ACS Appl. Mater. Interfaces*, **6**, 1243 (2014).
30. Tian, J., Zhao, Z., Kumar, A., Boughton, R.I. and Liu, H., "Recent progress in design, synthesis, and applications of one-dimensional TiO₂ nanostructured surface heterostructures: a review," *Chem. Soc. Rev.*, **43**, 6920 (2014).
31. Kaur, J. and Pal, B., "Selective formation of benzo[c]cinnoline by photocatalytic reduction of 2, 2'-dinitrobiphenyl using TiO₂ and under UV light irradiation," *Chem. Comm.*, **51**, 8500 (2015).
32. Chen, X. and Mao, S.S., "Titanium dioxide nanomaterials: synthesis, properties, modifications and applications," *Chem. Rev.*, **107**, 2891 (2007).
33. Mondal, C., Sinha, A.K., Ganguly, M., Pal, J., Dhara, S., Negishi, Y. and Pal, T., "Deposition of zinc oxide nanomaterial on different substrates for useful application," *CrystEngComm*, **16**, 4322 (2014).
34. Moezzi, A., McDonagh, A.M. and Cortie, M.B., "Zinc oxide particles: synthesis, properties and applications," *Chem. Eng. J.*, **185-186**, 1 (2012).
35. Zhang, X., Zheng, Y., Yang, H., Wang, Q. and Zhang, Z., "Controlled synthesis of mesocrystal magnesium oxide parallelogram and its catalytic performance," *CrystEngComm*, **17**, 2642 (2015).
36. Zhang, L., Zhu, W., Zhang, H., Bi, S. and Zhang, Q., "Hydrothermal-thermal conversion synthesis of hierarchical porous MgO microrods as efficient adsorbents for lead (II) and chromium (VI) removal," *RSC Adv.*, **4**, 30542 (2014).
37. Wang, F., Ta, N. and Shen, W.J., "MgO nanosheets, nanodisks, and nanofibres for the Meerwein-Ponndorf-Verley reaction," *Appl. Catal. A*, **475**, 76 (2014).

Bibliography

38. Gangwar, J., Gupta, B.K., Tripathi, S.K. and Srivastava, A.K., "Phase dependent thermal and spectroscopic responses of Al₂O₃ nanostructures with different morphologies," *Nanoscale*, **7**, 13313 (2015).
39. Shen, S., Ng, W.K., Chia, L.S.O., Dong, Y. and Tan, R.B.G., "Morphology controllable synthesis of nanostructured boehmite and γ -alumina by facile dry gel conversion," *Crys. Growth Des.*, **12**, 4987 (2012).
40. Sharma, Y.C., Srivastava, V. and Mukherjee, A.K., "Synthesis and application of nano-Al₂O₃ powder for the reclamation of hexavalent chromium from aqueous solutions," *J. Chem. Eng. Data*, **55**, 2390 (2010).
41. Devan, R.S., patil, R.A., Lin, J.-H. and Ma, Y.-R., "One-dimensional metal-oxide nanostructures: Recent developments in synthesis, characterization, and applications," *Adv. Funct. Mater.*, **22**, 3326 (2012).
42. Matteo, F., Pineda, A., Romero, A.A., Colmenares, J.C., Vargas, C., Monteleone, M. and Luque, R., "Efficient and simple reactive milling preparation of photocatalytically active porous ZnO nanostructures using biomass derived polysaccharides," *Green Chem.*, **16**, 2876 (2014).
43. Yin, Z.F., Wu, L., Yang, H.G. and Su, Y.H., "Recent progress in biomedical applications of titanium dioxide," *Phys. Chem. Chem. Phys.*, **15**, 4844 (2013).
44. Alex, W., Westerhoff, P., Fabricius, L., Hristovski, K. and von Goetz, N., "Titanium dioxide nanoparticles in food and personal care products," *Environ. Sci. Technol.*, **46**, 2242 (2012).
45. Weintraub, B., Zhou, Z., Li, Y. and Deng, Y., "Solution synthesis of one-dimensional ZnO nanomaterials and their applications," *Nanoscale*, **2**, 1573 (2010).
46. Zhang, Y., Nayak, T.R., Hong, H. and Cai, W., "Biomedical application of zinc oxide nanomaterials," *Curr Mol Med.*, **13**, 1633 (2013).

Bibliography

47. Espitia, P.J.P., Soares, N.D.F.F., Coimbra, J.S.D.R., Andrade, N.J.D., Cruz, R.S. and Medeiros, E.A.A., "Zinc oxide nanoparticles: synthesis, antimicrobial activity and food packaging applications," *Food Bioprocess. Technol.*, **5**, 1447 (2012).
48. Patel, M.K., Ali, M.A., Zafaryab M., Agrawal, V.V., Rizvi, M.M.A., Ansari, Z.A., Ansari, S.G. and Malhotra, B.D., "Biocompatible nanostructured magnesium oxide-chitosan platform for genosensing application," *Biosens. Bioelectron.*, **45**, 181 (2013).
49. Hua, M., Zhang, S., Pan, B., Zhang, W., Lv, L. and Zhang, Q., "Heavy metal removal from water/wastewater by nanosized metal oxides: a review," *J. Hazard. Mater.*, **211-212**, 317 (2012).
50. Jin, T. and He, Y., "Antibacterial activities of magnesium oxide (MgO) nanoparticles against foodborne pathogens," *J. Nanopart. Res.*, **13**, 6877 (2011).
51. Kim, B.-N., Hiraga, K., Morita, K. and Sakka, Y., "A high-strain-rate superplastic ceramic," *Nature*, **413**, 288 (2001).
52. Li, G., Jiang, Z., Jiang, A. and Zhang, L., "Strengthening of porous Al₂O₃ ceramics through nanoparticle addition," *Nanostruct. Mater.*, **8**, 749 (1997).
53. Jansen, M., "High performance non-oxide ceramics I (structure and bonding)," Springer-Verlag Berlin Heidelberg (2002).
54. Eddy, C.R. and Gaskill, D.K., "Silicon carbide as a platform for power electronic," *Science*, **324**, 1398 (2009).
55. Xu, J., Liu, Y.-M., Xue, B., Li, Y.-X., Cao, Y. and Fan, K.-N., "A hybrid sol-gel synthesis of mesostructured SiC with tunable porosity and its application as a support for propane oxidative dehydrogenation," *Phys. Chem. Chem. Phys.*, **13**, 10111 (2011).
56. Johnson, J.C., Choi, H.-J., Knutsen, K.P., Schaller, R.D., Yang, P. and Saykally, R.J., "Single gallium nitride nanowire lasers," *Nature Mater.*, **1**, 106 (2002).
57. Naslain, R., "Design, preparation and properties of non-oxide CMCs for application in engines and nuclear reactors: an overview," *Compos. Sci. Technol.*, **64**, 155 (2004).

Bibliography

58. Yakimova, R., Petoral, R.M.Jr., Yazdi, G.R., Vahlberg, C., Spetz, A.L. and Uvdal, K., "Surface functionalization and biomedical applications based on SiC," *J. Phys. D: Appl. Phys.*, **40**, 6435 (2007).
59. Nabi, G., Cao, C., Hussain, S., Khan, W.S., Sagar, R.R., Ali, Z., Butt, F.K., Usman, Z. and Yu, D., "Synthesis, photoluminescence and field emission properties of well aligned/well patterned conical shape GaN nanorods," *CrystEngComm*, **14**, 8492 (2012).
60. Lei, W., Liu, D., Zhang, J., Liu, B., Zhu, P., Cui, T., Cui, Q. and Zou, G., "AlN nanostructures: tunable architectures and optical properties," *Chem. Commun.*, 1365 (2009).
61. Cao, T., Cheng, Y., Zhang, H., Yan, B. and Cheng, Y., "High rate fabrication of room temperature red photoluminescence SiC nanocrystals," *J. Mater. Chem. C*, **3**, 4876 (2015).
62. Dhiman, R., Johnson, E., Skou, E.M., Morgen, P. and Andersen, S.M., "SiC nanocrystals as pt catalyst supports for fuel cell applications," *J. Mater. Chem. A*, **1**, 6030 (2013).
63. Hu, P., Dong, S., Gui, K., Deng, X. and Zhang, X., "Ultra-long SiC nanoires synthesized by a simple method," *RSC Adv.*, **5**, 66403 (2015).
64. Choi, J.H., Ahn, H.Y., Lee, Y.S., Park, K., Kim, T.-H., Cho, K.S., Baik, C.W., Kim, S.II., Yoo, H., Lee, E.H., Choi, B.L., Kim, S.-D., Kim, Y.-W., Kim, M. and Hwang, S., "GaN light-emitting diodes on glass substrates with enhanced electroluminescence," *J. Mater. Chem.*, **22**, 22942 (2012).
65. Coffey, J.L., Johnson, M.A. and Zhang, L., "Influence of precursor route on the photoluminescence of bulk nanocrystalline gallium nitride," *Chem. Mater.*, **9**, 2671 (1997).

Bibliography

66. Wu, Q., Liu, N., Zhang, Y., Qian, W., Wang, X. and Hu, Z., "Tuning the fireld emission properties of AlN nanocones by doping," *J. Mater. Chem. C*, **3**, 1113 (2015).
67. Zheng, J., Yang, Y., Yu, B., Song, X. and Li, X., "[0001] oriented aluminium nitride one-dimensional nanostructures: synthesis, structure evolution, and electrical properties," *ACS Nano*, **2**, 134 (2008).
68. Fuchs, F., Soltamov, V.A., V ath, S., Baranov, P.G., Mokhov, E.N., Astakhov, G.V. and Dyakonov, V., "Silicon carbide light-emitting diode as a prospective room temperature source for single photons," *Sci. Rep.*, **3**, 1637 (2013).
69. Kumari, T.S.D., Jeyakumar, D. and Kumar, T.P., "Nano silicon carbide: a new lithium-insertion anode material on the horizon," *RSC Adv.*, **3**, 15028 (2013).
70. Pearton, S.J. and Ren, F., "GaN electronics," *Adv. Mater.*, **12**, 1571 (2000).
71. Jewett, S.A., Makowski, M.S., Andrews, B., Manfra, M.J. and Ivanisevic, A., "Gallium nitride is biocompatible and non-toxic before and after functionalization with peptides," *Acta Biomater.*, **8**, 728 (2012).
72. Foster, C.M., Collazo, R., Sitar, Z. and Ivanisevic, A., "Aqueous stability of Ga- and N-polar gallium nitride," *Langmuir*, **29**, 216 (2013).
73. Ionescu, E., Kleebe, H.-J. and Riedel, R., "Silicon-containing polymer derived ceramic nanocomposites (PDC-NCs): preparative approaches and properties," *Chem. Soc. Rev.*, **41**, 5032 (2012).
74. Zaheer, M., Schmalz, T., Motz, G. and Kempe, R., "Polymer derived non-oxide ceramics modified with late transition metals," *Chem. Soc. Rev.*, **41**, 5102 (2012).
75. Walker, L.S., Marotto, V.R., Rafiee, M.A., Koratkar, N. and Corral, E.L., "Toughening in graphene ceramic composites," *ACS Nano*, **5**, 3182 (2011).
76. Chen, K., Fang, M., Huang, Z., Huang, J. and Liu, Y.G., "Catalytic synthesis and growth mechanism of SiC@SiO₂ nanowires and their photoluminescence properties," *CrysEngComm*, **15**, 9032 (2013).

Bibliography

77. Zhan, G.-D. and Mukherjee, A.K., "Carbon nanotube reinforced alumina-based ceramics with novel mechanical, electrical, and thermal properties," *Int. J. Appl. Ceram. Technol.*, **1**, 161 (2004).
78. Jiang, L. and Gao, L., "Carbon nanotubes-magnetite nanocomposites from solvothermal processes: formation, characterization, and enhanced electrical properties," *Chem. Mater.*, **15**, 2848 (2003).
79. Kaur, R. and Pal, B., "Plasmonic coinage metal-TiO₂ hybrid nanocatalysts for highly efficient photocatalytic oxidation under sunlight irradiation," *New J. Chem.*, **39**, 5966 (2015).
80. Dong, X., Cao, Y., Wang, J., Chan-Park., M.B., Wang, L., Huang, W. and Chen, P., "Hybrid structure of zinc oxide nanorods and three dimensional graphene foam for supercapacitor and electrochemical sensor applications," *RSC Adv.*, **2**, 4364 (2012).
81. Huang, C., Zhou, Y., Tang, Z., Guo, X., Qian, Z. and Zhou, S., "Synthesis of multifunctional Fe₃O₄ core/hydroxyapatite shell nanocomposites by biomineralization," *Dalton Trans.*, **40**, 5026 (2011).
82. Li, J. and Zhang, J.Z., "Optical properties and applications of hybrid semiconductor nanomaterials," *Coord. Chem. Rev.*, **253**, 3015 (2009).
83. Cohen, M.L. and Chelikowsky, J.R., "Electronic structure and optical properties of semiconductors," 2nd Edition, Springer-Verlag (2012).
84. Demortière, A., Panissod, P., Pichon, B.P., Pourroy, G., Guillon, D., Donnio, B. and Bègin-Colin, S., "Size-dependent properties of magnetic iron oxide nanocrystals," *Nanoscale*, **3**, 225 (2011).
85. Lai, C.-H., Lu, M.-Y. and Chen, L.-J., "Metal sulfide nanostructures: synthesis, properties and applications in energy conversion and storage," *J. Mater. Chem.*, **22**, 19 (2012).

Bibliography

86. Liu., B., Chen, R., Xu, X.L., Li, D.H., Zhao, Y.Y., Shen, Z.X., Xiong, Q.H. and Sun, H.D., "Exciton – related photoluminescence and lasing in CdS nanobelts," *J. Phys. Chem. C*, **115**, 12826 (2011).
87. Li, J. and Wu, N., "Semiconductor – based photocatalysts and photoelectrochemical cells for solar fuel generation: a review," *Catal. Sci. Technol.*, **5**, 1360 (2015).
88. Xiao, G., Wang, Y., Ning, J., Wei, Y., Liu, B., Yu, W.W., Zou, G. and Zou, B., "Recent advances in IV-VI semiconductor nanocrystals: synthesis, mechanism and applications," *RSC Adv.*, **3**, 8104 (2013).
89. Li, X. and Coffey, J.L., "Effect of pressure on the photoluminescence of polynucleotide-stabilized cadmium sulfide nanocrystals," *Chem. Mater.*, **11**, 2326 (1999).
90. Kumar, A. and Kumar, V., "Biotemplated inorganic nanostructures: supramolecular directed nanosystems of semiconductor(s)/metal(s) mediated by nucleic acids and their properties," *Chem. Rev.*, **114**, 7044 (2014).
91. Zhao, X., Jin, W., Cai, J., Ye, J., Li, Z., Ma, Y., Xie, J. and Qi, L., "Shape- and size-controlled synthesis of uniform anatase TiO₂ nanocuboids enclosed by active {100} and {001} facets," *Adv. Funct. Mater.*, **21**, 3554 (2011).
92. Utama, M.I.B., Zhang, J., Chen, R., Xu, X., Li, D., Sun, H. and Xiong, Q., "Synthesis and optical properties of II-VI 1D nanostructures," *Nanoscale*, **4**, 1422 (2012).
93. Burda, C., Chen, X., Narayanan, R. and El-Sayed, M.A., "Chemistry and properties of nanocrystals of different shapes," *Chem. Rev.*, **105**, 1025 (2005).
94. Gao, M-R., Xu, Y.-F., Jiang, J. and Yu, S.-H., "Nanostructured metal chalcogenides: synthesis, modification, and applications in energy conversion and storage devices," *Chem. Soc. Rev.*, **42**, 2986 (2013).
95. Zhuang, Z., Peng, Q. and Li, Y., "Controlled synthesis of semiconductor nanostructures in the liquid phase," *Chem. Soc. Rev.*, **40**, 5492 (2011).

Bibliography

96. Mo, Y.-m., Tang, Y., Gao, F., Yang, J. and Zhang, Y.-m., "Synthesis of fluorescent CdS quantum dots of tunable light emission with a new in situ produced capping agent," *Ind. Eng. Chem. Res.*, **51**, 5995 (2012).
97. Singh, S., Rath, M.C., Singh, A.K., Mukherjee, T., Jayakumar, O.D., Tyagi, A.K. and Sarkar, S.K., "CdSe nanoparticles grown via radiolytic methods in aqueous solutions," *Radiat. Phys. Chem.*, **80**, 736 (2011).
98. Kan, S., Aharoni, A., Mokari, T. and Banin, U., "Shape control of III-V semiconductor nanocrystals: synthesis and properties of InAs quantum dots," *Faraday Discuss.*, **125**, 23 (2004).
99. Dick, K.A. and Caroff, P., "Metal-seeded growth of III-V semiconductor nanowires: towards gold-free synthesis," *Nanoscale*, **6**, 3006 (2014).
100. Lu, A.-H., Salabas, E.L. and Schüth, F., "Magnetic nanoparticles: synthesis, protection, functionalization, and application," *Angew. Chem. Int. Ed.*, **46**, 1222 (2007).
101. Lu, J.G., Chang, P. and Fan, Z., "Quasi-one-dimensional metal oxide materials- synthesis, properties and applications," *Mater. Sci. and Eng*, **52**, 49 (2006).
102. Lewis, D.J., Kevin, P., Bakr, O., Muryn, C.A., Malik, M.A. and O'Brien, P., "Routes to tin chalcogenides materials as thin films or nanoparticles: a potentially important class of semiconductor for sustainable solar energy conversion," *Inorg. Chem. Front.*, **1**, 577 (2014).
103. Boadi, N.O., Malik, M.A., O'Brien, P. and Awudza, A.M., "Single source molecular precursor routes to lead chalcogenide," *Dalton Trans.*, **41**, 10497 (2012).
104. Urbanova, V., Magro, M., Gedanken, A., Baratella, D., Vianello, F. and Zboril, R., "Nanocrystalline iron oxides, composites, and related materials as a platform for electrochemical, magnetic, and chemical biosensors," *Chem. Mater.*, **26**, 6653 (2014).

Bibliography

105. Zhang, N., Liu, S. and Xu, Y.-J., "Recent progress on metal core@semiconductor shell nanocomposites as a promising type of photocatalysts," *Nanoscale*, **4**, 2227 (2012).
106. Reiss, P., Couderc, E., Girolamo, J.D. and Pron, A., "Conjugated polymers/semiconductor nanocrystals hybrid materials-preparation, electrical transport properties and application," *Nanoscale*, **3**, 446 (2011).
107. Kumar, A. and Kumar, V., "Supramolecular-directed synthesis of RNA-mediated CdS/ZnS nanotubes," *Chem. Commun.*, 5433 (2009).
108. Gao, N. and Fang, X., "Synthesis and development of graphene-inorganic semiconductor nanocomposites," *Chem. Rev.*, **115**, 8294 (2015).
109. Kumar, A. and Singhal, A., "Optical and magnetic behavior of Ag encapsulated β -Fe₂O₃ core-shell hollow nanotubes," *Mater. Chem. Phys.*, **131**, 230 (2011).
110. Agnihotri, S., Bajaj, G., Mulherji, S. and Mukherji, S., "Arginine-assisted immobilization of silver nanoparticles on ZnO nanorods: an enhanced and reusable antibacterial substrate without human cell cytotoxicity," *Nanoscale*, **7**, 7415 (2015).
111. Khan, M.M., Ansari, S.A., Amal, M.I., Lee, J. and Cho, M.H., "Highly visible light active Ag@TiO₂ nanocomposites synthesized using an electrochemically active biofilm: a novel biogenic approach," *Nanoscale*, **5**, 4427 (2013).
112. Kumar, A. and Chaudhary, V., "Time resolved emission studies of Ag-adenine-templated CdS (Ag/CdS) nano hybrids," *Nanotechnology*, **20**, 095703 (2009).
113. Hu, W., Liu, H., Ye, F., Ding, Y. and Yang, J., "A facile route for the synthesis of PbSe-Au nanocomposites with different morphologies," *CrystEngComm*, **14**, 7049 (2012).
114. Dunpall, R., Lewis, E.A., Haigh, S.J., O'Brien, P. and Revaprasadu, N., "Synthesis of biocompatible Au-ZnTe core-shell nanoparticles," *J. Mater. Chem. B*, **3**, 2826 (2015).

Bibliography

115. Leung, K.C.-F., Xuan, S., Zhu, X., Wang, D., Chak, C.-P., Lee, S.-F., Ho, W.K.-W. and Chung, B.C.-T., "Gold and iron oxide hybrid nanocomposites materials," *Chem. Soc. Rev.*, **41**, 1911 (2012).
116. Herring, N.P., AbouZeid, K., Mohamed, M.B., Pinks, J. and El-Shall, M.S., "Formation mechanism of gold-zinc oxide hexagonal nanopyramids by heterogeneous nucleation using microwave synthesis," *Langmuir*, **27**, 15146 (2011).
117. Hao, B., Yan, Y., Wang, X. and Chen, G., "Biomimetic layer-by-layer co-mineralization approach towards TiO₂/Au nanosheets with high rate performance for lithium ion batteries," *Nanoscale*, **5**, 10472 (2013).
118. Shanmugapriya, T. and Ramamurthy, P., "Photoluminescence enhancement of nanogold decorated CdS quantum dots," *J. Phys. Chem. C*, **117**, 12272 (2013).
119. Kumar, A. and Singhal, A., "Optical, photophysical and magnetic behavior of GMP-templated binary (β -Fe₂O₃/CdS) and ternary (β -Fe₂O₃/Ag/CdS) nanohybrids," *J. Mater. Chem.*, **21**, 481 (2011).
120. Kumar, A. and Jakhmola, A., "Photophysics and charge dynamics of Q-PbS based mixed ZnS/PbS and PbS/ZnS semiconductor nanoparticles," *J. Colloid Interface Sci.*, **297**, 607 (2006).
121. Kumar, A., Jakhmola, A. and Chaudhary, V., "Synthesis and photophysics of colloidal ZnS/PbS/ZnS nanocomposites-An analysis of dynamics of charge carriers," *J. Photochem. Photobiol. A*, **208**, 195 (2009).
122. Feng, Y., Feng, N., Wei, Y. and Zhang, G., "An *in situ* gelatin-assisted hydrothermal synthesis of ZnO-reduced graphene oxide composites with enhanced photocatalytic performance under ultraviolet and visible light," *RSC Adv.*, **4**, 7933 (2014).
123. Daniel, M.-C. and Astruc, D., "Gold nanoparticles: assembly, supramolecular chemistry, quantum-size-related properties, and applications toward biology, catalysis, and nanotechnology," *Chem. Rev.*, **104**, 293 (2004).

Bibliography

124. Link, S. and El-Sayed, M., "Optical properties ultrafast dynamics of metallic nanocrystals," *Annu. Rev. Chem.*, **54**, 331 (2003).
125. Feldheim, D.L. and Foss, C.A., "Metal nanoparticles: synthesis, characterization, and applications," Marcel Dekker, Inc. (2002).
126. Arvizo, R.R., Bhattacharyya, S., Kudgus, R.A., Giri, K., Bhattacharya, R. and Mukherjee, P., "Intrinsic therapeutic application of noble metal nanoparticles: past, present and future," *Chem. Soc. Rev.*, **41**, 2943 (2012).
127. Polavarapu, L., Mourdikoudis, S., Pastoriza-Santos, I. and Pérez-Juste, J., "Nanocrystal engineering of noble metals and metal chalcogenides: controlling the morphology, composition and crystallinity," *CrystEngComm*, **17**, 3727 (2015).
128. Guo, S. and Wang, E., "Synthesis and electrochemical applications of gold nanoparticles," *Anal. Chim. Acta*, **598**, 181 (2007).
129. Cheong, S., Watt, J.D. and Tilley, R.D., "Shape control of platinum and palladium nanoparticles for catalysis," *Nanoscale*, **2**, 2045 (2010).
130. Link, S. and El-Sayed, M., "Spectral properties and relaxation dynamics of surface plasmon electronic oscillations in gold and silver nanodots and nanorods," *J. Phys. Chem. B*, **103**, 8410 (1999).
131. Link, S., Mohamed, M.B. and El-Sayed, M.A., "Simulation of the optical absorption spectra of gold nanorods as a function of their aspect ratio and the effect of the medium dielectric constant," *J. Phys. Chem. B*, **103**, 3073 (1999).
132. Campion, A. and Kambhampati, P., "Surface-enhanced Raman scattering," *Chem. Soc. Rev.*, **27**, 241 (1998).
133. Betz, J.F., Yu, W.W., Cheng, Y., White, I.M. and Rubloff, G.W., "Simple SERS substrates: powerful, portable, and full of potential," *Phys. Chem. Chem. Phys.*, **16**, 2224 (2014).

Bibliography

134. Sharma, B., Frontiera, R.R., Henry, A.-I., Ringe, E. and Duynes, R.P.V., "SERS: materials, applications and the future," *Mater. Today*, **15**, 16 (2012).
135. Nie, S. and Emory, S.R., "Probing single molecules and single nanoparticles by surface-enhanced Raman scattering," *Science*, **275**, 1102 (1997).
136. Wiley, B., Sun, Y. and Xia, Y., "Synthesis of silver nanostructures with controlled shapes and properties," *Acc. Chem. Res.*, **40**, 1067 (2007).
137. Punties, V.F., Krishnan, K.M. and Alivisatos, A.P., "Colloidal nanocrystal shape and size control: the case of cobalt," *Science*, **291**, 2115 (2001).
138. You, H., Yang, S., Ding, B. and Yang, H., "Synthesis of colloidal metal and metal alloy nanoparticles for electrochemical energy applications," *Chem. Soc. Rev.*, **42**, 2880 (2013).
139. Monga, A. and Pal, B., "Morphological and physicochemical properties of Ag-Au binary nanocomposites prepared using different surfactant capped Ag nanoparticles," *RSC Adv.*, **5**, 39954 (2015).
140. Ahmadi, T.S., Wang, Z.L., Green, T.C., Henglein, A. and El-Sayed, M.A., "Shape-controlled synthesis of colloidal platinum nanoparticles," *Science*, **272**, 1924 (1996).
141. Toshima, N. and Yonezawa, T., "Bimetallic nanoparticles-novel materials for chemical and physical applications," *New J. Chem.*, **22**, 1179 (1998).
142. Sankar, M., Dimitratos, N., Miedziak, P.J., Wells, P.P., Kiely, C.J. and Hutchings, G.J., "Designing bimetallic catalysts for a green and sustainable future," *Chem. Soc. Rev.*, **41**, 8099 (2012).
143. Gu, J., Zhang, Y.-W. and Tao, F., "Shape control of bimetallic nanocatalysts through well-designed colloidal chemistry approaches," *Chem. Soc. Rev.*, **41**, 8050 (2012).
144. Panáček, A., Kvítek, L., Pucek, R., Kolář, M., Večeřová, R., Pizúrová, N., Sharma, V.K., Nevěčná, T. and Zboril, R., "Silver colloid nanoparticles: synthesis,

Bibliography

- characterization, and their antibacterial activity,” *J. Phys. Chem. B*, **110**, 16248 (2006).
145. Zhang, J., Li, X., Sun, X. and Li, Y., “Surface enhanced Raman scattering effects of silver colloids with different shapes,” *J. Phys. Chem. B*, **109**, 12544 (2005).
146. El-Nour, K.M.M.A., Eftaiha, A., Al-Warthan, A. and Ammar, R.A.A., “Synthesis and applications of silver nanoparticles,” *Arab. J. Chem.*, **3**, 135 (2010).
147. Premkumar, T. and Geckeler, K.E., “Facile synthesis of silver nanoparticles using unmodified cyclodextrin and their surface-enhanced Raman scattering activity,” *New J. Chem.*, **38**, 2847 (2014).
148. Alam, M.M., Ji, W., Luitel, H.M., Ozaki, Y., Watari, T. and Nakashima, K., “Template free synthesis of dendritic silver nanostructures and their application in surface-enhanced Raman scattering,” *RSC Adv.*, **4**, 52686 (2014).
149. Saha, S., Pal, A., Kundu, S., Basu, S. and Pal, T., “Photochemical green synthesis of calcium-alganite and their catalytic application to 4-nitrophenol reduction,” *Langmuir*, **26**, 2885 (2010).
150. Li, H.B., Liu, Y., Liang, Y., Xiao, J. and Yang, G.W., “Super-SERS-active and highly effective antimicrobial Ag nanodendrites,” *Nanoscale*, **4**, 5082 (2012).
151. Hirsch, A., “The era of carbon allotropes,” *Nature Mater.*, **9**, 868 (2010).
152. Dresselhaus, M.S. and Terrones, M., “Carbon-based nanomaterials from a historical perspective,” *Proc. IEEE*, **101**, 1522 (2013).
153. Mukhopadhyay, P. and Gupta, R.K., “Graphite, graphene and their polymer nanocomposites,” CRC Press, Taylor & Francis Group (2013).
154. Kidalov, S.V. and Shakhov, F.M., “Thermal conductivity of diamond composites,” *Materials*, **2**, 2467 (2009).
155. Kroto, H.W., Heath, J.R., O’Brien, S.C., Curl, R.F. and Smalley, R.E., “C60: Buckminsterfullerene,” *Nature*, **318**, 162 (1985).

Bibliography

156. Krätschmer, W., Lamb, L.D., Fostiropoulos, K. and Huffman, D.R., "Solid C₆₀: a new form of carbon," *Nature*, **347**, 354 (1990).
157. Iijima, S., "Helical microtubules of graphitic carbon," *Nature*, **354**, 56 (1991).
158. Boehm, H.P., Clauss, A., Fischer, G.O. and Hofmann, U., "Dünnsche Kohlenstoff-Folien," *Z. Naturforsch.*, **17**, 150 (1962).
159. Boehm, H.P., Clauss, A., Fischer, G.O. and Hofmann, U., "Das adsorptionsverhalten sehr dünner kohlenstoff-folien," *Anorg. Allg. Chem.*, **316**, 119 (1962).
160. Novoselov, K.S., Geim, A.K., Morozov, S.V., Jiang, D., Zhang, Y., Dubonos, S.V., Grigorieva, I.V. and Firsov, A.A., "Electric field effect in atomically thin carbon films," *Science*, **306**, 666 (2004).
161. Novoselov, K.S., "Nobel lecture: Graphene: materials in the flatland," *Rev. Mod. Phys.*, **83**, 837 (2011).
162. Prato, M., "[60] Fullerene chemistry for materials science applications," *J. Mater. Chem.*, **7**, 1097 (1997).
163. Lu, X. and Chen, Z., "Curved Pi-conjugation, aromaticity, and the related chemistry of small fullerenes (< C₆₀) and single-walled carbon nanotubes," *Chem. Rev.*, **105**, 3643 (2005).
164. Diederich, F. and Whetten, R.L., "Beyond C₆₀: The higher fullerenes," *Acc. Chem. Res.*, **25**, 119 (1992).
165. Krueger, A., "Carbon materials and nanotechnology," Wiley-VCH Verlag GmbH & Co. KGaA, Weinheim (2010).
166. Scrivens, W.A. and Tour, J.M., "Synthesis of gram quantities of C₆₀ by plasma discharge in a modified round-bottom flask. Key parameters for yield optimization and purification," *J. Org. Chem.*, **57**, 6932 (1992).
167. Scott, L.T., "Methods for the chemical synthesis of fullerenes," *Angew. Chem. Int. Ed.*, **43**, 4994 (2004).

Bibliography

168. Ruoff, R.S., Tse, D.S., Malhotra, R. and Lorents, D.C., "Solubility of C₆₀ in a variety of solvents," *J. Phys. Chem.*, **97**, 3379 (1993).
169. Nath, S., Pal, H., Palit, D.K., Sapre, A.V. and Mittal J.P., "Aggregation of fullerene, C₆₀ in benzonitrile," *J. Phys. Chem. B*, **102**, 10158 (1998).
170. Ghosh, H.N., Sapre, A.V. and Mittal, J.P., "Aggregation of C₇₀ in solvent mixtures," *J. Phys. Chem.*, **100**, 9439 (1996).
171. Bonifazi, D., Enger, O. and Diederich, F., "Supramolecular [60]fullerene chemistry on surfaces," *Chem. Soc. Rev.*, **36**, 390 (2007).
172. Palit, D.K., Sapre, A.V., Mittal, J.P. and Rao, C.N.R., "Photophysical properties of the fullerenes, C₆₀ and C₇₀," *Chem. Phys. Lett.*, **195**, 1 (1992).
173. Jariwala, D., Sangwan, V.K., Lauhon, L.J., Marks, T.J. and Hersam, M.C., "Carbon nanomaterials for electronics, optoelectronics, photovoltaics, and sensing," *Chem. Soc. Rev.*, **42**, 2824 (2013).
174. Li, Q., Mahendra, S., Lyon, D.Y., Brunet, L., Liga, M.V., Li, D. and Alvarez, P.J.J., "Antimicrobial nanomaterials for water disinfection and microbial control: potential applications and implications," *Water Res.*, **42**, 4591 (2008).
175. Bosi, S., Ros, T.D., Spalluto, G. and Prato, M., "Fullerene derivatives: an attractive tool for biological applications," *Eur. J. Med. Chem.*, **38**, 913 (2003).
176. Jarvid, M., Johansson, A., Kroon, R., Bjuggren, J.M., Wutzel, H., Englund, V., Gubanski, S., Andersson, M.R. and Müller, C., "A new application area for fullerenes: voltage stabilizers for power cable insulation," *Adv. Mater.*, **27**, 897 (2015).
177. De Volder, M.F.L., Tawfick, S.H., Baughman, R.H. and Hart, A.J., "Carbon nanotubes: present and future commercial applications," *Science*, **339**, 535 (2013).
178. Gooding, J.J., "Nanostructuring electrodes with carbon nanotubes: a review on electrochemistry and applications for sensing," *Electrochimica Acta*, **50**, 3049 (2005).

Bibliography

179. Odom, T.W., Huang, J.-L., Kim, P. and Lieber, C.M., "Structure and electronic properties of carbon nanotubes," *J. Phys. Chem. B*, **104**, 2794 (2000).
180. Odom, T.W., Huang, J.-L., Kim, P. and Lieber, C.M., "Atomic structure and electronic properties of single-walled carbon nanotubes," *Nature*, **391**, 62 (1998).
181. Dresselhaus, M.S., Dresselhaus, G. and Avouris, P., "Carbon Nanotubes: synthesis, structure, properties, and applications," Springer-Verlag Berlin Heidelberg, New York (2001).
182. Prasek, J., Drbohlavova, J., Chomoucka, J., Hubalek, J., Jasek, O., Adam, V. and Kizek, R., "Methods for carbon nanotubes synthesis- review," *J. Mater. Chem.*, **21**, 15872 (2011).
183. Terrones, M., "Science and technology of the twenty-first century: synthesis, properties, and applications of carbon nanotubes," *Annu. Rev. Mater. Res.*, **33**, 419 (2003).
184. See, C.H. and Harris, A.T., "A review of carbon nanotube synthesis via fluidized-bed chemical vapor deposition," *Ind. Eng. Chem. Res.*, **46**, 997 (2007).
185. Hu, L., Hecht, D.S. and Grüner, G., "Carbon nanotube thin films: fabrication, properties, and applications," *Chem. Rev.*, **110**, 5790 (2010).
186. Dillon, A.C., "Carbon nanotubes for photoconversion and electrical energy storage," *Chem. Rev.*, **110**, 6856 (2010).
187. Chen, T. and Dai, L., "Flexible supercapacitors based on carbon nanomaterials," *J. Mater. Chem. A*, **2**, 10756 (2014).
188. Kharisov, B.I., Kharissova, O.V., Gutierrez, H.L. and Méndez, U.O., "Recent advances on the soluble Carbon naotubes," *Ind. Eng. Chem. Res.*, **48**, 572 (2009).
189. Wen, J., Xu, Y., Li, H., Lu, A. and Sun, S., "Recent applications of carbon nanomaterials in fluorescence biosensing and bioimaging," *Chem. Comm.*, **51**, 11346 (2015).

Bibliography

190. Marega, R. and Bonifazi, D., "Filling carbon nanotubes for nanobiotechnological applications," *New J. Chem.*, **38**, 22 (2014).
191. Geim, A.K. and Novoselov, K.S., "The rise of graphene," *Nature Mater.*, **6**, 183 (2007).
192. Brodie, B.C., "On the atomic weight of graphite," *Phil. Trans. R. Soc. Lond.*, **149**, 249 (1859).
193. Geim, A.K., "Random Walk to garphene," *Int. J. Mod. Phys. B.*, **25**, 4055 (2011).
194. Ruess, G. and Vogt, F., "Höchstlamellarer kohlenstoff aus graphitoxhydroxyd," *Monatsh. Chem.* **78**, 222 (1948).
195. Dreyer, D.R., Ruoff, R.S. and Bielawski, C.W., "From conception to realization: an historical account of graphene and some perspectives for its future," *Angew. Chem. Int. Ed.*, **49**, 9336 (2010).
196. Boehm, H.P., Setton, R. and Stumpp, E., "Nomenclature and terminology of graphite intercalation compounds," *Carbon*, **24**, 241 (1986).
197. Ferrari, A.C., *et al.* "Science and technology roadmap for graphene related two-dimensional crystals, and hybrid systems," *Nanoscale*, **7**, 4598 (2015).
198. Warner J.H., Schäffel, F., Rümmeli, M.H. and Bachmatiuk, A., "Graphene: fundamentals and emergent applications," 1st Edition, Elsevier (2013).
199. Edwards, R.S. and Coleman, K.S., "Graphene synthesis: relationship to applications," *Nanoscale*, **5**, 38 (2013).
200. Terrones, M., Botello-Méndez, A.R., Campos-Delgado, J., López-Urías, F., Vega-Cantú, Y.I., Rodríguez-Macías, F.J., Elías, A.L., Munoz-Sandoval, E., Cano-Márquez, A.G., Charlier, J.-C. and Terrones, H., "Graphene and graphite nanoribbons: morphology, properties, synthesis, defects and applications," *Nano Today*, **5**, 315 (2010).

Bibliography

201. Jariwala, D., Srivastava, A. and Ajayan, P.M., “Graphene synthesis and band gap opening,” *J. Nanosci. Nanotechnol.*, **11**, 6621 (2011).
202. Huang, X., Qi, X., Boey, F. and Zhang, H., “Graphene-based composites,” *Chem. Soc. Rev.*, **41**, 666 (2012).
203. Novoselov, K.S., Geim, A.K., Morozov, S.V., Jiang, D., Katsnelson, M.I., Grigorieva, I.V., Dubonos, S.V. and Firsov, A.A., “Two-dimensional gas of massless Dirac fermions in graphene,” *Nature*, **438**, 197 (2005).
204. Du, X., Skachko, I., Barker, A. and Andrei, E.Y., “Approaching ballistic transport in suspended graphene” *Nat. Nanotechnol.*, **3**, 491 (2008).
205. Zhang, Y., Tan, Y.-W., Stormer, H.L. and Kim, P., “Experimental observation of the quantum Hall effect and Berry’s phase in graphene,” *Nature*, **438**, 201 (2005).
206. Novoselov, K.S., Jiang, Z., Zhang, Y., Morozov, S.V., Stormer, H.L., Zeitler, U., Maan, J.C., Boebinger, G.S., Kim, P. and Geim, A.K., “Room-temperature quantum hall effect in graphene,” *Science*, **315**, 1379 (2007).
207. Pumera, M., “Electrochemistry of graphene: new horizons for sensing and energy storage,” *Chem. Rec.*, **9**, 211 (2009).
208. Rao, C.N.R., Sood, A.K., Voggu, R. and Subrahmanyam, K.S., “Some novel attributes of graphene,” *J. Phys. Chem. Lett.*, **1**, 572 (2010).
209. Nair, R.R., Blake, P., Grigorenko, A.N., Novoselov, K.S., Booth, T.J., Stauber, T., Peres, N.M.R. and Geim, A.K., “Fine structure constant defines visual transparency of graphene,” *Science*, **320**, 1328 (2008).
210. Mak, K.F., Ju, L., Wang, F. and Heinz, T.F., “Optical spectroscopy of graphene: from the far infrared to the ultraviolet,” *Solid State Commun.*, **152**, 1341 (2012).
211. Wang, F., Zhang, Y., Tian, C., Girit, C., Zettl, A., Crommie, M. and Shen, Y.R., “Gate-variable optical transitions in graphene,” *Science*, **320**, 206 (2008).

Bibliography

212. Yao, J., Sun, Y., Yang, M. and Duan, Y., “Chemistry, physics, and biology of graphene based nanomaterials: new horizons for sensing, imaging and medicine,” *J. Mater. Chem.*, **22**, 14313 (2012).
213. Balandin, A.A., Ghosh, S., Bao, W., Calizo, I., Teweldebrhan, D., Miao, F. and Lau, C.N., “Superior thermal conductivity of single-layer graphene,” *Nano Lett.*, **8**, 902 (2008).
214. Seol, J.H., Jo, I., Moore, A.L., Lindsay, L., Aitken, Z.H., Pettes, M.T., Li, X., Yao, Z., Huang, R., Broido, D., Mingo, N., Ruoff, R.S. and Shi, L., “Two-dimensional phonon transport in supported graphene,” *Science*, **328**, 213 (2010).
215. Pop, E., Varshney, V. and Roy, A.K., “Thermal properties of graphene: fundamentals and applications,” *MRS Bull.*, **37**, 1273 (2012).
216. Lee, C., Wei, X., Kysar, J.W. and Hone, J., “Measurement of the elastic properties and intrinsic strength of monolayer graphene,” *Science*, **321**, 385 (2008).
217. Pumera, M., “Graphene-based nanomaterials and their electrochemistry,” *Chem. Soc. Rev.*, **39**, 4146 (2010).
218. Guo, S. and Dong, S., “Graphene nanosheets: synthesis, molecular, engineering, thin film, hybrids, and energy and analytical applications,” *Chem. Soc. Rev.*, **40**, 2644 (2011).
219. Kulia, T., Mishra, A.K., Khanra, P., Kim, N.H. and Lee, J.H., “Recent advances in the efficient reduction of graphene oxide and its application as energy storage electrode materials,” *Nanoscale*, **5**, 52 (2013).
220. Wang, G., Zhang, L. and Zhang, J., “A review of electrode materials for electrochemical supercapacitors,” *Chem. Soc. Rev.*, **41**, 797 (2012).
221. Hou, J., Shao, Y., Ellis, M.W., Moore, R.B. and Yi, B., “Graphene-based electrochemical energy conversion and storage: fuel cells, supercapacitors and lithium ion batteries,” *Phys. Chem. Chem. Phys.*, **13**, 15384 (2011).

Bibliography

222. Simon, P. and Gogotsi, Y., “Materials for electrochemical capacitors,” *Nature Mater.*, **7**, 845 (2008).
223. Huang, Y., Liang, J. and Chen, Y., “An overview of the applications of graphene-based materials in supercapacitors,” *Small*, **8**, 1805 (2012).
224. Zhang, L.L., Zhou, R. and Zhao, X.S., “Graphene-based materials as supercapacitor electrodes,” *J. Mater. Chem.*, **20**, 5983 (2010).
225. Rakhi, R.B., Chen, W., Cha, D. and Alshareef, H.N., “High performance supercapacitors using metal oxide anchored graphene nanosheets electrodes,” *J. Mater. Chem.*, **21**, 16197 (2011).
226. Grover, S., Goel, S., Sahu, V., Singh, G. and Sharma, R.K., “Asymmetric supercapacitive characteristics of PANI embedded holey graphene nanoribbons,” *ACS Sustainable Chem. Eng.*, **3**, 1460 (2015).
227. Miller, J.R. and Simon, P., “Electrochemical capacitors for energy management,” *Science*, **321**, 651 (2008)
228. Kularatna, N., “Energy storage devices for electronic systems: rechargeable batteries and supercapacitors,” Elsevier (2015)
229. Tan, Y.B. and Lee, J.-M., “Graphene for supercapacitor applications,” *J. Mater. Chem. A*, **1**, 14814 (2013).
230. Chen, T. and Dai, L., “Carbon nanomaterials for high-performance supercapacitors,” *Mater. Today*, **16**, 272 (2013).
231. Lin, Z., Yao, Y., Hildreth, O.J., Li, Z., Moon, K. and Wong, C.-P., “Superior capacitance of functionalized graphene,” *J. Phys. Chem. C*, **115**, 7120 (2011).
232. Frackowiak, E. and Béguin, F., “Carbon materials for the electrochemical storage of energy in capacitors,” *Carbon*, **39**, 937 (2001).

Bibliography

233. Kwon, T., Nishihara, H., Itoi, H., Yang, Q.-H. and Kyotani, T., "Enhancement mechanism of electrochemical capacitance in nitrogen-/boron-doped carbons with uniform straight nanochannels," *Langmuir*, **25**, 11961 (2009).
234. Wang, X., Sun, G., Routh, P., Kim, D.-H., Huang, W. and Chen, P., "Heteroatom-doped graphene materials: syntheses, properties and applications," *Chem. Soc. Rev.*, **43**, 7067 (2014).
235. Schwierz, F. "Graphene transistors," *Nat. Nanotechnol.*, **5**, 487 (2010).
236. Kim, K.S., Zhao, Y., Jang, H., Lee, S.Y., Kim, J.M., Kim, K.S., Ahn, J.-H., Kim, P., Choi, J.-Y. and Hong, B.H., "Large-scale pattern growth of graphene films for stretchable transparent electrodes," *Nature*, **457**, 706 (2009).
237. Wang, X., Zhi, L. and Müllen, K., "Transparent, conductive graphene electrodes for dye-sensitized solar cells," *Nano Lett.*, **8**, 323 (2008).
238. Bonaccorso, F., Sun, Z., Hasan, T. and Ferrari, A.C., "Graphene photonics and optoelectronics," *Nat. photonics*, **4**, 611 (2010).
239. Shahil, K.M.F. and Balandin, A.A., "Thermal properties of graphene and multilayer graphene: applications in thermal interface materials," *Solid State Commun.*, **152**, 1331 (2012).
240. Bunch, J.S., van der Zande, A.M., Verbridge, S.S., Frank, I.W., Tanenbaum, D.M., Parpia, J.M., Craighead, H.G. and McEuen, P.L., "Electromechanical resonators from graphene sheets," *Science*, **315**, 490 (2007).
241. Pei, S. and Cheng, H.-M., "The reduction of graphene oxide," *Carbon*, **50**, 3210 (2012).
242. Hernandez, Y., Nicolosi, V., Lotya, M., Blighe, F.M., Sun, Z., De, S., McGovern, I.T., Holland, B., Byrne, M., Gun'Ko Y.K., Boland, J.J., Niraj, P., Duesberg, G., Krishnamurthy, S., Goodhue, R., Hutchison, J., Scardaci, V., Ferrari, A.C. and

Bibliography

- Coleman, J.N., "High-yield production of graphene by liquid-phase exfoliation of graphite," *Nat. Nanotechnol.*, **3**, 563 (2008).
243. Chen, D., Feng, H. and Li, J., "Graphene Oxide: preparation, functionalization, and electrochemical applications," *Chem. Rev.*, **112**, 6027 (2012).
244. Paredes, J.I., Villar-Rodil, S., Martínez-Alonso, A. and Tascon, J.M.D., "Graphene oxide dispersions in organic solvents," *Langmuir*, **24**, 10560 (2008).
245. Dreyer, D.R., Park, S., Bielawski, C.W. and Ruoff, R.S., "The chemistry of graphene oxide," *Chem. Soc. Rev.*, **39**, 228 (2010).
246. Staudenmaier, L., "Verfahren zur darstellung der graphitsäure," *Ber. Dtsch. Chem. Ges.*, **31**, 1481 (1898).
247. Hummers, W.S. and Offeman, R.E., "Preparation of graphitic oxide," *J. Am. Chem. Soc.*, **80**, 1339 (1958).
248. Koch, K.R. and Krause, P.F., "Oxidation by Mn_2O_7 : an impressive demonstration of the powerful oxidizing property of dimanganeseheptoxide," *J. Chem. Educ.*, **59**, 973 (1982).
249. Kovtyukhova, N.I., Ollivier, P.J., Martin, B.R., Mallouk, T.E., Chizhik, S.A., Buzaneva, E.V. and Gorchinskiy, A.D., "Layer-by-Layer assembly of ultrathin composite films from micron-sized graphite oxide sheets and polycations," *Chem. Mater.*, **11**, 771 (1999).
250. Marcano, D.C., Kosynkin, D.V., Berlin, J.M., Sinitskii, A., Sun, Z., Slesarev, A., Alemany, L.B., Lu, W. and Tour, J.M., "Improved synthesis of graphene oxide," *ACS Nano*, **4**, 4806 (2010).
251. Chen, J., Yao, B., Li, C. and Shi, G., "An improved Hummers method for eco-friendly synthesis of graphene oxide," *Carbon*, **64**, 225 (2013).
252. Cai, W., Piner, R.D., Stadermann, F.J., Park, S., Shaibat, M.A., Ishii, Y., Yang, D., Velamakanni, A., An, S.J., Stoller, M., An, J., Chen, D. and Ruoff, R.S., "Synthesis

Bibliography

- and solid-state NMR structural characterization of ^{13}C -labeled graphite oxide,” *Science*, **321**, 1815 (2008).
253. Gao, W., Alemany, L.B., Ci, L. and Ajayan, P.M., “New insights into the structure and reduction of graphite oxide,” *Nat. Chem.*, **1**, 403 (2009).
254. Dubin, S., Gilje, S., Wang, K., Tung, V.C., Cha, K., Hall, A.S., Farrar, J., Varshneya, R., Yang, Y. and Kaner, R.B., “A one-step, solvothermal reduction method for producing reduced graphene oxide dispersions in organic solvents,” *ACS Nano*, **4**, 3845 (2010).
255. Zhou, Y., Bao, Q., Tang, L.A.L., Zhong, Y. and Loh, K.P., “Hydrothermal dehydration for the “green” reduction of exfoliated graphene oxide to graphene and demonstration of tunable optical limiting properties,” *Chem. Mater.*, **21**, 2950 (2009).
256. Yang, D., Velamakanni, A., Bozoklu, G., Park, S., Stoller, M., Piner, R.D., Stankovich, S., Jung, I., Field, D.A., Ventrice Jr., C.A. and Ruoff, R.S., “Chemical analysis of graphene oxide films after heat and chemical treatments by X-ray photoelectron and micro-Raman spectroscopy,” *Carbon*, **47**, 145 (2009).
257. Toh, S.Y., Loh, K.S., Kamarudin, S.K. and Daud, W.R.W., “Graphene production via electrochemical reduction of graphene oxide: synthesis and characterization,” *Chem. Eng. J.*, **251**, 422 (2014).
258. Huang, L., Liu, Y., Ji, L.-C., Xie, Y.-Q., Wang, T. and Shi, W.-Z., “Pulsed laser assisted reduction of graphene oxide,” *Carbon*, **49**, 2431 (2011).
259. Ding, Y.H., Zhang, P., Zhou, Q., Ren, H.M., Yang, Z.M. and Jiang, Y., “A green approach to the synthesis of reduced graphene oxide nanosheets under UV irradiation,” *Nanotechnology*, **22**, 215601 (2011).
260. Eswaraiah, V., Aravind, S.S.J. and Ramaprabhu, S., “Top down method for synthesis of highly conducting graphene by exfoliation of graphite oxide using focused solar radiation,” *J. Mater. Chem.*, **21**, 6800 (2011).

Bibliography

261. Georgakilas, V., Otyepka, M., Bourlinas, A.B., Chandra, V., Kim, N., Kemp, K.C., Hobza, P., Zboril, R. and Kim, K.S., “Functionalization of graphene: covalent and non-covalent approaches, derivatives and applications,” *Chem. Rev.*, **112**, 6156 (2012).
262. Luo, J., Jang, H.D. and Huang, J., “Effect of sheet morphology on the scalability of graphene-based ultracapacitors,” *ACS Nano*, **7**, 1464 (2013).
263. Parades, J.I., Villar-Rodil, S., Fernández-Merino, M.J., Guardia, L., Martínez-Alonso, A. and Tascón, J.M.D., “Environmentally friendly approaches toward the mass production of processable graphene from graphite oxide,” *J. Mater. Chem.*, **21**, 298 (2011).
264. Shin, H.-J., Kim, K.K., Benayad, A., Yoon, S.-M., Park, H.K., Jung, I.-S., Jin, M.H., Jeong, H.-K., Kim, J.M., Choi, J.-Y. and Lee, Y.H., “Efficient reduction of graphite oxide by sodium borohydride and its effect on electrical conductance,” *Adv. Funct. Mater.*, **19**, 1987 (2009).
265. Ambrosi, A., Chua, C.K., Bonanni, A. and Pumera, M., “Lithium aluminium hydride as reducing agent for chemically reduced graphene oxides,” *Chem. Mater.*, **24**, 2292 (2012).
266. Pei, S., Zhao, J., Du, J., Ren, W. and Cheng, H.-M., “Direct reduction of graphene oxide films into highly conductive and flexible graphene films by hydrohalic acids,” *Carbon*, **48**, 4466 (2010).
267. Chen, Y., Zhang, X., Zhang, D., Yu, P. and Ma, Y., “High performance supercapacitors based on reduced graphene oxide in aqueous and ionic liquid electrolytes,” *Carbon*, **49**, 573 (2011).
268. Fan, X., Peng, W., Li, Y., Li, X., Wang, S., Zhang, G. and Zhang, F., “Deoxygenation of exfoliated graphite oxide under alkaline conditions: a green route to graphene preparation,” *Adv. Mater.*, **20**, 4490 (2008).

Bibliography

269. Teng, X., Yan, M. and Bi, H., "Spectra investigation on surface characteristics of graphene oxide nanosheets treated with tartaric, malic and oxalic acids," *Spectrochim. Acta, Part A*, **118**, 1020 (2014).
270. Song, P., Zhang, X., Sun, M., Cui, X. and Lin, Y., "Synthesis of graphene nanosheets via oxalic acid-induced chemical reduction of exfoliated graphite oxide," *RSC Adv.*, **2**, 1168 (2012).
271. Zhu, C., Guo, S., Fang, Y. and Dong, S., "Reducing sugar: new functional molecules for the green synthesis of graphene nanosheets," *ACS Nano*, **4**, 2429 (2010).
272. Kim, Y.-K., Kim, M.-H. and Min, D.-H., "Biocompatible reduced graphene oxide prepared by using dextran as a multifunctional reducing agent," *Chem. Commun.*, **47**, 3195 (2011).
273. Fernández-Merino, M.J., Villar-Rodil, S., Paredes, J.I., Solís-Fernández P., Guardia, L., García, R., Martínez-Alonso, A. and Tascón, J.M.D., "Identifying efficient natural bioreductants for the preparation of graphene and graphene-metal nanoparticle hybrids with enhanced catalytic activity from graphite oxide," *Carbon*, **63**, 30 (2013).
274. Bo, Z., Shuai, X., Mao, S., Yang, H., Qian, J., Chen, J., Yan, J. and Cen, K., "Green preparation of reduced graphene oxide for sensing and energy storage," *Sci. Rep.*, **4**, 4684 (2014).
275. Li, J., Xiao, G., Chen, C., Li, R. and Yan, D., "Superior dispersions of reduced graphene oxide synthesized by using gallic acid as a reductant and stabilizer," *J. Mater. Chem. A*, **1**, 1481 (2013).
276. Fan, Z., Wang, K., Wei, T., Yan, J., Song, L. and Shao, B., "An environmentally friendly and efficient route for the reduction of graphene oxide by aluminium powder," *Carbon*, **48**, 1670 (2010).

Bibliography

277. Liu, Y., Li, Y., Zhong, M., Yang, Y., Wen, Y. and Wang, M., "A green and ultrafast approach to the synthesis of scalable graphene nanosheets with Zn powder for electrochemical energy storage," *J. Mater. Chem.*, **21**, 15449 (2011).
278. Kim, N.H., Khanra, P., Kulia, T., Jung, D. and Lee, J.H., "Efficient reduction of graphene oxide using tin-powder and its electrochemical performances for use as an energy storage electrode material," *J. Mater. Chem. A*, **1**, 11320 (2013).
279. Wang, Y., Shi, Z. and Yin, J., "Facile synthesis of soluble graphene via a green reduction of graphene oxide in tea solution and its biocomposites," *ACS Appl. Mater. Interfaces*, **3**, 1127 (2011).
280. Jana, M., Saha, S., Samanta, P., Murmu, N.C., Lee, J.H. and Kulia, T., "Investigation of the capacitive performance of tobacco solution reduced graphene oxide," *Mater. Chem. Phys.*, **151**, 72 (2015).
281. Khan, M., Al-Marri, A.H., Khan, M., Mohri, N., Adil, S.F., Al-Warthan, A., Siddiqui, M.R.H., Alkathlan, H.Z., Berger, R., Tremel, W. and Tahir, M.N., "Pulicariaia Glutinosa Plant extract: a green and eco-friendly reducing agent for the preparation of highly reduced graphene oxide," *RSC Adv.*, **4**, 24119 (2014).
282. Thakur, S. and Karak, N., "Green reduction of graphene oxide by aqueous phytoextracts," *Carbon*, **50**, 5331 (2012).
283. Jana, M., Saha, S., Khanra, P., Murmu, N.C., Srivastava, S.K., Kulia, T. and Lee, J.H., "Bio-reduction of graphene oxide using drained water from soaked mung beans (*Phaseolus aureus* L.) and its application as energy storage electrode material," *Mater. Sci. Eng. B*, **186**, 33 (2014).
284. Feng, Y., Feng, N. and Du, G., "A green reduction of graphene oxide via starch-based materials," *RSC Adv.*, **3**, 21466 (2013).

Bibliography

285. Khanra, P., Kuila, T., Kim, N.H., Bae, S.H., Yu, D.-S. and Lee, J.H., "Simultaneous bio-functionalization and reduction of graphene oxide by baker's yeast," *Chem. Eng. J.*, **183**, 526 (2012).
286. Gurunathan, S., Han, J.W., Eppakayala, V. and Kim, J.-H., "Microbial reduction of graphene oxide by Escherichia coli: a green chemistry approach," *Colloids Surf. B*, **102**, 772 (2013).
287. Wang, G., Qian, F., Saltikov, C.W., Jiao, Y. and Li, Y., "Microbial reduction of graphene oxide by Shewanella," *Nano Res.*, **4**, 563 (2011).
288. Kuila, T., Bose, S., Khanra, P., Mishra, A.K., Kim, N.H. and Lee, J.H., "A green approach for the reduction of graphene oxide by wild carrot root," *Carbon*, **50**, 914 (2012).
289. Liu, J., Fu, S., Yuan, B., Li, Y. and Deng, Z., "Toward a universal "Adhesive Nanosheet" for the assembly of multiple nanoparticles based on a protein-induced reduction/decoration of graphene oxide," *J. Am. Chem. Soc.*, **132**, 7279 (2010).
290. Zhang, J., Yang, H., Shen, G., Cheng, P., Zhang, J. and Guo, S., "Reduction of graphene oxide via L-ascorbic acid," *Chem. Commun.*, **46**, 1112 (2010).
291. Fernández-Merino, M.J., Guardia, L., Paredes, J.I., Villar-Rodil, S., Solínez-Alonso, A. and Tascón, J.M.D., "Vitamin C is an ideal substitute for hydrazine in the reduction of graphene oxide suspensions," *J. Phys. Chem. C.*, **114**, 6426 (2010).
292. Gao, J., Liu, F., Liu, Y., Ma, N., Wang, Z. and Zhang, X., "Environment-friendly method to produce graphene that employs vitamin C and amino acid," *Chem. Mater.*, **22**, 2213 (2010).
293. Wan, W., Zhao, Z., Hu, H., Gogotsi, Y. and Qiu, J., "Highly controllable and green reduction of graphene oxide to flexible graphene film with high strength," *Mater. Res. Bull.*, **48**, 4797 (2013).

Bibliography

294. Haghghi, B. and Tabrizi, M.A., “Green-synthesis of reduced graphene oxide nanosheets using rose water and a survey on their characteristics and applications,” *RSC Adv.*, **3**, 13365 (2013).
295. Shen, J., Zhu, Y., Yang, X. and Li, C., “Graphene quantum dots: emergent nanolights for bioimaging, sensors, catalysis and photovoltaic devices,” *Chem. Commun.*, **48**, 3686 (2012).
296. Yan, Z., Liu, Y., Lin, J., Peng, Z., Wang, G., Pembroke, E., Zhou, H., Xiang, C., Raji, A.-R.O., Samuel, E.L.G., Yu, T., Yakobson, B.I. and Tour, J.M., “Hexagonal graphene onion rings,” *J. Am. Chem. Soc.*, **135**, 10755 (2013).
297. Paraknowitsch, J.P. and Thomas, A., “Doping carbons beyond nitrogen: an overview of advanced heteroatom doped carbons with boron, sulphur and phosphorus for energy applications,” *Energy Environ. Sci.*, **6**, 2839 (2013).
298. Fujisawa, K., Cruz-Silva, R., Yang, K.-S., Kim, Y.A., Hayashi, T., Endo, M., Terrones, M. and Dresselhaus, M.S., “Importance of open, heteroatom-decorated edges in chemically doped-graphene for supercapacitor applications,” *J. Mater. Chem. A*, **2**, 9532 (2014).
299. Martin, A., Hernández-Ferrer, J., Vázquez, L., Martínez, M.-T. and Escarpa, A., “Controlled chemistry of tailored graphene nanoribbons for electrochemistry: a rational approach to optimizing molecule detection,” *RSC Adv.*, **4**, 132 (2014).
300. Dhakate, S.R., Chauhan, N., Sharma, S. and Mathur, R.B., “The production of multi-layer graphene nanoribbons from thermally reduced unzipped multi-walled carbon nanotubes,” *Carbon*, **49**, 4170 (2011).
301. Zhang, S., Tang, S., Lei, J., Dong, H. and Ju, H., “Functionalization of graphene nanoribbons with porphyrin for electrocatalysis and amperometric biosensing,” *J. Electroanal. Chem.*, **656**, 285 (2011).

Bibliography

302. Chen, Z., Lin, Y.-M., Rooks, M.J. and Avouris, P., "Graphene nano-ribbon electronics," *Phys. E*, **40**, 228 (2007).
303. Darbari, S., Ahmadi, V., Afzali, P. and Abdi, Y., "Photocatalytic reduction of GO/ZnO to achieve GNRs for optoelectronic applications," *J. Phys. D: Appl. Phys.*, **46**, 385101 (2013).
304. Villegas, C.E.P., Mendonça, P.B. and Rocha, A.R., "Optical spectrum of bottom-up graphene nanoribbons: towards efficient atom-thick excitonic solar cells," *Sci. Rep.*, **4**, 6579 (2014).
305. Wei, D., Liu, Y., Zhang, H., Huang, L., Wu, B., Chen, J. and Yu, G., "Scalable synthesis of few-layer graphene ribbons with controlled morphologies by a template method and their applications in nanoelectromechanical switches," *J. Am. Chem. Soc.*, **131**, 11147 (2009).
306. Bhardwaj, T., Antic, A., Pavan, B., Barone, V. and Fahlman, B.D., "Enhanced electrochemical lithium storage by graphene nanoribbons," *J. Am. Chem. Soc.*, **132**, 12556 (2010).
307. Vineesh, T.V., Alwarappan, S. and Narayanan, T.N., "The improved electrochemical performance of cross-linked 3D graphene nanoribbons monolith electrodes," *Nanoscale*, **7**, 6504 (2015).
308. Sahu, V., Shekhar, S., Sharma, R.K. and Singh, G., "Ultrahigh performance supercapacitors from lacey reduced graphene oxide nanoribbons," *ACS Appl. Mater. Interfaces*, **7**, 3110 (2015).
309. Wong, C.H.A. and Pumera, M., "Highly conductive graphene nanoribbons from the reduction of graphene oxide nanoribbons with lithium aluminium hydride," *J. Mater. Chem. C*, **2**, 856 (2014).

Bibliography

310. Damien, D., Babu, B., Narayanan, T.N., Reddy, A.L., Ajayan, P.M. and Shaijumon, M.M., "Eco-efficient synthesis of graphene nanoribbons and its application in electrochemical supercapacitors," *Graphene*, **1**, 37 (2013).
311. Kosynkin, D.V., Higginbotham, A.L., Sinitskii, A., Lomeda, J.R., Dimiev, A., Price, B.K. and Tour, J.M., "Longitudinal unzipping of carbon nanotubes to form graphene nanoribbons," *Nature*, **458**, 872 (2009).
312. James, D.K. and Tour, J.M., "The chemical synthesis of graphene nanoribbons - a tutorial review," *Macromol. Chem. Phys.*, **213**, 1033 (2012).
313. Fan, Y., Li, J., Liu, X., Wang, L., Chen, X., Sun, S., Kawasaki, A. and Jiang, W., "A microexplosion method for the synthesis of graphene nanoribbons," *Carbon*, **49**, 1439 (2011).
314. Yoon, W., Lee, Y., Jang, H., Jang, M., Kim, J.S., Lee, H.S., Im, S., Boo, D.W., Park, J. and Ju, S.-Y., "Graphene nanoribbons formed by a sonochemical graphene unzipping using flavin mononucleotide as a template," *Carbon*, **81**, 629 (2015).
315. Choucair, M., Gong, B. and Stride, J.A., "Versatile and scalable synthesis of graphene nanoribbons," *Mater. Lett.*, **119**, 75 (2014).
316. Zhang, D., Ma, Q., Fan, H., Yang, H. and Liu, S., "Millimeter-long multilayer graphene nanoribbons prepared by wet chemical processing," *Carbon*, **71**, 120 (2014).
317. Lv, R. and Terrones, M., "Towards new graphene materials: doped graphene sheets and nanoribbons," *Mater. Lett.*, **78**, 209 (2012).
318. Wang, H., Maiyalagan, T. and Wang, X., "Review on recent progress in nitrogen-doped graphene: synthesis, characterization, and its potential applications," *ACS Catal.*, **2**, 781 (2012).
319. Xu, X., Pan, L., Liu, Y., Lu, T. and Sun, Z., "Enhanced capacitive deionization performance of graphene by nitrogen doping," *J. Colloid Interface Sci.*, **445**, 143 (2015).

Bibliography

320. Sun, H., Wang, Y., Liu, S., Ge, L., Wang, L., Zhu, Z. and Wang, S., "Facile synthesis of nitrogen doped reduced graphene oxide as a superior metal-free catalyst for oxidation," *Chem. Commun.*, **49**, 9914 (2013).
321. Guo, H.-L., Su, P., Kang, X. and Ning, S.-K., "Synthesis and characterization of nitrogen-doped graphene hydrogels by hydrothermal route with urea as reducing-doping agents," *J. Mater. Chem. A*, **1**, 2248 (2013).
322. Deng, D., Pan, X., Yu, L., Cui, Y., Jiang, Y., Qi, J., Li, W.-X., Fu, Q., Ma, X., Xue, Q., Sun, G. and Bao, X., "Toward N-doped graphene via solvothermal synthesis," *Chem. Mater.*, **23**, 1188 (2011).
323. Quan, B., Yu, S.-H., Chung, D.Y., Jin, A., Park, J.H., Sung, Y.-E. and Piao, Y., "Single source precursor-based solvothermal synthesis of heteroatom-doped graphene and its energy storage and conversion," *Sci. Rep.*, **4**, 5639 (2014).
324. Stankovich, S., Dikin, D.A., Piner, R.D., Kohlhaas, K.A., Kleinhammes, A., Jia, Y., Wu, Y., Nguyen, S.T. and Ruoff, R.S., "Synthesis of graphene-based nanosheets via chemical reduction of exfoliated graphite oxide," *Carbon*, **45**, 1558 (2007).
325. Tung, V.C., Allen, M.J., Yang, Y. and Kaner, R.B., "High-throughput solution processing of large-scale graphene," *Nat. Nanotechnol.*, **4**, 25 (2009).
326. Zhang, W., Zhang, Y., Tian, Y., Yang, Z., Xiao, Q., Guo, X., Jing, L., Zhao, Y., Yan, Y., Feng, J. and Sun, K., "Insight into the capacitive properties of reduced graphene oxide," *ACS Appl. Mater. Interfaces*, **6**, 2248 (2014).
327. Wang, R., Wang, Y., Xu, C., Sun, J. and Gao, L., "Facile one-step hydrazine-assisted solvothermal synthesis of nitrogen-doped reduced graphene oxide: reduction effect and mechanisms," *RSC Adv.*, **3**, 1194 (2013).
328. Stankovich, S., Dikin, D.A., Dommett, G.H.B., Kohlhaas, K.M., Zimney, E.J., Stach, E.A., Piner, R.D., Nguyen, S.T. and Ruoff, R.S., "Graphene-based composite materials," *Nature*, **442**, 282 (2006).

Bibliography

329. Chen, Y., Zhang, X., Yu, P. and Ma, Y., “Stable dispersions of graphene and highly conducting graphene films: a new approach to creating of graphene monolayers,” *Chem. Commun.*, 4527 (2009).
330. Chen, P., Yang, J.-J., Li, S.-S., Wang, Z., Xiao, T.-Y., Qian, Y.-H. and Yu, S.-H., “Hydrothermal synthesis of macroscopic nitrogen-doped graphene hydrogels for ultrafast supercapacitors,” *Nano Energy*, **2**, 249 (2013).
331. Mao, S., Yu, K., Cui, S., Bo, Z., Lu, G. and Chen, J., “A new reducing agent to prepare single-layer, high-quality reduced graphene oxide for device applications,” *Nanoscale*, **3**, 2849 (2011).
332. Wang, G., Yang, J., Park, J., Gou, X., Wang, B., Liu, H. and Yao, J., “Facile synthesis and characterization of graphene nanosheets,” *J. Phys. Chem. C*, **112**, 8192 (2008).
333. Sun, L., Wang, L., Tian, C., Tan, T., Xie, Y., Shi, K., Li, M. and Fu, H., “Nitrogen-doped graphene with high nitrogen level *via* a one-step hydrothermal reaction of graphene oxide with urea for superior capacitive energy storage,” *RSC Adv.*, **2**, 4498 (2012).
334. Janowska, I., Chizari, K., Ersen, O., Zafeiratos, S., Soubane, D., Costa, V.D., Speisser, V., Boeglin, C., Houllé, M., Bégin, D., Plee, D., Ledoux, M.-J. and Pham-Huu, C., “Microwave synthesis of large few-layer graphene sheets in aqueous solutions of ammonia,” *Nano Res.*, **3**, 126 (2010).
335. Jiang, B., Tian, C., Wang, L., Sun, L., Chen, C., Nong, X., Qiao, Y. and Fu, H., “Highly concentrated, stable nitrogen-doped graphene for supercapacitors: simultaneous doping and reduction,” *Appl. Surf. Sci.*, **258**, 3438 (2012).
336. Amarnath, C.A., Hong, C.E., Kim, N.H., Ku, B.-C., Kulia, T. and Lee, J.H., “Efficient synthesis of graphene sheets using pyrrole as a reducing agent,” *Carbon*, **49**, 3497 (2011).

Bibliography

337. Lee, J.W., Ko, J.M. and Kim, J.-D., "Hydrothermal preparation of nitrogen-doped graphene sheets via hexamethylenetetramine for application as supercapacitor electrodes," *Electrochim. Acta*, **85**, 459 (2012).
338. Zhang, Y., Fugane, K., Mori, T., Niu, L. and Ye, J., "Wet Chemical synthesis of nitrogen-doped graphene towards oxygen reduction electrocatalysts without high-temperature pyrolysis," *J. Mater. Chem.*, **22**, 6575 (2012).
339. Bose, S., Kulia, T., Mishra, A.K., Kim, N.H. and Lee, J.H., "Dual role of glycine as a chemical functionalizer and a reducing agent in the preparation of graphene: an environmentally friendly method," *J. Mater. Chem.* **22**, 9696 (2012).
340. Wang, T., Wang, L., Wu, D., Xia, W., Zhao, H. and Jia, D., "Hydrothermal synthesis of nitrogen-doped graphene hydrogels using amino acids with different acidities as doping agents," *J. Mater. Chem. A*, **2**, 8352 (2014).
341. Tran, D.N.H., Kabiri, S. and Losic, D., "A green approach for the reduction of graphene oxide nanosheets using non-aromatic amino acids," *Carbon*, **76**, 193 (2014).
342. Ahn, H., Kim, T., Choi, H., Yoon, C., Um, K., Nam, J., Ahn, K.H. and Lee, K., "Gelation of graphene oxides induced by different types of amino acids," *Carbon*, **71**, 229 (2014).
343. Fan, M., Zhu, C., Feng, Z.-Q., Yang, J., Liu, L. and Sun, D., "Preparation of N-doped graphene by reduction of graphene oxide with mixed microbial system and its haemocompatibility," *Nanoscale*, **6**, 4882 (2014).
344. Ahmed, M.S., You, J.-M., Han, H.S., Jeong, D.-C. and Jeon, S., "A green preparation of nitrogen doped graphene using urine for oxygen reduction in alkaline fuel cells" *J. Nanosci. Nanotechnol.*, **14**, 5722 (2014).
345. Khan, M., Tahir, M.N., Adil, S.F., Khan, H.U., Siddiqui, M.R.H., Al-warthan, A.A. and Tremel, W., "Graphene based metal and metal oxide nanocomposites: synthesis, properties and their applications," *J. Mater. Chem. A*, **3**, 18753 (2015).

Bibliography

346. Li, Q., Mahmood, N., Zhu, J., Hou, Y. and Sun, S., "Graphene and its composites with nanoparticles for electrochemical energy applications," *Nano Today*, **9**, 668 (2014).
347. Leong, K.H., Sim, L.C., Bahnemann, D., Jang, M., Ibrahim, S. and Saravanan, P., "Reduced graphene oxide and Ag wrapped TiO₂ photocatalyst for enhanced visible light photocatalysis," *APL Mat.*, **3**, 104503 (2015).
348. Babu, S.G., Vinoth, R., Narayana, S., Bahnemann, D. and Neppolian, B., "Reduced graphene oxide wrapped Cu₂O supported on C₃N₄: an efficient visible light responsive semiconductor photocatalyst," *APL Mat.*, **3**, 104415 (2015).
349. Tan, C., Huang, X. and Zhang, H., "Synthesis and applications of graphene-based noble metal nanostructures," *Mater. Today*, **16**, 29 (2013).
350. Huang, X., Yin, Z., Wu, S., Qi, X., He, Q., Zhang, Q., Yan, Q., Boey, F. and Zhang, H., "Graphene-based materials: synthesis, characterization, properties, and applications," *Small*, **7**, 1876 (2011).
351. Kim, K., Hong, K., Koo, B., Lee, I. and Lee, J.-L., "Transparency controllable silver-based electrode for flexible optoelectronics," *Appl. Phys. Lett.*, **102**, 081118 (2013).
352. Lu, G., Li, H., Liusman, C., Yin, Z., Wu, S. and Zhang, H., "Surface enhanced Raman scattering of Ag or Au nanoparticle-decorated reduced graphene oxide for detection of aromatic molecules," *Chem. Sci.*, **2**, 1817 (2011).
353. Zhang, Y., Liu, S., Wang, L., Qin, X., Tian, J., Lu, W., Chang, G. and Sun, X., "One-pot green synthesis of Ag nanoparticles-graphene nanocomposites and their applications in SERS, H₂O₂, and glucose sensing," *RSC Adv.*, **2**, 538 (2012).
354. Hsu, K.-C. and Chen, D.-H., "Microwave-assisted green synthesis of Ag/reduced graphene oxide nanocomposites as a surface-enhanced Raman scattering substrate with high uniformity," *Nanoscale Res. Lett.*, **9**, 193 (2014).
355. Dutta, S., Ray, C., Sarkar, S., Pradhan, M., Negishi, Y. and Pal, T., "Silver nanoparticle decorated reduced graphene oxide (rGO) nanosheets: a platform for

Bibliography

- SERS based low-level detection of uranyl ion,” *ACS Appl. Mater. Interfaces*, **5**, 8724 (2013).
356. Zheng, L., Zhang, G., Zhang, M., Guo, S. and Liu, Z.-H., “Preparation and capacitance performance of Ag-graphene based nanocomposites,” *J. Power Sources*, **201**, 376 (2012).
357. Tian, J., Liu, S., Zhang, Y., Li, H., Wang, L., Luo, Y., Asiri, A.M., Al-Youbi, A. and Sun, X., “Environmentally friendly, one-pot synthesis of Ag nanoparticle-decorated reduced graphene oxide composites and their application to photocurrent generation,” *Inorg. Chem.*, **51**, 4742 (2012).
358. Hassan, H.M.A., Abdelsayed, V., Khder, A.R.S., AbouZeid, K.M., Ternier, J., El-Shall, M.S., Al-Resayes, S.I. and El-Azhary, A.A., “Microwave synthesis of graphene sheets supporting metal nanocrystals in aqueous and organic media,” *J. Mater. Chem.*, **19**, 3832 (2009).
359. Barman, B.K. and Nanda, K.K., “Hexamethylenetetramine mediated simultaneous nitrogen doping and reduction of graphene oxide for a metal-free SERS substrate,” *RSC Adv.*, **4**, 44146 (2014).
360. Tang, X.-Z., Cao, Z., Zhang, H.-B., Liu, J. and Yu, Z.-Z., “Growth of silver nanocrystals on graphene by simultaneous reduction of graphene oxide and silver ions with a rapid and efficient one-step approach,” *Chem. Commun.*, **47**, 3084 (2011).
361. Pasricha, R., Gupta, S. and Srivastava, A.K., “A facile and novel synthesis of Ag-graphene-based nanocomposites,” *Small*, **5**, 2253 (2009).
362. Liu, S., Tian, J., Wang, L. and Sun, X., “A method for the production of reduced graphene oxide using benzylamine as a reducing and stabilizing agent and its subsequent decoration with Ag nanoparticles for enzymeless hydrogen peroxide detection,” *Carbon*, **49**, 3158 (2011).

Bibliography

363. Yuan, W., Gu, Y. and Li, L., "Green synthesis of graphene/Ag nanocomposites," *Appl. Surf. Sci.*, **261**, 753 (2012).
364. Liu, J., Liu, L., Wu, X., Zhang, X. and Li, T., "Environmentally friendly synthesis of graphene-silver composites with surface-enhanced Raman scattering and antibacterial activity via reduction with L-ascorbic acid/water vapor," *New J. Chem.*, **39**, 5272 (2015).
365. Sedki, M., Mohamed, M.B., Fawzy, M., Abdelrehim, D.A. and Abdel-Mottaleb, M.M.S.A., "Photosynthesis of silver-reduced graphene oxide (Ag-RGO) nanocomposites with an enhanced antibacterial effect using *Potamogeton pectinatus* extract," *RSC Adv.*, **5**, 17358 (2015).
366. Jeon, E.K., Seo, E., Lee, E., Lee, W., Um, M.-K. and Kim, B.-S., "Mussel-inspired green synthesis of silver nanoparticles on graphene oxide nanosheets for enhanced catalytic applications," *Chem. Commun.*, **49**, 3392 (2013).
367. Tang, X.-Z., Li, X., Cao, Z., Yang, J., Wang, H., Pu, X. and Yu, Z.-Z., "Synthesis of graphene decorated with silver nanoparticles by simultaneous reduction of graphene oxide and silver ions with glucose," *Carbon*, **59**, 93 (2013).
368. Roy, I., Rana, D., Sarkar, G., Bhattachayya, A., Saha, N.R., Mondal, S., Pattanayak, S., Chattopadhyay, S. and Chattopadhyay, D., "Physical and electrochemical characterization of reduced graphene oxide/silver nanocomposites synthesized by adopting a green approach," *RSC Adv.*, **5**, 25357 (2015).
369. Zhang, D., Liu, X. and Wang, X., "Green synthesis of graphene oxide sheets decorated by silver nanoprisms and their anti-bacterial properties," *J. Inorg. Biochem.*, **105**, 1181 (2011).
370. Fan, J., Shi, Z., Ge, Y., Wang, J., Wang, Y. and Yin, J., "Gum arabic assisted and fabrication of Ag-graphene-based hybrids," *J. Mater. Chem.*, **22**, 13764 (2012).

Bibliography

371. Mayavan, S., Sim, J.-B. and Choi, S.-M., "Easy synthesis of nitrogen-doped graphene-silver nanoparticle hybrids by thermal treatment of graphite oxide with glycine and silver nitrate," *Carbon*, **50**, 5148 (2012).
372. Bosch-Navarro, C., Coronado, E., Martí-Gastaldo, C., Sánchez-Royo, J.F. and Gómez, M.G., "Influence of the pH on the synthesis of reduced graphene oxide under hydrothermal conditions," *Nanoscale*, **4**, 3977 (2012).
373. Subramanian, N. and Viswanathan, B., "Nitrogen- and oxygen-containing activated carbons from sucrose for electrochemical supercapacitor applications," *RSC Adv.*, **5**, 63000 (2015).
374. Roy, K., Vinod, C.P. and Gopinath, C.S., "Design and performance aspects of a custom built ambient pressure photoelectron spectrometer toward bridging the pressure gap: oxidation of Cu, Ag, and Ag surfaces at 1 mbar O₂ pressure," *J. Phys. Chem. C*, **117**, 4717 (2013).
375. Holzwarth, U. and Gibson, N., "The Scherrer equation versus the 'Debye-Scherrer equation'," *Nat. Nanotechnol.*, **6**, 534 (2011).
376. Schroder, D.K., "Semiconductor material and device characterization," 3rd Edition, Wiley-Interscience, John Wiley & Sons (2006).
377. Khanra, P., Kulia, T., Bae, S.H., Kim, N.H. and Lee, J.H., "Electrochemically exfoliated graphene using 9-anthracene carboxylic acid for supercapacitor application," *J. Mater. Chem.*, **22**, 24403 (2012).
378. Zheng, C., Zhou, X.F., Cao, H.L., Wang, G.H. and Liu, Z.P., "Edge-enriched porous graphene nanoribbons for high energy density supercapacitors," *J. Mater. Chem. A*, **2**, 7484 (2014).
379. Mhamane, D., Unni, S.M., Suryawanshi, A., Game, O., Rode, C., Hannover, B., Kurungot, S. and Ogale, S., "Trigol based reduction of graphite oxide to graphene with enhanced charge storage activity," *J. Mater. Chem.*, **22**, 11140 (2012).

Bibliography

380. Yang, J. and Zou, L., "Graphene films of controllable thickness as binder-free electrodes for high performance supercapacitors," *Electrochim. Acta*, **130**, 791 (2014).
381. El-Khodary, S.A., El-Enany, G.M., El-Okr, M. and Ibrahim, M., "Preparation and characterization of microwave reduced graphite oxide for high-performance supercapacitors," *Electrochim. Acta*, **150**, 269 (2014).
382. Ghosh, D., Giri, S., Moniruzzaman, M., Basu, T., Mandal, M. and Das, C.K., " α MnMoO₄/graphene hybrid composite: high energy density supercapacitor electrode material," *Dalton Trans.*, **43**, 11067 (2014).
383. Liu, K., Zhang, J.-J., Cheng, F.-F., Zheng, T.-T., Wang, C. and Zhu, J.J., "Green and facile synthesis of highly biocompatible graphene nanosheets and its application for cellular imaging and drug delivery," *J. Mater. Chem.*, **21**, 12034 (2011).
384. Kumar, N.A., Nolan, H., McEvoy, N., Rezvani, E., Doyle, R.L., Lyons, M.E.G. and Duesberg, G.S., "Plasma-assisted simultaneous reduction and nitrogen doping of graphene oxide nanosheets," *J. Mater. Chem. A*, **1**, 4431 (2013).
385. Tamboli, S.K., Kim, B.S., Choi, G., Lee, H., Lee, D., Patil, U.M., Lim, J., Kulkarni, S.B., Jun, S.C. and Cho, H.H., "Post-heating effects on the physical and electrochemical capacitive properties of reduced graphene oxide paper," *J. Mater. Chem. A*, **2**, 5077 (2014).
386. Liu, H., Zhang, L., Guo, Y., Cheng, C., Yang, L., Jiang, L., Yu, G., Hu, W., Liu, Y. and Zhu, D., "Reduction of graphene oxide to highly conductive graphene by Lawesson's reagent and its electrical applications," *J. Mater. Chem. C*, **1**, 3104 (2013).
387. Su, P., Guo, H.-L., Tian, L. and Ning, S.-K., "An efficient method of producing stable graphene suspensions with less toxicity using dimethyl ketoxime," *Carbon*, **50**, 5351 (2012).

Bibliography

388. Dey, R.S., Hajra, S., Sahu, R.K., Raj, C.R. and Panigrahi, M.K., "A rapid room temperature chemical route for the synthesis of graphene: metal-mediated reduction of graphene oxide," *Chem. Commun.*, **48**, 1787 (2012).
389. Botas, C., Álvarez, P., Blanco, C., Santamaría, R., Granda, M., Gutiérrez, M.D., Rodríguez-Reinoso, F. and Menéndez, R., "Critical temperature in the synthesis of graphene-like materials by thermal exfoliation-reduction of graphite oxide," *Carbon*, **52**, 476 (2013).
390. Ganguly, A., Sharma, S., Papanikolaou, P. and Hamilton, J., "Probing the thermal deoxygenation of graphene oxide using high-resolution in situ X-ray-based spectroscopies," *J. Phys. Chem. C*, **115**, 17009 (2011).
391. Haubner, K., Murawski, J., Olk, P., Eng, L.M., Ziegler, C., Adolphi, B. and Jaehne, E., "The route to functional graphene oxide," *ChemPhysChem*, **11**, 2131 (2010).
392. Liu, X., Zhan, D., Chao, D., Cao, B., Yin, J., Zhao, J., Li, Y., Lin, J. and Shen, Z., "Microwave-assisted production of giant graphene sheets for high performance energy storage applications," *J. Mater. Chem. A*, **2**, 12166 (2014).
393. Xiao, N., Lau, D., Shi, W., Zhu, J., Dong, X., Hng, H.H. and Yan, Q., "A simple process to prepare nitrogen-modified few-layer graphene for a supercapacitor electrode," *Carbon*, **57**, 184 (2013).
394. Eda, G. and Chhowalla, M., "Chemically derived graphene oxide: towards large-area thin-film electronics and optoelectronics," *Adv. Mater.*, **22**, 2392 (2010).
395. Solís-Fernández, P., Rozada, R., Paredes, J.I., Villar-Rodil, S., Fernández-Merino, M.J., Guardia, L., Martínez-Alonso, A. and Tascón, J.M.D., "Chemical and microscopic analysis of graphene prepared by different reduction degrees of graphene oxide," *J. Alloys Compd.*, **536S**, S532 (2012).

Bibliography

396. Rosenthal, D., Ruta, M., Schlögl, R. and Kiwi-Minsker, L., “Combined XPS and TPD study of oxygen-functionalized carbon nanofibers grown on sintered metal fibers,” *Carbon*, **48**, 1835 (2010).
397. Zhang, D., Zhang, X., Chen, Y., Wang, C. and Ma, Y., “An environmental-friendly route to synthesize reduced graphene oxide as a supercapacitor electrode material,” *Electrochim. Acta*, **69**, 364 (2012).
398. Campos-Delgado, J., Romo-Herrera, J.M., Jia, X., Cullen, D.A., Muramatsu, H., Kim, Y.A., Hayashi, T., Ren, Z., Smith, D.J., Okuno, Y., Ohba, T., Kanoh, H., Kaneko, K., Endo, M., Terrones, H., Dresselhaus, M.S. and Terrones, M., “Bulk production of a new form of sp^2 carbon: crystalline graphene nanoribbons,” *Nano Lett.*, **8**, 2773 (2008).
399. Punckt, C., Muckel, F., Wolff, S., Aksay, I.A., Chavarin, C.A., Bacher, G. and Mertin, W., “The effect of degree of reduction on the electrical properties of functionalized graphene sheets,” *Appl. Phys. Lett.*, **102**, 023114 (2013).
400. Rajagopalan, B. and Chung, J.S., “Reduced chemically modified graphene oxide for supercapacitor electrode,” *Nanoscale Res. Lett.*, **9**, 535 (2014).
401. Xiao, N., Lau, D., Shi, W., Zhu, J., Dong, X., Hng, H.H. and Yan, Q., “A simple process to prepare nitrogen-modified few-layer graphene for a supercapacitor electrode,” *Carbon*, **57**, 184 (2013).
402. Du, X., Zhou, C., Liu, H.-Y., Mai, Y.-W. and Wang, G., “Facile chemical synthesis of nitrogen-doped graphene sheets and their electrochemical capacitance,” *J. Power Sources*, **241**, 460 (2013).
403. Liu, M., Tjiu, W.W., Pan, J., Zhang, C., Gao, W. and Liu, T., “One-step synthesis of graphene nanoribbons– MnO_2 hybrids and their all-solid-state asymmetric supercapacitors,” *Nanoscale*, **6**, 4233 (2014).

Bibliography

404. Liu, M., Miao, Y.-E., Zhang, C., Tjiu, W.W., Yang, Z., Peng, H. and Liu, T., “Hierarchical composites of polyaniline-graphene nanoribbons-carbon nanotubes as electrode materials in all-solid-state supercapacitors,” *Nanoscale*, **5**, 7312 (2013).
405. Sahu, V., Grover, S., Tulachan, B., Sharma, M., Srivastva, G., Roy, M., Saxena, M., Sethy, N., Bhargava, K., Philip, D., Kim, H., Singh, G., Singh, S.K., Das, M. and Sharma, R.K., “Heavily nitrogen doped, graphene supercapacitor from silk cocoon,” *Electrochim. Acta*, **160**, 244 (2015).
406. Tian, Y., Wang, F., Liu, Y., Pang, F. and Zhang, X., “Green synthesis of silver nanoparticles on nitrogen-doped graphene for hydrogen peroxide detection,” *Electrochim. Acta*, **146**, 646 (2014).
407. Kaufman, J.H., Metin, S. and Saperstein, D.D., “Symmetry breaking in nitrogen-doped amorphous carbon: infrared observation of the Raman-active G and D bands,” *Phys. Rev. B.*, **39**, 13053 (1989).
408. Chang, D.W., Lee, K.E., Park, E.Y., Yu, H., Choi, H.-J., Jeon, I.-Y., Sohn, G.-J., Shin, D., Park, N., Oh, J.H., Dai, L. and Baek, J.-B., “Nitrogen-doped graphene nanoplatelets from simple solution edge-functionalization for n-type field-effect transistors,” *J. Am. Chem. Soc.*, **135**, 8981 (2013).
409. Bhat, S.A., Rather, M.A., Pandit, S.A., Ingole, P.P. and Bhat, M.A., “Oxides in silver-graphene nanocomposites: electrochemical signatures and electrocatalytic implications,” *Analyst*, **140**, 5601 (2015).
410. Shao, W., Liu, X., Min, H., Dong, G., Feng, Q. and Zuo, S., “Preparation, characterization, and antibacterial activity of silver nanoparticle-decorated graphene oxide nanocomposites,” *ACS Appl. Mater. Interfaces*, **7**, 6966 (2015).
411. Liu, G., Wang, Y., Pu, X., Jiang, Y., Cheng, L. and Jiao, Z., “One-step synthesis of high conductivity silver nanoparticle-reduced graphene oxide composite films by electron beam irradiation,” *Appl. Surf. Sci.*, **349**, 570 (2015).

Bibliography

412. Srinivas, G., Zhu, Y., Piner, R., Skipper, N., Ellerby, M. and Ruoff, R., "Synthesis of graphene-like nanosheets and their hydrogen adsorption capacity," *Carbon*, **48**, 630 (2010).
413. Lin, Z., Song, M.-k., Ding, Y., Liu, Y., Liu, M. and Wong, C.-p., "Facile preparation of nitrogen-doped graphene as a metal-free catalyst for oxygen reduction reaction," *Phys. Chem. Chem. Phys.*, **14**, 3381 (2012).
414. Kumar, N.A. and Baek, J.-B., "Doped graphene supercapacitors," *Nanotechnology*, **26**, 492001 (2015).
415. Wang, J., Zhao, Y., Ma, F.-X., Wang, K., Wang, F.-B. and Xia, X.-H., "Synthesis of a hydrophilic poly-L-lysine/graphene hybrid through multiple non-covalent interactions for biosensors," *J. Mater. Chem. B*, **1**, 1406 (2013).
416. Brady, O.L. and Elsmie, G.V., "The use of 2:4-dinitrophenylhydrazine as a reducing agent for aldehydes and ketones," *Analyst*, **51**, 77 (1926).
417. Mitchell, J., Kolthoff, I.M., Proskauer, E.S. and Weissberger, A., "Organic analysis," Interscience Publishers, New York (1961).
418. Lee, Y.-H., Chang, K.-H. and Hu, C.-C., "Differentiate the pseudocapacitance and double-layer capacitance contributions for nitrogen-doped reduced graphene oxide in acidic and alkaline electrolytes," *J. Power Sources*, **227**, 300 (2013).
419. Hassan, F.M., Chabot, V., Li, J., Kim, B.K., Richardez-Sandoval, L., Yu, A., "Pyrrolic-structure enriched nitrogen doped graphene for highly efficient next generation supercapacitors," *J. Mater Chem. A*, **1**, 2904 (2013).
420. Wang, T., Wang, L.-X., Wu, D.-L., Xia, W. and Jia, D.-Z., "Interaction between nitrogen and sulfur in co-doped graphene and synergetic effect in supercapacitor," *Sci. Rep.*, **5**, 9591 (2015).

Bibliography

421. Wang, D., Min, Y., Yu, Y. and Peng, B., “A general approach for fabrication of nitrogen-doped graphene sheets and its applications in supercapacitors,” *J. Colloid Interface Sci.*, **417**, 270 (2014).